BioMed Research International

Bioinformatics, Experimental and Computational Biology for Personalized Medicine in Chronic Diseases 2021

Lead Guest Editor: Bing Niu
Guest Editors: Jianxin Li, Zhiyu Zeng, Cheng Li, and Suren Rao Sooranna

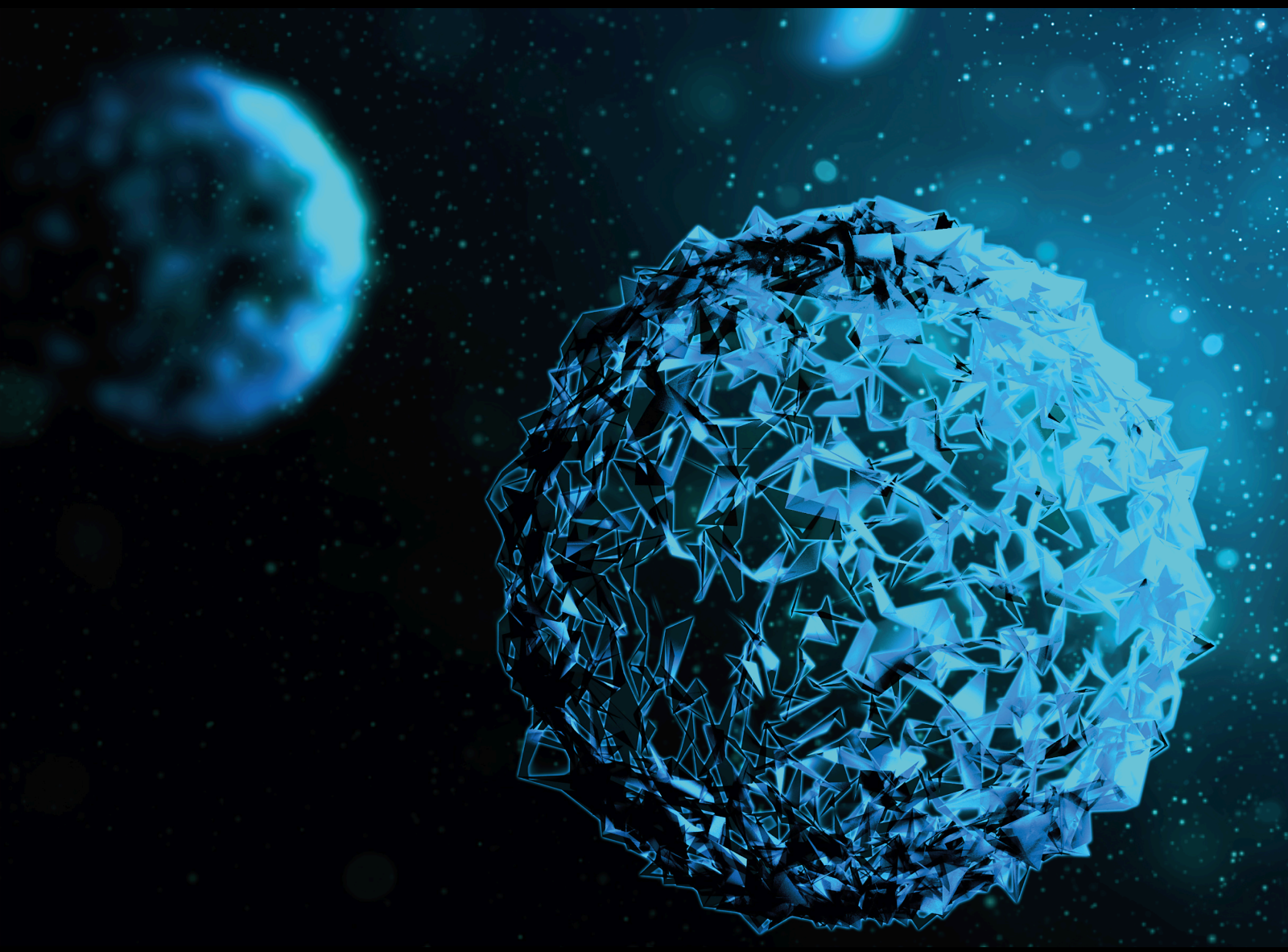

Bioinformatics, Experimental and Computational Biology for Personalized Medicine in Chronic Diseases 2021

BioMed Research International

Bioinformatics, Experimental and Computational Biology for Personalized Medicine in Chronic Diseases 2021

Lead Guest Editor: Bing Niu
Guest Editors: Jianxin Li, Zhiyu Zeng, Cheng Li, and Suren Rao Sooranna

Section Editors

Penny A. Asbell, USA
David Bernardo, Spain
Gerald Brandacher, USA
Kim Bridle, Australia
Laura Chronopoulou, Italy
Gerald A. Colvin, USA
Aaron S. Dumont, USA
Pierfrancesco Franco, Italy
Raj P. Kandpal, USA
Fabrizio Montecucco, Italy
Mangesh S. Pednekar, India
Letterio S. Politi, USA
Jinsong Ren, China
William B. Rodgers, USA
Harry W. Schroeder, USA
Andrea Scribante, Italy
Germán Vicente-Rodriguez, Spain
Momiao Xiong, USA
Hui Zhang, China

Academic Editors

Bioinformatics

Contents

Hindawi
BioMed Research International
Volume 2024, Article ID 9894173, 1 page
https://doi.org/10.1155/2024/9894173

Retraction

Retracted: Finite versus Indefinite Nucleos(t)ide Analogue Therapy of Patients with Chronic Hepatitis B Exhibiting Negative HBsAg Levels after Treatment

BioMed Research International

Received 12 March 2024; Accepted 12 March 2024; Published 20 March 2024

This article has been retracted by Hindawi following an investigation undertaken by the publisher [1]. This investigation has uncovered evidence of one or more of the following indicators of systematic manipulation of the publication process:

(1) Discrepancies in scope

(2) Discrepancies in the description of the research reported

(3) Discrepancies between the availability of data and the research described

(4) Inappropriate citations

(5) Incoherent, meaningless and/or irrelevant content included in the article

(6) Manipulated or compromised peer review

The presence of these indicators undermines our confidence in the integrity of the article's content and we cannot, therefore, vouch for its reliability. Please note that this notice is intended solely to alert readers that the content of this article is unreliable. We have not investigated whether authors were aware of or involved in the systematic manipulation of the publication process.

Wiley and Hindawi regrets that the usual quality checks did not identify these issues before publication and have since put additional measures in place to safeguard research integrity.

We wish to credit our own Research Integrity and Research Publishing teams and anonymous and named external researchers and research integrity experts for contributing to this investigation.

The corresponding author, as the representative of all authors, has been given the opportunity to register their agreement or disagreement to this retraction. We have kept a record of any response received.

References

[1] H. Sun, Y. Liu, Y. Zhang et al., "Finite versus Indefinite Nucleos(t)ide Analogue Therapy of Patients with Chronic Hepatitis B Exhibiting Negative HBsAg Levels after Treatment," *BioMed Research International*, vol. 2022, Article ID 6069781, 10 pages, 2022.

Hindawi
BioMed Research International
Volume 2024, Article ID 9845801, 1 page
https://doi.org/10.1155/2024/9845801

Retraction

Retracted: Comparison of Curative Complications between Mammotome-Assisted Minimally Invasive Resection and Conventional Open Resection for Breast Neoplasm: A Retrospective Clinical Study

BioMed Research International

Received 12 March 2024; Accepted 12 March 2024; Published 20 March 2024

This article has been retracted by Hindawi following an investigation undertaken by the publisher [1]. This investigation has uncovered evidence of one or more of the following indicators of systematic manipulation of the publication process:

(1) Discrepancies in scope

(2) Discrepancies in the description of the research reported

(3) Discrepancies between the availability of data and the research described

(4) Inappropriate citations

(5) Incoherent, meaningless and/or irrelevant content included in the article

(6) Manipulated or compromised peer review

The presence of these indicators undermines our confidence in the integrity of the article's content and we cannot, therefore, vouch for its reliability. Please note that this notice is intended solely to alert readers that the content of this article is unreliable. We have not investigated whether authors were aware of or involved in the systematic manipulation of the publication process.

Wiley and Hindawi regrets that the usual quality checks did not identify these issues before publication and have since put additional measures in place to safeguard research integrity.

We wish to credit our own Research Integrity and Research Publishing teams and anonymous and named external researchers and research integrity experts for contributing to this investigation.

The corresponding author, as the representative of all authors, has been given the opportunity to register their agreement or disagreement to this retraction. We have kept a record of any response received.

References

[1] R. Li, J. Li, S. Chen, B. Xiao, L. Liu, and N. Zhu, "Comparison of Curative Complications between Mammotome-Assisted Minimally Invasive Resection and Conventional Open Resection for Breast Neoplasm: A Retrospective Clinical Study," *BioMed Research International*, vol. 2021, Article ID 7739628, 4 pages, 2021.

Hindawi
BioMed Research International
Volume 2024, Article ID 9836392, 1 page
https://doi.org/10.1155/2024/9836392

Retraction

Retracted: Lineage Contribution of PDGFRα-Expressing Cells in the Developing Mouse Eye

BioMed Research International

Received 12 March 2024; Accepted 12 March 2024; Published 20 March 2024

This article has been retracted by Hindawi following an investigation undertaken by the publisher [1]. This investigation has uncovered evidence of one or more of the following indicators of systematic manipulation of the publication process:

(1) Discrepancies in scope

(2) Discrepancies in the description of the research reported

(3) Discrepancies between the availability of data and the research described

(4) Inappropriate citations

(5) Incoherent, meaningless and/or irrelevant content included in the article

(6) Manipulated or compromised peer review

The presence of these indicators undermines our confidence in the integrity of the article's content and we cannot, therefore, vouch for its reliability. Please note that this notice is intended solely to alert readers that the content of this article is unreliable. We have not investigated whether authors were aware of or involved in the systematic manipulation of the publication process.

Wiley and Hindawi regrets that the usual quality checks did not identify these issues before publication and have since put additional measures in place to safeguard research integrity.

We wish to credit our own Research Integrity and Research Publishing teams and anonymous and named external researchers and research integrity experts for contributing to this investigation.

The corresponding author, as the representative of all authors, has been given the opportunity to register their agreement or disagreement to this retraction. We have kept a record of any response received.

References

[1] D. Zhuo, Y. Diao, X. Li, Y. Huang, and L. Wang, "Lineage Contribution of PDGFRα-Expressing Cells in the Developing Mouse Eye," *BioMed Research International*, vol. 2021, Article ID 4982227, 10 pages, 2021.

Hindawi
BioMed Research International
Volume 2024, Article ID 9784929, 1 page
https://doi.org/10.1155/2024/9784929

Retraction

Retracted: A Bioinformatics Approach for the Prediction of Immunogenic Properties and Structure of the SARS-COV-2 B.1.617.1 Variant Spike Protein

BioMed Research International

Received 12 March 2024; Accepted 12 March 2024; Published 20 March 2024

This article has been retracted by Hindawi following an investigation undertaken by the publisher [1]. This investigation has uncovered evidence of one or more of the following indicators of systematic manipulation of the publication process:

(1) Discrepancies in scope

(2) Discrepancies in the description of the research reported

(3) Discrepancies between the availability of data and the research described

(4) Inappropriate citations

(5) Incoherent, meaningless and/or irrelevant content included in the article

(6) Manipulated or compromised peer review

The presence of these indicators undermines our confidence in the integrity of the article's content and we cannot, therefore, vouch for its reliability. Please note that this notice is intended solely to alert readers that the content of this article is unreliable. We have not investigated whether authors were aware of or involved in the systematic manipulation of the publication process.

Wiley and Hindawi regrets that the usual quality checks did not identify these issues before publication and have since put additional measures in place to safeguard research integrity.

We wish to credit our own Research Integrity and Research Publishing teams and anonymous and named external researchers and research integrity experts for contributing to this investigation.

The corresponding author, as the representative of all authors, has been given the opportunity to register their agreement or disagreement to this retraction. We have kept a record of any response received.

References

[1] V. K. Srivastava, S. Kaushik, G. Bhargava, A. Jain, J. Saxena, and A. Jyoti, "A Bioinformatics Approach for the Prediction of Immunogenic Properties and Structure of the SARS-COV-2 B.1.617.1 Variant Spike Protein," *BioMed Research International*, vol. 2021, Article ID 7251119, 8 pages, 2021.

Hindawi
BioMed Research International
Volume 2024, Article ID 9781094, 1 page
https://doi.org/10.1155/2024/9781094

Retraction

Retracted: Analgesic Effects of Different κ-Receptor Agonists Used in Daytime Laparoscopic Cholecystectomy

BioMed Research International

Received 12 March 2024; Accepted 12 March 2024; Published 20 March 2024

This article has been retracted by Hindawi following an investigation undertaken by the publisher [1]. This investigation has uncovered evidence of one or more of the following indicators of systematic manipulation of the publication process:

(1) Discrepancies in scope

(2) Discrepancies in the description of the research reported

(3) Discrepancies between the availability of data and the research described

(4) Inappropriate citations

(5) Incoherent, meaningless and/or irrelevant content included in the article

(6) Manipulated or compromised peer review

The presence of these indicators undermines our confidence in the integrity of the article's content and we cannot, therefore, vouch for its reliability. Please note that this notice is intended solely to alert readers that the content of this article is unreliable. We have not investigated whether authors were aware of or involved in the systematic manipulation of the publication process.

Wiley and Hindawi regrets that the usual quality checks did not identify these issues before publication and have since put additional measures in place to safeguard research integrity.

We wish to credit our own Research Integrity and Research Publishing teams and anonymous and named external researchers and research integrity experts for contributing to this investigation.

The corresponding author, as the representative of all authors, has been given the opportunity to register their agreement or disagreement to this retraction. We have kept a record of any response received.

References

[1] W. Zhou, J. Wang, C. Hu et al., "Analgesic Effects of Different κ-Receptor Agonists Used in Daytime Laparoscopic Cholecystectomy," *BioMed Research International*, vol. 2021, Article ID 2396008, 8 pages, 2021.

Hindawi
BioMed Research International
Volume 2024, Article ID 9894173, 1 page
https://doi.org/10.1155/2024/9894173

Retraction

Retracted: Finite versus Indefinite Nucleos(t)ide Analogue Therapy of Patients with Chronic Hepatitis B Exhibiting Negative HBsAg Levels after Treatment

BioMed Research International

Received 12 March 2024; Accepted 12 March 2024; Published 20 March 2024

This article has been retracted by Hindawi following an investigation undertaken by the publisher [1]. This investigation has uncovered evidence of one or more of the following indicators of systematic manipulation of the publication process:

(1) Discrepancies in scope

(2) Discrepancies in the description of the research reported

(3) Discrepancies between the availability of data and the research described

(4) Inappropriate citations

(5) Incoherent, meaningless and/or irrelevant content included in the article

(6) Manipulated or compromised peer review

The presence of these indicators undermines our confidence in the integrity of the article's content and we cannot, therefore, vouch for its reliability. Please note that this notice is intended solely to alert readers that the content of this article is unreliable. We have not investigated whether authors were aware of or involved in the systematic manipulation of the publication process.

Wiley and Hindawi regrets that the usual quality checks did not identify these issues before publication and have since put additional measures in place to safeguard research integrity.

We wish to credit our own Research Integrity and Research Publishing teams and anonymous and named external researchers and research integrity experts for contributing to this investigation.

The corresponding author, as the representative of all authors, has been given the opportunity to register their agreement or disagreement to this retraction. We have kept a record of any response received.

References

[1] H. Sun, Y. Liu, Y. Zhang et al., "Finite versus Indefinite Nucleos(t)ide Analogue Therapy of Patients with Chronic Hepatitis B Exhibiting Negative HBsAg Levels after Treatment," *BioMed Research International*, vol. 2022, Article ID 6069781, 10 pages, 2022.

Hindawi
BioMed Research International
Volume 2022, Article ID 6069781, 10 pages
https://doi.org/10.1155/2022/6069781

Research Article

Finite versus Indefinite Nucleos(t)ide Analogue Therapy of Patients with Chronic Hepatitis B Exhibiting Negative HBsAg Levels after Treatment

Haixia Sun,[1] Yinhui Liu,[2] Yufeng Zhang,[1] Yusheng Jie,[1] Yuankai Wu,[1] Zhanyi Li,[1] Xuxia Wei,[3] and Xiangyong Li[1]

[1]*Department of Infectious Diseases, The Third Affiliated Hospital of Zhongshan University, No. 600 Tianhe Road, Guangzhou, 510000 Guangdong, China*
[2]*Department of Infectious Diseases, People's Hospital of Foshan Sanshui District, No. 16 Southwest Guanghai Avenue West, Foshan 528100, Guangdong Province, China*
[3]*Department of Surgical Intensive Care Unit, The Third Affiliated Hospital of Zhongshan University, No. 600 Tianhe Road, Guangzhou, 510000 Guangdong, China*

Correspondence should be addressed to Xuxia Wei; weixuxia06@163.com and Xiangyong Li; lxy2005123@126.com

Received 11 July 2021; Revised 14 December 2021; Accepted 17 December 2021; Published 15 July 2022

Academic Editor: Bing Niu

Aim. To determine whether a decrease in HBsAg to <0.05 IU/mL could be a criterion for cessation of finite nucleos(t)ide analogue (NUC) therapy in patients with chronic hepatitis B (CHB). *Methods*. This was a retrospective analysis of 6715 patients with CHB between January 1998 and May 2016. Patients were followed up every 12–24 weeks. Among 104 patients achieving HBsAg levels < 0.05 IU/mL, 71 were eligible for inclusion in the analysis: 31 received finite NUC therapy, and 40 received indefinite NUC therapy. In the finite therapy group, 9 patients received no NUC consolidation therapy, 6 received short-term (<1 year) consolidation, and 16 received long-term (>1 year) consolidation. The outcome measures were alanine aminotransferase (ALT), total bilirubin, albumin, hepatitis B virus DNA, and HBsAg levels. *Results*. Baseline parameters and characteristics at the time when HBsAg levels had fallen to <0.05 IU/mL were similar between the finite and indefinite therapy groups. No patients experienced viral breakthrough/relapse during a median follow-up of 120 weeks. There were little or no differences in long-term outcomes between the finite and indefinite therapy groups and between the short-term and long-term consolidation groups. *Conclusions*. Discontinuation of NUCs may be acceptable in patients whose HBsAg levels fall to <0.05 IU/mL. Consolidation therapy lasting <1 year appears adequate to prevent poor long-term prognosis.

1. Introduction

Clinical decision-making regarding the discontinuation of nucleos(t)ide analogue (NUC) therapy in patients with chronic hepatitis B (CHB) has recently become a subject of heated debate [1–3]. Conflicting factors that complicate whether to discontinue NUC therapy include the risks of viral breakthrough and relapse, hepatocellular carcinoma (HCC), liver cirrhosis, and patient preference [4, 5]. The ideal outcomes of NUC therapy are a sustained off-treatment viral response, normal alanine aminotransferase (ALT) level, and persistently reduced risk of HCC [1–3, 6, 7]. However, these outcomes are often difficult to achieve due to the stable integration of the covalently closed circular DNA into the host genome [8].

Finite therapy with NUCs is an attractive strategy because indefinite use of NUCs is limited by several factors such as the economic burden of a long treatment course, risk of nonadherence to treatment, incidence of viral breakthrough, and increasing risk of adverse effects with increasing treatment time [1–3]. Nevertheless, viral relapse and consequent exacerbation of hepatitis after cessation of NUCs are nonnegligible risks of the finite approach to treatment [9, 10]. The key requirement for finite therapy is the

identification of an evidence-based marker for discontinuation. For hepatitis B e antigen- (HBeAg-) positive patients, HBeAg seroconversion was considered a potential marker for NUC discontinuation [1]. Unfortunately, several studies have demonstrated that a large proportion of patients experience viral relapse and elevations of ALT upon discontinuation of NUC treatment following HBeAg seroconversion [1, 7, 8, 11]. As an alternative criterion, loss of hepatitis B surface antigen (HBsAg) was found to be a much safer potential endpoint since NUC discontinuation after loss of HBsAg did not result in adverse events in most cases [5]. However, no studies have directly compared finite and indefinite NUC therapy for patients achieving HBsAg loss following treatment. In addition, recent technological advances now allow the detection of very low levels of HBsAg, whereas previous guidelines relied on detection thresholds that may not have reliably identified the loss of HBsAg [2–4, 6].

Prospective trials to investigate this issue are unfeasible because of the low frequency and unpredictability of the endpoints. Therefore, the present retrospective study is aimed at determining whether a decrease in HBsAg to very low levels (<0.05 IU/mL) could be used as a marker for cessation of NUC therapy by comparing the benefits and outcomes of the finite and indefinite approaches.

2. Methods

2.1. Study Design and Patients. This was a retrospective analysis of consecutive patients with CHB seen at our hospital (Guangzhou, China) between January 1998 and May 2016. This study was approved by the Clinical Ethics Review Board at our hospital. Written informed consent was obtained from all patients at the time of recruitment.

The inclusion criteria were as follows: (1) age ≥ 18 years; (2) HBsAg-positive for more than 6 months; (3) met the indications for antiviral therapy described in the guidelines for the prevention and treatment of CHB drawn up by the Chinese Society of Hepatology and the Chinese Society of Infectious Diseases (Chinese Medical Association); (4) received NUCs at our hospital according to the applicable guidelines at the time of recruitment [2–6]; and (5) HBsAg levels fell to < 0.05 IU/mL (considered as HBsAg-negative) during NUC therapy. The exclusion criteria were as follows: (1) coinfection with another hepatitis virus; (2) coexistence of alcoholic, drug-induced, or autoimmune liver disease; (3) pregnant or breast-feeding woman; (4) liver cirrhosis; (5) liver cancer; (6) lost to follow-up; and (7) inadequate serum available for analysis.

2.2. Follow-Up. All patients were followed up at intervals of 12–24 weeks. Serum levels of hepatitis B virus (HBV) DNA, HBsAg, HBeAg, ALT, albumin, and total bilirubin were tested at each follow-up visit. The last follow-up was on 31 March 2016.

2.3. Data Collection. Age, gender, diagnosis of fatty liver, HBeAg status, and serum levels of ALT, albumin, total bilirubin, and HBV DNA were documented at each follow-up. Serum levels of HBV DNA, HBsAg, HBeAg, and anti-HBe were reanalyzed using serum samples stored at -80°C to avoid potential bias caused by the use of different testing techniques during follow-up. HBV DNA levels were measured using a real-time PCR assay (DAAN Gene Co., Ltd., Guangzhou, China), which had a detection threshold of 100 IU/mL. HBsAg, HBeAg, and anti-HBe were measured using commercially available chemiluminescence assay kits (Roche Diagnostics, Indianapolis, IN, USA).

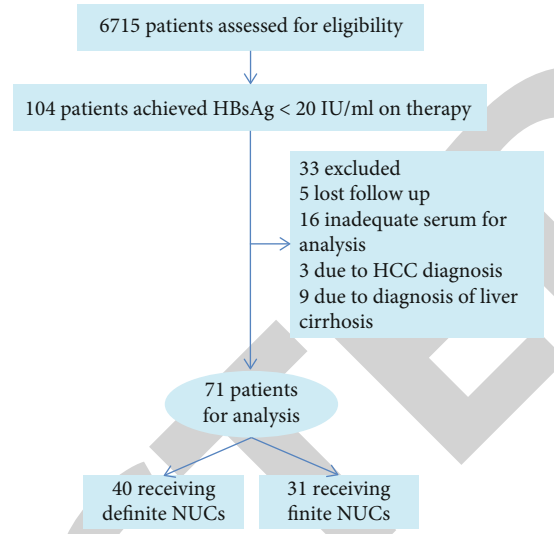

Figure 1: Patient enrolment. HBsAg: hepatitis B surface antigen; HCC: hepatocellular carcinoma; NUCs: nucleos(t)ide analogues.

2.4. Definitions of Treatment Approaches. Finite treatment was defined as a finite duration of NUC therapy after the patient had achieved HBsAg level < 0.05 IU/mL with or without consolidation therapy. Indefinite treatment was defined as the continuous administration of NUCs without interruption or cessation. Consolidation therapy was defined as prolonged uninterrupted administration of NUCs after the HBsAg level had fallen to <0.05 IU/mL in patients undergoing finite NUC therapy. Short-term consolidation was defined as consolidation therapy lasting <1 year, while long-term consolidation was defined as consolidation therapy for ≥1 year.

2.5. Outcome Measures. The outcome after discontinuation of therapy was classified as either "sustained response" or "virological relapse." Sustained response was defined as a serological, virological, and biochemical response that was sustained after cessation of therapy [7]. Virological relapse was defined as off-therapy HBV DNA levels > 2000 IU/mL in at least two measurements performed >4 weeks apart. Virological breakthrough was defined as HBV DNA levels > 2000 IU/mL in at least two determinations performed >2 weeks apart during NUC therapy [8]. Abnormal levels of ALT, albumin, and total bilirubin were defined as levels greater than the upper limits of normal.

2.6. Statistical Analysis. Normally distributed continuous variables are presented as the mean ± standard deviation and were analyzed using Student's t-test. Nonnormally distributed variables are presented as median (range) and were analyzed using the Mann–Whitney U test. Categorical

Table 1: Demographic and clinical characteristics of the patients.

Characteristic	Indefinite NUC group ($n = 40$)	Finite NUC group ($n = 31$)	P
Gender			0.999
Male	34 (85.0%)	27 (87.1%)	
Female	6 (15.0%)	4 (12.9%)	
Fatty liver	12 (30.0%)	10 (32.3%)	0.999
Initial NUC used			0.316
Lamivudine	11 (27.5%)	12 (38.7%)	
Entecavir	11 (27.5%)	9 (29.0%)	
Telbivudine	14 (35.0%)	5 (16.1%)	
Adefovir	4 (10.0%)	5 (16.1%)	
At start of NUC therapy			
Age (years)	41.2 (27.3–78.9)	38.9 (19.67–61.84)	0.397
HBeAg-positive	19 (47.5%)	16 (51.6%)	0.917
HBV DNA (copies/mL)	3.86×10^5 (4.90×10^2–6.82×10^7)	1.52×10^6 (1.00×10^3–4.6×10^8)	0.059
ALT (U/L)	113 (7–2293)	85 (21–752)	0.664
Albumin (g/L)	44 (30.1–49)	45.0 (35.8–51.8)	0.128
Total bilirubin (μmol/L)	15.39 (4.7–75.4)	17.9 (5.4–45.9)	0.423
At HBsAg reaching <0.05 IU/mL			
Age (years)	45.8 (29.4–79.4)	47.4 (28.1–65.5)	0.531
Time for HBsAg to reach <0.05 IU/mL (weeks)	240 (1–672)	192 (12–480)	0.848
ALT (U/L)	29.5 (12–84)	24 (13–65)	0.407
Albumin (g/L)	45.9 (31.9–53)	47 (31.5–50.1)	0.118
Total bilirubin (μmol/L)	12.8 (5.7–28.9)	14.4 (7.3–42.5)	0.958

Data are presented as n (%) or median (range). ALT: alanine aminotransferase; HBeAg: Hepatitis B e antigen; HBsAg: hepatitis B surface antigen; HBV: hepatitis B virus; NUC: nucleos(t)ide analogue.

Table 2: Characteristics of the patients in the finite NUC group at the time when HBsAg reached <0.05 IU/mL and the time when NUC therapy was withdrawn.

Characteristic	NUC withdrawal	HBsAg < 0.05 IU/mL	P
Age (years)	47.4 (28.1–65.5)	44.9 (25.7–65.5)	0.668
ALT (U/L)	24 (13–65)	27.5 (13–106)	0.756
Albumin (g/L)	47 (31.5–50.1)	46.9 (32.5–49.9)	0.822
Total bilirubin (μmol/L)	14.4 (7.3–42.5)	13.7 (5.6–48.0)	0.927

variables are presented as frequencies and were analyzed using the chi-squared test or Fisher's exact test, as appropriate. Statistical analysis was performed using SPSS 20.0 (IBM Corp., Armonk, NY, USA). Two-sided P values < 0.05 were considered statistically significant.

3. Results

3.1. Characteristics of the Patients. A total of 6715 patients were assessed for eligibility, and 104 of these achieved HBsAg < 0.05 IU/mL during treatment with NUCs. Thirty-three of these 104 patients were excluded for the following reasons: inadequate serum for analysis ($n = 16$), liver cirrhosis ($n = 9$), lost to follow-up ($n = 5$), and hepatocellular carcinoma ($n = 3$). Therefore, 71 patients were eligible for this analysis (Figure 1). Among the 71 patients included in the final analysis, 31 received finite NUC therapy (finite NUC group) and 40 received indefinite NUC therapy (indefinite NUC group).

The baseline demographic and clinical characteristics did not differ significantly between the two groups of patients, both at the time when NUC therapy was started and at the time when the HBsAg level fell to <0.05 IU/mL (Table 1). Moreover, the baseline characteristics remained unchanged when the patients in the finite NUC group discontinued NUCs after different durations of consolidation therapy (Table 2). The 71 patients included in the analysis were followed up for a median of 120 weeks (range: 24–240 weeks).

3.2. Indefinite NUC Therapy Did Not Improve Long-Term Outcomes Compared with Finite NUC Therapy. The long-term outcomes for finite and indefinite treatment with NUCs were compared to determine the benefits of a finite treatment approach for patients achieving very low levels

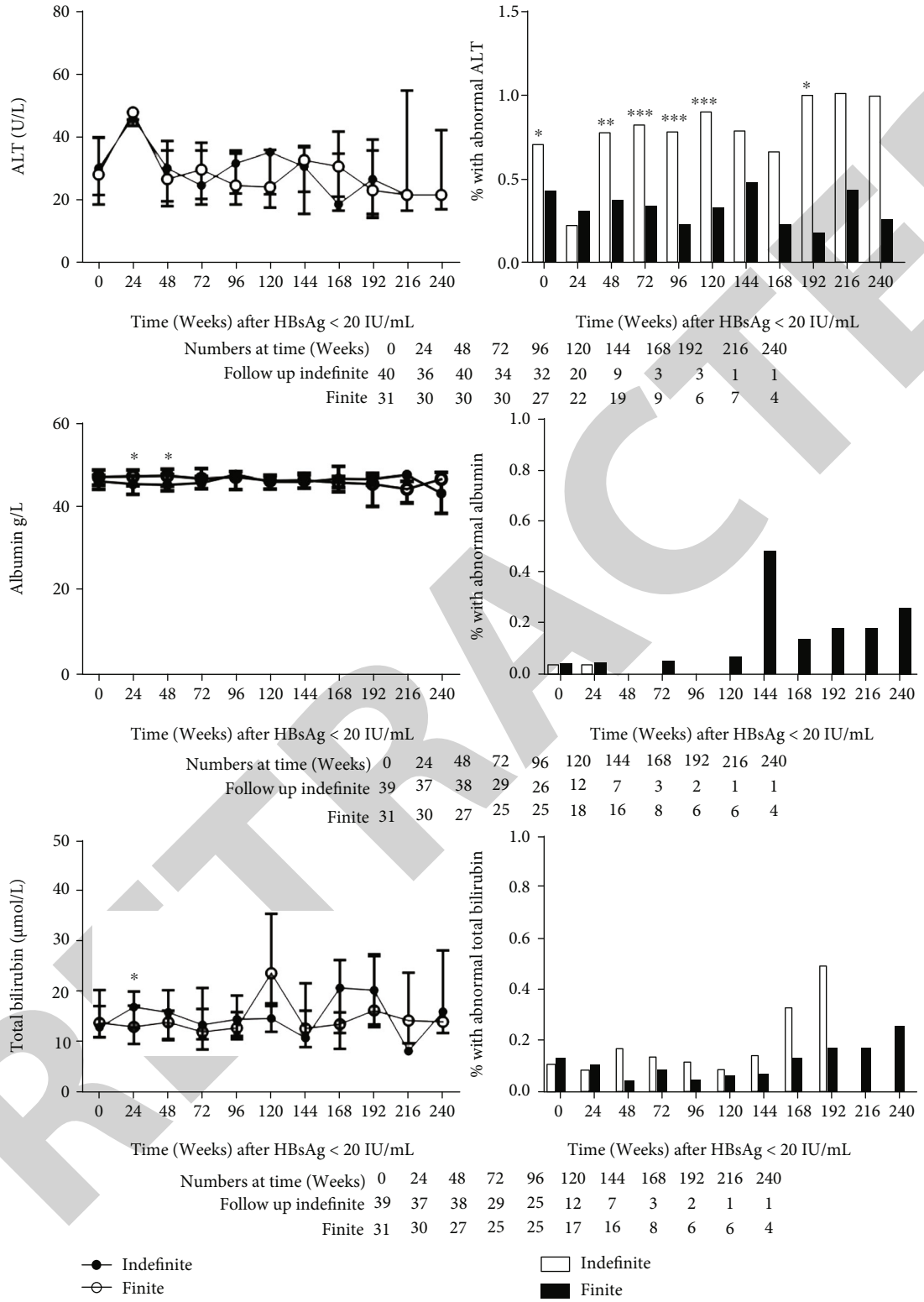

Figure 2: Long-term outcomes of patients with chronic hepatitis B given finite or indefinite NUC therapy after HBsAg had reached < 0.05 IU/mL. $^{*}P < 0.05$, $^{**}P < 0.01$, and $^{***}P < 0.001$. ALT: alanine aminotransferase; HBsAg: hepatitis B surface antigen; NUCs: nucleos(t)ide analogues.

of HBsAg. None of the patients in either treatment group experienced viral breakthrough/relapse once HBsAg levels had fallen below 0.05 IU/mL; only one patient in the finite NUC group exhibited a transient increase in HBsAg levels, but this was without consequence and did not require the readministration of NUCs. ALT levels were not significantly

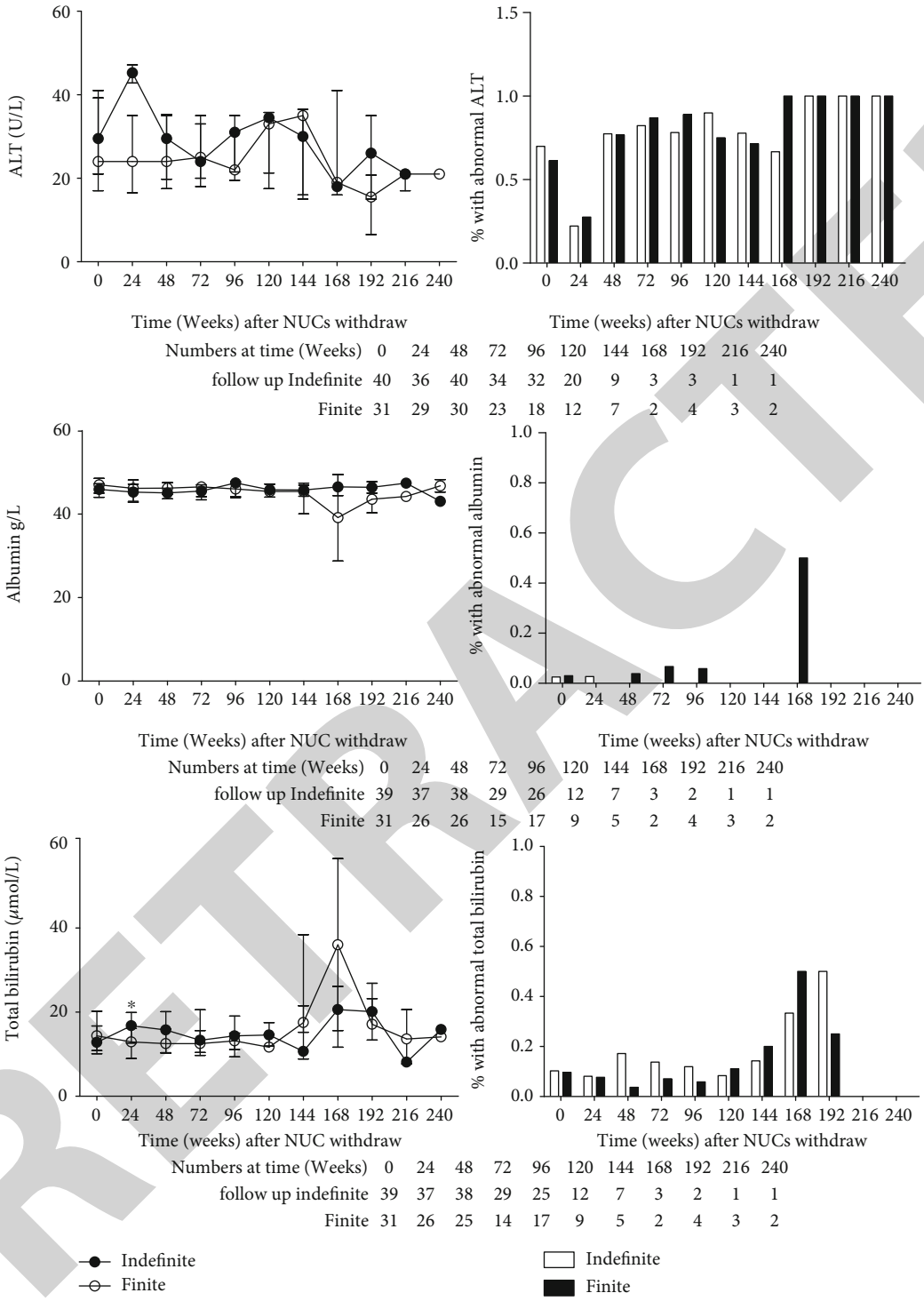

Figure 3: Long-term outcomes of patients with chronic hepatitis B given finite NUC therapy that was withdrawn when HBsAg reached < 0.05 IU/mL or indefinite NUC therapy after HBsAg reached <0.05 IU/mL. $^*P < 0.05$. ALT: alanine aminotransferase; HBsAg: hepatitis B surface antigen; NUCs: nucleos(t)ide analogues.

different between the two groups (Figure 2). However, patients receiving indefinite NUC therapy exhibited a higher incidence of abnormalities than those in the finite treatment group ($P < 0.05$ at the start of treatment and $P < 0.01$ after 48, 72, 96, and 120 weeks of follow-up; Figure 2). Albumin levels were slightly lower in the indefinite treatment group at 24 and 48 weeks after HBsAg had fallen to <0.05 IU/mL ($P < 0.05$; Figure 2). Total bilirubin levels showed a significant increase in the finite treatment group at 24 weeks after HBsAg had reached <0.05 IU/mL ($P < 0.05$), but overall, the total bilirubin levels and rates of abnormality were similar between the two groups (Figure 2).

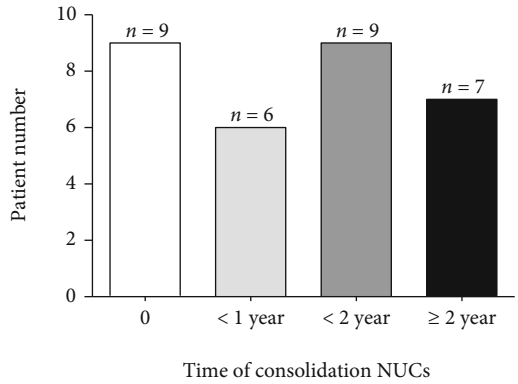

Figure 4: Distribution of the duration of NUC consolidation therapy after HBsAg had fallen to <0.05 IU/mL in the finite NUC group. NUCs: nucleos(t)ide analogues; HBsAg: hepatitis B surface antigen.

Table 3: Characteristics of the patients in the finite NUC group with short-term (<1 year) or long-term (≥1 year) consolidation therapy with NUCs.

Characteristic	Short-term NUC consolidation ($n = 15$)	Long-term NUC consolidation ($n = 16$)	P
Gender			0.043
Male	11 (73.3%)	0 (0.0%)	
Female	4 (26.7%)	16 (100.0%)	
Fatty liver	3 (20.0%)	7 (43.8%)	0.252
Initial NUC used			0.491
Lamivudine	7 (46.7%)	5 (31.2%)	
Entecavir	4 (26.7%)	5 (31.2%)	
Telbivudine	1 (6.7%)	4 (25.0%)	
Adefovir	3 (20.0%)	2 (12.5%)	
At start of NUC therapy			
Age (years)	43.7 (23.3–61.8)	36.5 (19.7–60.1)	0.247
HBeAg-positive	6 (40.0%)	10 (62.5%)	0.372
HBV DNA (copies/mL)	5.84×10^5 (1.00×10^3–1.00×10^8)	3.77×10^6 (1.00×10^3–4.60×10^8)	0.101
ALT (U/L)	76 (21–752)	91 (25–752)	0.470
Albumin (g/L)	45 (40.8–51.8)	44.2 (35.8–49.7)	0.281
Total bilirubin (μmol/L)	20.5 (9.6–45.9)	15.8 (5.4–39.5)	0.188
At HBsAg reaching <0.05 IU/mL			
Age (years)	48.2 (32.6–65.5)	41.0 (28.1–65.1)	0.323
Time for HBsAg to reach <0.05 IU/mL (weeks)	192 (12–480)	192 (60–408)	0.705
ALT (U/L)	21 (13–51)	28 (14–65)	0.066
Albumin (g/L)	47.0 (42.7–49.9)	47.4 (31.5–50.1)	0.843
Total bilirubin (μmol/L)	14.8 (7.3–26.7)	13.7 (7.5–42.5)	0.812
At withdraw of NUCs			
Age (years)	48.2 (32.6–65.5)	39.7 (25.7–62.9)	0.167
ALT (U/L)	21 (13–106)	35 (17–73)	0.050
Albumin (g/L)	47 (42.7–49.9)	46.6 (32.5–49.7)	0.874
Total bilirubin (μmol/L)	14.2 (7.5–26.7)	12.7 (5.6–48.0)	0.678

Data are presented as n (%) or median (range). ALT: alanine aminotransferase; HBeAg: Hepatitis B e antigen; HBsAg: hepatitis B surface antigen; HBV: hepatitis B virus; NUC: nucleos(t)ide analogue.

To avoid bias caused by different consolidation periods, the prognoses of the patients in the finite NUC group after discontinuation of therapy were compared with the prognoses of patients in the indefinite treatment group. ALT levels, albumin levels, and the rates of abnormality in ALT and albumin levels were not significantly different between the two groups (Figure 3). Total bilirubin levels were higher in the indefinite NUC group at 24 weeks after HBsAg had reached very low levels than in the finite NUC group at 24 weeks after NUC withdrawal ($P < 0.05$), although no

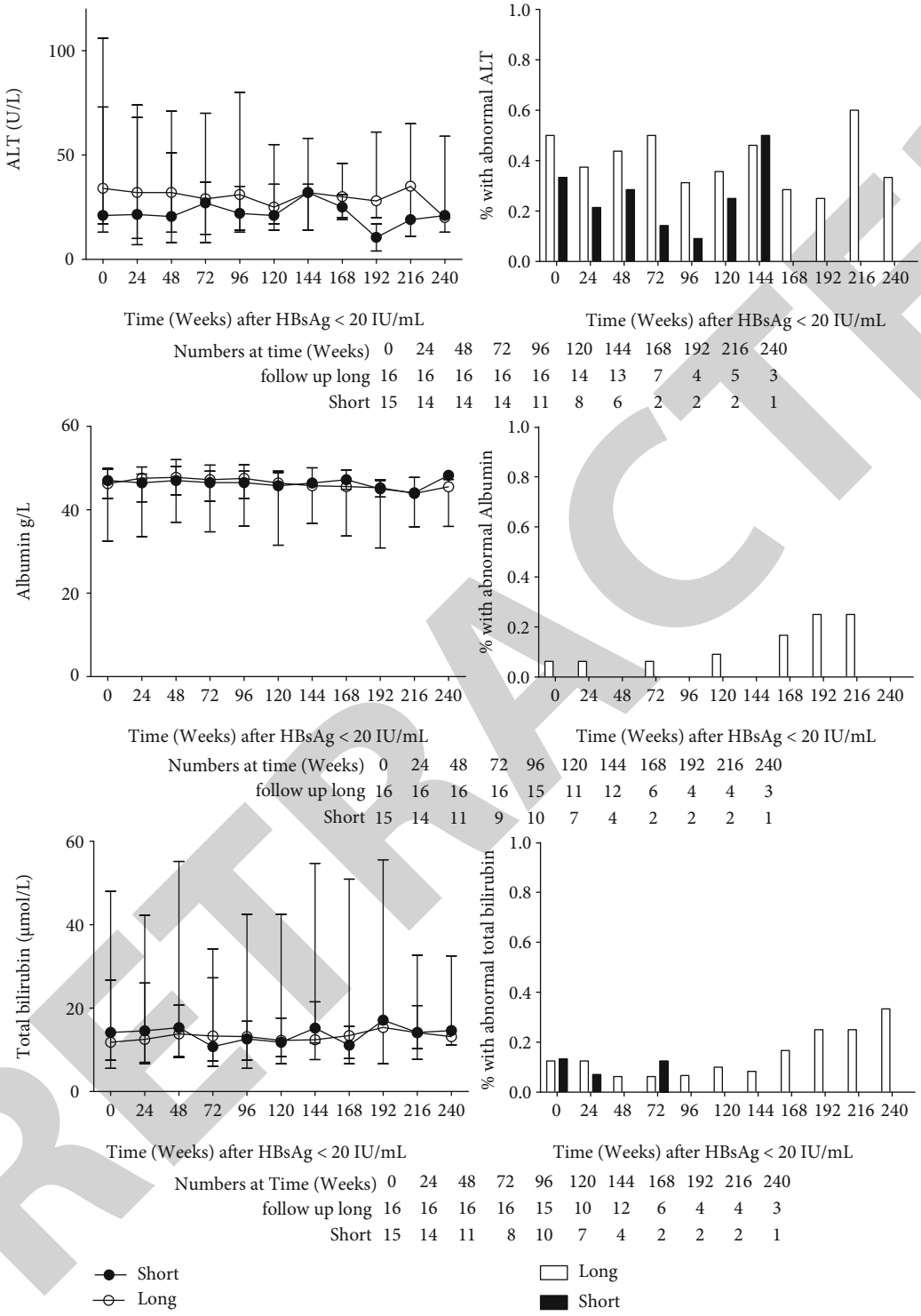

Figure 5: Long-term outcomes of patients with chronic hepatitis B given long-term or short-term consolidation therapy with NUCs after HBsAg had reached <0.05 IU/mL. ALT: alanine aminotransferase; HBsAg: hepatitis B surface antigen; NUCs: nucleos(t)ide analogues.

significant differences were observed at all other time points (Figure 3). Furthermore, both groups had similar rates of abnormality in total bilirubin level (Figure 3).

3.3. Baseline Characteristics of the Finite NUC Group according to the Duration of the Consolidation Therapy with NUCs. In the finite treatment group, 9 patients did not receive consolidation therapy; i.e., NUC therapy was discontinued when their HBsAg levels reached <0.05 IU/mL. Among those patients in the finite treatment group receiving consolidation with NUCs, 6 patients received short-term (<1 year) consolidation therapy while 16 patients were given long-term (≥1 year) consolidation therapy (Figure 4). Seven of the 16 patients receiving long-term consolidation therapy

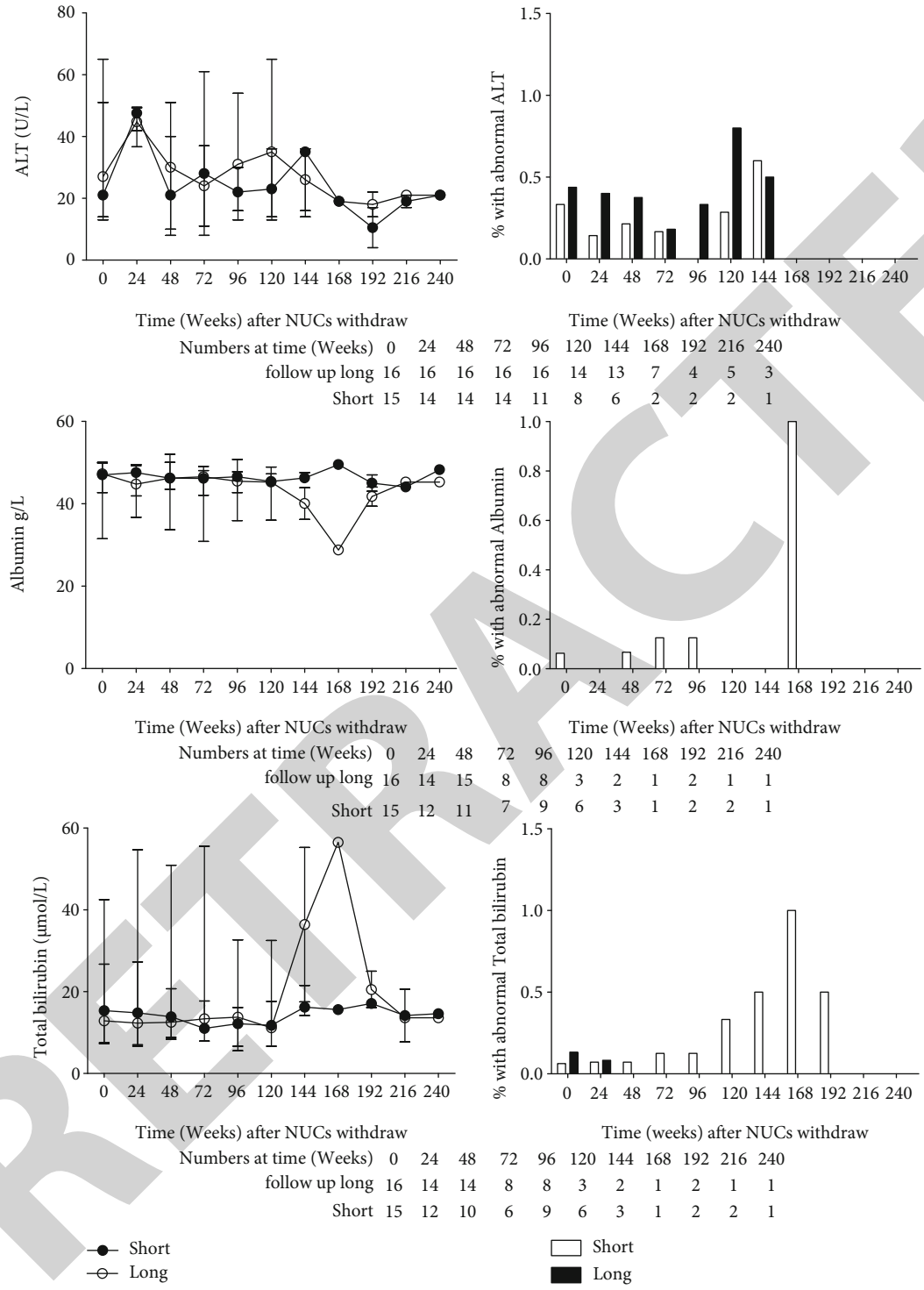

Figure 6: Long-term outcomes of patients with chronic hepatitis B after withdrawal of long-term or short-term consolidation therapy with NUCs. ALT: alanine aminotransferase; HBsAg: hepatitis B surface antigen; NUCs: nucleos(t)ide analogues.

were given >2 years of treatment (Figure 4). Although the long-term consolidation therapy group had a lower proportion of male patients than the short-term consolidation therapy group (0.0% vs. 73.3%, $P = 0.043$), the other baseline characteristics did not differ significantly between groups both at the time when the HBsAg level reached <0.05 IU/mL and at the time of NUC discontinuation (Table 3).

3.4. Long-Term NUC Consolidation Therapy Does Not Improve Long-Term Outcomes Compared with Short-Term NUC Consolidation Therapy. Assessment of long-term outcomes revealed that the ALT, total bilirubin, and albumin levels were similar between the short-term consolidation therapy group and long-term consolidation therapy group (Figures 5 and 6).

4. Discussion

The aim of the present study was to compare finite versus indefinite NUC therapy in patients with CHB who had achieved HBsAg levels < 0.05 IU/mL following treatment. The results suggest that discontinuation of NUCs may be acceptable in patients whose HBsAg levels fall to <0.05 IU/mL. Furthermore, consolidation therapy lasting <1 year appears to be adequate in the prevention of a poor long-term prognosis.

An important finding of this study was that indefinite NUC therapy did not provide any additional benefits compared with finite NUC therapy during a median follow-up of 120 weeks. None of the patients in the finite NUC group experienced viral relapse upon discontinuation of the treatment and none required the readministration of NUCs. Since most patients in the finite NUC group received consolidation therapy of varying durations, the outcomes of the finite and indefinite treatment strategies were compared using withdrawal of the NUCs as the start of the follow-up for the finite NUC group; the results of this analysis indicated that the outcomes were similar between groups. Previous studies of the outcomes of patients with HBsAg conversion reported safety profiles that agreed with our findings [5, 12], but it must be stressed that there were several differences between the studies in terms of the study population (country, ethnicity, life habits, and healthcare system) and study design. Nevertheless, in the systematic review by Chang et al. [12], the clinical benefits and risks were found to be similar between the finite and indefinite treatment approaches, consistent with the observations of the present study. Nonetheless, defining an appropriate criterion for withdrawal of NUC therapy will be critical for the successful implementation of a finite NUC treatment strategy in clinical practice [12]. Based on the data in the present study, discontinuation of NUCs after the HBsAg level reaches < 0.05 IU/mL could be an acceptable treatment strategy, especially when the nonclinical benefits of the finite approach, such as lower cost and better adherence to treatment, are taken into consideration.

The duration of any NUC consolidation therapy after achieving the criterion for cessation of treatment is another issue that must be addressed when optimizing the finite therapy approach [6, 7]. Previous guidelines have suggested the use of 6–12 months of NUC consolidation therapy after HBeAg seroconversion [1–3], but there is no evidence-based suggestion for discontinuation of finite therapy after the loss of HBsAg. In the present study, long-term consolidation with NUCs (>1 year) did not improve patient outcomes compared with short-term consolidation (<1 year). Notably, 9 (60%) of the patients in the finite NUC group received no consolidation therapy at all, suggesting that elimination of NUC therapy when HBsAg levels fall below 0.05 IU/mL could be an acceptable choice.

A number of laboratory methods and brands are available to measure HBsAg, and there is variability among them [13]. Therefore, additional research is needed to assess whether these various techniques are sufficiently similar to each other or whether standardization of the methodology is required.

The optimal experimental design to identify the endpoint of finite NUC therapy would be a randomized clinical trial. However, the potential endpoints currently under study do not occur frequently and are hard to predict, making a randomized clinical trial an impractical and uneconomical study design. For this reason, cohort studies and retrospective analyses make up the majority of completed studies in this field. Other limitations of this study also have to be considered. The sample size was small because of the rarity of loss of HBsAg, and the patients were from a single center. In addition, it was not possible to analyze some markers because their data were not included in the original database.

5. Conclusions

In conclusion, discontinuation of NUC therapy in patients with CHB could be acceptable in those in whom the HBsAg level falls to <0.05 IU/mL. Furthermore, consolidation therapy lasting <1 year could be adequate for the prevention of a poor long-term prognosis.

Data Availability

The data set supporting the results of this article is included within the article.

Conflicts of Interest

The authors declare that there is no conflict of interest regarding the publication of this paper.

Authors' Contributions

Haixia Sun and Yinhui Liu contributed equally to this study and share first authorship.

Acknowledgments

This study was supported by grants from Science and Technology Planning Project of Guangdong Province, China (2019B020228001); National Key Research and Development Program (2018YFC1315400); National Natural Science Foundation of China (81773176); Sun Yat-sen University Clinical Research 5010 Programme (2016009); Science and Technology Program of Guangzhou, China (201804010474); Natural Science Foundation of Guangdong (2018A030310272); Guangdong Medical Science and Technology Research Fund (A2018366); "3rd Affiliated Hospital of Sun Yat-sen University, Clinical Research Program (P000-277); and Meizhou Science and Technology Project (2019B0203003).

Supplementary Materials

Two statistical databases (PDF) of this study have been placed in supplementary files. *(Supplementary Materials)*

References

[1] S. Shen, G. L. Wong, Z. Kuang et al., "Development and validation of a model for hepatitis B e antigen seroconversion in

Hindawi
BioMed Research International
Volume 2022, Article ID 4304419, 9 pages
https://doi.org/10.1155/2022/4304419

Research Article

Tex264 Binding to SNX27 Regulates Itgα5 Receptor Membrane Recycling and Affects Cell Migration

Xiao-hui Xu,[1,2] **Qian-wen Yang**,[2] **Chang-ling Yue**,[2] **Yun-yi Zhu**,[2] **and Zhao-huan Zhang**[3]

[1]*School of Preclinical Medicine, Wannan Medical College, Wuhu 241002, China*
[2]*School of Life Sciences, Shanghai University, Shanghai 200444, China*
[3]*Department of Laboratory Medicine, Changzheng Hospital, Naval Medical University, Shanghai 200003, China*

Correspondence should be addressed to Zhao-huan Zhang; zhaohuanpost2016@163.com

Xiao-hui Xu, Qian-wen Yang, and Chang-ling Yue contributed equally to this work.

Received 3 January 2022; Accepted 20 June 2022; Published 4 July 2022

Academic Editor: Cheng Li

Tex264 is an endoplasmic reticulum (ER) membrane protein that was recently demonstrated to act as an ER-phagy receptor under starvation conditions to mediate endoplasmic reticulum autophagy. However, how Tex264 functions in the central nervous system (CNS) and tumors is unclear. Here, we identified 89 proteins from the rat brain that may specifically interact with Tex264 and confirmed the interaction between sorting nexin 27 (SNX27) and Tex264 by coimmunoprecipitation and immunofluorescence. Our results indicated that Tex264 may promote recycling of membrane proteins from endosomes to the cell plasma membrane by recruiting SNX27 retromer vesicles. siRNA-mediated knockdown of TEX264 in HeLa cells did not affect cell proliferation but did significantly inhibit cell migration through a mechanism that may involve a reduction in SNX27-mediated Itgα5 receptor membrane recycling. Results of this study helped identify potential binding Tex264 partners and provide insights into Tex264 functions in the CNS and in tumors.

1. Introduction

The endoplasmic reticulum (ER) is a fundamental organelle that plays multiple roles in cell function including glucose homeostasis, lipid biosynthesis, Ca^{2+} stores, protein export, and regulation of cell organelle activity [1]. Proteomic quantification of cellular differences in response to nutritional stress showed that Tex264 binds to ATG8 and then fuses with lysosomes to promote endoplasmic reticulum autophagy, demonstrating that Tex264 acts as an ER-phagy receptor under starvation conditions [2]. The TEX264 protein contains an N-terminal hydrophobic region, cytosolic gyrase inhibitor-like domain, and a C-terminal unstructured intrinsically disordered region [2, 3]. The Tex264 N-terminal transmembrane segment drives its localization to the ER [2]. Meanwhile, the C-terminal region and central GyrI-like domain are exposed in the cytoplasm [2]. Another report indicated that a subset of Tex264 anchors in the nuclear inner membrane and associates with DNA replication forks to counteract TOP1 cleavage complex (TOP1cc) during DNA replication [4]. There is limited information concerning the role of TEX264 in the central nervous system (CNS) and in tumors, although there is evidence that TEX264 does have an ER autophagy-promoting function in these tissues. For example, in Alzheimer-associated neuroinflammation, an anti-inflammatory anthranilate analogue enhances autophagy through mTOR and promotes TEX264-mediated ER turnover [5]. The autophagic cell death- (ACD-) triggering compound loperamide induced reticulophagy and cell death that are predominantly mediated through the reticulophagy receptor RETREG1/FAM134B and TEX264, which together promote proliferation of glioblastoma cells ACD [6].

Together, these previous studies highlight the role of Tex264 in pathological conditions. Furthermore, bioinformatics analyses of Tex264 gene expression profiles based on GEO datasets suggest that Tex264 may be involved in development of oligodendrocyte progenitor cells (OPCs) and neurons as well as in disorders associated with autism. Thus, Tex264 may have a broader function than has been previously reported.

To reveal new biological functions for Tex264, in this study, we explored the Tex264 interactome using global proteomic analyses of rat brain tissues to identify proteins that interact with Tex264. We identified 89 specific binding partners and confirmed the interaction of sorting nexin 27 (SNX27) with Tex264 by coimmunoprecipitation and immunofluorescence. We further found that TEX264 can affect cell migration by regulating SNX27-mediated recycling of Itgα5 membrane receptors.

2. Materials and Methods

2.1. Animals. The animals used in this study were purchased from Shanghai Jiesijie Laboratory Animal Co., Ltd. Animal experiments were conducted according to National Institutes of Health *Guide for the Care and Use of Laboratory Animals*, and the study protocol was approved by the Animal Care and Use Committee of Shanghai University.

2.2. Rat Brain Lysis. Rat brain tissues were subjected to two freeze-thaw cycles in lysis buffer (2.5 mM EGTA, 20 mM HEPES, 0.1 M KCl, 1 mM EDTA, 1× protease inhibitor mixture, 0.5% *v*/*v* NP-40, and 1 mM DTT, final pH 7.4) before centrifugation for 1 h at 4°C at 11,000 rpm. The supernatants were transferred to a new tube that was centrifuged again at 11,000 rpm for 1 h at 4°C. The supernatant was transferred to a new tube and labeled as the soluble fraction.

2.3. Antibodies and siRNAs. Mouse anti-SNX27 (sc-51570, Santa Cruz), rabbit anti-Tex264 (ab272575, Abcam), rabbit anti-Itgα5 (A0832, ABclonal), and HRP-conjugated monoclonal anti-GAPDH (KC-5G5, Kangcheng) were used. For Tex264 knockdown, siRNA (SiTEX264) had sequences that corresponded to previous reports [3] and were as follows: antisense 5′-UGUCAUAGUAGACAGCGAUGGAGCG-3′ and sense 5′-CGCUCCAUCGCUGUCUACUAUGACA-3′. The control scramble siRNA had nucleotide changes at 5 random positions.

2.4. GST Protein Expression and Purification. Plasmids were constructed by Generay Biotech Co., Ltd. (Shanghai). GST-Tex264 fusion proteins were expressed in *Escherichia coli* BL21 (DE3) cells. Expression of fusion proteins was induced with 0.2 mM IPTG at 25°C for 6 h. The cells were centrifuged in 2 × 250 mL volumes at 4,000 g for 10 min at 4°C. The bacterial pellets were resuspended in 25 mL lysis buffer (PBS, 1 mM PMSF, 1 mg/mL lysozyme, pH 7.4) and incubated for 30 min before addition of 0.5% *v*/*v* Triton X-100 with 1 mM PMSF and 5 mM DTT incubation on ice for another 30 min. The lysates were then centrifuged at 12,000g for 30 min at 4°C. The pellets were discarded, and the supernatants were incubated with 1 mL of a 50% *v*/*v* slurry of glutathione-Sepharose beads for 1 h at 4°C. The mixtures were centrifuged at 3,000 rpm for 1 min at 4°C, and the resulting pellets were washed once with PBS (10 mL, pH 7.4) followed by centrifugation at 3,000 rpm for 1 min at 4°C. The glutathione-Sepharose beads were then washed 3 times in wash buffer (1 mL, 100 mM KCl, 1 mM DTT, 20 mM HEPES, and 1× protease inhibitor cocktail, pH 7.4) at room temperature and then with binding buffer (2.5 mM EGTA, 1 mM EDTA, 20 mM HEPES, 1 mM DTT, 0.1 M KCl, and 1× protease inhibitor cocktail, pH 7.4). A Lowry assay was used to determine the concentration of the purified protein.

2.5. GST Pull-Down Assay. To exclude proteins with nonspecific binding, the soluble fraction of rat brain lysates was preincubated with beads followed by GST-beads. The remaining supernatants were incubated with GST-Tex264-beads at 4°C for 2 h before washing with binding buffer (1% NP40, 1× protease inhibitors, and 2 mM DTT in 1× PBS) and washing buffer (20 mM HEPES, 2.5 mM EGTA, 1× protease inhibitor cocktail, 0.1 M KCl, 1 mM EDTA, and1 mM DTT with 25 mM GSH, pH 7.4). Finally, the proteins were concentrated in PBS using an ultrafiltration column (Amicon® Ultra filters) with a 3 kDa cutoff.

2.6. Mass Spectrometry and Data Analysis. The purified proteins were sent to the Mass Spectrometry Core at Shanghai University for LC-MS/MS analysis, which was performed on a Q Exactive mass spectrometer and coupled with Easy-nLC (Thermo Fisher Scientific) running in positive ion mode. A data-dependent top 10 method was used to acquire MS data that allowed dynamic selection of the most abundant precursor ions for HCD fragmentation from the survey scan (300-1800 m/z). Automatic gain control (AGC) of the target (3e6), a 10 ms maximum inject time, and 40 s dynamic exclusion duration were used. Survey scans were acquired at a resolution of 70,000 at m/z with a 2 m/z 200 isolation width, and the HCD spectral resolution was 17,500 at m/z 200. The normalized collision energy was 30 eV with a 0.1% under fill ratio. Mascot2.2 software was used to analyze the MS data with the following parameters: trypsin enzyme, rat (35719) taxonomy, two missed cleavage sites, UniProt database, 20 ppm MS/MS tolerance, carbamidomethylation of cysteine and oxidation of methionine as fixed and dynamic modifications, protein FDR 0.01, peptide FDR 0.01, and filter by score of 20.

2.7. Immunofluorescence Staining. Brain slices from Sprague-Dawley rats or cultured cells were washed in 0.01 M PBS and then fixed with 4% paraformaldehyde (PFA) for 30 min at room temperature (RT). The samples were treated with 0.1% Triton X-100 in 0.01 M PBS for 30 min, blocked with 1% bovine serum albumin (BSA) in 0.01 M PBS (RT, 1 h), and subsequently incubated with a primary antibody at 4°C overnight. After washing 5 times, the samples were incubated with fluorescently labeled secondary antibody (1 : 100, Santa Cruz).

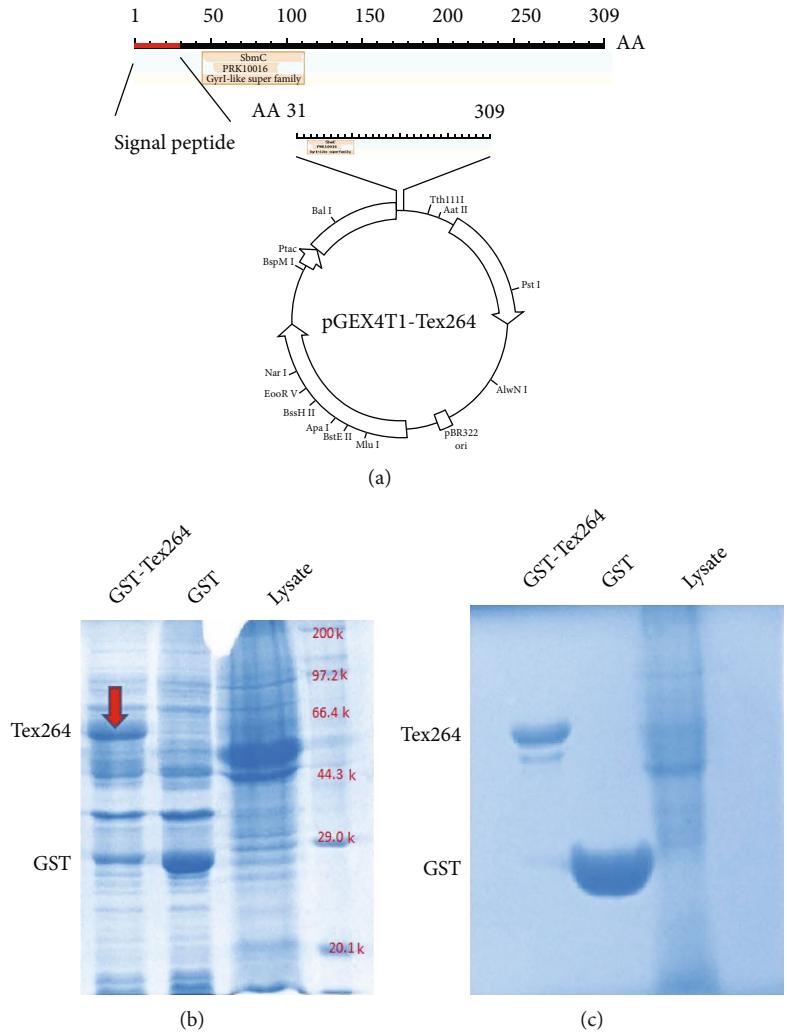

Figure 1: Construction of the GST-TEX264 expression vector and GST-TEX264 fusion protein expression. (a) Construction of the TEX264 expression plasmid using the pGEX4T1 vector. (b) Coomassie blue staining to confirm successful expression of GST-TEX264 and GST protein. (c) Purified GST-TEX264 and GST protein assessed by Coomassie blue staining.

2.8. 5-Ethynyl-2′-deoxyuridine (EdU) Labeling. HeLa cells seeded in 24-well plates at 1.5×10^5 cells/mL were cultured in EdU solution for 1 d and then fixed for 0.5 h at RT in 4% PFA. The cells were then permeabilized with 0.5% Triton X-100 in PBS for 20 min, incubated with 1× Apollo® reaction cocktail for 30 min, stained with DAPI for 15 min, and imaged under a fluorescent microscope. The proliferation rate was defined as the ratio of EdU-positive cells (red) to DAPI-positive cells (blue).

2.9. Surface Labeling of Itgα5. Surface labeling of membrane proteins was carried out as previously described [7]. Briefly, HeLa cells were transfected with siTex264 or scramble siRNA and 72 h later were seeded on coverslips before incubation with a mouse anti-Itgα5 antibody (1 : 100, 1% BSA and 5% FBS in DMEM) for 60 min at 37°C. The cells were then washed four times with culture medium and treated with 4% PFA for 30 min at RT. Then, the cells were washed three times and incubated with secondary antibodies (Alexa 488 donkey anti-rabbit IgGs) for 2 h. Microscopic images were acquired using an Axio Observer A1 inverted confocal microscope.

2.10. Wound Healing Assay. HeLa cells were transfected with siTex264 or scramble siRNA, seeded on 6-well plates, and cultured until confluency was achieved. A 200 μL pipette tip was used to make a straight scratch across the cell layer to form a wound. After removing the medium, cells were washed 2 times with 0.01 M PBS, and then, 1.5 mL DMEM containing 2% FBS was added. The scratched area was photographed 0 h, 6 h, 12 h, and 24 h after wounding. Images were analyzed using ImageJ (NIH). The cell migration was quantified and expressed as the average width (pixels) of the scratch area.

2.11. Statistics. GraphPad Prism 5 software was used for statistical analysis of all data, and Student's t-test or one-way analysis of variance methods was used as indicated.

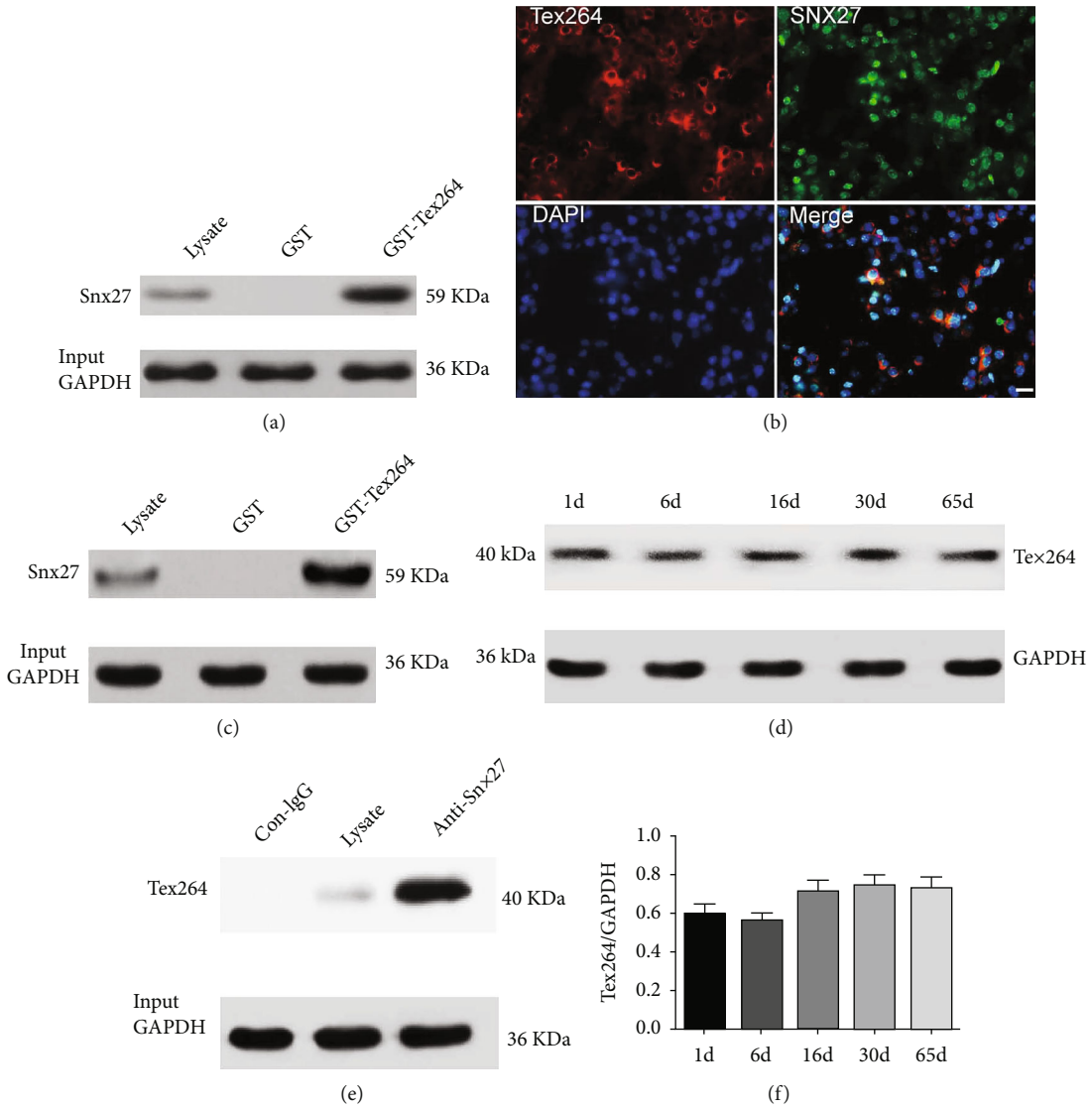

FIGURE 2: Identification of SNX27 as a TEX264-binding protein. (a) GST pull-down assay to confirm direct binding of GST-TEX264 with SNX27 in vitro. Rat brain lysates were incubated with GST-TEX264 or GST-coated beads. After washing and elution, western blotting for SNX27 on brain lysates was carried out with an input control (input) performed in parallel. (b, c) Immunoprecipitation (IP) shows interaction of endogenous TEX264 (b) and SNX27 (c) in rat brain tissues. Equal amounts of total lysates were set as the input control. Control IgG was used as the immunoprecipitation control. (d) Immunofluorescence staining to show colocalization of TEX264 with SNX27 in P0 rat brain cortex sections. Blue: DAPI staining of nuclei; green: anti-SNX27 staining; red: anti-TEX264 antibody staining. Bar = 20 μm. (e) Western blotting to detect TEX264 expression in rat brains at different developmental stages. (f) Quantification of TEX264 expression. TEX264 blots were compared with GAPDH levels, and a ratio was determined and then presented as ratio data. Data shown are the mean ± SD of three independent experiments. No significant difference: one-way ANOVA statistics.

3. Results

3.1. Cloning and Expression of Rat Tex264 in E. coli. In this study, Tex264 from the Rattus norvegicus testis NM_001007665.1 (accession number) was cloned into the pGEX-4T-1 expression vector (Figure 1(a)). The construct did not include the signal peptide, such that the expressed Tex264 had 840 nucleotides encoding 279 amino acids.

To confirm successful expression of the Tex264 GST fusion protein, cells were transformed with pGEX-4T1-Tex264 (GST-Tex264) or empty pGEX-4T1 vector (control). Total cell lysates of the transfected cells were analyzed by SDS-PAGE with Coomassie blue staining, which showed a major band for GST-Tex264 that corresponded to the expected molecular weight of around 60 kDa (Figure 1(b)). After purification, both GST-Tex264 and GST yielded clear bands at the expected positions on PAGE gels (Figure 1(c)).

3.2. LC-MS/MS Analysis to Identify Proteins Interacting with Tex264. To purify Tex264-specific binding proteins, we used a preclearing strategy similar to that described in our previous work [7–9]. After clearing and pull-down, rat brain proteins were analyzed by LC/LC-MS/MS (tandem liquid chromatography-tandem mass spectrometry). Raw data

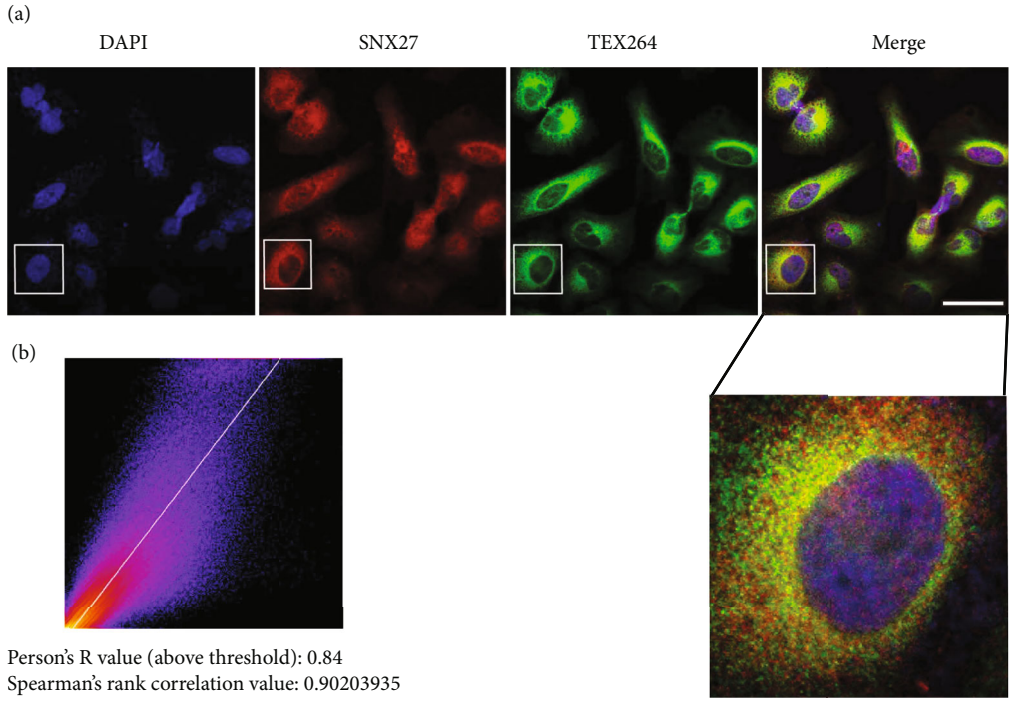

FIGURE 3: TEX264 colocalized with SNX27 in HeLa cells. (a) Immunofluorescence staining shows TEX264 colocalization with SNX27 in HeLa cells. Blue: DAPI staining of nuclei; green: anti-SNX27 staining; red: anti-TEX264 antibody staining. Bar = 20 μm. (b) Immunofluorescence images were analyzed for TEX264 and SNX27 colocalization using the Coloc2 ImageJ plug-in. The 2D intensity histogram shows that the majority of these proteins colocalized, and the colocalization coefficients were higher.

were analyzed with Mascot2.2 software, using a high stringency filtering (score ≥ 20), and then compared to the UniProt database (rat (35719)). Among the 124 proteomes, 260 interacting proteins were identified (Supplemental Figure 1 and Supplemental Table 1). Comparison with GST pull-down proteins removed several common nonspecific binding proteins such as microtubule and microfilament protein and myosin, leaving 89 possible Tex264-specific binding proteins. Based on information in the BioGRID database, we exported 57 validated TEX264-interacting proteins, which were compared with the 89 proteins that we identified in this study and displayed as a Venn diagram (http://bioinformatics.psb.ugent.be/webtools/Venn/). Of the 89 proteins, 4 (GABARAP, F13A1, ASAP2, and CSNK1A1) had been previously described. The remaining 85 proteins were novel Tex264-interacting partners.

3.3. KEGG and GO Analysis of Tex264-Interacting Proteins. Function annotation by KEGG and GO analyses using the online software Metascape and PANTHER15.0 was next carried out. The GO analyses showed the most relevant and meaningful enriched items ($p < 0.01$) among the TEX264 binding proteins in terms of biological function (Supplemental Figure 2). The 89 TEX264 binding proteins were classified and annotated according to cellular compartment (CC) (Supplemental Figure 3), biological process (BP) (Supplemental Figure 3), protein class (PC), and molecular function (MF) (Supplemental Figure 4). TEX264-interacting proteins were involved in a range of BP including development, cell adhesion, growth, signaling pathway, and metabolic process. CC analysis revealed 18 membrane proteins, 27 organellar proteins, and 2 proteins in the synapse. MF analysis revealed that 29.06% were involved in binding, 27.9% have catalytic activity, 10.46% have transcription factor regulation activity, and 3.48% have transporter activity. PC analysis revealed 6.7% as metabolite interconversion enzymes, 5.6% are gene-specific transcriptional regulators, 2.2% are membrane trafficking proteins, 4.5% are nucleic acid binding proteins, 4.5% are cytoskeleton proteins, and 3.4% are transporters.

3.4. SNX27 Interacts with TEX264. Based on a search of MS data that revealed more frequent appearance of SNX27 peptides, GST-TEX264 pull-down proteins were immunoblotted with an anti-SNX27 antibody. This immunoblotting produced a specific band in brain lysates or in GST-TEX264-transfected cells but not in the GST (control) group. This result suggested that bacterially expressed TEX264 could specifically bind to rat brain SNX27 in vitro.

We subsequently performed coimmunoprecipitation and immunoblotting experiments to further confirm whether endogenous TEX264 and SNX27 can form natural complexes in the rat brain. An anti-TEX264 antibody or control IgG (control) was first used to immunoprecipitate rat brain lysates with total brain lysates used in parallel as an input control. Immunoblotting was then performed with an anti-SNX27 antibody. The results showed that SNX27 was detected in immunoprecipitates of the anti-TEX264 antibody group and brain lysate group (input control), whereas no SNX27 was detected in immunoprecipitates of

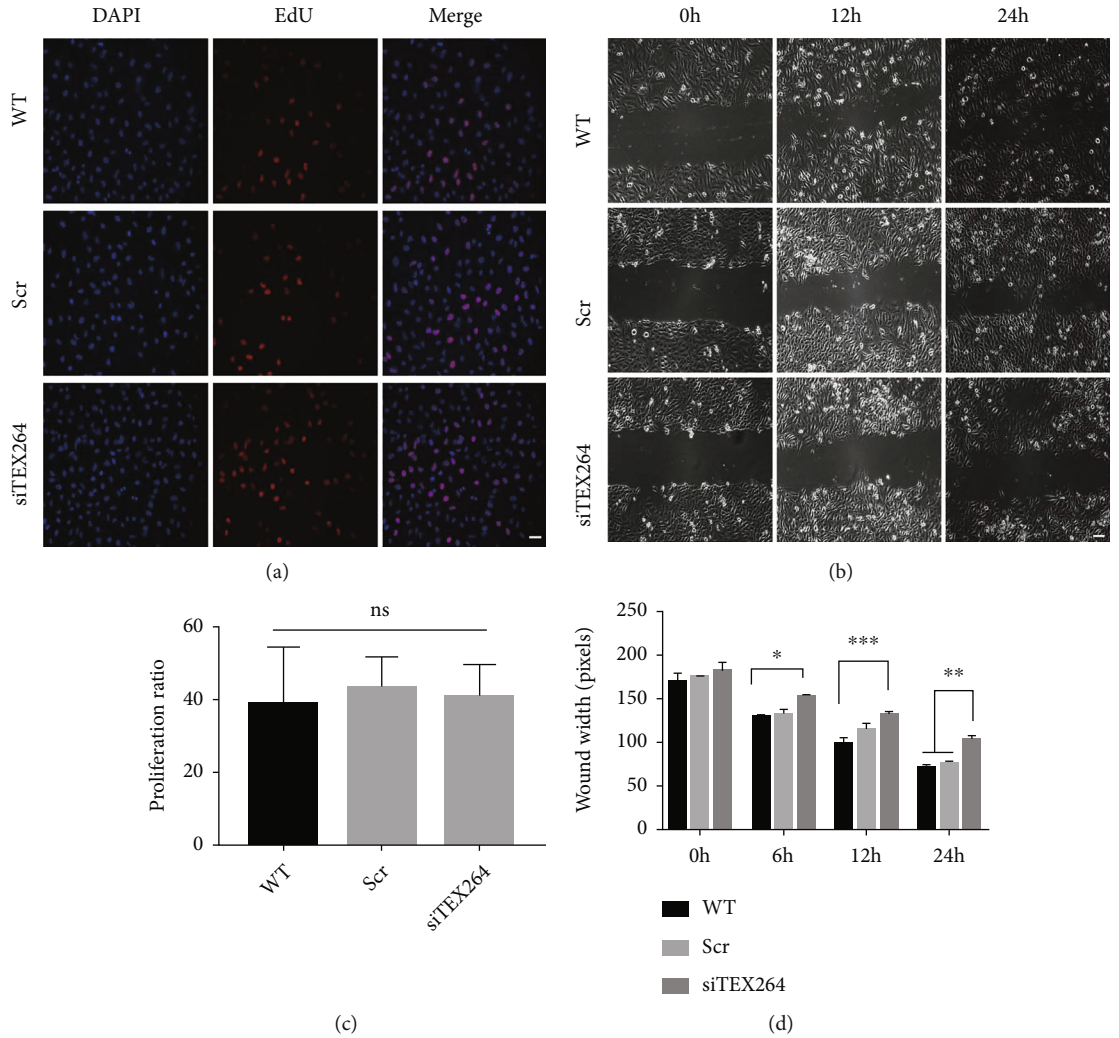

Figure 4: TEX264 knockdown affects HeLa cell migration but not proliferation. (a) HeLa cells were transfected with siTEX264 or scramble siRNA (Scramble) and seeded on 24-well plates for the EdU assay. The proliferation rate was defined as the ratio of EdU-positive cells (red) to DAPI-positive cells (blue). (b) Quantitative data for the EdU assay. Data are the mean ± SD ($n = 3$); nd = no difference. (c) Migration of TEX264-knockdown HeLa cells determined using a wound-healing assay. HeLa cells were transfected with siTEX264 or scramble siRNA (Scramble), seeded on 6-well plates, and cultured to confluency. WT (untransfected HeLa cells). Cell-free gaps were created, and images of the closed gaps were taken at the indicated time point. The wound width was measured at five sites. (d) TEX264 knockdown significantly inhibits HeLa cell migration. $^{*}p < 0.01$, $^{**}p < 0.005$, and $^{***}p < 0.001$ compared to the Scramble or WT cells.

the control IgG group (Figure 2(b)). This result demonstrates that endogenous TEX264 can form a coprecipitable protein complex with endogenous SNX27 in the rat brain. Rat brain lysates were also immunoprecipitated with the anti-SNX27 antibody and then immunoblotted against TEX264, which was detected only in anti-SNX27 immunoprecipitates and brain lysates. Immunofluorescence imaging also showed that endogenous TEX264 and SNX27 are widely expressed in rat brain tissue and partially colocalize in neuronal cells (Figure 2(d)). High-power confocal fluorescence images showed that TEX264 and SNX27 are highly colocalized in cultured HeLa cells (Figure 3).

3.5. TEX264 Knockdown Affects Cell Migration. To further understand the physiological role of TEX264 in cells, we knocked down TEX264 expression in HeLa cells with TEX264-specific siRNA. Proliferation of HeLa cells with TEX264 knockdown was not changed, but substantial changes in cell migration were seen. No difference in positive Edu staining was seen in staining when comparing TEX264 knockdown and control groups (Figures 4(a) and 4(b)). These results were supported by wound healing experiments showing that TEX264 knockdown significantly inhibited HeLa cell migration (Figures 4(c) and 4(d)).

3.6. Knockdown of TEX264 Affects the Cellular Localization of SNX27 and Membrane Localization of Itgα5. SNX27 vesicles are reported to be related to recycling of many membrane receptors and membrane proteins. Membrane receptors like integrin receptors are closely related to cell migration. Thus, we speculate that inhibition of TEX264 will impact SNX27-mediated recycling of membrane proteins to the cell membrane that results in aberrant membrane distribution of integrin receptors and in turn decreased cell

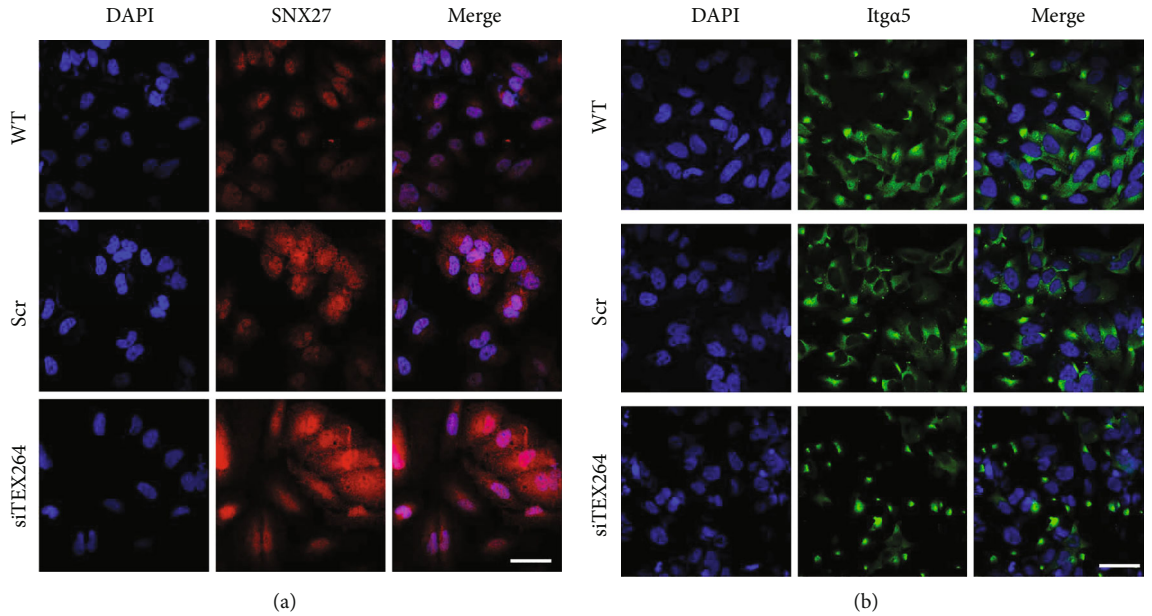

Figure 5: TEX264 knockdown affects SNX27 cell localization and inhibits membrane localization of Itgα5 integrin receptors. (a) HeLa cells were transfected with siTEX264 or scramble siRNA and stained with an antibody against SNX27 24 h later. Scale bar, 20 μm. (b) HeLa cells transfected with siTEX264 or scramble siRNA. After 48 h, cells were live-stained with an antibody against Itgα5 48 h after transfection to reveal surface levels of the Itgα5 integrin receptor. Scale bar, 20 μm.

migration. To examine this possibility, we assessed SNX27 membrane localization by immunofluorescence and cell surface staining to quantify membrane distribution of the Itgα5 integrin receptor, which is recycled by SNX27. Cells with TEX264 knockdown had more diffuse distribution of SNX27, and the cell size increased slightly (Figure 5(a)). Staining intensity for membrane surface Itgα5 was lower in the TEX264 knockdown group compared to control cells, suggesting that TEX264 plays a role in Itgα5 membrane localization (Figure 5(b)).

4. Discussion

Although several interacting proteins have been reported for TEX264, the function of TEX264 in the CNS and tumors is largely unclear. The continuous and stable expression of TEX264 in the brain tissue of developing and young adult rats (Figures 2(e) and 2(f)) suggests that TEX264 may play an important role in maintaining normal physiological function of the CNS.

Our mass spectrometry results showed that the most frequent peptides from TEX264 pull-down corresponded to sorting nexin 27 (SNX27) (Supplemental Table 1). This result indicated that SNX27 likely interacts with TEX264 in rat brains, and results of biochemical and immunofluorescence experiments supported this possibility (Figures 2 and 3). SNX27 belongs to the sorting nexin protein family, whose members are involved in endosome recycling as well as endosomal sorting and signaling. SNX27 facilitates recycling of endocytic transmembrane proteins from endosomes to the plasma membrane [10]. Many cell surface proteins such as the copper transporter ATP7A, glucose transporter 1 (GLUT1), and numerous signaling receptors can interact with SNX27 and require SNX27-endosomal sorting to prevent lysosomal degradation and maintain plasma membrane surface levels [11–13].

SNX27 can directly interact with K-ras GTPase and recruit K-ras into SNX27-positive endosomes through a Ca^{2+}/CaM-dependent mechanism that promotes synaptic transmission of homomeric GluA1 receptors. Knockdown of SNX27 inhibits LTP and related transport of AMPAR to the membrane. Snx27-knockout mice have severe neuronal defects in the hippocampus and cortex [14, 15].

TEX264 expression is increased in tumor cells [6, 16]. To further understand the physiological functions of TEX264 in culture cells, we used siTEX264 to knock down endogenous TEX264 expression in HeLa cells. Cells with TEX264 knockdown had significantly inhibited migration that could be related to cell surface expression of several relevant receptors. Integrin receptors are known to be closely related to cell migration [17], and SNX27 is reported to be closely related to the membrane display of integrin receptor subtype Itgα5 [18]. SNX27 knockdown indeed reduces Itgα5 membrane localization. The interaction between TEX264 and SNX27 we found here together with the role for SNX27 in regulating membrane receptor recycling suggests that the decrease in HeLa cell migration may indicate a role for TEX264 in SNX27-mediated membrane insertion of Itgα5. The interaction of TEX264 and SNX27 under physiological conditions could promote SNX27-mediated recycling of some membrane proteins and membrane receptors to the cell membrane that are important for maintaining normal cell physiological functions. Given the effect of the TEX264 and SNX27 interaction on tumor cell migration, development of drugs that block this interaction could inhibit tumor invasion and metastasis in vivo. Furthermore, SNX27 and Itgα5 are expressed in the

CNS, suggesting that TEX264 could also promote migration of neural precursor cells during early CNS development.

In summary, we identified 85 new TEX264 binding proteins using GST-pulldown and LS-MS technology. These proteins are ubiquitous throughout cells and have many functions, including endosome recycling, mitochondrial organization, transcription factor binding, RNA splicing, and apoptosis. The discovery of these new TEX264 binding proteins indicates that TEX264 not only promotes ER autophagy but also plays a role in a broad range of biological functions. To better understand the function of TEX264, future studies to validate the physiological relevance of TEX264-interacting proteins are needed. Taken together, the results of the current studies can form the basis for future research on the role of TEX264 in physiological processes and in disease pathology.

Data Availability

The data used to support the findings of this study are available from the corresponding author upon request.

Conflicts of Interest

The authors declare that they have no conflict of interest.

Authors' Contributions

Xiao-hui Xu designed and supervised the experiments. Zhao-huan Zhang and Xiao-hui Xu carried out the GST-pull-down, cell transfection, IP, and western blot experiments. Qian-wen Yang performed cell proliferation, cell migration, and cell Itgα5 surface staining experiments, as well as colocalization experiments of Tex264 and SNX27. Chang-ling Yue did the LS/MS assay experiments. Xiao-hui Xu and Yun-yi Zhu analyzed the LS/MS data. Zhao-huan Zhang cultured cells and did the IHC experiments. Xiao-hui Xu and Zhao-huan Zhang wrote the manuscript. Xiao-hui Xu, Qian-wen Yang, and Chang-ling Yue contributed equally to this work.

Acknowledgments

This work was supported by the National Natural Science Foundation of China (nos. 81671263 and 81370031) and the major projects of Anhui Department of Education, China (KJ2021ZD0094).

Supplementary Materials

Supplementary 1. Supplementary Figure 1: Venn diagram depicting Tex264 binding proteins. Venn diagram showing unique and shared proteins between 2 groups (1 is that 57 proteins had been reported binding with Tex264, and 2 is our newly identified 85 proteins). The protein details are listed in the lower table.

Supplementary 2. Supplementary Figure 2: GO analysis of Tex264-interacting proteins. (A) GO classification of the Tex264 interactors. (B) Meanwhile, the enriched pathways were further listed in the lower table.

Supplementary 3. Supplementary Figure 3: classification of Tex264-interacting proteins based on the biological process (BP) and cellular compartment (CC). Pie chart representation of Gene Ontology classification of putative molecular functions of Tex264-interacting proteins from where they localized (CC) and the biological processes (BP) in which they are involved.

Supplementary 4. Supplementary Figure 4: classification of Tex264-interacting proteins based on protein class (PC) and molecular function (MF). Pie chart representation of Gene Ontology classification of Tex264-interacting proteins according to protein class (PC) and molecular function (MF).

Supplementary 5. Supplementary Figure 5: the PPI map of Tex264-interacting proteins. The PPI (protein-protein interaction) map based on GST-Tex264-specific pull-down proteins analyzed by the STRING database.

Supplementary 6. Supplementary Table 1: mass spectrometry results of Tex264-specific pull-down proteins.

References

[1] C. J. Stefan, "Endoplasmic reticulum-plasma membrane contacts: principals of phosphoinositide and calcium signaling," *Current Opinion in Cell Biology*, vol. 63, pp. 125–134, 2020.

[2] H. An, A. Ordureau, J. A. Paulo, C. J. Shoemaker, V. Denic, and J. W. Harper, "TEX264 Is an Endoplasmic Reticulum-Resident ATG8-Interacting Protein Critical for ER Remodeling during Nutrient Stress," *Mol Cell*, vol. 74, no. 5, pp. 891–908.e10, 2019.

[3] H. Chino, T. Hatta, T. Natsume, and N. Mizushima, "Intrinsically disordered protein TEX264 mediates ER-phagy," *Mol Cell*, vol. 74, no. 5, pp. 909–921.e6, 2019.

[4] J. Fielden, K. Wiseman, I. Torrecilla et al., "TEX264 coordinates p97- and SPRTN-mediated resolution of topoisomerase 1-DNA adducts," *Nature Communications*, vol. 11, no. 1, p. 1274, 2020.

[5] Z. Wang, J. Huang, S. P. Yang, and D. F. Weaver, "Anti-inflammatory anthranilate analogue enhances autophagy through mTOR and promotes ER-turnover through TEX264 during Alzheimer-associated neuroinflammation," *ACS Chemical Neuroscience*, vol. 13, no. 3, pp. 406–422, 2022.

[6] S. Zielke, S. Kardo, L. Zein et al., "ATF4 links ER stress with reticulophagy in glioblastoma cells," *Autophagy*, vol. 17, no. 9, pp. 2432–2448, 2021.

[7] X. H. Xu, C. Y. Deng, Y. Liu et al., "MARCKS regulates membrane targeting of Rab10 vesicles to promote axon development," *Cell Research*, vol. 24, no. 5, pp. 576–594, 2014.

[8] Z. H. Zhang, H. Zhang, Y. R. Wang, X. L. Liu, H. Huang, and X. H. Xu, "SIRT 1 binding with PKM and NSE and modulate their acetylation and activities," *Biochim Biophys Acta Proteins Proteom*, vol. 1867, no. 9, pp. 794–801, 2019.

[9] Z. H. Zhang, X. L. Liu, Y. Y. Zhu, H. Huang, and X. H. Xu, "Revealing PAK2's function in the cell division through MKLP1's interactome," *BioMed Research International*, vol. 2020, Article ID 8854245, 2020.

[10] P. Temkin, B. Lauffer, S. Jager, P. Cimermancic, N. J. Krogan, and M. von Zastrow, "SNX27 mediates retromer tubule entry and endosome-to-plasma membrane trafficking of signalling

receptors," *Nature Cell Biology*, vol. 13, no. 6, pp. 715–721, 2011.

[11] F. Steinberg, M. Gallon, M. Winfield et al., "A global analysis of SNX27-retromer assembly and cargo specificity reveals a function in glucose and metal ion transport," *Nature Cell Biology*, vol. 15, no. 5, pp. 461–471, 2013.

[12] E. F. Halff, B. R. Szulc, F. Lesept, and J. T. Kittler, "SNX27-mediated recycling of neuroligin-2 regulates inhibitory signaling," *Cell Rep*, vol. 29, no. 9, pp. 2599–2607.e6, 2019.

[13] P. Sharma, S. Parveen, L. V. Shah et al., "SNX27-retromer assembly recycles MT1-MMP to invadopodia and promotes breast cancer metastasis," *J Cell Biol*, vol. 219, no. 1, 2020.

[14] L. S. Loo, N. Tang, M. Al-Haddawi, G. S. Dawe, and W. Hong, "A role for sorting nexin 27 in AMPA receptor trafficking," *Nature Communications*, vol. 5, no. 1, p. 3176, 2014.

[15] X. Wang, Y. Zhao, X. Zhang et al., "Loss of sorting nexin 27 contributes to excitatory synaptic dysfunction by modulating glutamate receptor recycling in Down's syndrome," *Nature Medicine*, vol. 19, no. 4, pp. 473–480, 2013.

[16] M. Gotoh, H. Ichikawa, E. Arai et al., "Comprehensive exploration of novel chimeric transcripts in clear cell renal cell carcinomas using whole transcriptome analysis," *Genes, Chromosomes & Cancer*, vol. 53, no. 12, pp. 1018–1032, 2014.

[17] H. Hamidi and J. Ivaska, "Every step of the way: integrins in cancer progression and metastasis," *Nature Reviews. Cancer*, vol. 18, no. 9, pp. 533–548, 2018.

[18] F. Steinberg, K. J. Heesom, M. D. Bass, and P. J. Cullen, "SNX17 protects integrins from degradation by sorting between lysosomal and recycling pathways," *The Journal of Cell Biology*, vol. 197, no. 2, pp. 219–230, 2012.

Hindawi
BioMed Research International
Volume 2022, Article ID 4792374, 18 pages
https://doi.org/10.1155/2022/4792374

Research Article

Experimental Study of Potential CD8$^+$ Trivalent Synthetic Peptides for Liver Cancer Vaccine Development Using Sprague Dawley Rat Models

Sidra Zafar,[1] **Baogang Bai**,[2,3,4] **Jinlei Guo**,[5] **Syed Aun Muhammad**,[1] **Syeda Tahira Qousain Naqvi**,[1] **Muhammad Nauman Shabbir**,[6] **Imran Imran**,[7] **Rehan Sadiq Shaikh**,[8] **and Amjad Ali**[9]

[1]*Institute of Molecular Biology and Biotechnology, Bahauddin Zakariya University, Multan, Pakistan*
[2]*School of Information and Technology, Wenzhou Business College, Wenzhou, Zhejiang, China*
[3]*Engineering Research Center of Intelligent Medicine, Wenzhou, Zhejiang, China*
[4]*The 1st School of Medical, School of Information and Engineering, The 1st Affiliated Hospital of Wenzhou Medical University, Zhejiang, China*
[5]*School of Medical Engineering, Sanquan College of Xinxiang Medical University, Henan, China*
[6]*Department of Statistics, Bahauddin Zakariya University, Multan, Pakistan*
[7]*Department of Pharmacology, Faculty of Pharmacy, Bahauddin Zakariya University, Multan, Pakistan*
[8]*Centre for Applied Molecular Biology, University of the Punjab, Lahore, Pakistan*
[9]*Atta-ur-Rahman School of Applied Biosciences (ASAB), National University of Sciences and Technology (NUST), Islamabad, Pakistan*

Correspondence should be addressed to Syed Aun Muhammad; draun@bzu.edu.pk

Received 16 December 2021; Revised 2 May 2022; Accepted 6 May 2022; Published 31 May 2022

Academic Editor: Bing Niu

Background. Liver cancer (LC) is the most devastating disease affecting a large set of populations in the world. The mortality due to LC is escalating, indicating the lack of effective therapeutic options. Immunotherapeutic agents may play an important role against cancer cells. As immune cells, especially T lymphocytes, which are part of cancer immunology, the design of vaccine candidates for cytotoxic T lymphocytes may be an effective strategy for curing liver cancer. *Results*. In our study, based on an immunoinformatics approach, we predicted potential T cell epitopes of MHC class I molecules using integrated steps of data retrieval, screening of antigenic proteins, functional analysis, peptide synthesis, and experimental *in vivo* investigations. We predicted the binding affinity of epitopes LLECADDRADLAKY, VSEHRIQDKDGLFY, and EYILSLEELVNGMY of LC membrane-bounded extracellular proteins including butyrophilin-like protein-2 (BTNL2), glypican-3 (GPC3), and serum albumin (ALB), respectively, with MHC class I molecules (allele: HLA-A∗01:01). These T cell epitopes rely on the level of their binding energy and antigenic properties. We designed and constructed a trivalent immunogenic model by conjugating these epitopes with linkers to activate cytotoxic T cells. For validation, the nonspecific hematological assays showed a significant rise in the count of white blood cells (5×10^9/l), lymphocytes (13×10^9/l), and granulocytes (5×10^9/l) compared to the control after administration of trivalent peptides. Specific immunoassays including granzyme B and IgG ELISA exhibited the significant concentration of these effector molecules in blood serum, indicating the activity of cytotoxic T cells. Granzyme concentration increased to 1050 pg/ml at the second booster dose compared to the control (95 pg/ml), while the concentration of IgG raised to 6 g/l compared to the control (2 g/l). *Conclusion*. We concluded that a potential therapeutic trivalent vaccine can activate and modulate the immune system to cure liver cancer on the basis of significant outcomes of specific and nonspecific assays.

1. Introduction

Liver cancer is the sixth most prevalent type of cancer around the world [1]. Countries where people ages 20 years or less are suffering from this disease are considered high risk, while countries are at lower risk where LC is less prevalent in people of age 50. The available treatment for LC includes chemotherapy, radiotherapy, liver resection, and laparoscopic hepatectomy [2]. These treatments may show negative effects on normal cells and may cause reoccurrence of cancer, toxicity issues, and expensive procedures [3]. Medical specialists and oncologists have some concerns over conventional procedures [4]. Although these treatments are available options, still there is a need for safe and alternative therapeutic strategies.

Immunotherapy can be the best frontier for the treatment of cancer, and it is considered valuable and effective in curing liver and other cancers. Although a number of recent developments have been made in this area, however, still we need further investigations to design therapeutic vaccines for liver cancer [5, 6]. Immunotherapeutic peptides boost up the body's natural immune system to fight against cancer cells. The efficacy of immunotherapy can be recognized by the fact that for the destruction of tumor cells, they use immune components. Therefore, immunotherapy is considered an important alternative for LC treatment [7]. To understand the pattern of liver cancer proliferation, some important regulatory immune components like $CD8^+$ and $CD4^+$ T cells, NK cells, myeloid-derived suppressor cells (MDSCs), and regulatory T cells are some types of cells that are studied in detail. On activation, these lymphocytes provoke other immune system components and activate either cell-mediated or humoral immunity or both [8]. Immunological facts of an immune response are now explored and understood by a basic scientific approach with computational tools [9]. Whole-genome analysis contributes to the development of vaccine candidates that will fight against specific targets. Currently, a newly emerging technique, reverse vaccinology, instead of using the culture, only requires the genomic sequence of the target protein, which is further utilized for vaccine preparation [10, 11]. The complete genomic sequence helps in the prediction of potential target epitopes, and vaccines can be designed against the respective organism [10, 12].

New computational tools, software, and genomic and proteomic databases are an important part of immunoinformatics and reverse vaccinology approaches for the prediction of specific epitopes. Hence, immunoinformatics is a computational study related to biological compounds, their modeling, and complications of the immune response. These integrated techniques provide the basis of vaccine development [13] involving analysis of genomic to proteomic sequences, identification of B and T cell antigenic sites, and cellular responses [14] until there is no approved prophylactic and therapeutic vaccine for liver cancer [5, 15]. However, it has been reported that immunotherapeutic vaccines for liver cancer are under preclinical or clinical trials but not yet approved [16]. In this investigation, our main objective is to seek out the LC-specific epitopes to provoke an adaptive immune response. With the help of software, online servers, and databases, we designed specific T cell immunogenic peptides. The efficacy of these immunogenic peptides was evaluated by hematological assay, antibody-specific (IgG) assay, and granzyme ELISA. For this purpose, *in vivo* experimental trials were carried out on the Sprague Dawley rat model. This study describes the significance of immunoinformatics for the prediction of liver cancer epitopes and the efficiency of predicted potential immunogenic candidates by *in vivo* trials.

2. Methodology

2.1. Ethical Approval and Study Design. All animals were kept under standard conditions as per ARRIVE guidelines reported for animal handling. These experimental procedures were approved by the Bioethics Committee for Animals of the Institute of Molecular Biology and Biotechnology, Bahauddin Zakariya University, Multan, Pakistan, with Approval No. IMBB/02/2019. In this study, we predicted the T cell epitopes of cytotoxic T lymphocytes (CTLs) ($CD8^+$ cells) based on an immunoinformatics approach [17]. These epitopes were docked to MHC class I molecules to analyze the binding affinity. Based on the binding energy, three epitopes were linked to construct a potential trivalent vaccine candidate. Our hypothesis involves the activation of $CD8^+$ cytotoxic T lymphocytes (CTLs) as they have MHC class I receptors to boost up the natural immune system to target cancerous cells. Granzymes and other chemical mediators are released upon activation of CTLs [18]. These granzymes and chemical molecules have a significant role in the apoptosis of cancer cells. Granzyme B is secreted from CTLs and NK cells; according to our hypothesis, secretion of granzyme B in immune cells may help in killing the cancerous cells. IL-4 and IL-10 released by a subpopulation of CTLs activate B lymphocytes resulting in antibody production [19–21]. The hypothesis of our study reflects this mechanism, and animal investigation indicated that our trivalent molecule is antigenic in nature, which is potentially able to activate the B and T lymphocytes (Figure 1). In this study, we focused on tumor-specific and tumor-associated antigens to report newly designed potential epitopes as immunotherapeutic agents for liver cancer. For screening of liver cancer antigens, we used the TRON Cell Line Portal [22] and Tumor-Specific Neoantigen Database (TSNAdb) [23] to give a specific category to each protein. Moreover, these proteins also have high expression in the liver. With the help of the GenomicScape server, these proteins were further tested for their expression levels in the liver [24]. The system-level analysis of these peptides showed the significant level of production of antibodies, interferons, granzymes, and other mediators. The study framework was designed based on integrated steps (Figure 2) using different bioinformatics tools, databases, and software, *in vivo* (Table 1).

2.2. Screening of Liver Cancer-Associated Proteomic Data. The Human Protein Atlas database was used for the retrieval of liver cancer-associated proteins [25, 26] (Supplementary Table 1 and 2). We used the compared two-list procedure

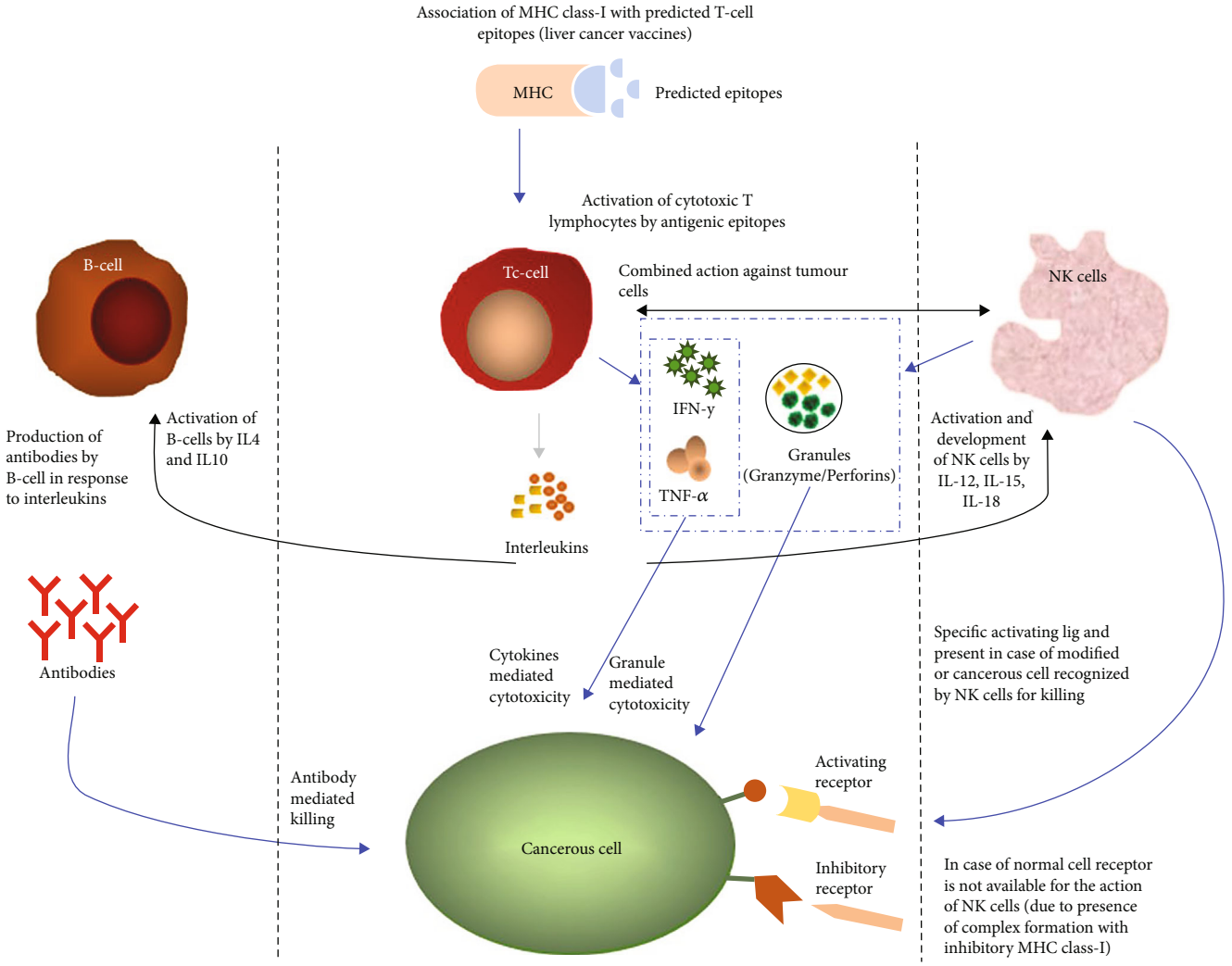

Figure 1: Schematic representation of our hypothesis.

of the Whitehead BaRC public tool to screen liver cancer proteins from all cancer data. The FASTA sequences of screened proteins were accessed from the UniProt Knowledgebase (UniProtKB) database [27]. The extracellular and membrane-bound proteins were predicted by the CELLO subcellular localization predictor tool [28].

2.3. MHC Class I T Cell Epitopes and Immunogenicity Prediction. The T cell epitopes of liver cancer-associated antigenic proteins were predicted using the Immune Epitope Database (IEDB) and selected based on the lower percentile rank (0.1%) cutoff parameters [29]. The predicted T cell epitopes showed the connotation of the HLA-A∗01:01 allele of MHC class I molecules expressed in the maximum number of populations. The conservation of these epitopes was determined by IEDB [30] indicating the optimal allelic binding affinity [17, 31].

The ability of an epitope used as a vaccine candidate depends on the features of antigenicity and immunogenicity, and these were studied by the VaxiJen server and IEDB [32]. The ExPASy Compute pI/Mw tool was applied for molecular weight prediction [33].

2.4. Physicochemical Properties. The physicochemical properties of the peptides were predicted using online servers [34]. Tools PEPlife, ToxinPred, ExPASy, Peptide 2.0, and PredSTP were used to predict physicochemical properties [35–37]. Half-life is the time taken by half the amount of protein to remove from the body after entering the cell. Stability of a peptide in the test tube or in the synthesized drug form is indicated by the value of the instability index. For a protein to be soluble in water, it must have a charge on it. Detailed knowledge of the hydropathicity of an individual amino acid enables us to predict the overall three-dimensional structure of a protein from its amino acid sequence. Toxicity profiles of peptides must be predicted unless we cannot use them in clinical trials. The SVM (Support Vector Machine) model of amino acid composition was used to predict the toxicity.

2.5. Construction and Modeling of Trivalent Molecules. The HADDOCK server was used to predict the ranking and best binding combinations of epitopes based on an algorithmic score [38]. The refinement interface of this server was used to get the refined C port modules of epitopes and their active

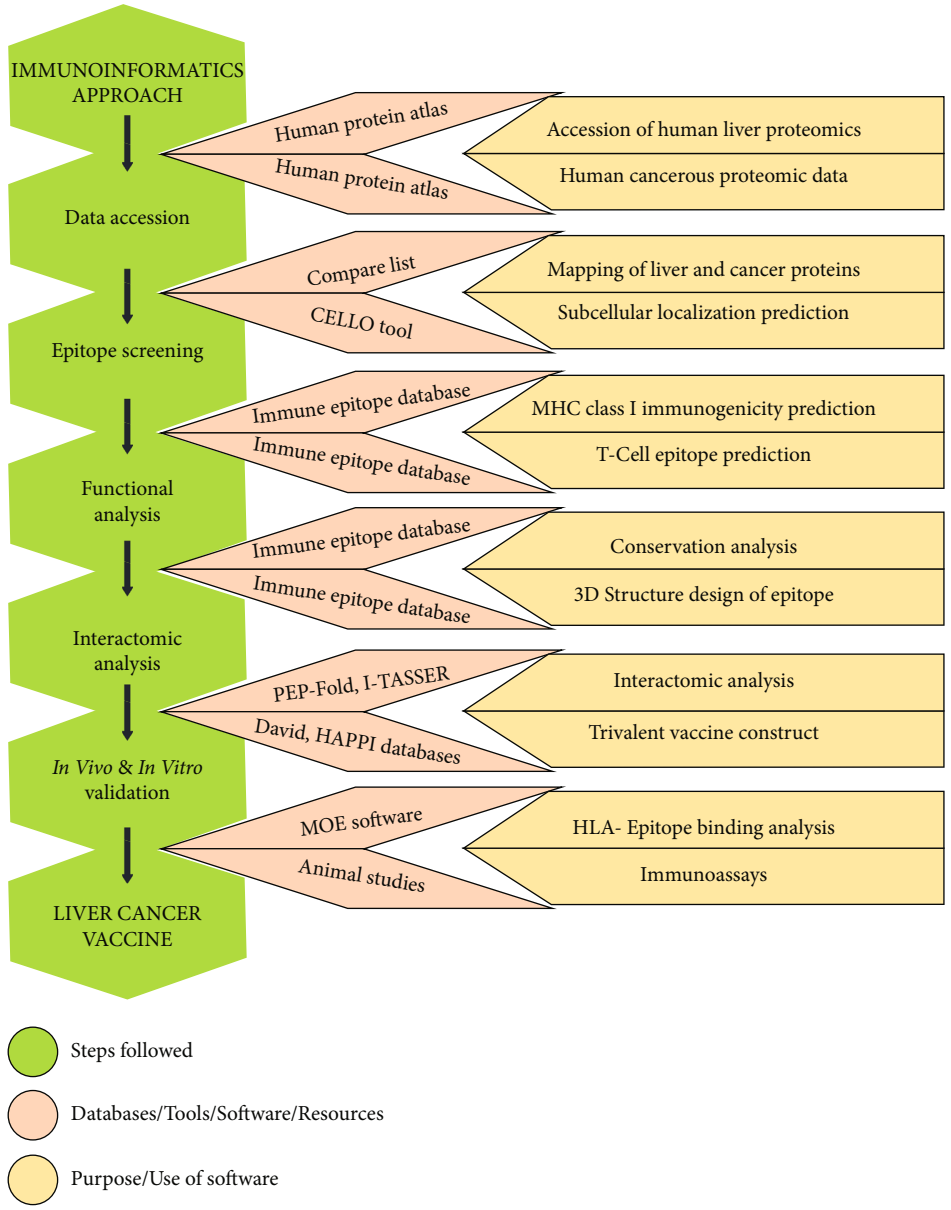

Figure 2: The integrated steps of our framework used for the prediction of T cell epitopes.

and passive residues [39]. Suitable linkers were applied between epitopes to avoid unwanted joining and denaturation of the trivalent constructs. The functionality of the trivalent construct and the arrangement of epitopes also depend on these linkers [40]. AAY is the most commonly used linker for HLA-I epitopes [41, 42]. The trivalent construct was modeled using the I-TASSER server [43], and the quality of configuration of the trivalent model was defined by a 3Drefine tool [44]. Molecular Operating Environment (MOE) software was used for the estimation of the binding energy of a trivalent multiallelic molecule to MHC class I receptors based on the Root-Mean-Square Deviation (RMSD) and binding energy (E score). For verification, the potential epitopes were analyzed and assessed using various software and tools.

2.6. HLA Epitope Binding Analysis. The 3D model of HLA-I (MHC class I) was accessed from the Protein Data Bank (PDB). The binding affinity between predicted T cell epitopes (trivalent model) and HLA molecules was carried out by molecular docking analysis using MOE software.

2.7. Synthesis of Trivalent Peptides. The trivalent construct (LCPV09) with >95% purity was synthesized commercially by Shanghai Research Institute of Chemical Industry (Shanghai TECH. Chemical Industry Testing Co., Ltd., China).

2.8. Animal Immunization. Animals were obtained from the breeding unit of the Department of Pharmacology, Faculty of Pharmacy, Bahauddin Zakariya University, Multan, Pakistan. Preclinical trials are performed on animal models

Table 1: List of databases/servers used in the research work for the screening of liver cancer proteins and prediction of epitopes.

Sr. #	Tools/servers/databases	Purpose	Web links	References
1	Human Protein Atlas	Human cancer database	http://www.proteinatlas.org	[26]
2	Bioinformatics and Research Computing	For protein comparisons	http://jura.wi.mit.edu/bioc/tools/compare.php	[66]
3	UniProtKB (UniProt Knowledgebase)	Protein database	https://www.uniprot.org/	[67]
4	CELLO	Subcellular localization prediction	http://cello.life.nctu.edu.tw/	[28]
5	VaxiJen 2.0	Antigenicity prediction	http://www.ddghttp://pharmfac.net/vaxijen/VaxiJen/VaxiJen.html	[32]
6	ANTIGENpro	—	http://scratch.proteomics.ics.uci.edu/explanation.html	[68]
7	Immunomedicine Group	—	http://imed.med.ucm.es/Tools/antigenic.html	—
8	CamSol	Solubility prediction	http://www-vendruscolo.ch.cam.ac.uk/camsolmethod.html	[69]
9	SOLpro	—	http://scratch.proteomics.ics.uci.edu/explanation.html#SOLpro	[70]
10	PROSO	—	http://mbiljj45.bio.med.uni-muenchen.de:8888/proso/proso.seam	[69]
11	Immune Epitope Database (IEDB)	Epitope prediction	http://tools.iedb.org/main/	[71]
12	HLAPred		http://crdd.osdd.net/raghava/hlapred/ref.html	[72]
13	ProPred		http://crdd.osdd.net/raghava/propred1/	[73]
14	ToxinPred	Physicochemical properties	https://webs.iiitd.edu.in/raghava/toxinpred/design.php	[36]
15	ProtParam	—	https://web.expasy.org/protparam/	[74]
16	PlifePred	—	https://webs.iiitd.edu.in/raghava/plifepred/index.php	[75]
17	AllergenFP	Allergenecity prediction	http://www.ddg-pharmfac.net/AllergenFP/	
18	AlgPred	—	http://crdd.osdd.net/raghava/algpred/submission.html	[76]
19	PDB (Protein Data Bank)	Protein database	http://www.rcsb.org/pdb/home/home	[77]
20	PEP-FOLD server	Epitope modeling	http://bioserv.rpbs.univ-paris-diderot.fr/PEP-FOLD/	[78]
21	I-TASSER	Protein modeling	https://zhanglab.ccmb.med.umich.edu/I-TASSER/	[79]
22	Molecular Operating Environment	HLA epitope binding prediction	—	—

for the validation and optimization of peptide doses [42] and experimental trials. After screening and optimization of vaccine candidates, human tissues/hepatic cell lines and disease animal models are used in the next step. Efficacy analyses are performed on animal models for the validation and optimization of peptide doses. Sprague Dawley rats of weight 150 grams, 5-6 weeks old, were used. Rats were divided into four groups ($n = 6$/group). One group of rats was immunized with a 150 μl solution of 160 μg of trivalent molecules alone. The second group was given 150 μl of an adjuvant which is aluminum hydroxide solution (G-Alum™ Adjuvant Kit, Cat. # 786-1216), and the third group was immunized with a combined solution of trivalent molecules plus 2 times of aluminum hydroxide solution. The fourth group was taken as the control group, and nothing was given to those rats. The doses were injected into the lower abdomen subcutaneously. A first booster dose of 240 μg and a second booster dose of 320 μg were given with the same pattern to each of the four groups to get the optimized results. After immunization of rats with different doses, they were kept under observation for 2-3 weeks. Three weeks postimmunization, blood samples were taken from rats for immunoassay. Blood samples were collected by rupturing the vein in the eyes of rats using capillaries of 75 mm length and 1.1-1.2 mm inner diameter.

2.9. Hematological Assays. Serum was separated from blood by centrifugation in a gel clot vial. 150 μl sample serum was added to the detection buffer and mixed by inverting the tube 10 times. Two drops (75 μl) of the sample mixture were dispensed in the sample cartridge. The cartridge was loaded into the reader immediately. After scanning, the CRP reading was displayed on the screen of the reader. The results were expressed in mg/l. Similarly, the levels of total white blood cells (WBC), lymphocytes (LYM), and granulocytes (GRA) in the blood of immunized rats were analyzed by Beckman Coulter, USA. The Coulter principle was used for the counting of WBC, LYM, and GRA in the blood. The results were observed in either percentage (%) or 10^9 cells/liter [45].

2.10. Liver Function Tests. Liver function tests (LFTs) including serum alkaline phosphatase (ALP), alanine

transaminase (ALT), aspartate transaminase (AST), and alpha-fetoprotein (AFP) were performed to detect the integrity of the liver of immunized rats and to observe the liver toxicity.

2.11. IgG ELISA. Serum samples of each group were analyzed for IgG after three weeks of immunization using the ELISA kit as per the manufacturer's guidelines (Roche: Mouse IgG ELISA) and the microplate reader (BioTek 800TS). Specific ELISA was performed using the Antigen-Down ELISA Development kit in which the LCPV09 antigen was coated in the wells to quantify the IgG. Its ELISA-based technique is in which a specific antigen of animals is coated on wells to record the IgG. The coating reagents (Na_2CO_3 buffer 0.95 *w*/*v* of 0.5 M sodium azide at a pH of 9) with 50 μl of the capturing antibody in the final concentration of 25 μl/ml were dispensed in wells with appropriate dilution. The microwell plate was incubated for 90 minutes, and after incubation, the solutions were discarded and dried on cellulose paper. 200 μl of the washing solution which contains 0.9% *w*/*v* NaCl and 0.1% *v*/*v* Tween-20 was used to wash the wells. 200 μl of the 1x blocking reagent (1 : 10) containing gelatin powder, NaCl, and Tris-HCl buffer was added and incubated for 90 minutes. Then, the solutions were removed and a 200 μl solution of antibodies extracted from serum at a concentration of 25 ng/ml was added to a microtiter plate. Steps of removing the solution and washing were repeated after incubation. The anti-mouse (POD) conjugate solution of 50 μl along with 1 ml of the blocking reagent was poured into the wells. The wells were incubated and washed. Finally, 50 μl of the substrate (2,2′-azino-bis(3-ethylbenzothiazoline-6-sulfonic acid)) was added and the fluorescence was recorded at 492 nm to analyze the enzyme-substrate interaction indicating the concentration of IgG in samples (g/l). The mean value ± SD of IgG of control rats was taken as the standard [46].

2.12. Granzyme B Assay. The blood of immunized rats was analyzed for granzyme B concentration. Serum was separated from whole blood by using a gel clot vial. ELISA was performed by using the Granzyme B Platinum ELISA kit (Thermo Fisher Scientific, Catalog # BMS2027) according to the manufacturer's guidelines. The first step was washing the microwell plate twice by using the 400 μl washing buffer (PBS with 1% Tween-20). Wells were dried after 10-15 seconds of washing by tapping a paper towel. The microwell plate was used immediately after washing and drying. 75 μl of the dilution buffer was added in duplicate to sample wells (A1/A2) and 100 μl to standard wells (B1/2, G1/2) in duplicate. Wells A1/2 were then filled with 75 μl of the prepared standard solution of granzyme B. Solutions of the wells were mixed carefully so that the base of the wells must not get scratched. 50 μl solution was transferred into wells B1/2. This process was continued until two rows of wells were covered with a standard solution of granzyme B ranging from 480 to 0.7 pg/ml. 50 μl of the solution from each well was disposed of. 100 μl of the dilution buffer was added to blank wells and 50 μl to sample wells in duplicate. Each sample solution of 50 μl was dispensed into sample wells. Adhesive film was used to cover the wells and incubated for 60 minutes at 15-25°C. The plate was placed on a shaker at 400 rpm. Adhesive film was removed after incubation time, and all wells were washed with 100 μl of the biotin conjugate. After incubation, 100 μl of the streptavidin-HRP dilution was added to all wells. Adhesive film was used to cover the plate, and an incubation time of 30 minutes was given at 18-25°C with shaking at 400 rpm. After that, the wells were washed carefully and 100 μl of TMB as the substrate was added to all wells. After incubation of 15 minutes, color was observed in each well. Upon dark blue appearance, 100 μl of the stop solution was added to stop the enzyme reaction. Stop solutions must be distributed equally throughout the well. The microplate reader (BioTek 800TS) was used to examine the absorbance of each well at a primary wavelength of 450 nm and a reference wavelength of 620 nm. The concentration of granzyme B was calculated and recorded in pg/ml. The standard was determined by the mean estimation of granzyme B of control rats' serum ± SD [47].

2.13. Statistical Analysis. Statistical analysis was performed on the mean values of the results of all replicates with standard error of the mean (SEM) and standard deviation (SD). Mean values of immunized groups were compared with the control group to check the level of significance using Minitab software. To carry out data interpretation, one-way analysis of variance (ANOVA) was calculated by using SPSS software. p value less than 1.0×10^2 (>0.01) is statistically significant ± SEM [17, 48].

3. Results

3.1. Screening of Liver Cancer Proteins. We screened 60 LC-associated proteins from a total of 1700 cancer proteins and 435 liver proteins. The proteins with high molecular weight were antigenic, having the antigenicity threshold score of 0.5 [32]. Based on the antigenicity score and molecular weight (>50 kDa), three proteins including ALB, GPC3, and BTNL2 were selected (Figure 3). Subcellular localization showed that ALB protein is present in the extracellular matrix, while GPC3 and BTNL2 proteins are membrane bounded. These proteins are tumor-specific proteins, and they are expressed only in the case of liver tumors (http://biopharm.zju.edu.cn/tsnadb/). All genes and proteins of the body are interlinked with each other in other organs of the body directly or indirectly. We screened the proteins on the basis of their optimal expression in the liver. These three proteins have the maximum expression levels in the liver or fetal liver (http://genomicscape.com/microarray/expression.php). ALB is a liver tissue enriched gene expressed in the right lobe of the liver (UniProtKB). There are many reported liver diseases associated with this protein. Serum albumin is mainly plasma protein and produced by the liver. Levels of this protein were checked in blood analysis for diagnosis of liver diseases. There are many therapeutic uses of albumin in liver diseases [49]. Clinical trials have evaluated that glypican-3 (GPC3), a tumor-specific antigen, is expressed in all hepatocellular cancers. It is usually found anchored

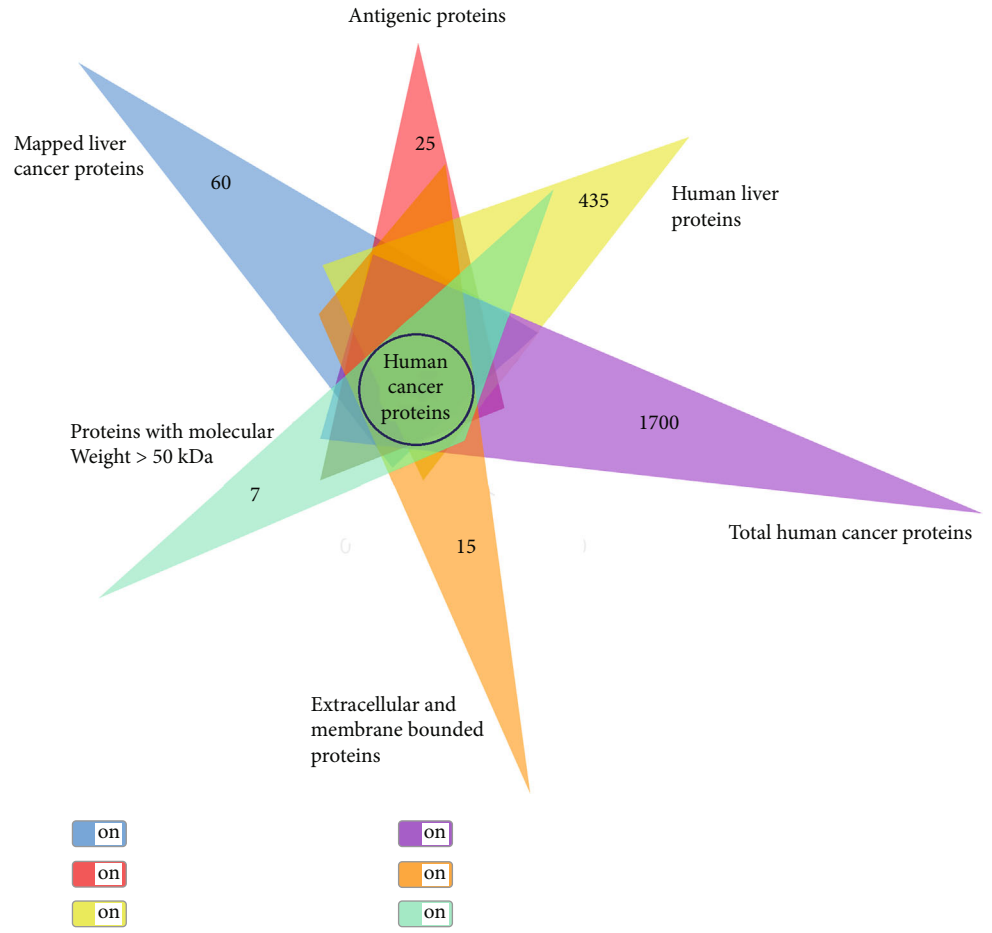

Figure 3: Screening of liver cancer-associated proteins for the prediction of antigenic peptides.

to a protein expressed on the cell surface known as glycosylphosphatidylinositol (GPI). Glypican-3 (GPC3) is a promising target for anticancer immunotherapy against HCC even in its early stages because its expression is specifically observed in >80% of HCCs [50]. A peptide vaccine prepared from GPC3 was efficacious and safe in promoting tumor infiltration by cytotoxic T cells [5]. BTNL2, a butyrophilin-like protein, has been found to regulate the immune response. The expression of BTNL2 has been linked to sarcoidosis in the liver [51, 52]. It has been shown in several *in vitro* studies that B cells have surface receptors for BTNL2, while $CD8^+$ and $CD4^+$ cells express such receptors upon activation. Thus, it can be employed as a therapeutic agent to reestablish immune tolerance in such inflammatory conditions. Furthermore, BTNL2 can be modulated to arbitrate the immune response for developing innovative therapeutics if the relationship between its structure and function can be fully illustrated at the molecular level [51].

3.2. T Cell Epitope Prediction. T cell epitopes complexed with MHC class I are strongly immunogenic and induce the immune system robustly. The predicted T cell epitopes of BTNL2, GPC3, and ALB were EYILSLEELVNGMY, LLECADDRADLAKY, and VSEHRIQDKDGLFY, respectively. These potential T cell epitopes have the potential to target the maximum number of alleles indicating conservation in the entire population. Such multiallelic epitope-based vaccine candidates have more spectral features compared to those candidates that target one type of allele.

3.3. Physicochemical Properties. Half-lives of epitopes are linked to their stability as well as toxicity. The half-life of a good epitope must be less than hours to make it stable and to activate the immune components. Half-lives of our predicted epitopes were less than 10 hours presenting stability and less toxicity. The instability index also measures the stability of the peptide [52]. These epitopes have a less instability index presenting the stable drug form. Our epitopes showed water solubility, and amino acids are either hydrophobic or hydrophilic. The lesser value of hydropathicity means a more hydrophilic character of epitopes. Almost all predicted epitopes have a less value of hydropathicity [53]. The algorithmic SVM score of the software was used to classify the epitope as being either toxic or nontoxic (nontoxicity threshold value < 5) [37, 54]. The predicted epitopes are nontoxic, having an SVM score of less than 5 (Table 2).

3.4. Trivalent Construct against Liver Cancer. The trivalent construct was formulated by integrating three epitopes VSEHRIQDKDGLFY, LLECADDRADLAKY, and

Table 2: Physicochemical properties of the individual epitopes and trivalent construct.

UniProt ID	Peptide sequence	SVM score	Toxicity prediction	Hydropathicity	Charge	Half-life	Instability index
ALBU_HUMAN	LLECADDRADLAKY	-0.36	Nontoxin	-0.31	-2	5.5 hours	23.16
BTNL2_HUMAN	VSEHRIQDKDGLFY	-1.17	Nontoxin	-0.91	-0.5	10 hours	48
GPC3_HUMAN	EYILSLEELVNGMY	-0.57	Nontoxin	0.3	-3	1 hour	52
TRIVALENT	VSEHRIQDKDGLFYAAYLLECADDRADLAKYAAYEYILSLEELVNGMY	-0.84	Nontoxin	-0.221	-6.5	100 hours	34.49

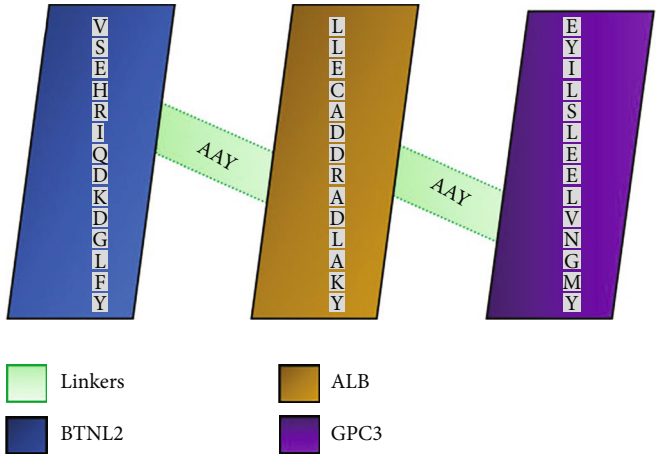

(a)

Properties of trivalent vaccine	
Antigencity	0.6920
M/W (kDa)	5.55021
Solubility	0.669752 (Soluble)
Binding energy (kCal/mol)	−17
Immunogenecity	−0.63436

(b)

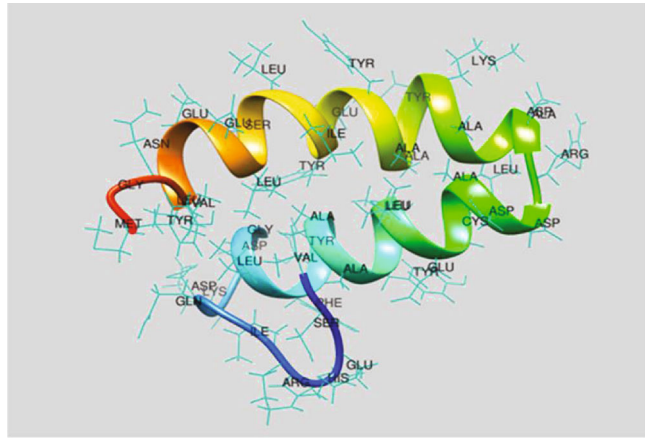

(c)

Figure 4: Schematic representation of the trivalent construct. (a) Trivalent contains 48 amino acid residues. MHC class I-predicted epitopes of three proteins (blue, yellow, and purple) linked with linkers AAY (green). (b) Physical properties of the trivalent. (c) 3D model of the trivalent modeled by the I-TASSER online server.

EYILSLEELVNGMY of BTNL2, ALB, and GPC3 proteins. A total of 48 amino acid residues in the trivalent molecule including AAY linkers VSEHRIQDKDGLFYAAYLLECADDRADLAKYAAYEYILSLEELVNGMY were constructed. The trivalent was modeled with a confidence score (*C*score) of -2.34, TM score of0.44 ± 0.14, and RMSD of7.3 ± 4.2 Å. The antigenicity score of the trivalent model was 0.69 (Figure 4).

3.5. Molecular Docking. The quality and reliability of the predicted epitopes and trivalent construct were estimated by their 3D models. 3D models were used to reveal their binding affinities with MHC class I molecules. MOE software was used to predict the binding affinities between the trivalent construct and the MHC class I molecules (allele: HLA-A∗ 01:01). A significant binding affinity of -17.004 kcal/mol was observed between the trivalent construct and the target protein (Table 3) involving the residues SER54, HIS151, ASN53, ASP27, GLN155, GLU154, LEU28, VAL158, TYR34, ALA33, THR95, LYS64, ALA49, ASP95, PHE13, TYR14, LYS9, GLU20, CYS21, ASP10, GLY11, and LEU12 of MHC class I target molecules (Figure 5).

3.6. Verification and Assessments of Potential Epitopes. The epitopic sequence and physicochemical properties of potential peptides verified by different tools and software indicated the uniformity and consistency in the sequence and properties (Tables 4 and 5).

3.7. Immunoassays and Serological Assays. The activity of potential epitopes was investigated by *in vivo* animal studies with and without an adjuvant. Immune response to synthetic peptides was analyzed 3 weeks postimmunization of rats. The rats were monitored for 3 weeks daily to observe the side effects of the administrated doses. Negative phenotypic signs indicated that there were no side effects of the trivalent peptides (Table 6).

3.8. Hematological Assays. We examined the blood component analysis after immunization. The efficacy of the trivalent (LCPV09) was tested with or without the adjuvant using the rat model. Hematological assays show the primary response to peptides. To compare with the sampled animals, control rats were used and kept under the same conditions. Substantial increases in the count of blood

Table 3: Screening parameters of the predicted T cell epitopes and trivalent construct.

Sr. no.	EPITOPE_HLA (target)	Sequence	Antigenicity	M/W (kDa)	Solubility	Immunogenicity	Binding energy (kcal/mol)
1	ALB_MHC class I, allele 1	LLECADDRADLAKY	1.0188	1.59579	0.984845	-0.00437	-11.3124
2	BTNL2_MHC class I, allele 1	VSEHRIQDKDGLFY	0.5641	1.69276	0.904257	0.23389	-10.6156
3	GPC3_MHC class I, allele 1	EYILSLEELVNGMY	0.7682	1.7159	0.833942	-0.02795	-8.4656
7	TRIVALENT_MHC class I, allele 1	VSEHRIQDKDGLFYAAYLLECADDRADLAKYAAYEYILSLEELVNGMY	0.6920	5.55021	0.669752	-0.63436	-17.0048

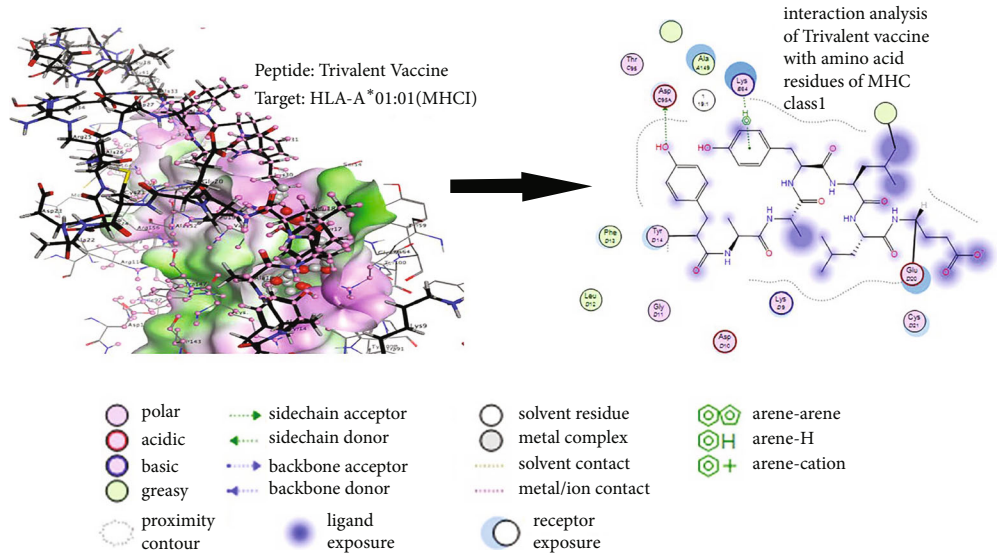

	mol	rseq	mseq	S	rmsd_refine	E_conf	E_place	E_score1	E_refine	E_score2
1	trivalent.pdb	1	1	−17.0048	4.6157	−1320.3651	226.6145	21.6568	-72.9284	-17.0048

Figure 5: Molecular docking analysis of the trivalent construct with the target HLA-A∗01:01 allele of MHC class 1.

Table 4: Verification of the peptide/epitopic sequence and antigenicity using different databases.

UniProt ID	Peptide sequence	Software		
		IEDB [70]	HLAPred [71]	ProPred [72]
ALBU_HUMAN	LLECADDRADLAKY	Antigenic peptide	Antigenic peptide	Antigenic peptide
BTNL2_HUMAN	VSEHRIQDKDGLFY	Antigenic peptide	Antigenic peptide	Antigenic peptide
GPC3_HUMAN	EYILSLEELVNGMY	Antigenic peptide	Antigenic peptide	Antigenic peptide

Table 5: Verification of physicochemical properties of predicted peptides using different software.

Properties	Software		
Toxicity	ToxinPred [54]	ProtParam [73]	—
Hydropathicity	ToxinPred	ProtParam	PlifePred [74]
SVM	ToxinPred	ProtParam	—
Charge	ToxinPred	ProtParam	PlifePred
Molecular weight	ToxinPred	ExPASy	PlifePred
Allergenecity	AlgPred [75]	AllergenFP	—
Antigenecity	VaxiJen [32]	Immunomedicine Group	ANTIGENpro [67]
Subcellular localization	CELLO [79]	UniProtKB [66]	—
Solubility	CamSol [68]	SOLPro [69]	PROSO [68]

components were recorded. The second booster dose of 320 μg indicated significant results with the adjuvant ($p < 1.0 \times 10^{-4}$). Significance was found in samples immunized with peptide alone compared to peptides in combination with aluminum hydroxide as an adjuvant. Higher numbers of lymphocytes, white blood cells, and granulocytes (10, 13, and5×10^9/l, respectively) were observed compared to the control (Figure 6).

3.9. Liver Function Tests. At given doses of trivalent peptides, liver toxicity and function were not disturbed and the level of enzymes was comparable to the controls indicating the safety of these peptides (Figure 7).

3.10. IgG ELISA. The level of IgG was tested after 3 weeks in the blood serum of the immunized rats. We observed the significant IgG production at the second booster dose of

Table 6: Phenotypic signs/symptoms observed after immunization of rats with synthetic peptides.

Sr. #	Signs/symptoms observed	Presence (yes)/absence (no)
1	Inflammation	No
2	Swelling around eyes	No
3	Bleeding	No
4	Diarrhea	No
5	Vomiting	No
6	Dizziness	No
7	Redness/swelling or pain at the site of injection	No
8	Temperature	No
9	Shivery	No
10	Any casualty	Nil

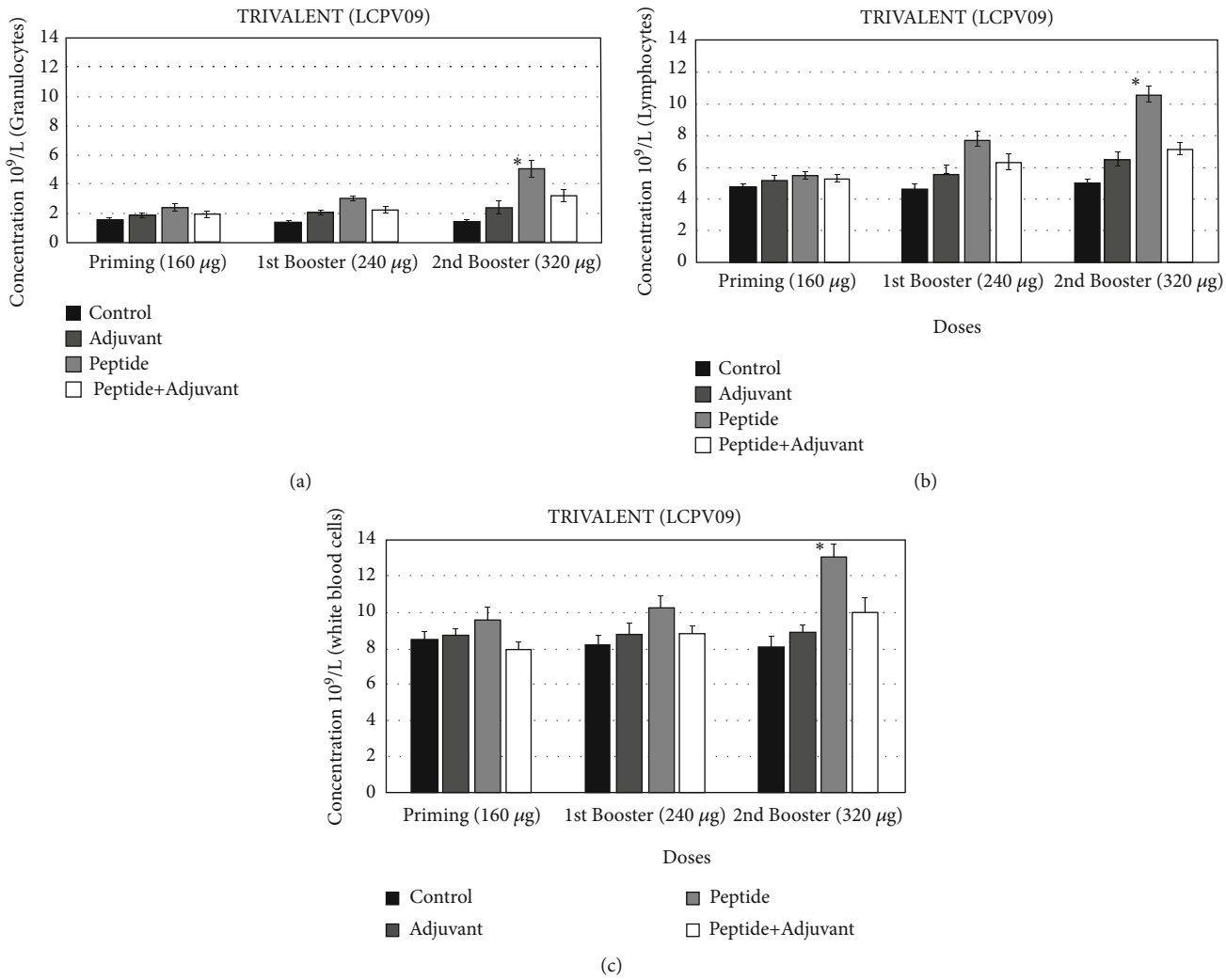

Figure 6: Hematological results were recorded after three weeks of immunization of rats with LCPV09. Blood components were counted using Beckman Coulter, USA. The significance has been shown by $*p < 0.01 \pm$ SEM. (a) Granulocytes. (b) Lymphocytes. (c) White blood cells.

320 μg. The concentration of IgG increased to 6 g/l after taking the peptide without the adjuvant compared to the control (2 g/l) ($p < 1.0 \times 10^{-4}$), while initial doses of the trivalent showed lower antibody production (Figure 8).

3.11. Granzyme B ELISA. Due to the immune response, cytotoxic T lymphocytes become activated and secreted granzymes and perforins to destroy cancerous cells through apoptosis [48]. The concentration of granzyme B (GrB) in

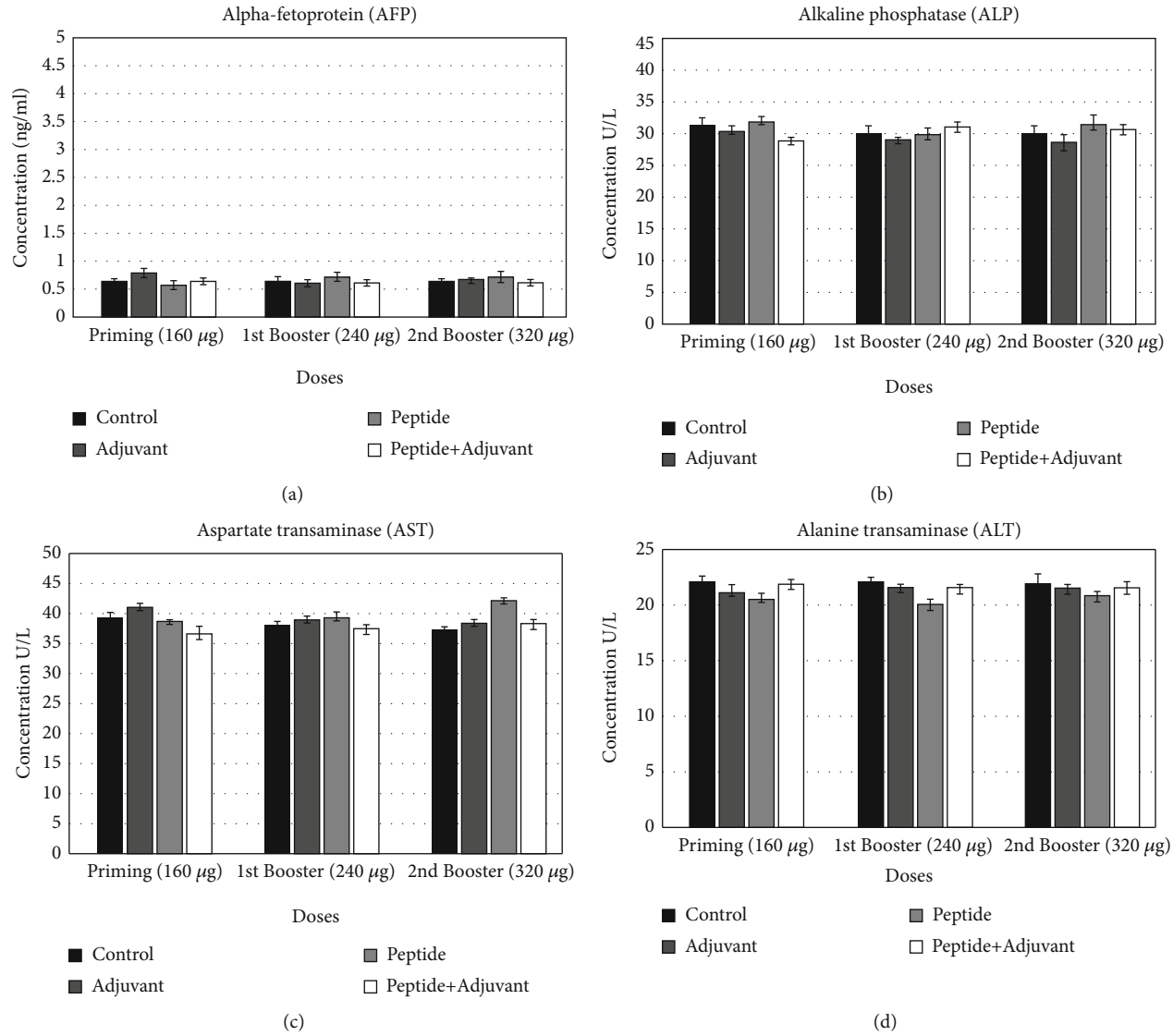

Figure 7: Liver function tests (LFTs) were performed after immunization of rats with each dose. (a) Alpha-fetoprotein (AFP). (b) Serum alkaline phosphatase (ALP). (c) Aspartate transaminase (AST). (d) Alanine transaminase (ALT).

blood serum was analyzed by measuring the absorbance at 450 nm. Granzyme concentration significantly increased to 1050 pg/ml at the second booster dose of peptides compared to the control (95 pg/ml). Statistical studies revealed that in the serum of trivalent-treated rats, a significant level of GrB was found at $(p < 1.0 \times 10^{-4}) \pm \text{SEM}$ (Figure 9).

4. Discussion

Liver cancer is becoming a great risk to human health due to its increased rate of recurrence, mortality, and metastatic nature [55]. To overcome conventional treatment issues, peptide vaccines have been in consideration for many years despite a few clinical trials. Considering all these aspects, vaccines related to reverse vaccinology have gained attention in cancer treatment [56]. We reported monovalent peptides in our previous studies [17] indicating substantial immune response; however, the present analysis showed the efficacy of trivalent peptides designed from liver-specific antigenic proteins. We observed that these trivalent peptides are antigenic and increased the titer rate of IgG antibodies, granzyme B, interferons, and other chemical mediators. These results indicate that different epitopes of various liver-specific proteins are effective for liver cancer disease. Reverse vaccinology is a cost- and time-effective approach [57], and it has been reported that the GVAX vaccine is the only FDA-approved therapeutic vaccine for prostate cancer designed by this approach. The therapeutic vaccines for pancreatic, lung, breast, and renal cancers are clinical trials [58]. Cancer peptide vaccines composed of small amino acids linked by peptide bonds are an initiative towards anticancer drug development [59]. A vaccine is a noteworthy defining factor in clinical trials. Previous experimental trials were focused on the treatment of predictable cancers. However, in massive tumor disease, the potential immune response is depressed due to progressive tumors, which ultimately leads

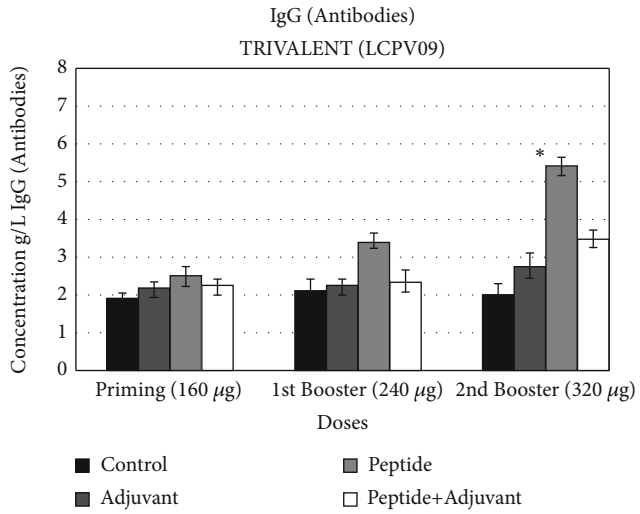

Figure 8: IgG antibodies (g/l). ELISA after each dose by taking four groups of rats. Each group has 6 replicates. Significant results were observed at the second booster dose of LCPV09. The significance has been shown by $*p < 0.01 \pm$ SEM.

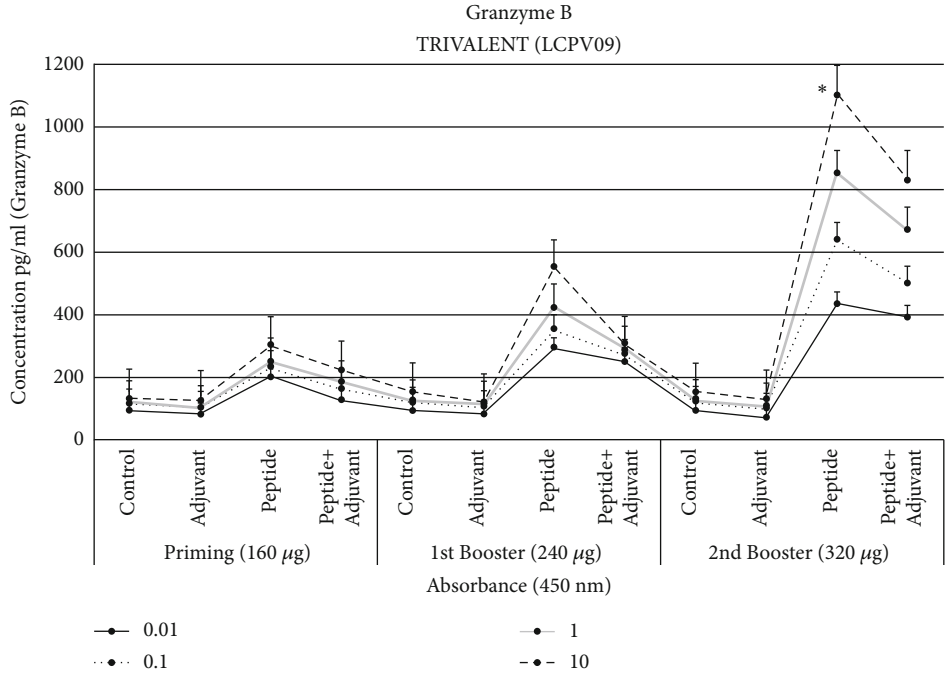

Figure 9: Granzyme B assay was performed, and absorbance was taken at 450 nm after each dose of LCPV09 by taking four groups of rats. Each group has 6 replicates. Significant results were observed at the second booster dose. The significance has been shown by $*p < 0.01 \pm$ SEM.

to immunosuppression. Emerging technology has been focused on low or no symptomatic diseases as a result of immunization response. A distinct way of vaccine immunization is peptide-based vaccines. T cells provoke immunity against cancer cells, which may be direct or indirect by inducing adaptive or innate immunity. Antibody response in immunity can be ducked by antigenic drift over time, while cell-mediated immunity is long-term immunity with memory [60].

In our study, we used tissue-specific antigenic proteins that are highly expressive in liver cancer compared to the BORIS cancer-testis antigen and hydatid cyst wall antigens that are not expressive in liver cells and may not have a role in the treatment and designing of liver cancer vaccines [61, 62]. Although these parasite antigens showed substantial immunogenicity and high epitope homology with cancer antigens, however, these proteins are not expressed in the liver [62]. We used protein data related to specific liver

cancer to find potential vaccine candidates that can improve existing vaccine specificity. There may be a risk of occurrence of any side effect in the body by using hydatid cyst wall antigens and nonspecificity of the recognition pattern of liver cancer cells. The antitumor effects of protein cancer vaccines were assessed in metastatic nonimmunogenic 4T1 mammary carcinoma in BALB/c mice compared to this study that was carried out in Sprague Dawley rat models presenting increased serum levels of IgG and interferon-γ. Our method of prediction is generalized and can be applied to infectious diseases and genetic disorders [63].

Many cancer vaccines have recently been designed to prevent the spread of cancer. To produce multiepitope DNA and peptide cancer vaccines, different bioinformatics techniques were used to determine the most immunodominant epitopes of acrosin-binding protein (ACRBP) and synaptonemal complex protein 1 (SYCP1) antigens. The peptide vaccination resulted in a considerable rise in serum IgG antibodies and interferon levels. In the murine melanoma model, the results show that the proposed multiepitope peptide vaccination has high effectiveness for immune system activation and antitumor preventive effects [64]. In the following study, the potential of antigenic epitopes to stimulate the immune system against liver cancer was studied. Liver cancer proteins were screened, and their antigenicities were predicted. The extracellular matrix and membrane-bounded antigenic proteins of higher molecular weight > 23 kDa were selected for the activation of immune components. Through the different steps of bioinformatics approaches, the three best antigenic proteins ALB, GPC3, and BTNL2 were screened. These proteins have high expression in the liver, and GPC3 has already gone under clinical trials [50]. Epitopes of length 14 amino acid residues were predicted indicating a maximum binding affinity for MHC class I molecules. The potential trivalent vaccine candidate is designed from these three proteins and synthesized for the generation of an effective immune response. To prevent any alteration in epitope arrangement and functionality, AAY linkers were added to a trivalent containing 48 amino acid residues. In *in vivo* analysis, the predicted trivalent vaccine stimulates cytotoxic T lymphocytes because of their affinity to receptors of MHC class I. Analysis of the interaction and function associations between predicted epitopes and other proteins also describes their significance in liver cancer immunotherapy. Rat models were used to study the immune responses. Hematological immune system components such as granulocytes, lymphocytes, and white blood cells showed substantial results as an immunotherapeutic response at the second booster dose of the trivalent adjuvant. The raised count of lymphocytes, white blood cells, and granulocytes was compared with controls indicating a significant immune response. Similarly, the production of IgG antibodies is secreted as a humoral immune response. The increased concentration of IgG compared to the controls presented substantial outcomes ($p < 1.0 \times 10^{-4}$).

The *in vitro* cytotoxicity test revealed the granzyme presence in the supernatants. Granzyme concentration significantly increased (1050 pg/ml) at the second booster dose compared to the control. Cytotoxic cells become activated, and granzymes are released when target cells activate them as a usual immune response [63]. NK cells and cytotoxic cells also release granules on stimulation through foreign molecules, and these granules contain granzymes within them [65].

Antigens associated with these tumors open up new opportunities for cancer immunotherapy. This approach helps us to classify possible natural candidates for unique vaccines for customized cancer [63].

5. Conclusion

Immunoinformatics is helpful in enhancing the potential of computational practices through which vaccines designed to fight against cancer become more important. Different cancerous antigenic peptides were identified by means of computational methods that offer an advantage for effective vaccine development against liver cancer. The trivalent construct may be a potential vaccine candidate to bind MHC class I molecules. The animal models' different experiments were applied for the confirmation of the effectiveness of these epitopes that are involved in the designing of a vaccine against liver cancer. It is concluded that the design of T cell epitope-based vaccines for liver cancer through the immunoinformatics approach is efficient, practical, cost-effective, and time-effective. The revolutionary changes in the field of reverse vaccinology can be used in disease treatment of both humans and animals as the basic protocol for the design of vaccines using bioinformatics tools.

Data Availability

Data is available in supplementary information files.

Ethical Approval

These experimental procedures were approved by the Bioethics Committee for Animals of the Institute of Molecular Biology and Biotechnology, Bahauddin Zakariya University, Multan, Pakistan, with Approval No. IMBB/02/2019.

Conflicts of Interest

The authors declare that they have no competing interests.

Authors' Contributions

SM and AA supervised the study. SZ, JG, and SN collected the data. SM, II, and AA analyzed the data. MS and II provided guidance for study design and data analysis. All authors contributed to manuscript writing and editions. All authors read and approved the final manuscript. Sidra Zafar and Baogang Bai contributed equally to this work.

Acknowledgments

This study is funded and supported by the Higher Education Commission, Pakistan, under Award Project No. 8445/Punjab/NRPU/R&D/HEC/2017.

Supplementary Materials

Supplementary Table 1: cancer genomic data. Supplementary Table 2: liver proteomic data. *(Supplementary Materials)*

References

[1] I. M. Ariel and G. T. Pack, "Treatment of inoperable cancer of the liver by intra-arterial radioactive isotopes and chemotherapy," *Cancer*, vol. 20, no. 5, pp. 793–804, 1967.

[2] W. Wang, Z. Huang, B. Guo, S. Liu, W. Xiao, and J. Liang, "Short- and long-term outcomes of laparoscopic hepatectomy in elderly patients with hepatocellular carcinoma," *Journal of BUON*, vol. 23, no. 4, pp. 971–978, 2018.

[3] S. Jin, Q. Fu, G. Wuyun, and T. Wuyun, "Management of post-hepatectomy complications," *World Journal of Gastroenterology: WJG*, vol. 19, no. 44, pp. 7983–7991, 2013.

[4] C. A. Damyanov, I. K. Maslev, V. S. Pavlov, and L. Avramov, "Conventional treatment of cancer realities and problems," *Annals of Complementary and Alternative Medicine*, vol. 1, no. 1, 2018.

[5] C. S. Floudas, G. Brar, and T. F. Greten, "Immunotherapy: current status and future perspectives," *Digestive Diseases and Sciences*, vol. 64, no. 4, pp. 1030–1040, 2019.

[6] J. W. Ogony, D. C. Radisky, K. J. Ruddy et al., "Immune responses and risk of triple-negative breast cancer: implications for higher rates among African American women," *Cancer Prevention Research*, vol. 13, no. 11, pp. 901–910, 2020.

[7] V. Mitra and J. Metcalf, "Metabolic functions of the liver," *Anaesthesia & Intensive Care Medicine*, vol. 10, no. 7, pp. 334-335, 2009.

[8] E. Vivier, D. H. Raulet, A. Moretta et al., "Innate or adaptive immunity? The example of natural killer cells," *Science*, vol. 331, no. 6013, pp. 44–49, 2011.

[9] S. Gandini, E. Botteri, S. Iodice et al., "Tobacco smoking and cancer: a meta-analysis," *International Journal of Cancer*, vol. 122, no. 1, pp. 155–164, 2008.

[10] H. H. Lara, E. N. Garza-Treviño, L. Ixtepan-Turrent, and D. K. Singh, "Silver nanoparticles are broad-spectrum bactericidal and virucidal compounds," *Journal of Nanobiotechnology*, vol. 9, no. 1, p. 30, 2011.

[11] C. Donati and R. Rappuoli, "Reverse vaccinology in the 21st century: improvements over the original design," *Annals of the New York Academy of Sciences*, vol. 1285, no. 1, pp. 115–132, 2013.

[12] M. Enayatkhani, M. Salimi, K. Azadmanesh, and L. Teimoori-Toolabi, "In-silico identification of new inhibitors for low-density lipoprotein receptor-related protein6 (LRP6)," *Journal of Biomolecular Structure and Dynamics*, vol. 18, pp. 1–11, 2020.

[13] S. Kaliamurthi, G. Selvaraj, M. Junaid, A. Khan, K. Gu, and D. Q. Wei, "Cancer immunoinformatics: a promising era in the development of peptide vaccines for human papillomavirus-induced cervical cancer," *Current Pharmaceutical Design*, vol. 24, no. 32, pp. 3791–3817, 2018.

[14] N. Tomar and R. K. De, "Immunoinformatics: an integrated scenario," *Immunology*, vol. 131, no. 2, pp. 153–168, 2010.

[15] M. P. Johnston and S. I. Khakoo, "Immunotherapy for hepatocellular carcinoma: current and future," *World Journal of Gastroenterology*, vol. 25, no. 24, pp. 2977–2989, 2019.

[16] L. H. Butterfield, A. Ribas, V. B. Dissette et al., "A phase I/II trial testing immunization of hepatocellular carcinoma patients with dendritic cells pulsed with four α-fetoprotein peptides," *Clinical Cancer Research*, vol. 12, no. 9, pp. 2817–2825, 2006.

[17] S. A. Muhammad, S. Zafar, S. Z. Rizvi et al., "Experimental analysis of T-cell epitopes for designing liver cancer vaccine predicted by system level immunoinformatics approach," *American Journal of Physiology. Gastrointestinal and Liver Physiology*, vol. 318, no. 6, pp. G1055–G1069, 2020.

[18] S. Paul and G. Lal, "The molecular mechanism of natural killer cells function and its importance in cancer immunotherapy," *Frontiers in Immunology*, vol. 8, pp. 1124–1124, 2017.

[19] D. K. Flaherty, *Immunology for pharmacy*, Elsevier, 2012.

[20] M. I. Vazquez, J. Catalan-Dibene, and A. Zlotnik, "B cells responses and cytokine production are regulated by their immune microenvironment," *Cytokine*, vol. 74, no. 2, pp. 318–326, 2015.

[21] J. Bonner, *Biology*, J. W. Kimball, Ed., Nature publishing group Macmillan building, crinan ST, London N1 9XW, England, 1984.

[22] J. Scholtalbers, S. Boegel, T. Bukur et al., "TCLP: an online cancer cell line catalogue integrating HLA type, predicted neo-epitopes, virus and gene expression," *Genome Medicine*, vol. 7, no. 1, pp. 1–7, 2015.

[23] J. Wu, W. Zhao, B. Zhou et al., "TSNAdb: a database for tumor-specific neoantigens from immunogenomics data analysis," *Genom Proteom Bioinform*, vol. 16, no. 4, pp. 276–282, 2018.

[24] A. Kassambara, T. Rème, M. Jourdan et al., "GenomicScape: an easy-to-use web tool for gene expression data analysis. Application to investigate the molecular events in the differentiation of B cells into plasma cells," *PLoS Computational Biology*, vol. 11, no. 1, article e1004077, 2015.

[25] M. Uhlén, L. Fagerberg, B. M. Hallström et al., "Proteomics. Tissue-based map of the human proteome," *Science*, vol. 347, no. 6220, article 1260419, 2015.

[26] M. Uhlén, L. Fagerberg, B. M. Hallström et al., "Tissue-based map of the human proteome," *Science*, vol. 347, no. 6220, p. 1260419, 2015.

[27] Y. Chen, W. Liang, S. Yang et al., "Human infections with the emerging avian influenza A H7N9 virus from wet market poultry: clinical analysis and characterisation of viral genome," *Lancet*, vol. 381, no. 9881, pp. 1916–1925, 2013.

[28] C. S. Yu, Y. C. Chen, C. H. Lu, and J. K. Hwang, "Prediction of protein subcellular localization," *Proteins*, vol. 64, no. 3, pp. 643–651, 2006.

[29] G. Dhiman, N. Lohia, S. Jain, and M. Baranwal, "Metadherin peptides containing $CD4^+$ and $CD8^+$ T cell epitopes as a therapeutic vaccine candidate against cancer," *Journal of Microbiology, Immunology and Infection*, vol. 60, no. 9, pp. 646–652, 2016.

[30] S. Tenzer, B. Peters, S. Bulik et al., "Modeling the MHC class-I pathway by combining predictions of proteasomal cleavage, TAP-transport and MHC binding," *Cellular and Molecular Life Sciences CMLS*, vol. 62, no. 9, 2004.

[31] H.-H. Bui, J. Sidney, W. Li, N. Fusseder, and A. Sette, "Development of an epitope conservancy analysis tool to facilitate the design of epitope-based diagnostics and vaccines," *BMC Bioinformatics*, vol. 8, no. 1, 2007.

[32] I. A. Doytchinova and D. R. Flower, "VaxiJen: a server for prediction of protective antigens, tumour antigens and subunit vaccines," *BMC Bioinformatics*, vol. 8, no. 1, 2007.

[33] P. Stothard, "The sequence manipulation suite: JavaScript programs for analyzing and formatting protein and DNA sequences," *Biotechniques*, vol. 28, no. 6, pp. 1102–1104, 2000.

[34] E. Gasteiger, C. Hoogland, A. Gattiker et al., "Protein identification and analysis tools on the ExPASy server," in *The Proteomics Protocols Handbook*, pp. 571–607, Springer, 2005.

[35] A. Tharwat, Y. S. Moemen, and A. E. Hassanien, "Classification of toxicity effects of biotransformed hepatic drugs using whale optimized support vector machines," *Journal of Biomedical Informatics*, vol. 68, pp. 132–149, 2017.

[36] S. Gupta, P. Kapoor, K. Chaudhary et al., "In silico approach for predicting toxicity of peptides and proteins," *PloS One*, vol. 8, no. 9, article e73957, 2013.

[37] S. A. Islam, T. Sajed, C. M. Kearney, and E. J. Baker, "PredSTP: a highly accurate SVM based model to predict sequential cystine stabilized peptides," *BMC Bioinformatics*, vol. 16, no. 1, p. 210, 2015.

[38] C. Dominguez, R. Boelens, and A. M. Bonvin, "HADDOCK: a protein– protein docking approach based on biochemical or biophysical information," *Journal of the American Chemical Society*, vol. 125, no. 7, pp. 1731–1737, 2003.

[39] G. C. P. van Zundert, J. P. G. L. M. Rodrigues, M. Trellet et al., "The HADDOCK2.2 web server: user-friendly integrative modeling of biomolecular complexes," *Journal of Molecular Biology*, vol. 428, no. 4, pp. 720–725, 2016.

[40] N. Nezafat, Y. Ghasemi, G. Javadi, M. J. Khoshnoud, and E. Omidinia, "A novel multi-epitope peptide vaccine against cancer: an in silico approach," *Journal of Theoretical Biology*, vol. 349, pp. 121–134, 2014.

[41] M. Ali, R. K. Pandey, N. Khatoon, A. Narula, A. Mishra, and V. K. Prajapati, "Exploring dengue genome to construct a multi-epitope based subunit vaccine by utilizing immunoinformatics approach to battle against dengue infection," *Scientific Reports*, vol. 7, no. 1, p. 9232, 2017.

[42] P. Thevenet, Y. Shen, J. Maupetit, F. Guyon, P. Derreumaux, and P. Tuffery, "PEP-FOLD: an updated de novo structure prediction server for both linear and disulfide bonded cyclic peptides," *Nucleic Acids Research*, vol. 40, no. W1, pp. W288–W293, 2012.

[43] Y. Zhang, "I-TASSER server for protein 3D structure prediction," *BMC Bioinformatics*, vol. 9, no. 1, 2008.

[44] D. Bhattacharya and J. Cheng, "i3Drefine software for protein 3D structure refinement and its assessment in CASP10," *PLoS One*, vol. 8, no. 7, article e69648, 2013.

[45] N. M. Said and O. Abiola, "Haematological profile shows that inbred Sprague Dawley rats have exceptional promise for use in biomedical and pharmacological studies," *Asian Journal of Biomedical and Pharmaceutical*, vol. 4, no. 37, pp. 33–37, 2014.

[46] M. Agallou, E. Athanasiou, O. Koutsoni, E. Dotsika, and E. Karagouni, "Experimental validation of multi-epitope peptides including promising MHC class I-and II-restricted epitopes of four known Leishmania infantum proteins," *Frontiers in Immunology*, vol. 5, p. 268, 2014.

[47] S. F. Cai, T. A. Fehniger, X. Cao et al., "Differential expression of granzyme B and C in murine cytotoxic lymphocytes," *Journal of Immunology*, vol. 182, no. 10, pp. 6287–6297, 2009.

[48] X. Li, L. Guo, M. Kong et al., "Design and evaluation of a multi-epitope peptide of human metapneumovirus," *Intervirology*, vol. 58, no. 6, pp. 403–412, 2016.

[49] R. Spinella, R. Sawhney, and R. Jalan, "Albumin in chronic liver disease: structure, functions and therapeutic implications," *Hepatology International*, vol. 10, no. 1, pp. 124–132, 2016.

[50] D. Nobuoka, T. Yoshikawa, Y. Sawada, T. Fujiwara, and T. Nakatsura, "Peptide vaccines for hepatocellular carcinoma," *Human Vaccines & Immunotherapeutics*, vol. 9, no. 1, pp. 210–212, 2013.

[51] A. J. Basak, S. Maiti, A. Hansda et al., "Structural insights into N-terminal IgV domain of BTNL2, a T cell inhibitory molecule, suggests a non-canonical binding interface for its putative receptors," *Journal of Molecular Biology*, vol. 432, no. 22, pp. 5938–5950, 2020.

[52] C. H. Elisabeth Gasteiger, "Protein identification and analysis tools on the ExPASy server," in *The proteomics protocols handbook*pp. 571–607, Humana Press.

[53] J. Kyte and R. F. Doolittle, "A simple method for displaying the hydropathic character of a protein," *Journal of Molecular Biology*, vol. 157, no. 1, pp. 105–132, 1982.

[54] S. Gupta, P. Kapoor, K. Chaudhary, A. Gautam, R. Kumar, and G. P. S. Raghava, "Peptide toxicity prediction," *Methods in Molecular Biology*, vol. 1268, pp. 143–157, 2015.

[55] D. Amit, S. Tamir, T. Birman, O. N. Gofrit, and A. Hochberg, "Development of targeted therapy for bladder cancer mediated by a double promoter plasmid expressing diphtheria toxin under the control of IGF2-P3 and IGF2-P4 regulatory sequences," *International Journal of Clinical and Experimental Medicine*, vol. 4, no. 2, pp. 91–102, 2011.

[56] Y. F. Xiao, M. M. Jie, B. S. Li et al., "Peptide-based treatment: a promising cancer therapy," *Journal of Immunology Research*, vol. 2015, Article ID 761820, 13 pages, 2015.

[57] R. Moxon, P. A. Reche, and R. Rappuoli, "Reverse vaccinology," *Frontiers in Immunology*, vol. 10, 2019.

[58] I. Melero, G. Gaudernack, W. Gerritsen et al., "Therapeutic vaccines for cancer: an overview of clinical trials," *Nature reviews Clinical oncology*, vol. 11, no. 9, pp. 509–524, 2014.

[59] G. Parmiani, V. Russo, C. Maccalli, D. Parolini, N. Rizzo, and M. Maio, "Peptide-based vaccines for cancer therapy," *Human Vaccines & Immunotherapeutics*, vol. 10, no. 11, pp. 3175–3178, 2014.

[60] A. P. Galvani, M. L. Ndeffo-Mbah, N. Wenzel, and J. E. Childs, "Ebola vaccination: if not now, when?," *Annals of Internal Medicine*, vol. 161, no. 10, pp. 749-750, 2014.

[61] E. Mahdevar, A. Safavi, A. Abiri et al., "Exploring the cancer-testis antigen BORIS to design a novel multi-epitope vaccine against breast cancer based on immunoinformatics approaches," *Journal of Biomolecular Structure and Dynamics*, pp. 1–18, 2021.

[62] M. Shakibapour, A. Kefayat, M. R. Mofid et al., "Anti-cancer immunoprotective effects of immunization with hydatid cyst wall antigens in a non-immunogenic and metastatic triple-negative murine mammary carcinoma model," *International Immunopharmacology*, vol. 99, article 107955, 2021.

[63] P. Loetscher, M. Seitz, I. Clark-Lewis, M. Baggiolini, and B. Moser, "Activation of NK cells by CC chemokines. Chemotaxis, Ca^{2+} mobilization, and enzyme release," *Journal of Immunology*, vol. 156, no. 1, pp. 322–327, 1996.

[64] A. Safavi, A. Kefayat, F. Sotoodehnejadnematalahi, M. Salehi, and M. H. Modarressi, "Production, purification, and *in vivo* evaluation of a novel multiepitope peptide vaccine consisted of immunodominant epitopes of SYCP1 and ACRBP antigens as a prophylactic melanoma vaccine," *International Immunopharmacology*, vol. 76, article 105872, 2019.

[65] S. Isaaz, K. Baetz, K. Olsen, E. Podack, and G. M. Griffiths, "Serial killing by cytotoxic T lymphocytes: T cell receptor triggers degranulation, re-filling of the lytic granules and secretion of lytic proteins via a non-granule pathway," *European Journal of Immunology*, vol. 25, no. 4, pp. 1071–1079, 1995.

[66] Q. Liu, B. Yuan, K. A. Lo, H. C. Patterson, Y. Sun, and H. F. Lodish, "Adiponectin regulates expression of hepatic genes critical for glucose and lipid metabolism," *PNAS*, vol. 109, no. 36, pp. 14568–14573, 2012.

[67] S. Pundir, M. J. Martin, C. O'Donovan, and The UniProt Consortium, "UniProt tools," *Current Protocols in Bioinformatics*, vol. 53, no. 1, 2016.

[68] M. A. Naeem, M. M. Adeel, A. Kanwal et al., "Reconnoitering Mycobacterium tuberculosis lipoproteins to design subunit vaccine by immunoinformatics approach," *Advancements in Life Sciences*, vol. 8, no. 3, pp. 300–306, 2021.

[69] P. Sormanni and M. Vendruscolo, "Protein solubility predictions using the CamSol method in the study of protein homeostasis," *Cold Spring Harbor Perspectives in Biology*, vol. 11, no. 12, article a033845, 2019.

[70] C. N. Magnan, A. Randall, and P. Baldi, "SOLpro: accurate sequence-based prediction of protein solubility," *Bioinformatics*, vol. 25, no. 17, pp. 2200–2207, 2009.

[71] M. Nielsen, C. Lundegaard, P. Worning et al., "Reliable prediction of T-cell epitopes using neural networks with novel sequence representations," *Protein Science*, vol. 12, no. 5, pp. 1007–1017, 2003.

[72] E. Keitel, A. Santos, M. Alves et al., "Immunosuppression protocols for HLA identical renal transplant recipients," in *Transplantation proceedings*, vol. 35, no. 3pp. 1074-1075, Elsevier, 2003.

[73] H. Singh and G. Raghava, "ProPred: prediction of HLA-DR binding sites," *Bioinformatics*, vol. 17, no. 12, pp. 1236-1237, 2001.

[74] A. Joshi, B. C. Joshi, M. A. Mannan, and V. Kaushik, "Epitope based vaccine prediction for SARS-CoV-2 by deploying immuno-informatics approach," *Informatics in Medicine Unlocked*, vol. 19, article 100338, 2020.

[75] D. Mathur, S. Singh, A. Mehta, P. Agrawal, and G. P. S. Raghava, "In silico approaches for predicting the half-life of natural and modified peptides in blood," *PLoS One*, vol. 13, no. 6, article e0196829, 2018.

[76] S. Saha and G. P. S. Raghava, "AlgPred: prediction of allergenic proteins and mapping of IgE epitopes," *Nucleic Acids Research*, vol. 34, no. Web Server, pp. W202–W209, 2006.

[77] P. W. Rose, A. Prlić, A. Altunkaya et al., "The RCSB Protein Data Bank: integrative view of protein, gene and 3D structural information," *Nucleic Acids Research*, vol. 45, no. D1, pp. D271–D281, 2017.

[78] J. Maupetit, P. Derreumaux, and P. Tufféry, "A fast method for large-scale de novo peptide and miniprotein structure prediction," *Journal of Computational Chemistry*, vol. 31, no. 4, pp. 726–738, 2010.

[79] J. Yang and Y. Zhang, "Protein structure and function prediction using I-TASSER," *Current Protocols in Bioinformatics*, vol. 52, no. 1, 2015.

Hindawi
BioMed Research International
Volume 2022, Article ID 3206594, 8 pages
https://doi.org/10.1155/2022/3206594

Research Article

Causes of Mortality in Korean Patients with Neurodegenerative Dementia

Hyo Geun Choi,[1,2] **Bumjung Park**,[2] **Ji Hee Kim**,[3] **Joo-Hee Kim**,[4] **Mi Jung Kwon**,[5] **and Miyoung Kim**[6]

[1]*Hallym Data Science Laboratory, Hallym University College of Medicine, Anyang, Republic of Korea*
[2]*Department of Otorhinolaryngology-Head & Neck Surgery, Hallym University Sacred Heart Hospital, Hallym University College of Medicine, Anyang, Republic of Korea*
[3]*Department of Neurosurgery, Hallym University Sacred Heart Hospital, Hallym University College of Medicine, Anyang, Republic of Korea*
[4]*Division of Pulmonary, Allergy, And Critical Care medicine, Department of Medicine, Hallym University Sacred Heart Hospital, Hallym University College of Medicine, Anyang, Republic of Korea*
[5]*Department of Pathology, Hallym University Sacred Heart Hospital, Hallym University College of Medicine, Anyang, Republic of Korea*
[6]*Department of Laboratory Medicine, Asan Medical Center, University of Ulsan College of Medicine, 88 Olympic-ro 43-gil, Songpa-gu, Seoul 05505, Republic of Korea*

Correspondence should be addressed to Miyoung Kim; miyoungkim@amc.seoul.kr

Received 2 December 2021; Accepted 16 March 2022; Published 25 April 2022

Academic Editor: Cheng Li

The prevalence of neurodegenerative dementia is increasing owing to the rapid growth of the older population. We investigated risks and causes of mortality in Korean patients with neurodegenerative dementia using data from the Korean Health Insurance Review and Assessment Service-National Sample Cohort with the aim to improve their care. From a pool of 1,125,691 patients, 11,215 patients aged ≥60 years who were diagnosed with dementia between 2002 and 2013 were examined along with 44,860 matched controls. A Cox proportional hazard model was used to calculate crude and adjusted hazard ratios (HRs). During the follow-up period, 34.5% and 18.8% of individuals in the neurodegenerative dementia and control groups, respectively, died ($P < 0.001$). The adjusted HR for mortality in the neurodegenerative dementia group was 2.11 (2.41 and 1.96 in men and women, respectively). Moreover, the adjusted HRs in patients with neurodegenerative dementia were 3.25, 2.77, and 1.84 for those diagnosed at ages 60–69, 70–79, and ≥80 years, respectively. The highest odds ratio for mortality was noted among patients with neurologic disease (15.93) followed by those with mental disease (4.89). These data show that the risk of mortality increased regardless of age and sex in Korean patients with neurodegenerative dementia.

1. Introduction

Dementia is the loss of function in one or more cognitive domains to an extent severe enough to interfere with independent social or occupational activities [1, 2]. It is commonly associated with more than one neuropathological disorder, usually Alzheimer's disease (AD) with cerebrovascular pathology [1, 2]. As the global proportion of the older population has grown in recent decades, the prevalence of dementia has also increased rapidly [3]. The Global Burden of Diseases, Injuries, and Risk Factors study of 2016 revealed that the rate of this condition increased from 383 per 100,000 population in 1990 to 593 per 100,000 population in 2016 (a 54.7% jump) [3]. The number of individuals who live with dementia worldwide increased from 20.2 million in 1990 to 43.8 million in 2016 [3]. Indeed, the

prevalence of dementia is expected to increase in the coming years, as is its impact on society (including the burden imposed on caregivers) [4, 5].

Dementia not only worsens patients' quality of life but may also subject them to a higher risk of death. Thus, understanding the risks and causes of mortality among individuals with dementia is important for patients, caregivers, health professionals, and health policymakers [6]. Previous Western studies consistently showed that the life expectancy of older people with dementia is shorter than that of their healthy counterparts [6–8].

The growth rate of the older population in Korea is one of the highest in the world [9]. The nation has been projected to become a "super-aged" society by 2026, with 37.6% of the population (17.9 million individuals) expected to be over 65 years of age by 2050 [9]. As the society has aged, the prevalence of dementia has also increased rapidly in Korea [9, 10]. A meta-analysis published in 2014 found that the prevalence of dementia in patients aged ≥65 years was 9.2%, which was higher than that in similarly aged counterparts in Western and other Asian countries [9]. Studies on this subject in Korea are scarce and have yielded conflicting results. A study of 724 Korean patients with AD showed that the median survival was 9.3 years, which was much longer than that found in studies of Caucasians [11]. However, results from a more recent study suggested that the risk of mortality in Korean patients with dementia is underestimated as the hazard ratio (HR) of individuals who had dementia at both the baseline and 2-year follow-up assessment was 2.82, while that of individuals who had no dementia at baseline assessment but had developed the disease by the time of the 2-year follow-up visit was 8.37 [12].

The risks and causes of mortality in patients with dementia could be ethnicity and environment specific; thus, reliable data from a representative Korean population with this disease are needed to better understand these aspects and assist patients with dementia in this country. As such, we performed this retrospective large-scale longitudinal follow-up study of risks and causes of mortality in patients with dementia in South Korea. Using a national cohort database, we could analyze a representative population over a maximum follow-up period of 12 years.

2. Materials and Methods

2.1. Study Population and Data Collection. The ethics committee of Hallym University approved the use of these data (2019-01-003); the requirement for written informed consent was waived by the Institutional Review Board. All methods were performed in accordance with the relevant guidelines as well as the tenants laid down in the Declaration of Helsinki. This national cohort study relied on data from the Korean Health Insurance Review and Assessment Service-National Sample Cohort [13, 14].

2.2. Participant Selection. Among 1,125,691 patients with 114,369,638 medical claim codes, we included 13,102 participants who were diagnosed with neurodegenerative dementia between 2002 and 2013. Neurodegenerative dementia included AD (International Classification of Diseases-(ICD-) 10 code G30) or dementia in AD (F00). For accurate diagnosis, we selected participants who were treated 2 or more times for neurodegenerative dementia; the reliability of the diagnosis was as described in our previous studies [15, 16]. The control participants were identified from among 1,112,589 individuals who had not been diagnosed with neurodegenerative dementia between 2002 and 2013.

Participants with neurodegenerative dementia were compared to control participants who were matched 1 : 4 for age, sex, income, region of residence, and past medical histories of hypertension, diabetes mellitus, and dyslipidemia. To prevent selection bias, control participants were each assigned a random number and then selected in descending numerical order. The index date was set as that of the diagnosis of dementia; participants in the control group were followed from the same index date as their matched counterparts. The follow-up duration was calculated from the index date to the date of death or that of the end of the study (December 31, 2013), and the participants were followed until death or were otherwise censored. Individuals in the control group who died before their matched counterparts in the neurodegenerative dementia group entered the study were excluded. The cause of death was defined according to the death certificate issued by medical doctors, which stated the most relevant reason for death. These data were obtained from Statistics Korea (http://kostat.go.kr/portal/eng/index.action).

Participants with neurodegenerative dementia for whom we could not identify a sufficient number of matching control individuals were excluded ($n = 1{,}375$), as were individuals who were diagnosed with neurodegenerative dementia before the age of 60 years ($n = 512$). Ultimately, 1 : 4 matching resulted in the inclusion of 11,215 individuals with dementia and 44,860 control participants (Figure 1); however, they were not matched for past medical histories of ischemic heart disease and stroke, as these events were relatively rare.

2.3. Variables. Each participant's age, sex, income, and region of residence were noted as described in our previous study [17]. The cause of death was determined according to the Korean standard classification of diseases, as also described in that same study [17].

The medical histories of the participants were evaluated using ICD-10 codes. For the accuracy of diagnosis, a patient was considered to have hypertension (I10 and I15), diabetes (E10–E49), and hyperlipidemia (E78) if treated 2 or more times for these conditions and was considered to have ischemic heart disease (I24 and I25) and stroke (I60–I66) if treated 1 or more times for either.

2.4. Statistical Analyses. The chi-square or Fisher's exact test was used to compare mortality rates between individuals in the neurodegenerative dementia and control groups according to the cause of death. The false discovery rate was calculated to adjust for an incorrectly rejected null hypothesis.

The Cox proportional hazard model was used to calculate the HR for mortality in patients with neurodegenerative

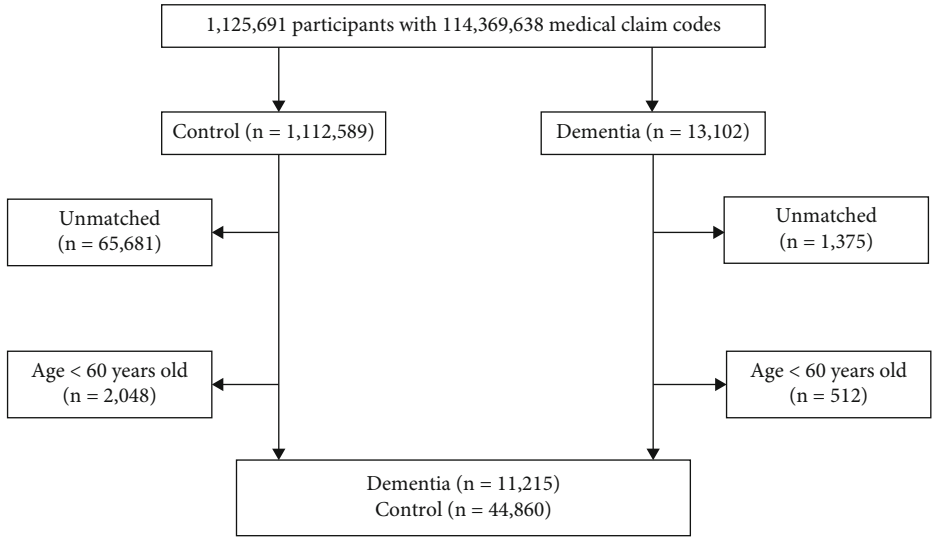

Figure 1: A schematic illustration of the participant selection process that was used in the present study. Of a total of 1,125,691 participants, 13,102 with neurodegenerative dementia were included; these patients were matched 1 : 4 with a control group of individuals not diagnosed with dementia. Ultimately, 11,215 participants with neurodegenerative dementia and 44,860 controls were included.

dementia. In this analysis, both a crude (simple) model and another adjusted for histories of ischemic heart disease and stroke were used; the 95% confidence intervals (CIs) were also calculated. Patients were stratified according to age, sex, income, region of residence, hypertension, diabetes, and hyperlipidemia status. Two-tailed analyses were conducted, and P values of < 0.05 were considered statistically significant. The results were analyzed using the SPSS software version 21.0 (IBM, Armonk, NY, USA).

3. Results

The mean follow-up durations were 35.9 months (standard deviation (SD) = 29.6 months) in the neurodegenerative dementia group and 41.9 months (SD = 32.4 months) in the control group. The survival rates during the study period are shown in Figure 2. Age, sex, income level, and region of residence were matched between the neurodegenerative dementia and control groups (Table 1). The incidence rates of hypertension, diabetes, and dyslipidemia did not differ between the 2 groups, whereas ischemic heart disease and stroke were more prevalent in the neurodegenerative dementia group. Furthermore, 34.5% (3,873/18,557) and 18.8% (8,434/44,860) of participants in the neurodegenerative dementia and control groups, respectively, died during the follow-up period ($P < 0.001$).

The crude and adjusted HRs for mortality in the neurodegenerative dementia group were 2.26 (95% CI = 2.17 – 2.35) and 2.11 (95% CI = 2.03 – 2.20), respectively (Table 2). This group had higher crude and adjusted HRs for mortality across all age- and sex-based subgroups than the control group (Table 2). The adjusted HR (95% CI) was the highest in patients with neurodegenerative dementia whose ages at the initial diagnosis were 60–69 years (3.25 [2.79–3.78]), which was lower in those aged 70–79 years (2.48 [2.32–2.65]), and lowest in those aged ≥80 years (1.78 [1.69–1.88]). The adjusted HRs (95% CIs) were 2.41 (2.26–2.57) and 1.96 (1.86–2.06) in men and women, respectively.

Analysis of mortality rates according to the cause of death showed an odds ratio (OR) for overall death of 2.28 (95% CI, 2.18–2.39) in the neurodegenerative dementia group (Table 3). Patients with neurodegenerative dementia who died during this study had elevated ORs for mortality regardless of the cause of death except for those with neoplasms (false discovery rate-adjusted $P < 0.05$). Neurologic disease showed the highest OR for mortality (15.93; 95% CI, 13.10–19.38) followed by mental disease (4.89; 95% CI, 3.78–5.57). The causes of death are detailed in Supplementary Table 1.

4. Discussion

Our investigation of the Korean population revealed an elevated mortality rate among patients with neurodegenerative dementia across all age- and sex-based subgroups. The adjusted HR was highest in patients whose ages at the time of neurodegenerative dementia diagnosis were 60–69 years and lowest in those diagnosed at ages ≥ 80 years. Mortality rates owing to any of the investigated causes other than neoplasms were higher in the neurodegenerative dementia group than in the control group. Among the causes of death of patients with neurodegenerative dementia, neurologic disease showed the highest OR, followed by mental disease.

The adjusted overall HRs calculated in previous studies of mortality among patients with dementia were similar to ours [7, 11, 12, 18–20]; the causes of death of these patients were also similar [7, 11, 19] even though the number of studies was too few to enable the type of analysis we were able to perform in this study. However, our observation of adjusted HRs differing between age groups was not consistent with previous studies that performed the same analyses [7, 18, 21]. Previous studies varied in terms of patient ethnicity

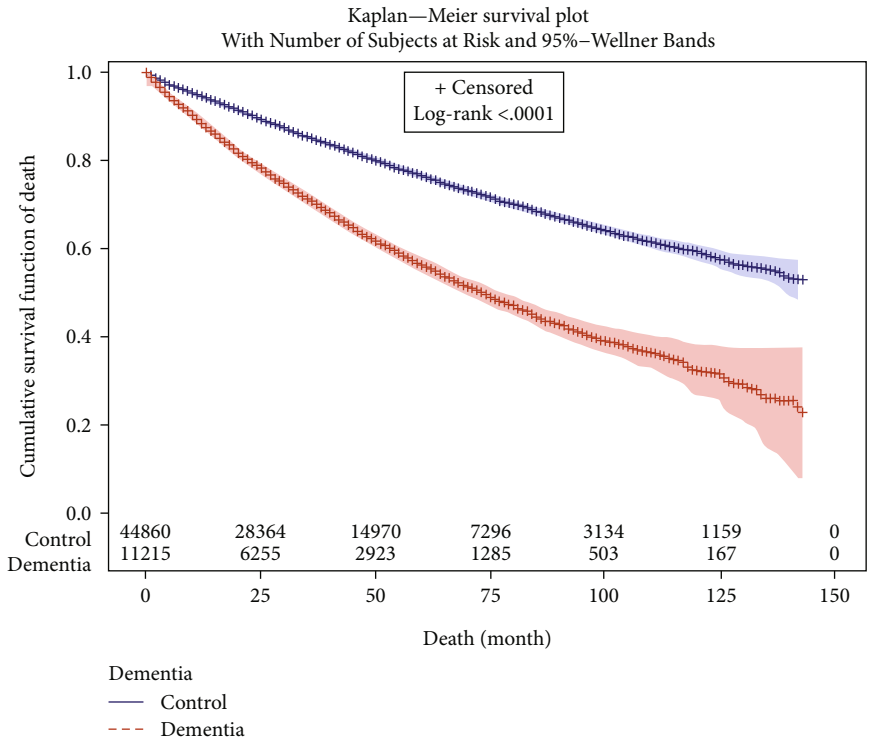

Figure 2: Kaplan–Meier curves showing mortality rates of Korean patients with dementia versus those of controls over the duration of the study.

and age, size of study population, underlying causes of dementia (e.g., AD or vascular dementia), types of dementia (e.g., incidental or prevalent), follow-up duration, and statistical analysis methods [7, 12, 18–23]. Such differences might have caused some of the inconsistences between previously derived data and ours; the characteristics of the previous studies are summarized in Supplementary Table 2.

Our derived adjusted HR for mortality in our neurodegenerative dementia group was 2.11, which was consistent with previous studies of patients with this condition [7, 11, 12, 18–20]. A study by C. Wolfson et al. in Canada [18] and another by Ganguli et al. in the United States [19] found HRs for mortality (95% CIs) to be 1.52 (1.30–1.72) and 1.4 (1.2–1.8), respectively. A study by Villarejo et al. in Spain found that the HRs for mortality (95% CIs) were 2.23 (1.77–2.82), 3.10 (2.47–3.89), and 4.98 (3.85–6.44) in patients with mild, moderate, and severe dementia, respectively [7]. Previous studies in Korea revealed that patients with dementia had higher HRs for mortality even though their designs (particularly patient recruitment methods) varied [11, 12, 20]. One study found that the mortality rates of Koreans with dementia were 1.8–5.8-fold higher than that of the general Korean population, depending on age [11]. Another study of individuals with "cognitive impairment but no dementia" and of 69 individuals with clinically diagnosed dementia found that the HRs for mortality (95% CIs) were 1.92 (1.46–2.54) in the former group and 3.20 (2.30–4.44) in the latter [20]. A recent study of patients with prevalent and incident dementia at baseline assessment showed HRs for mortality (95% CIs) of 2.82 (1.28–6.22) and 8.37 (4.23–16.54), respectively [12]. The HR values found in these studies (including ours) were similar implying that advances in the treatment of neurodegenerative dementia have not necessarily improved mortality rates even though they may have contributed to improving the quality of life of patients with this condition. Alternatively, the mortality rates of patients with neurodegenerative dementia may indeed have improved, but the impact of this was diluted owing to the life expectancy of the general population increasing during the same period.

We observed the highest HR for mortality in patients who were diagnosed with neurodegenerative dementia at 60–69 years of age (3.39), followed by those who were diagnosed at 70–79 years (2.46) and those who were diagnosed at ≥80 years (1.77). Only a few investigators have analyzed the risk of mortality in different age groups, with a fraction reporting the HRs (most of which showed findings inconsistent with ours). C. Wolfson et al.'s study in Canada revealed HRs (95% CIs) of 2.36 (1.36–4.06), 4.26 (2.51–7.17), and 8.08 (4.39–12.94) for those aged 65–74, 75–84, and ≥85 years, respectively [18]. Villarejo et al.'s study in Spain revealed HRs (95% CIs) of 1.77 (1.57–1.99) and 2.67 (2.21–3.22) in those aged 75–84 and ≥85 years, respectively (the 65–74-year age group served as the baseline) [7]. A study in Sweden by Garcia-Ptacek et al. revealed HRs for mortality (95% CIs) of 1.96 (1.57–2.44), 3.32 (2.72–4.17), and 6.17 (4.97–7.65) among those aged 65–74, 75–84, and ≥85 years, respectively [21]. These data were consistent with the notion that AD development in relatively younger individuals poses a higher risk of mortality than it does among

Table 1: General characteristics of the participants.

Characteristics	Total participants		
	Neurodegenerative dementia (*n*, %)	Control (*n*, %)	*P* value
Age (years)			1.000
60–64	580 (5.2)	2,320 (5.2)	
65–69	1,288 (11.5)	5,152 (11.5)	
70–74	2,321 (20.7)	9,284 (20.7)	
75–79	2,960 (26.4)	11,840 (26.4)	
80–84	2,588 (23.1)	10,352 (23.1)	
85+	1,478 (13.2)	5,912 (13.2)	
Sex			1.000
Male	3,568 (31.8)	14,272 (31.8)	
Female	7,647 (68.2)	30,588 (68.2)	
Income			1.000
1 (lowest)	1,280 (11.4)	5,120 (11.4)	
2	1,092 (9.7)	4,368 (9.7)	
3	447 (4.0)	1,788 (4.0)	
4	479 (4.3)	1,916 (4.3)	
5	519 (4.6)	2,076 (4.6)	
6	621 (5.5)	2,484 (5.5)	
7	711 (6.3)	2,844 (6.3)	
8	778 (6.9)	3,112 (6.9)	
9	1,067 (9.5)	4,268 (9.5)	
10	1,722 (15.4)	6,888 (15.4)	
11 (highest)	2,499 (22.3)	9,996 (22.3)	
Region of residence			1.000
Urban	4,493 (40.1)	17,972 (40.1)	
Rural	6,722 (59.9)	26,888 (59.9)	
Hypertension			1.000
Yes	8,200 (73.1)	32,800 (73.1)	
No	3,015 (26.9)	12,060 (26.9)	
Diabetes			1.000
Yes	3,942 (35.1)	15,768 (35.1)	
No	7,273 (64.9)	29,092 (64.9)	
Dyslipidemia			1.000
Yes	3,470 (30.9)	13,880 (30.9)	
No	7,745 (69.1)	30,980 (69.1)	
Ischemic heart disease			<0.001*
Yes	1,670 (14.9)	5,884 (13.1)	
No	9,545 (85.1)	38,976 (86.9)	
Stroke			<0.001*
Yes	5,425 (48.4)	11,356 (25.3)	
No	5,790 (51.6)	33,504 (74.7)	
Death			<0.001*
Yes	3,873 (34.5)	8,434 (18.8)	
No	7,342 (65.5)	36,426 (81.2)	

*Chi-square or Fisher's exact test. Significance set at a P value < 0.05.

older counterparts [24, 25], as early-onset dementia has a more debilitating course. In contrast, a Swedish study by Agüero-Torres et al. found that the relative risks (95% CIs) were 3.3 (1.4–9.1) in men aged 77–84 years, 1.7 (0.8–3.5) in men ≥85 years, 4.5 (2.2–8.9) in women 77–84 years, and 2.4 (1.8–3.2) in women ≥85 years [22]; these values were similar to ours. These findings could be attributed to the fact that patients who are diagnosed at an older age are more

Table 2: Crude and adjusted hazard ratios for mortality in patients with neurodegenerative dementia.

Characteristics	Hazard ratio (95% confidence interval)			
	Crude[†]	*P* value	Adjusted[†‡]	*P* value
Total participants ($n = 56,075$)				
Neurodegenerative dementia		<0.001*		<0.001*
Yes	2.26 (2.17–2.35)		2.11 (2.03–2.20)	
No	1.00		1.00	
Men ($n = 17,840$)				
Neurodegenerative dementia		<0.001*		<0.001*
Yes	2.59 (2.43–2.76)		2.41 (2.26–2.57)	
No	1.00		1.00	
Women ($n = 38,235$)				
Neurodegenerative dementia		<0.001*		<0.001*
Yes	2.09 (1.99–2.19)		1.96 (1.86–2.06)	
No	1.00		1.00	
Young (60–69 years, $n = 9,340$)				
Neurodegenerative dementia		<0.001*		<0.001*
Yes	3.81 (3.31–4.38)		3.25 (2.79–3.78)	
No	1.00		1.00	
Middle-aged (70–79 years, $n = 26,405$)				
Neurodegenerative dementia		<0.001*		<0.001*
Yes	2.77 (2.60–2.95)		2.48 (2.32–2.65)	
No	1.00		1.00	
Older (≥80 years, $n = 20,330$)				
Neurodegenerative dementia		<0.001*		<0.001*
Yes	1.84 (1.75–1.95)		1.78 (1.69–1.88)	
No	1.00		1.00	

*Cox proportional hazards regression model. Significance set at a P value < 0.05.
[†]Stratified by age, sex, income, region of residence, hypertension, diabetes, and dyslipidemia.
[‡]A model adjusted for ischemic heart disease and stroke histories.

Table 3: Differences in mortality rates between patients in the neurodegenerative dementia and control groups according to the cause of death.

Cause of death	Total participants			
	Neurodegenerative dementia ($n = 11,215$)	Control ($n = 44,860$)	Odds ratio (95% CI)	*P* value
All causes of death (*n*, %)	3,873 (34.5)	8,434 (18.8)	2.28 (2.18–2.39)	<0.001[§]
Infection (*n*, %)	100 (0.9)	197 (0.4)	2.04 (1.60–2.60)	<0.001*
Neoplasm (*n*, %)	408 (3.6)	1,846 (4.1)	0.88 (0.79–0.98)	0.021
Metabolic disease (*n*, %)	226 (2.0)	377 (0.8)	2.43 (2.06–2.87)	<0.001*
Mental diseases (*n*, %)	219 (2.0)	194 (0.4)	4.89 (3.78–5.57)	<0.001*
Neurologic disease (n, %)	489 (4.4)	128 (0.3)	15.93 (13.10–19.38)	<0.001*
Circulatory disease (*n*, %)	1,123 (10.0)	2,329 (5.2)	2.03 (1.89–2.19)	<0.001*
Respiratory disease (*n*, %)	441 (3.9)	812 (1.8)	2.22 (1.97–2.50)	<0.001*
Digestive disease (*n*, %)	88 (0.8)	257 (0.6)	1.37 (1.08–1.75)	0.010*
Muscular disease (*n*, %)	40 (0.4)	79 (0.2)	2.03 (1.39–2.97)	<0.001*
Genitourinary disease (*n*, %)	88 (0.8)	167 (0.4)	2.12 (1.63–2.74)	<0.001*
Trauma (*n*, %)	166 (1.5)	468 (1.0)	1.43 (1.19–1.70)	<0.001*
Other (*n*, %)	485 (4.3)	1,580 (3.5)	1.24 (1.12–1.37)	<0.001*

*Chi-square or Fisher's exact test. Significance set at a false discovery rate-adjusted P value of < 0.05. CI: confidence interval.

likely to die of other causes, which dilutes the impact of neurodegenerative dementia on the mortality rate. The discrepancy might also have been a consequence of differences in study design, as mentioned above. Further studies are required to investigate this issue.

All disease categories except neoplasms were associated with an elevated OR for mortality in the dementia group; neurologic disease had the highest OR (15.93) followed by mental disease (4.89), implying that neurologic diseases that are likely to arise from dementia are associated with the highest mortality rates. Only a few studies investigated the causes of mortality in patients with dementia [7, 11, 19]; their findings were similar to ours. Ganguli et al.'s study in the United States found that the death certificates of individuals with AD were significantly more likely to list other brain disorders as the cause of death than were those of persons without dementia (5.5% vs. 1.7%). Dementia/AD was listed as the cause of death in 12.3% of individuals with AD and in 0.4% of those without dementia; conversely, the former patients were less likely to die of cancer than the latter (12.3% vs. 26.2%) [19]. Villarejo et al.'s study in Spain found that dementia itself and cerebrovascular disorders were significantly more common primary causes of death among patients with dementia than among control individuals (20.0% vs. 5.2% and 14.9% vs. 7.7%, respectively), whereas cancer was significantly less frequent in patients with dementia than in control individuals (5.8% vs. 26.5%) [7]. A Korean study by Go et al. found that the causes of death in patients with AD were (in order of frequency) dementia (36.0%), senescence (10.4%), stroke (9.6%), malignancy (9.1%), diabetes mellitus (6.3%), cardiovascular diseases (6.1%), and pneumonia (4.7%) [11], although they did not compare these frequencies to those occurring within the control population. Possible explanations for our own observations are that (i) the most common causes of death in the general population (such as cardiovascular disease) are also common in patients with dementia even though their frequencies per se are not much different than those in the general population and/or (ii) cancer (which is another common cause of death in the general population) might be underdiagnosed in those who are cognitively impaired [7]. Our results imply that caregivers should pay more attention to screening for other diseases, particularly cancer, in patients with neurodegenerative dementia while managing the dementia itself.

Our study had a few limitations. First, we did not distinguish between prevalent and incidental neurodegenerative dementia even though the risk of mortality between these 2 types differ. Second, we were unable to determine the severity of neurodegenerative dementia, which is a factor that reportedly influences mortality rates. Third, we included only diagnosed, symptomatic neurodegenerative dementia and were thus unable to evaluate the impact of mild cognitive impairment on mortality. Lastly, the death certificates only listed a single condition as the cause of death, thereby potentially ignoring other underlying ailments that may have contributed to mortality. Nevertheless, our observations are representative considering the scale of the data, and our findings ought to provide deeper insights into improving care for Korean patients with neurodegenerative dementia and ultimately contribute to decreasing mortality rates.

5. Conclusions

We performed the largest study on the risk of mortality among patients with neurodegenerative dementia in South Korea using clearly defined inclusion criteria and found that the risk of mortality increased in these patients regardless of age and sex. The HR was the highest in those who were diagnosed at 60–69 years of age, followed by those who were diagnosed at 70–79 years and was lowest among those who were diagnosed at ≥80 years. Death by any cause other than neoplasms—particularly neurologic disease and mental disease—showed an elevated risk in the neurodegenerative dementia group, while the risk of death owing to neoplasms in this group was lower.

Data Availability

Release of the data by the researcher is not allowed legally. All of data are available from the database of National health Insurance Sharing Service (NHISS) https://nhiss.nhis.or.kr/.

Disclosure

The funder had no role in the commissioning, conception, planning, design, conduct, or analysis of the work; in the preparation or editing of the manuscript; or in the decision to publish.

Conflicts of Interest

The authors declare that there is no conflict of interest regarding the publication of this article.

Acknowledgments

This research was supported in part by the National Research Foundation of Korea, grant number NRF-2018-R1D1A1A0-2085328.

Supplementary Materials

Supplementary Table S1: the causes of death in patients with neurodegenerative dementia and their matched control groups. Supplementary Table S2: a comparison of studies that investigated the causes of death among patients with neurodegenerative dementia. *(Supplementary Materials)*

References

[1] S. A. Gale, D. Acar, and K. R. Daffner, "Dementia," *The American Journal of Medicine*, vol. 131, no. 10, pp. 1161–1169, 2018.

[2] Z. Arvanitakis, R. C. Shah, and D. A. Bennett, "Diagnosis and management of dementia: review," *The Journal of American Medical Association*, vol. 322, no. 16, pp. 1589–1599, 2019.

[3] E. Nichols, C. E. Szoeke, S. E. Vollset et al., "Global, regional, and national burden of Alzheimer's disease and other

dementias, 1990-2016: a systematic analysis for the Global Burden of Disease Study," *The Lancet Neurology*, vol. 18, no. 1, pp. 88–106, 2019.

[4] S. R. Sabat, "Dementia in developing countries: a tidal wave on the horizon," *The Lancet*, vol. 374, no. 9704, pp. 1805-1806, 2009.

[5] C. P. Ferri, M. Prince, C. Brayne et al., "Global prevalence of dementia: a Delphi consensus study," *The Lancet*, vol. 366, no. 9503, pp. 2112–2117, 2005.

[6] E. H. Kua, E. Ho, H. H. Tan, C. Tsoi, C. Thng, and R. Mahendran, "The natural history of dementia," *Psychogeriatrics*, vol. 14, no. 3, pp. 196–201, 2014.

[7] J. Villarejo, R. Benito-León, I. Trincado et al., "Dementia-associated mortality at thirteen years in the NEDICES cohort study," *Journal of Alzheimer's Disease*, vol. 26, no. 3, pp. 543–551, 2011.

[8] N. Scarmeas, J. A. Luchsinger, R. Mayeux, and Y. Stern, "Mediterranean diet and Alzheimer disease mortality," *Neurology*, vol. 69, no. 11, pp. 1084–1093, 2007.

[9] Y. J. Kim, J. W. Han, Y. S. So, J. Y. Seo, K. Y. Kim, and K. W. Kim, "Prevalence and trends of dementia in Korea: a systematic review and meta-analysis," *Journal of Korean Medical Science*, vol. 29, no. 7, pp. 903–912, 2014.

[10] J. H. Park, J. H. Eum, B. Bold, and H. K. Cheong, "Burden of disease due to dementia in the elderly population of Korea: present and future," *BMC Public Health*, vol. 13, no. 1, article 293, 2013.

[11] S. M. Go, K. S. Lee, S. W. Seo et al., "Survival of Alzheimer's disease patients in Korea," *Dementia and Geriatric Cognitive Disorders*, vol. 35, no. 3–4, pp. 219–228, 2013.

[12] J. B. Bae, J. W. Han, K. P. Kwak et al., "Is dementia more fatal than previously estimated? A population-based prospective cohort study," *Aging and Disease*, vol. 10, no. 1, pp. 1–11, 2019.

[13] S. Y. Kim, D. J. Oh, and H. G. Choi, "Tonsillectomy does not reduce asthma in children: a longitudinal follow-up study using a national sample cohort," *Scientific Reports*, vol. 9, no. 1, pp. 1–8, 2019.

[14] S. Y. Lee, I. G. Kong, D. J. Oh, and H. G. Choi, "Increased risk of benign paroxysmal positional vertigo in patients with a history of sudden sensory neural hearing loss: a longitudinal follow-up study using a national sample cohort," *Otology and Neurotology*, vol. 40, no. 2, pp. e135–e141, 2019.

[15] S. Y. Kim, J. S. Lim, I. G. Kong, and H. G. Choi, "Hearing impairment and the risk of neurodegenerative dementia: a longitudinal follow-up study using a national sample cohort," *Scientific Reports*, vol. 8, no. 1, pp. 1–8, 2018.

[16] S. Y. Lee, J. S. Lim, D. J. Oh, I. G. Kong, and H. G. Choi, "Increased risk of neurodegenerative dementia in women with migraines: a nested case-control study using a national sample cohort," *Medicine*, vol. 98, no. 7, article e14467, 2019.

[17] H. G. Choi, J. S. Lim, Y. K. Lee, S. Sim, and M. Kim, "Mortality and cause of death in South Korean patients with Parkinson's disease: a longitudinal follow-up study using a national sample cohort," *BMJ Open*, vol. 9, no. 9, article e029776, 2019.

[18] C. Wolfson, D. B. Wolfson, M. Asgharian et al., "A reevaluation of the duration of survival after the onset of dementia," *New England Journal of Medicine*, vol. 344, no. 15, pp. 1111–1116, 2001.

[19] M. Ganguli, H. H. Dodge, C. Shen, R. S. Pandav, and S. T. DeKosky, "Alzheimer disease and mortality: a 15-year epidemiological study," *Archives of Neurology*, vol. 62, no. 5, pp. 779–784, 2005.

[20] J. E. Park, J. Y. Lee, G. H. Suh, B. S. Kim, and M. J. Cho, "Mortality rates and predictors in community-dwelling elderly individuals with cognitive impairment: an eight-year follow-up after initial assessment," *International Psychogeriatrics*, vol. 26, no. 8, pp. 1295–1304, 2014.

[21] S. Garcia-Ptacek, B. Farahmand, I. Kåreholt, D. Religa, M. L. Cuadrado, and M. Eriksdotter, "Mortality risk after dementia diagnosis by dementia type and underlying factors: a cohort of 15,209 patients based on the Swedish Dementia Registry," *Journal of Alzheimer's Disease*, vol. 41, no. 2, pp. 467–477, 2014.

[22] H. Agüero-Torres, L. Fratiglioni, Z. Guo, M. Viitanen, and B. Winblad, "Mortality from dementia in advanced age: a 5-year follow-up study of incident dementia cases," *Journal of Clinical Epidemiology*, vol. 52, no. 8, pp. 737–743, 1999.

[23] S. C. Waring, R. S. Doody, V. N. Pavlik, P. J. Massman, and W. Chan, "Survival among patients with dementia from a large multi-ethnic population," *Alzheimer's Disease and Associated Disorders*, vol. 19, no. 4, pp. 178–183, 2005.

[24] U. Guehne, S. Riedel-Heller, and M. C. Angermeyer, "Mortality in dementia," *Neuroepidemiology*, vol. 25, no. 3, pp. 153–162, 2005.

[25] E. L. Koedam, Y. A. Pijnenburg, D. J. Deeg et al., "Early-onset dementia is associated with higher mortality," *Dementia and Geriatric Cognitive Disorders*, vol. 26, no. 2, pp. 147–152, 2008.

Hindawi
BioMed Research International
Volume 2022, Article ID 1717784, 15 pages
https://doi.org/10.1155/2022/1717784

Research Article

Identification of Key CircRNAs Related to Pulmonary Tuberculosis Based on Bioinformatics Analysis

Qin Yuan,[1] Zilu Wen,[2] Ke Yang,[1] Shulin Zhang,[3,4] Ning Zhang,[5] Yanzheng Song,[6] and Fuxue Chen[1]

[1]*School of Life Sciences, Shanghai University, Shanghai, China*
[2]*Department of Scientific Research, Shanghai Public Health Clinical Center, Fudan University, Shanghai, China*
[3]*Department of Immunology and Microbiology, Shanghai Jiao Tong University School of Medicine, Shanghai, China*
[4]*Tuberculosis Research Center, Shanghai Public Health Clinical Center, Shanghai, China*
[5]*Department of Hepatic Surgery, Fudan University Shanghai Cancer Center, Shanghai, China*
[6]*Department of Thoracic Surgery, Shanghai Public Health Clinical Center, Fudan University, Shanghai, China*

Correspondence should be addressed to Ning Zhang; zning818@163.com, Yanzheng Song; yanzhengsong@163.com, and Fuxue Chen; chenfuxue@staff.shu.edu.cn

Received 24 November 2021; Revised 10 January 2022; Accepted 1 March 2022; Published 4 April 2022

Academic Editor: Zhi-Yu Zeng

Pulmonary tuberculosis (TB) is a chronic infectious disease that is caused by respiratory infections, principally *Mycobacterium tuberculosis*. Increasingly, studies have shown that circular (circ)RNAs play regulatory roles in different diseases through different mechanisms. However, their roles and potential regulatory mechanisms in pulmonary TB remain unclear. In this study, we analyzed circRNA sequencing data from adjacent normal and diseased tissues from pulmonary TB patients and analyzed the differentially expressed genes. We then constructed machine learning models and used single-factor analysis to identify hub circRNAs. We downloaded the pulmonary TB micro (mi)RNA (GSE29190) and mRNA (GSE83456) gene expression datasets from the Gene Expression Omnibus database and performed differential expression analysis to determine the differentially expressed miRNAs and mRNAs. We also constructed a circRNA–miRNA–mRNA interaction network using Cytoscape. Gene Ontology enrichment analysis and Kyoto Encyclopedia of Genes and Genomes pathway analysis were used to predict the biological functions of the identified RNAs and determine hub genes. Then, the STRING database and cytoHubba were used to construct protein-protein interaction networks. The results showed 125 differentially expressed circRNAs in the adjacent normal and diseased tissues of pulmonary TB patients. Among them, we identified three hub genes associated with the development of pulmonary TB: hsa_circ_0007919 (upregulated), hsa_circ_0002419 (downregulated), and hsa_circ_0005521 (downregulated). Through further screening, we determined 16 mRNAs of potential downstream genes for hsa-miR-409-5p and hsa_circ_0005521 and established an interaction network. This network may have important roles in the occurrence and development of pulmonary TB. We constructed a model with 100% prediction accuracy by machine learning and single-factor analysis. We constructed a protein-protein interaction network among the top 50 hub mRNAs, with FBXW7 scoring the highest and SOCS3 the second highest. These results may provide a new reference for the identification of candidate markers for the early diagnosis and treatment of pulmonary TB.

1. Introduction

Pulmonary tuberculosis (TB) is a contagious disease that is caused by the slow-growing *Mycobacterium tuberculosis* (MTB), which is spread by aerosols [1]. The primary pathological feature of pulmonary TB is necrotizing granuloma infiltration [2]. TB infections mainly occur in the lungs but may also cause problems in other parts of the body [3]. Pulmonary TB has a long incubation period. When MTB enters the lungs, it usually forms capsules (granulomas), which are harmless in the lungs and cause latent pulmonary TB infection [4–6]. However, these capsules may be activated in the

future and develop into active pulmonary TB [7]. Although pulmonary TB can be cured, it remains one of the ten leading causes of death worldwide, particularly in developing countries [8, 9]. Latent pulmonary TB infections are asymptomatic, making this difficult to detect and treat on time [10]. Therefore, there is great interest in finding effective biomarkers for the early diagnosis and/or treatment of latent pulmonary TB [11].

Circular (circ)RNAs are a type of noncoding RNA molecule that lack a $5'$ cap and $3'$ tail and form a single-stranded circular structure by covalent bonds [12]. CircRNAs are formed by reverse splicing and are mainly divided into all-exon circRNAs, circRNAs composed of introns and exons, and lasso-shaped circRNAs composed of introns [13, 14]. CircRNAs are abundant and present in bodily fluids such as blood, saliva, cerebrospinal fluid, and urine [15]. Compared with linear RNAs, circRNAs are more stable and more resistant to degradation by RNase R. Therefore, circRNAs can be selectively enriched during sample processing [16, 17]. Compared with other types of RNAs, circRNAs are more suitable as candidate molecules for molecular diagnostic biomarkers and could be effective therapeutic targets [18].

Additionally, circRNAs can be used as micro (mi)RNA sponges to bind miRNAs through miRNA response elements, releasing the degradation or translational inhibition of downstream target mRNAs by disrupting the competitive endogenous (ce)RNA mechanism [19]. CircRNAs bind to and regulate the functions of RNA-binding protein (RBP), changing the stability of mRNAs. CircRNAs can also directly encode proteins [20–22]. According to a report by Li et al., who analyzed the expression profile of circRNAs in nonsmall cell lung cancer, a circRNA named CircNDUFB2 could inhibit nonsmall cell lung cancer progression by decreasing the stability of insulin-like growth factor 2 mRNA-binding proteins (IGF2BPs) and activating antitumor immunity [23]. Wang et al. studied the expression profile of circRNAs in the lung tissue of mice infected with influenza A virus (IAV) using high-throughput sequencing and RNA sequencing. They identified many differentially expressed circRNAs between the IAV group and the control group. Bioinformatic analysis revealed a potential role of circRNAs in the IAV-induced lung injury model [24]. Zhou et al. conducted RNA sequencing and correlation analysis on liver biopsies of untreated patients with chronic hepatitis B and healthy controls. They found that there was a strong positive correlation between hsa_circ_0000650 and TGFB2 expression and a negative correlation between hsa_circ_0000650 and miR-6873-3p expression. They confirmed that there were different circRNAs and circRNA/miRNA interactions in patients with chronic hepatitis B [25].

To summarize, many studies have shown that circRNAs are associated with the occurrence and development of a variety of respiratory and infectious diseases [3, 26–28]. Currently, there are few studies on circular RNAs and pulmonary TB. Pulmonary TB-related circRNA research could be important for the early diagnosis and treatment of pulmonary TB [29]. In this study, we sought to identify differentially expressed circRNAs and their downstream mRNAs using tissues from pulmonary TB patients to identify hub genes involved in pulmonary TB infection and provide references for the early diagnosis and treatment of pulmonary TB.

2. Materials and Methods

2.1. Data Collection. The Shanghai (Fudan University) Public Health Clinical Center provided all patient data used in this study. They performed positron emission tomography (PET) scans on the lungs of nine pulmonary TB patients and whole transcriptome sequencing of lung tissues with high PET (high metabolic activity) and normal PET (low metabolic activity) uptake. For raw sequencing data, please refer to PRJNA795290 (4∗2 samples) from the Sequence Read Archive (SRA) database and GSE158767 (5∗2 samples) from the Gene Expression Omnibus (GEO) database. All patients signed an informed consent form before obtaining tissue samples. RNA extraction, library construction, and sequencing were performed in the same way as previously described [30]. In this paper, we analyzed 8286 differentially expressed genes (DEGs) by bioinformatics.

2.2. Differential Expression Analysis of CircRNAs. First, the raw data were corrected, filtered, and normalized using the R package. Analyses of differentially expressed RNAs included fold change (FC), P value, and false discovery rate (FDR). The criteria for selecting differentially expressed circRNAs were $|\log 2FC| > 1$ and P value < 0.05. Scatter plots, volcano plots, and heat maps were used to show the differently expressed circRNAs.

2.3. Feature Selection. In machine learning applications, the number of features is often large, and there may be irrelevant features. With more features, the resulting model will be more complex. Feature selection can eliminate irrelevant or redundant features, reduce the number of features, improve model accuracy, reduce the running time, and simplify the model. We identified hub circRNAs using eight feature screening methods: CfsSubsetEval-BestFirst, PrincipalComponents-Ranker-T, CorrelationAttributeEval-Ranker-T, GainRatioAttributeEval-Ranker-T, InfoGainAttributeEval-Ranker-T, OneRAttributeEval-Ranker-T, ReliefFAttributeEval-Ranker-T, and SymmetricalUncertAttributeEval-Ranker-T.

2.4. Building the Machine Learning Models. We used 13 algorithms to build the models: ZeroR, Logistic, SMO, IBK, AttributeSelectedClassifier, OneR, DecisionStump, HoeffdingTree, J48, LMT, RandomForest, RandomTree, and REPTree. Comparisons of the average accuracy of the machine learning models established by different feature selection methods were then conducted. We also performed statistical and univariate analyses of the number of occurrences of circRNAs in various models to identify hub circRNAs.

2.5. Screening the Downstream miRNAs and mRNAs of CircRNAs and Constructing the CircRNA–miRNA–mRNA Regulatory Network. Predictions of potential miRNAs targets of the circRNAs were made through the ENCORI

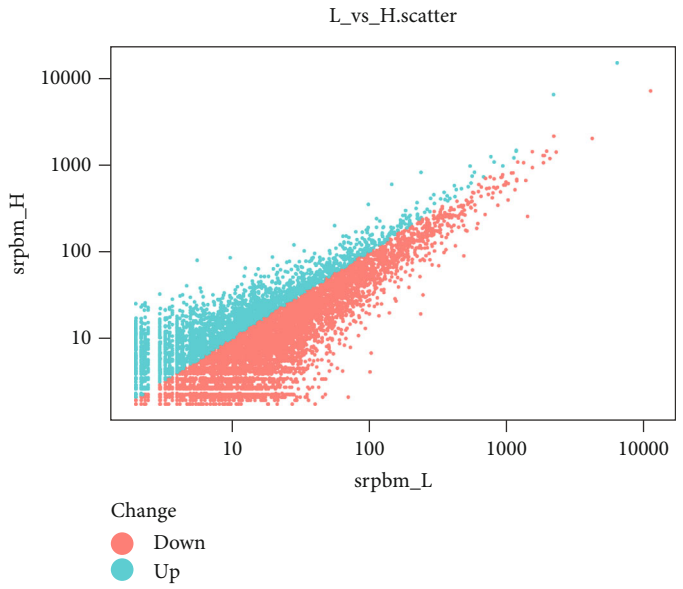

(a)

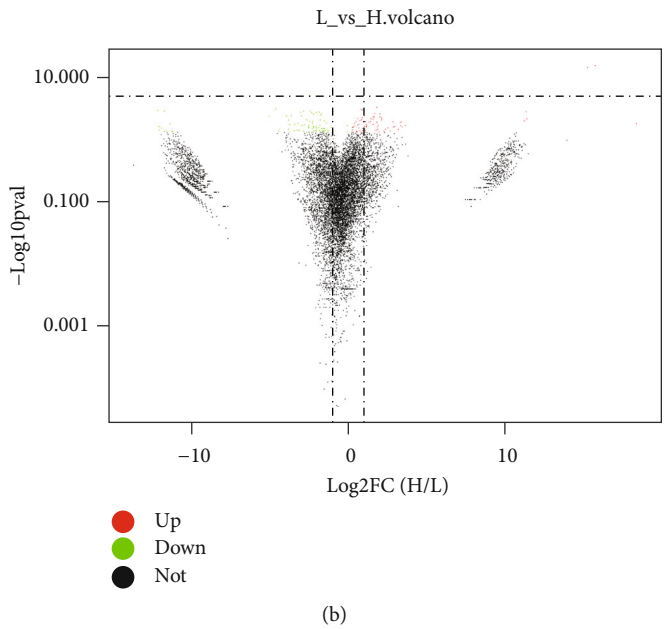

(b)

Figure 1: Continued.

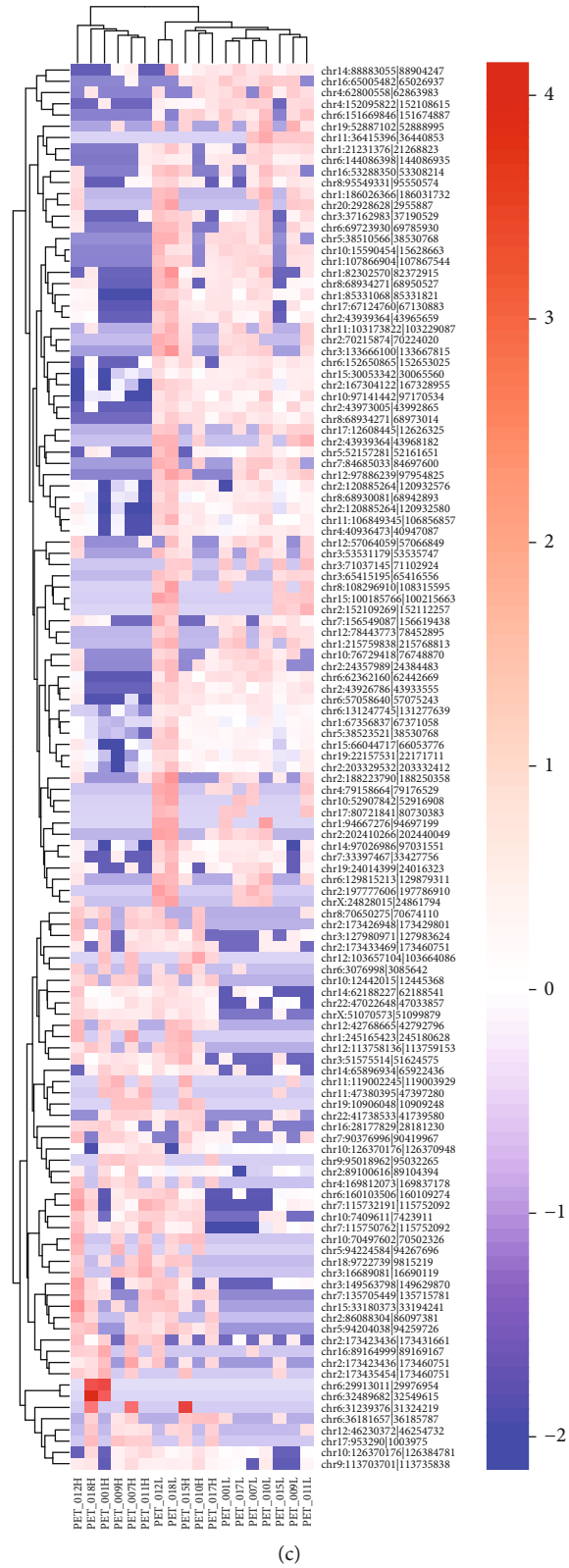

(c)

Figure 1: Sequencing data and differential expression analysis. (a) Scatter plot analysis of circRNA expression; (b) volcano plot of differential circRNA expression; (c) heat map of cluster analysis of the differentially expressed circRNAs.

Table 1: The top 10 differentially expressed genes between normal and diseased tissues.

circBase_ID	ID	log2FC (H/L)	*P* value	Regulate
_	chr6:32489682|32549615	18.39	0.016744549	Up
_	chr6:31239376|31324219	15.76	5.20E-16	Up
_	chr6:29913011|29976954	15.27	6.44E-15	Up
_	chr12:103657104|103664086	11.4	0.007540201	Up
hsa_circ_0007919	chr17:953290|1003975	11.37	0.001677147	Up
hsa_circ_0049335	chr19:10906048|10909248	11.25	0.010820527	Up
_	chr5:94224584|94267696	3.67	0.021390567	Up
hsa_circ_0006272	chr10:70497602|70502326	3.45	0.026522304	Up
hsa_circ_0071410	chr4:169812073|169837178	3.41	0.012791713	Up
hsa_circ_0006006	chr2:173435454|173460751	3.36	0.022707405	Up
_	chr2:152109269|152112257	-11.18	0.045132825	Down
hsa_circ_0005281	chr17:80721841|80730383	-11.21	0.047352003	Down
_	chr11:36415396|36440853	-11.36	0.017056129	Down
_	chr8:108296910|108315595	-11.59	0.043394725	Down
hsa_circ_0002419	chr12:78443773|78452895	-11.69	0.001451403	Down
hsa_circ_0001961	chr10:52907842|52916908	-11.71	0.046807666	Down
hsa_circ_0037054	chr15:100185766|100215663	-11.9	0.030332661	Down
hsa_circ_0013225	chr1:94667276|94697199	-12.02	0.038719442	Down
hsa_circ_0057608	chr2:197777606|197786910	-12.05	0.024486018	Down
hsa_circ_0005521	chr1:215759838|215768813	-12.11	0.001277288	Down

website (http://starbase.sysu.edu.cn/). We screened the pulmonary TB miRNA gene chip (GSE29190) dataset from the Gene Expression Omnibus (GEO) database (http://www.ncbi.nlm.nih.gov/geo) for differentially expressed miRNAs. The criteria for selecting differentially expressed miRNAs were $|\log 2FC| > 1$ and P value < 0.05. Predictions of potential mRNAs downstream of miRNAs were made by the miRTarBase database (http://mirtarbase.mbc.nctu.edu.tw/php/index.php). Then, the GEO database of pulmonary TB mRNA gene chip (GSE83456) was used to screen for differentially expressed mRNAs. The criteria for selecting differentially expressed mRNAs were $|\log 2FC| > 1$ and P value < 0.05. Finally, Cytoscape (http://www.cytoscape.org/) was used to construct the circRNA–miRNA–mRNA interaction network.

2.6. Biological Function Analysis. Gene ontology (GO) enrichment analysis and Kyoto Encyclopedia of Genes and Genomes (KEGG) pathway analysis were performed using the DAVID database (https://david.ncifcrf.gov) for the differentially expressed mRNAs satisfying $|\log 2FC| > 1$ and P value < 0.05. GO analysis is divided into three categories, cellular component (CC), molecular function (MF), and biological process (BP), and summarizes the biological functions, pathways, or cellular localization of gene enrichment. We used the KEGG database for pathway enrichment analysis.

2.7. Construction of Protein-Protein Interaction (PPI) Networks. For the 372 mRNAs, we identified from the previous screen; we analyzed them using the STRING database (https://string-db.org/) and uncovered information on the interactions of these proteins. Each node in the PPI network represents a protein. To identify the key nodes in the PPI network, we calculated the top 50 hub genes using the cytoHubba function in Cytoscape (http://www.cytoscape.org/). We then constructed a PPI network on the basis of these 50 hub genes.

Table 2: Feature screening information.

Feature-screening method	Number of circRNAs	Number of 100% correct algorithms
125 circRNA	125	3/13
CfsSubsetEval-BestFirst	14	3/13
PrincipalComponents-Ranker-T	5	0/13
CorrelationAttributeEval-Ranker-T	10	4/13
GainRatioAttributeEval-Ranker-T	12	0/13
InfoGainAttributeEval-Ranker-T	12	0/13
OneRAttributeEval-Ranker-T	16	2/13
ReliefFAttributeEval-Ranker-T	12	2/13
SymmetricalUncertAttributeEval-Ranker-T	12	0/13

3. Results

3.1. Preliminary Screening of Differentially Expressed Genes in Pulmonary TB. We initially conducted a differential expression analysis of pulmonary TB patient sequencing data. The larger the difference in DEGs between normal

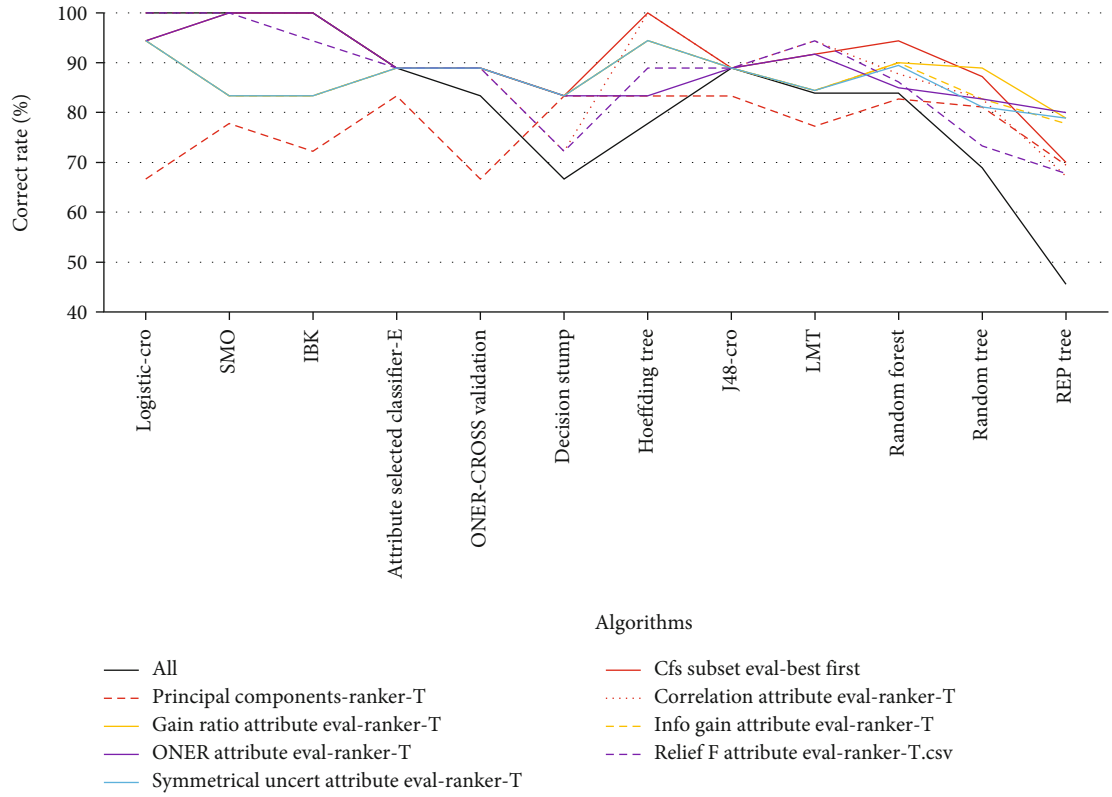

Figure 2: Comparison of the average accuracy of machine learning models built by different feature screening methods.

and diseased tissues, the stronger the association between the disease state and the DEG. A scatter plot was used to show gene expression. The genes clustered towards the middle show less differential expression, while those dispersed towards the sides show larger differential expression. Points on both sides are more likely to be disease hub genes (Figure 1(a)). The basic conditions for screening DEGs were a statistical significance measure $P < 0.05$ and the absolute change in differential gene expression (fold change, FC) > 2. There were 125 circRNAs expressed in the adjacent normal and diseased tissues of pulmonary TB patients that satisfied P value < 0.05 and $|\log 2FC| > 1$, among which 50 were upregulated and 75 were downregulated. There were more downregulated genes in normal tissues compared with diseased tissues (Figure 1(b)). Among the differentially expressed circRNAs, the top 10 up- and downregulated circRNAs are listed in Table 1. Next, we drew a heat map for cluster analysis on basis of circRNA expression in the different samples (Figure 1(c)). The results showed that there were more upregulated genes in diseased tissues. These conclusions were consistent with the volcano plots.

3.2. Building the Machine Learning Models

3.2.1. Construction of the Whole Gene Prediction Models. These machine learning models were built from the 125 differently expressed circRNAs. The prediction accuracy of the Logistic, SMO, and IBK algorithms were the highest, reaching 100%; the accuracy of the J48 algorithm also reached 89% (Table 2).

3.2.2. Feature Selection. The pathogenesis of pulmonary TB is complex. Predictive modeling of pulmonary TB hub genes by machine learning was then performed with the 125 differentially expressed circRNAs. First, we performed feature selection to screen the major influencing factors among the 125 circRNAs; the hub circRNAs were determined by eight feature selection methods. We constructed a machine learning model on the basis of the 125 circRNAs and feature-screened circRNAs. We built models separately using 13 different algorithms: ZeroR, Logistic, SMO, IBK, AttributeSelectedClassifier, OneR, DecisionStump, HoeffdingTree, J48, LMT, RandomForest, RandomTree, and REPTree (Tables S1–S9).

CorrelationAttributeEval-Ranker-T feature screening had four algorithms with a 100% accuracy rate (Logistic, SMO, IBK, and HoeffdingTree). The CfsSubsetEval-BestFirst feature screening method was the next best, and its three algorithms (SMO, IBK, and HoeffdingTree) had a 100% accuracy rate. OneRAttributeEval-Ranker-T feature screening had two algorithms (SMO and IBK) that showed a 100% accuracy rate. CfsSubsetEval-BestFirst feature screening also had two algorithms with a 100% correct rate (Logistic and SMO). Only CorrelationAttributeEval-Ranker-T had a better accuracy rate than the model constructed with 125 circRNAs. Therefore, the CorrelationAttributeEval-Ranker-T feature screening method

was more suitable for the 125 circRNAs (Table 2 and Figure 2). Among the eight feature screening methods, four reached 100% model correctness. These four methods contained 29 circRNAs, counting their occurrences. There were 14 circRNAs that appeared more than once in these four methods. Among them, hsa_circ_0007919, chr10:15590454|15628663, and hsa_circ_0002419 appeared in all four methods. This suggested that these genes may be closely related to the occurrence and development of pulmonary TB (Table 3).

3.3. Univariate Analysis and Confirmation of the Key CircRNAs

3.3.1. Univariate Analysis. To further clarify the effect of circRNAs on pulmonary TB, we built machine learning models for 14 circRNAs and performed univariate analysis. We calculated the average of the models with correct rates of over 80%, with random seeds taken from 1 to 10 (Table 4). The results showed that each circRNA had at least one algorithm with an accuracy greater than 80%. Among them, hsa_circ_0002419 had a strong correlation with pulmonary TB, and the accuracy of the four algorithms was 94%. Hsa_circ_0005521 had a strong correlation, and the correct rate was 89%.

3.3.2. Confirmation of the Key CircRNAs. To identify hub genes in the development of pulmonary TB, we made Venn diagrams that included 20 DEGs and 14 univariate analysis genes using Jvenn. We uncovered three hub circRNAs: hsa_circ_0007919 (upregulated), hsa_circ_0002419 (downregulated), and hsa_circ_0005521 (downregulated). We identified these three circRNAs as hub genes in the development of pulmonary TB (Figure 3 and Table 1).

3.4. Downstream Gene Prediction and Biological Function Analysis

3.4.1. The Downstream Genes of the Identified CircRNAs. The most interesting function of circRNAs is to serve as molecular sponges for miRNAs by binding and influencing miRNA expression. The potential miRNAs that interact with the hub circRNAs were predicted using the ENCORI database. The downstream mRNAs of the miRNAs were predicted by the miRTarBase database (Table 5). We used the miRNA Gene Chip GSE29190 of pulmonary TB from the GEO database and screened out 47 differentially expressed miRNAs ($P < 0.05$). We screened out potential miRNAs and differentially expressed miRNAs by Jvenn, which identified hsa-miR-409-5p (Figure 4(a)). The upstream molecule of hsa-miR-409-5p is hsa_circ_0005521, and the total number of potential downstream mRNAs is 31.

We used the mRNA Gene Chip GSE83456 of pulmonary TB from the GEO database to screen out 9272 differentially expressed mRNAs ($P < 0.05$). We screened out 16 potential downstream mRNAs for hsa-miR-409-5p, and their differential expression was analyzed using Jvenn. These mRNAs included RPS4X, NBEA, GSK3B, RGL2, ZNF512B, SOD2, ZNF12, KPNA3, AKAP1, RPRD2, ACAP2, RSU1, FDXR, EIF4EBP2, SRRD, and ZBTB34 (Figure 4(b)). Finally, the circRNA–miRNA–mRNA interaction network was constructed using Cytoscape (Figure 4(c)).

Table 3: Frequency of occurrence of 29 circRNAs in four classes of feature-screened circRNAs.

Number	CircRNA	Number of occurrences
1	hsa_circ_0007919	4/4
2	chr10:15590454|15628663	4/4
3	hsa_circ_0002419	4/4
4	chr10:76729418|76748870	3/4
5	hsa_circ_0005521	3/4
6	chr12:97886239|97954825	3/4
7	chr10:97141442|97170534	2/4
8	hsa_circ_0034293	2/4
9	hsa_circ_0013048	2/4
10	hsa_circ_0007769	2/4
11	chr6:62362160|62442669	2/4
12	chrX:51070573|51099879	2/4
13	chr8:68934271|68973014	2/4
14	hsa_circ_0002286	2/4
15	hsa_circ_0006272	1/4
16	chr12:103657104|103664086	1/4
17	chr11:36415396|36440853	1/4
18	chr16:65005482|65026937	1/4
19	chr1:21231376|21268823	1/4
20	hsa_circ_0008336	1/4
21	hsa_circ_0008223	1/4
22	hsa_circ_0057105	1/4
23	chr7:115750762|115752092	1/4
24	hsa_circ_0066452	1/4
25	hsa_circ_0084708	1/4
26	hsa_circ_0080947	1/4
27	hsa_circ_0003961	1/4
28	hsa_circ_0042103	1/4
29	hsa_circ_0076948	1/4

3.4.2. Biological Function Analysis of the Identified Genes. To study the effects of the identified mRNAs on pulmonary TB, we performed GO and KEGG analysis of the downstream mRNAs of the three hub circRNAs using the DAVID database. In BP analysis, DNA template, transcription, and positive regulation of transcription from RNA polymerase II promoter were the three terms with the highest enrichment (Figure 5(a)). Regarding CC, genes were enriched in the nucleus, cytoplasm, cytosol, nuclear plasma, and other components (Figure 5(b)). In MF analysis, protein binding, metal ion binding, and poly(A) RNA binding were the three terms with the highest enrichment (Figure 5(c)). Additionally, KEGG pathway analysis showed that the genes were enriched in the cancer pathway, PI3K-Akt signaling pathway, proteoglycan in cancer, Ras signaling pathway, HTLV-I infection, and other pathways (Figure 5(d)).

Table 4: Univariate analysis of 14 circRNAs.

circRNA	SMO(%)	IBK(%)	HoeffdingTree(%)	Logistic(%)
hsa_circ_0007919	—	83	83	83
chr10:15590454|15628663	83	94	83	83
hsa_circ_0002419	94	94	94	94
chr10:76729418|76748870	83	—	83	83
hsa_circ_0005521	89	89	89	89
chr12:97886239|97954825	89	83	89	89
chr10:97141442|97170534	—	94	83	—
hsa_circ_0034293	—	83	89	—
hsa_circ_0013048	—	89	—	—
hsa_circ_0007769	83	89	83	—
chr6:62362160|62442669	—	83	83	83
chrX:51070573|51099879	83	—	—	—
chr8:68934271|68973014	83	83	—	—
hsa_circ_0002286	83	—	83	83

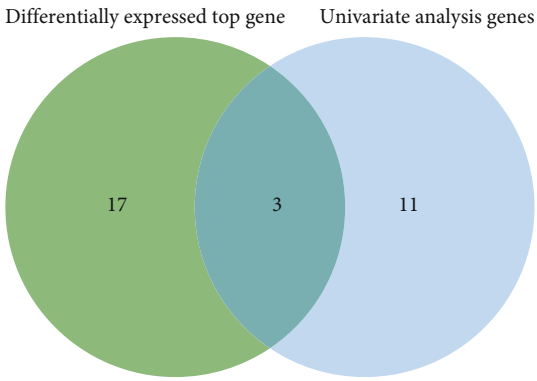

Figure 3: Cross-analysis of the top differentially expressed genes and genes identified by univariate analysis.

Collectively, these results show that the downstream mRNAs of the three key circRNAs play a major immunomodulatory role in the development of pulmonary TB.

3.5. PPI Network Construction. In this study, we have uncovered potential mRNAs downstream of three hub circRNAs. Among them, there were 1429 downstream mRNAs of hsa_circ_0007919, 2201 downstream mRNAs of hsa_circ_0002419, and 5401 downstream mRNAs of hsa_circ_0005521. We hypothesized that mRNAs simultaneously regulated by the three circRNAs may play important roles in the development of pulmonary TB. Therefore, we screened out 372 overlapping mRNAs using Jvenn and conducted further analysis (Figure 6(a)). To further find the hub genes among the 372 mRNAs in the network, we used the STRING database and Cytoscape. We found the top 50 hub genes according to the cytoHubba plugin in Cytoscape. We then constructed the PPI network on the basis of these top 50 genes (Table 6 and Figure 6(b)).

Table 5: Statistical analysis of downstream genes of the identified circRNAs.

circRNA	miRNA	mRNA
hsa_circ_0007919	13	1429
hsa_circ_0002419	15	2201
hsa_circ_0005521	46	5401

4. Discussion

Current laboratory tests for pulmonary TB include immunological- and molecular-based assays. Traditional smear staining has the disadvantages of a low positive rate and a long culture period [31]. With the further development of biomedical technologies, exosomal microRNA, real-time fluorescence quantitative PCR, and other techniques have been applied, but there is still a lack of rapid and reliable detection techniques for pulmonary TB [32, 33]. CircRNAs have several advantages as a biomarker, and their roles in the pathological regulation of pulmonary TB have received increasing attention in recent years [34]. Many studies have shown that circRNA expression is altered in the tissues and peripheral blood of pulmonary TB patients [35]. In this study, we uncovered three hub circRNAs by using differential gene expression, machine learning, and univariate analysis, including hsa_circ_0007919 (upregulated in diseased tissues) and hsa_circ_0002419 and hsa_circ_0005521 (downregulated in diseased tissues). To date, there have been no reports about hsa-circ-0002419 or hsa_circ_0005521. However, it has been found that potential downstream genes of hsa-miR-409-5p and hsa_circ_0005521 may also interact with hsa_circ_0028883, which has potential diagnostic value for pulmonary TB [36]. Wang et al. showed that hsa_circ_0007919 plays a role in ulcerative colitis by binding to hsa-miR-138 and hsa-let-7a to regulate the expression of VIPR1

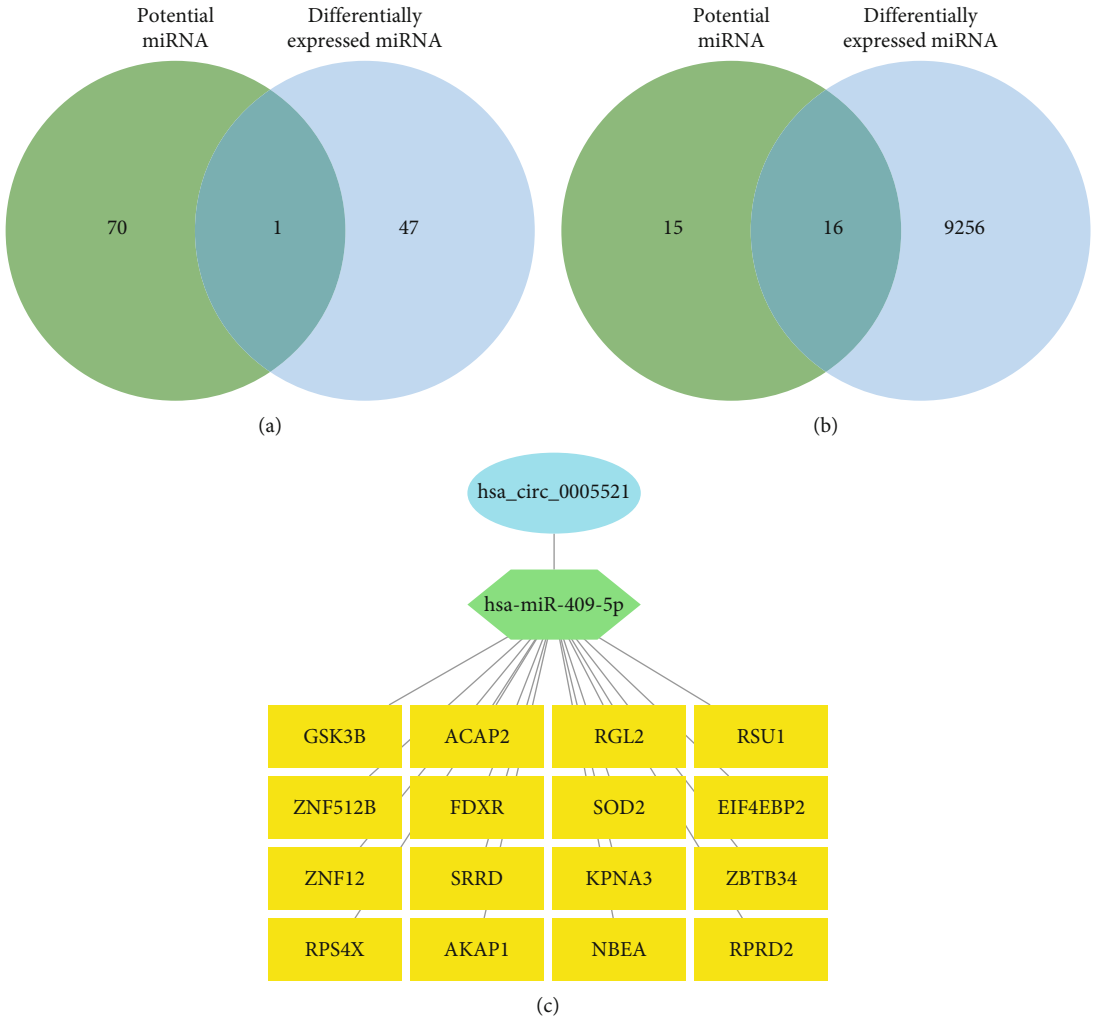

Figure 4: Analytical screening of downstream miRNAs and mRNAs. (a) Screening of downstream miRNAs using Jvenn cross-analysis of potential miRNAs and the differentially expressed miRNAs. (b) Screening of downstream mRNAs using Jvenn cross-analysis of potential mRNAs and the differentially expressed mRNAs. (c) The circRNA–miRNA–mRNA interaction network.

and EPC1, respectively [37]. Pulmonary TB also includes chronic inflammation, and the two diseases may share common pathways in terms of inflammation.

We further studied the effects of potential genes downstream of the hub circRNAs on pulmonary TB. According to GO and KEGG analysis, the genes were enriched in the PI3K-Akt signaling pathway, the proteoglycan pathway in cancer, and Ras signaling. Yang et al. showed that the inflammatory response of macrophage-like cells to MTB can be attenuated by modulating the PI3K/Akt/mTOR signaling pathway [38]. Other studies have shown that PI3K/AKT/mTOR signaling pathways are suppressed in patients with active pulmonary TB [39]. Gill et al. explained that the mechanism by which proteoglycans modulate inflammatory responses in the lung and showed that they may be part of a new treatment for inflammatory lung diseases and lung infections [40]. It has also been shown that hsa_circRNA_103571, which is differently expressed in the plasma of patients with active pulmonary TB, is also involved in the Ras pathway [41].

We uncovered 50 hub genes and then constructed a PPI network using the STRING database and cytoHubba. FBXW7 scored the highest, and SOCS3 was the next highest. We concluded that these genes may be associated with the development of pulmonary TB. Additionally, some of these genes have been reported to be involved in the development of pulmonary TB and other diseases. FBXW7 is an important tumor suppressor. Ni et al. found that miR-92a plays an oncogene role in nonsmall cell lung cancer by regulating FBXW7 [42]. It has been reported that FBXW7 plays a key role in regulating colitis by inducing CCL2 and CCL7 expression in macrophages and promoting the accumulation of pro-inflammatory mononuclear macrophages [43]. Cui et al. found that inactivation of FBXW7 in cancer cells, especially those with wild-type p53, may improve the efficacy of radiotherapy or chemotherapy, and thus improve patient survival [44]. Pulmonary TB is a risk factor for lung cancer, and the probability of developing lung cancer is much higher in pulmonary TB patients than in the general population. Therefore, FBXW7 may play a role in pulmonary TB

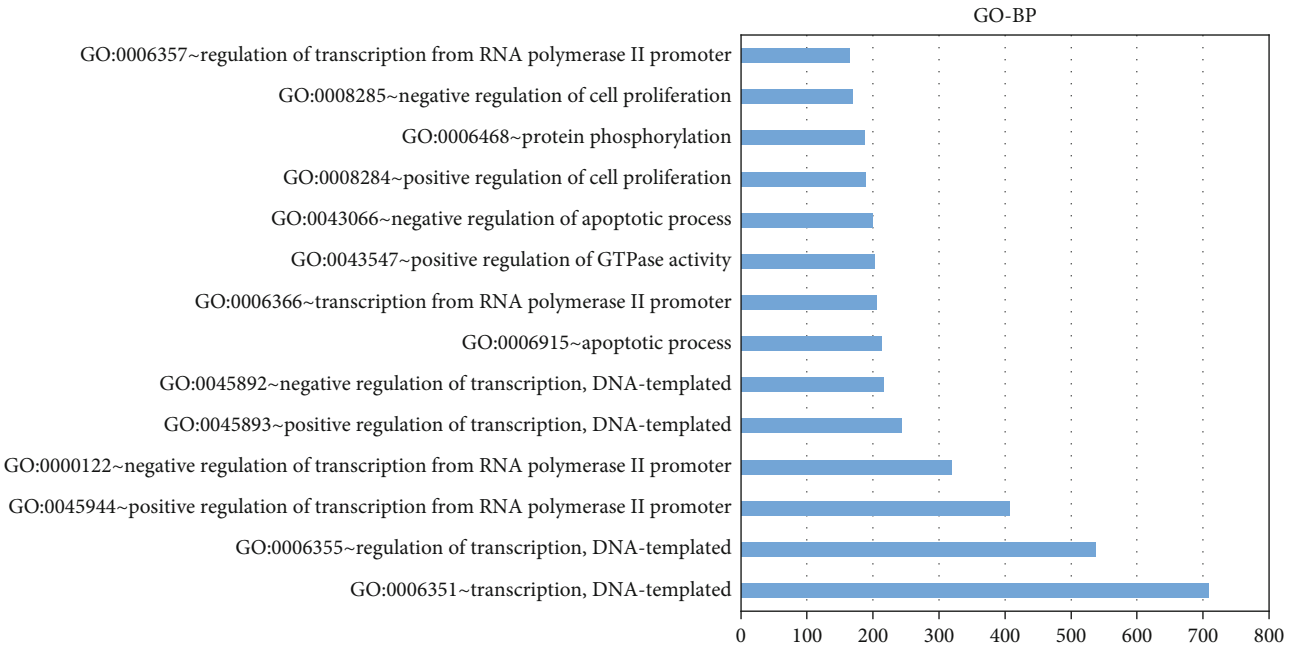

(a)

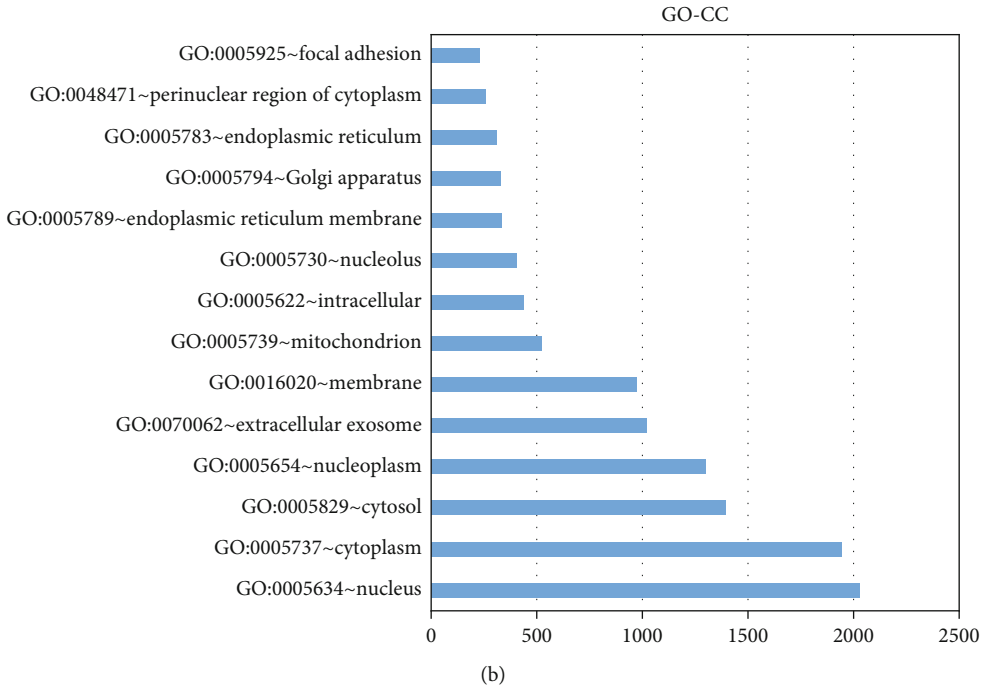

(b)

Figure 5: Continued.

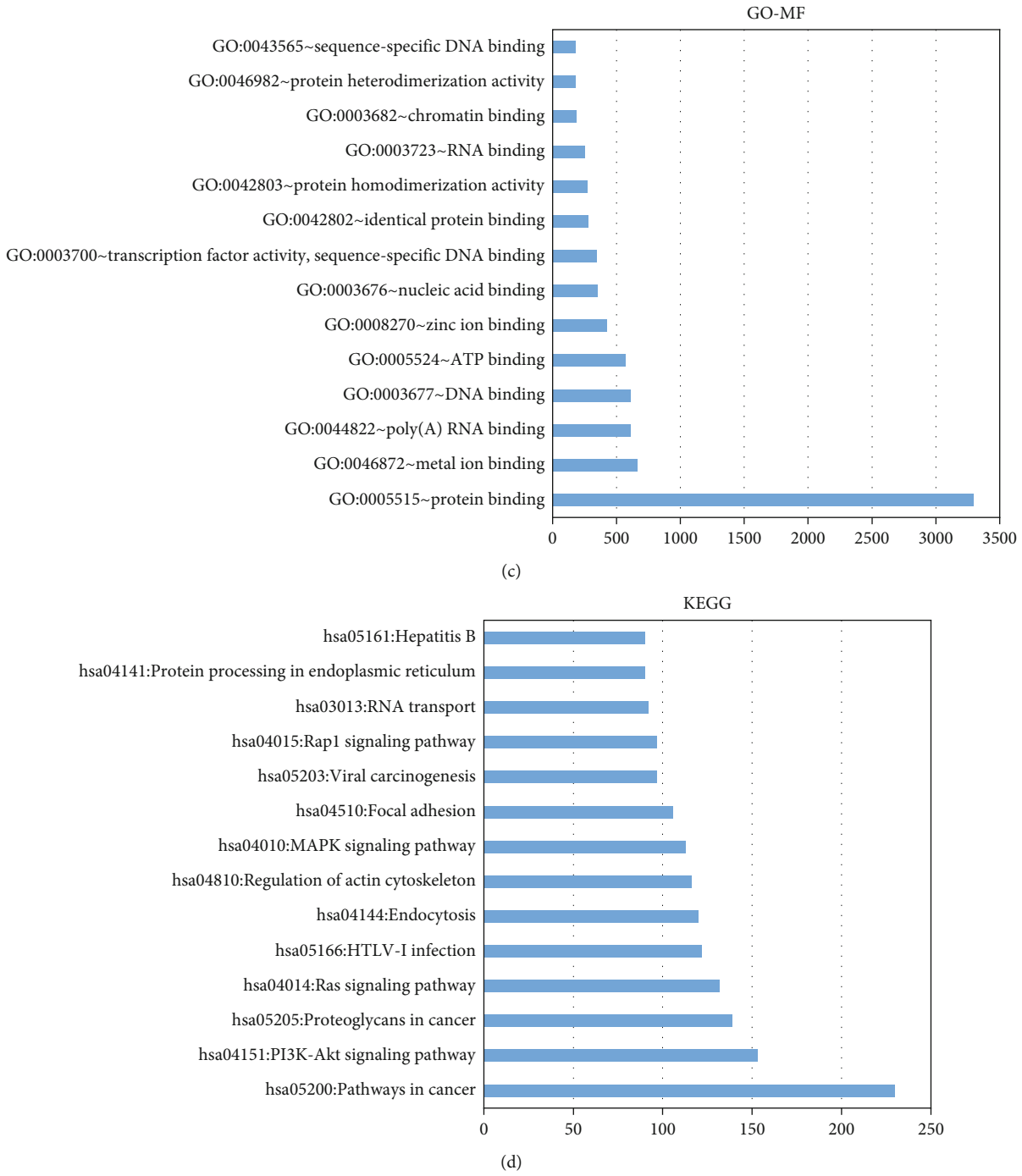

Figure 5: Biological function enrichment analysis. (a) Biological process (BP) enrichment analysis. (b) Cellular component (CC) enrichment analysis. (c) Molecular function (MF) enrichment analysis. (d) KEGG pathway enrichment analysis.

patients progressing to lung cancer through the above genes or pathways. SOCS3 is a suppressor of cytokine signaling; Feng et al. showed that stimulating G-protein-coupled receptor 120 (GPR120) induced SOCS3 expression and that GPR120-specific small molecule agonists improved autoimmune inflammation *via* dendritic cells [45]. Harling et al. showed that T cells are essential to prevent MTB infection and that T cell damage promotes the development of pulmonary TB. They concluded that high SOCS3 expression is a factor in the impaired T cell function of pulmonary TB patients [46].

However, this study had some limitations. First, expression levels of the DEGs need to be further verified by quantitative PCR. Second, the model with 100% prediction accuracy established in this study needs further parameter changes, optimization, and assessments before it can be widely used. Finally, the mechanisms of these DEGs in pulmonary TB need to be further explored by molecular experimentation.

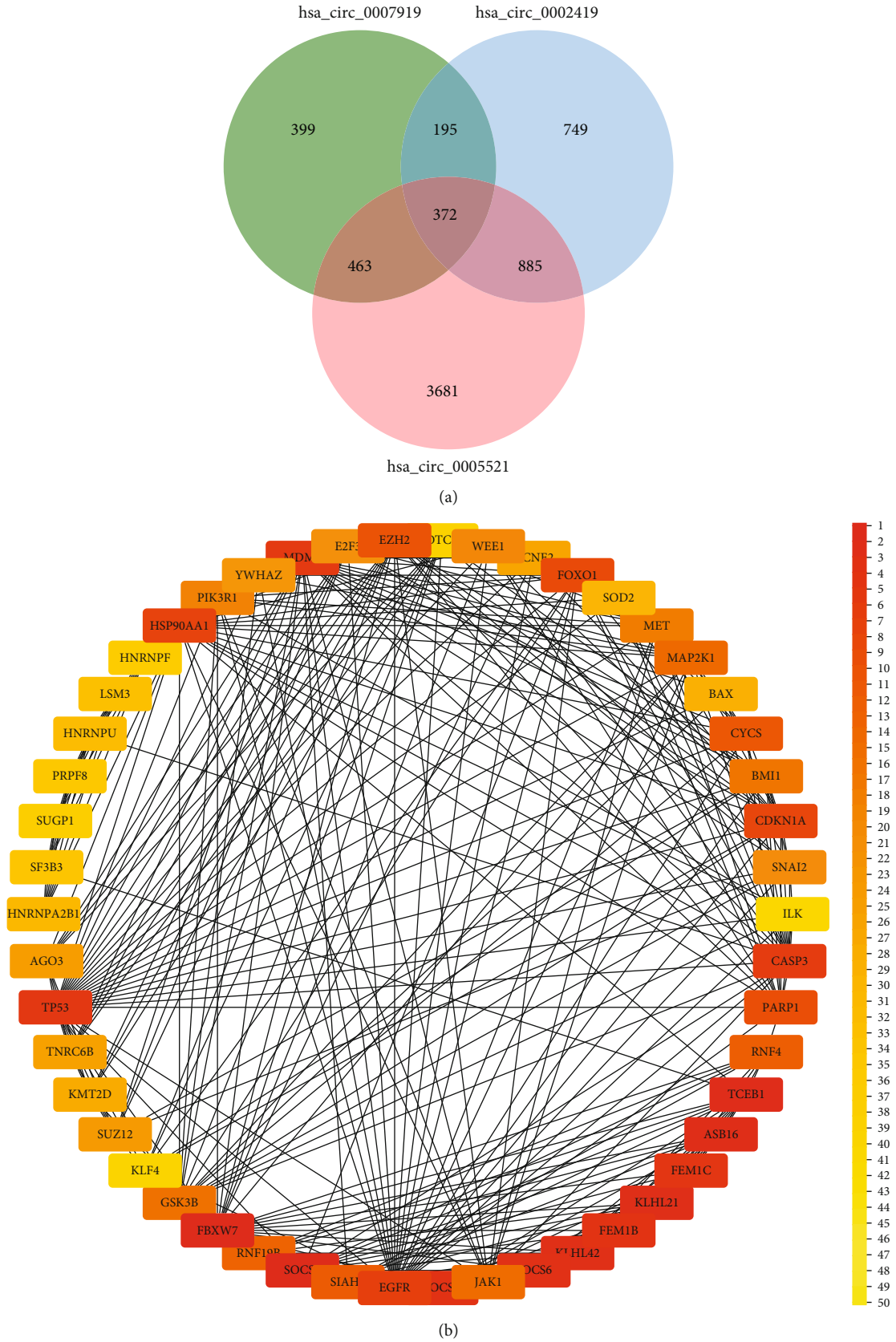

Figure 6: Screening the hub mRNAs. (a) Intersection analysis of potential downstream mRNAs of hsa_circ_0007919, hsa_circ_0002419, and hsa_circ_0005521. (b) PPI network of the top 50 hub mRNAs.

Table 6: Scores of the top 50 hub mRNAs.

mRNA	MCC
FBXW7	403816
SOCS3	403476
TCEB1	403213
ASB16	403206
KLHL21	403202
KLHL42	403200
SOCS6	362929
SOCS5	362928
FEM1B	362886
FEM1C	362882
TP53	139047
MDM2	135767
CASP3	124579
EGFR	123489
HSP90AA1	121780
CDKN1A	114332
FOXO1	94090
PARP1	92418
EZH2	59540
CYCS	57445
SIAH2	40341
RNF4	40323
RNF19B	40320
MAP2K1	22088
JAK1	16144
GSK3B	12798
BMI1	11425
MET	11221
PIK3R1	9141
WEE1	5886
SNAI2	5763
E2F3	3748
YWHAZ	2970
SUZ12	1957
AGO3	1848
TNRC6B	1825
CCNE2	1690
KMT2D	1119
BAX	864
SOD2	777
HNRNPA2B1	748
HNRNPU	736
LSM3	730
SF3B3	727
PRPF8	725
HNRNPF	724
SUGP1	720
NOTCH2	499
KLF4	442
ILK	265

5. Conclusions

In conclusion, we screened three hub circRNAs using the adjacent normal and diseased tissues of pulmonary TB patients. GO and KEGG enrichment were used to identify pathways associated with pulmonary TB. We identified hub genes through a PPI network. This study may provide a reference for finding candidate markers for the early diagnosis of pulmonary TB and provide new directions for possible pulmonary TB therapeutic targets.

Data Availability

The data can be seen in PRJNA795290, GSE158767, GSE29190, and GSE83456 and the Supplementary Materials.

Ethical Approval

All participants agreed to take part in this study; we received informed consent for the publication of data from the participants.

Conflicts of Interest

The authors declare that there is no conflict of interest regarding the publication of this paper.

Authors' Contributions

Qin Yuan, Zilu Wen, and Ke Yang contributed equally to this work.

Acknowledgments

We thank James P. Mahaffey, PhD, from Liwen Bianji (Edanz) (http://www.liwenbianji.cn) for editing the English text of a draft of this manuscript.

Supplementary Materials

The 13 algorithms used to build the machine learning models are shown in Tables S1–S9 in the supplementary material. *(Supplementary Materials)*

References

[1] K. Dheda, C. E. Barry 3rd, and G. Maartens, "Tuberculosis," *Lancet*, vol. 387, no. 10024, pp. 1211–1226, 2016.

[2] J. Furin, H. Cox, and M. Pai, "Tuberculosis," *Lancet*, vol. 393, no. 10181, pp. 1642–1656, 2019.

[3] J. Wang, M. Zhu, J. Pan, C. Chen, S. Xia, and Y. Song, "Circular RNAs: a rising star in respiratory diseases," *Respiratory Research*, vol. 20, no. 1, p. 3, 2019.

[4] A. T. Pezzella, "History of pulmonary tuberculosis," *Thoracic Surgery Clinics*, vol. 29, no. 1, pp. 1–17, 2019.

[5] A. Natarajan, P. M. Beena, A. V. Devnikar, and S. Mali, "A systemic review on tuberculosis," *The Indian Journal of Tuberculosis*, vol. 67, no. 3, pp. 295–311, 2020.

[6] M. Campo and L. M. Kawamura, "What is tuberculosis (TB)?," *American Journal of Respiratory and Critical Care Medicine*, vol. 195, no. 4, pp. P7–P8, 2017.

[7] P. V. Rogozhkin, A. V. Kolsanov, and E. A. Borodulina, "Surgical treatment of pulmonary tuberculosis," *Khirurgiia (Mosk)*, vol. 6, no. 6, pp. 104–108, 2020.

[8] F. Getnet, M. Demissie, N. Assefa, B. Mengistie, and A. Worku, "Delay in diagnosis of pulmonary tuberculosis in low-and middle-income settings: systematic review and meta-analysis," *BMC Pulmonary Medicine*, vol. 17, no. 1, p. 202, 2017.

[9] A. Niyonkuru, X. Chen, K. H. Bakari et al., "Evaluation of the diagnostic efficacy of 18F-fluorine-2-deoxy-D-glucose PET/CT for lung cancer and pulmonary tuberculosis in a tuberculosis-endemic country," *Cancer Medicine*, vol. 9, no. 3, pp. 931–942, 2020.

[10] B. Acharya, A. Acharya, S. Gautam et al., "Advances in diagnosis of tuberculosis: an update into molecular diagnosis of mycobacterium tuberculosis," *Molecular Biology Reports*, vol. 47, no. 5, pp. 4065–4075, 2020.

[11] S. M. Lyon and M. D. Rossman, "Pulmonary tuberculosis," *Microbiology Spectrum*, vol. 5, no. 1, 2017.

[12] I. L. Patop, S. Wust, and S. Kadener, "Past, present, and future of circRNAs," *The EMBO Journal*, vol. 38, no. 16, article e100836, 2019.

[13] L. S. Kristensen, M. S. Andersen, L. V. W. Stagsted, K. K. Ebbesen, T. B. Hansen, and J. Kjems, "The biogenesis, biology and characterization of circular RNAs," *Nature Reviews. Genetics*, vol. 20, no. 11, pp. 675–691, 2019.

[14] B. Han, J. Chao, and H. Yao, "Circular RNA and its mechanisms in disease: from the bench to the clinic," *Pharmacology & Therapeutics*, vol. 187, pp. 31–44, 2018.

[15] R. Shafabakhsh, N. Mirhosseini, S. Chaichian, B. Moazzami, Z. Mahdizadeh, and Z. Asemi, "Could circRNA be a new biomarker for pre-eclampsia?," *Molecular Reproduction and Development*, vol. 86, no. 12, pp. 1773–1780, 2019.

[16] L. L. Chen and L. Yang, "Regulation of circRNA biogenesis," *RNA Biology*, vol. 12, no. 4, pp. 381–388, 2015.

[17] K. K. Ebbesen, T. B. Hansen, and J. Kjems, "Insights into circular RNA biology," *RNA Biology*, vol. 14, no. 8, pp. 1035–1045, 2017.

[18] S. Meng, H. Zhou, Z. Feng et al., "CircRNA: functions and properties of a novel potential biomarker for cancer," *Molecular Cancer*, vol. 16, no. 1, p. 94, 2017.

[19] L. L. Chen, "The expanding regulatory mechanisms and cellular functions of circular RNAs," *Nature Reviews. Molecular Cell Biology*, vol. 21, no. 8, pp. 475–490, 2020.

[20] A. Huang, H. Zheng, Z. Wu, M. Chen, and Y. Huang, "Circular RNA-protein interactions: functions, mechanisms, and identification," *Theranostics*, vol. 10, no. 8, pp. 3503–3517, 2020.

[21] W. Y. Zhou, Z. R. Cai, J. Liu, D. S. Wang, H. Q. Ju, and R. H. Xu, "Circular RNA: metabolism, functions and interactions with proteins," *Molecular Cancer*, vol. 19, no. 1, p. 172, 2020.

[22] W. W. Du, C. Zhang, W. Yang, T. Yong, F. M. Awan, and B. B. Yang, "Identifying and characterizing circRNA-protein interaction," *Theranostics*, vol. 7, no. 17, pp. 4183–4191, 2017.

[23] B. Li, L. Zhu, C. Lu et al., "_circNDUFB2_ inhibits non-small cell lung cancer progression via destabilizing IGF2BPs and activating anti-tumor immunity," *Nature Communications*, vol. 12, no. 1, p. 295, 2021.

[24] J. Wang, Y. Zhang, F. Zhu et al., "CircRNA expression profiling and bioinformatics analysis indicate the potential biological role and clinical significance of circRNA in influenza a virus-induced lung injury," *Journal of Biosciences*, vol. 46, no. 2, 2021.

[25] T. C. Zhou, X. Li, L. J. Chen et al., "Differential expression profile of hepatic circular RNAs in chronic hepatitis B," *Journal of Viral Hepatitis*, vol. 25, no. 11, pp. 1341–1351, 2018.

[26] L. Yan and Y. G. Chen, "Circular RNAs in immune response and viral infection," *Trends in Biochemical Sciences*, vol. 45, no. 12, pp. 1022–1034, 2020.

[27] S. Liu, B. Zhou, J. D. Valdes, J. Sun, and H. Guo, "Serum hepatitis B virus RNA: a new potential biomarker for chronic hepatitis B virus infection," *Hepatology*, vol. 69, no. 4, pp. 1816–1827, 2019.

[28] H. Xie, H. Sun, R. Mu et al., "The role of circular RNAs in viral infection and related diseases," *Virus Research*, vol. 291, p. 198205, 2021.

[29] J. Li, D. Sun, W. Pu, J. Wang, and Y. Peng, "Circular RNAs in cancer: biogenesis, function, and clinical significance," *Trends Cancer*, vol. 6, no. 4, pp. 319–336, 2020.

[30] L. Wang, Z. Wen, H. Ma et al., "Long non-coding RNAs ENST00000429730.1 and MSTRG.93125.4 are associated with metabolic activity in tuberculosis lesions of sputum-negative tuberculosis patients," *Aging (Albany NY)*, vol. 13, no. 6, pp. 8228–8247, 2021.

[31] D. Machado, I. Couto, and M. Viveiros, "Advances in the molecular diagnosis of tuberculosis: from probes to genomes," *Infection, Genetics and Evolution*, vol. 72, pp. 93–112, 2019.

[32] A. Sinigaglia, E. Peta, S. Riccetti, S. Venkateswaran, R. Manganelli, and L. Barzon, "Tuberculosis-associated MicroRNAs: from pathogenesis to disease biomarkers," *Cell*, vol. 9, no. 10, p. 2160, 2020.

[33] S. M. Cho, S. Shin, Y. Kim et al., "A novel approach for tuberculosis diagnosis using exosomal DNA and droplet digital PCR," *Clinical Microbiology and Infection*, vol. 26, no. 7, pp. 942.e1–942.e5, 2020.

[34] X. H. Yi, B. Zhang, Y. R. Fu, and Z. J. Yi, "STAT1 and its related molecules as potential biomarkers in mycobacterium tuberculosis infection," *Journal of Cellular and Molecular Medicine*, vol. 24, no. 5, pp. 2866–2878, 2020.

[35] H. L. Luo, Y. Peng, H. Luo et al., "Circular RNA hsa_circ_0001380 in peripheral blood as a potential diagnostic biomarker for active pulmonary tuberculosis," *Molecular Medicine Reports*, vol. 21, no. 4, pp. 1890–1896, 2020.

[36] X. Zhang, Q. Zhang, Q. Wu et al., "Integrated analyses reveal hsa_circ_0028883 as a diagnostic biomarker in active tuberculosis," *Infection, Genetics and Evolution*, vol. 83, p. 104323, 2020.

[37] T. Wang, N. Chen, W. Ren et al., "Integrated analysis of circRNAs and mRNAs expression profile revealed the involvement of hsa_circ_0007919 in the pathogenesis of ulcerative colitis," *Journal of Gastroenterology*, vol. 54, no. 9, pp. 804–818, 2019.

[38] Y. Yang, Y. Sun, J. Xu et al., "Epithelial cells attenuate toll-like receptor-mediated inflammatory responses in monocyte-derived macrophage-like cells to mycobacterium tuberculosis by modulating the PI3K/Akt/mTOR signaling pathway," *Mediators of Inflammation*, vol. 2018, 2018.

[39] X. Zhang, T. Huang, Y. Wu et al., "Inhibition of the PI3K-Akt-mTOR signaling pathway in T lymphocytes in patients with active tuberculosis," *International Journal of Infectious Diseases*, vol. 59, pp. 110–117, 2017.

[40] S. Gill, T. N. Wight, and C. W. Frevert, "Proteoglycans: key regulators of pulmonary inflammation and the innate immune response to lung infection," *The Anatomical Record*, vol. 293, no. 6, pp. 968–981, 2010.

[41] Z. Yi, K. Gao, R. Li, and Y. Fu, "Dysregulated circRNAs in plasma from active tuberculosis patients," *Journal of Cellular and Molecular Medicine*, vol. 22, no. 9, pp. 4076–4084, 2018.

[42] D. Ni, J. Teng, Y. Cheng, Z. Zhu, B. Zhuang, and Z. Yang, "MicroRNA-92a promotes non-small cell lung cancer cell growth by targeting tumor suppressor gene FBXW7," *Molecular Medicine Reports*, vol. 22, no. 4, pp. 2817–2825, 2020.

[43] J. He, Y. Song, G. Li et al., "Fbxw7 increases CCL2/7 in CX3CR1hi macrophages to promote intestinal inflammation," *The Journal of Clinical Investigation*, vol. 129, no. 9, pp. 3877–3893, 2019.

[44] D. Cui, X. Xiong, J. Shu, X. Dai, Y. Sun, and Y. Zhao, "FBXW7 confers radiation survival by targeting p53 for degradation," *Cell Reports*, vol. 30, no. 2, pp. 497–509.e4, 2020.

[45] C. Feng, L. Li, Q. Li et al., "Docosahexaenoic acid ameliorates autoimmune inflammation by activating GPR120 signaling pathway in dendritic cells," *International Immunopharmacology*, vol. 97, p. 107698, 2021.

[46] K. Harling, E. Adankwah, A. Guler et al., "Constitutive STAT3 phosphorylation and IL-6/IL-10 co-expression are associated with impaired T-cell function in tuberculosis patients," *Cellular & Molecular Immunology*, vol. 16, no. 3, pp. 275–287, 2019.

Hindawi
BioMed Research International
Volume 2024, Article ID 9781094, 1 page
https://doi.org/10.1155/2024/9781094

Retraction

Retracted: Analgesic Effects of Different κ-Receptor Agonists Used in Daytime Laparoscopic Cholecystectomy

BioMed Research International

Received 12 March 2024; Accepted 12 March 2024; Published 20 March 2024

This article has been retracted by Hindawi following an investigation undertaken by the publisher [1]. This investigation has uncovered evidence of one or more of the following indicators of systematic manipulation of the publication process:

(1) Discrepancies in scope

(2) Discrepancies in the description of the research reported

(3) Discrepancies between the availability of data and the research described

(4) Inappropriate citations

(5) Incoherent, meaningless and/or irrelevant content included in the article

(6) Manipulated or compromised peer review

The presence of these indicators undermines our confidence in the integrity of the article's content and we cannot, therefore, vouch for its reliability. Please note that this notice is intended solely to alert readers that the content of this article is unreliable. We have not investigated whether authors were aware of or involved in the systematic manipulation of the publication process.

Wiley and Hindawi regrets that the usual quality checks did not identify these issues before publication and have since put additional measures in place to safeguard research integrity.

We wish to credit our own Research Integrity and Research Publishing teams and anonymous and named external researchers and research integrity experts for contributing to this investigation.

The corresponding author, as the representative of all authors, has been given the opportunity to register their agreement or disagreement to this retraction. We have kept a record of any response received.

References

[1] W. Zhou, J. Wang, C. Hu et al., "Analgesic Effects of Different κ-Receptor Agonists Used in Daytime Laparoscopic Cholecystectomy," *BioMed Research International*, vol. 2021, Article ID 2396008, 8 pages, 2021.

Hindawi
BioMed Research International
Volume 2021, Article ID 2396008, 8 pages
https://doi.org/10.1155/2021/2396008

Research Article

Analgesic Effects of Different κ-Receptor Agonists Used in Daytime Laparoscopic Cholecystectomy

Wanjun Zhou,[1] Jiawu Wang,[1] Chengyun Hu,[1] Feibiao Dai,[1] Zhetao Zhang,[2] Chuanyao Li,[1] Chaoliang Tang,[1] and Yanhu Xie[1]

[1]*Department of Anesthesiology, The First Affiliated Hospital of USTC, Division of Life Sciences and Medicine, University of Science and Technology of China, Hefei, Anhui 230001, China*
[2]*Department of Pharmacy, The First Affiliated Hospital of USTC, Division of Life Sciences and Medicine, University of Science and Technology of China, Hefei, Anhui 230036, China*

Correspondence should be addressed to Chuanyao Li; lichuanyao@sina.com, Chaoliang Tang; chaolt@ustc.edu.cn, and Yanhu Xie; xyh200701@sina.cn

Received 15 October 2021; Revised 30 November 2021; Accepted 6 December 2021; Published 29 December 2021

Academic Editor: Bing Niu

Background. Comparing the effect of two different κ-receptor agonists, nalbuphine and oxycodone, and regular morphine in patients for prophylactic analgesia of acute pain after daytime laparoscopic cholecystectomy. *Methods*. One hundred and twenty-four patients undergoing laparoscopic cholecystectomy were randomly allocated to receive nalbuphine (group N), oxycodone (group O), and morphine (group M). The three groups were all given intravenous injection (iv.) of 0.15 mg/kg injection before incision and 0.05 mg/kg injection at the end of pneumoperitoneum. The Visual Analogue Scale (VAS) scores (incision, visceral, and shoulder) and Ramsay sedation scores at 1, 2, 4, 8, 12, 16, 20, and 24 hours after surgery, the time of extubation, the incidence of postoperative adverse events, the satisfaction of pain treatment, and the duration of stay after surgery were all recorded. *Results*. Compared with group M, the VAS scores of visceral pain at rest decreased in group N and group O at 1-8 h after surgery ($P < 0.05$). The VAS scores of visceral pain at movement in group N decreased longer than those in group O ($P < 0.05$). Compared with that of group M, the postoperative time in Ramsay sedation score of group O increased longer than that of group N ($P < 0.05$). Compared with group N, patients had worse sleep quality in group O, longer length of stay in group M, and lower satisfaction in both groups. *Conclusion*. Compared with morphine, prophylactic use of the κ-receptor agonists, nalbuphine and oxycodone, during laparoscopic cholecystectomy can reduce postoperative visceral pain. Furthermore, the nalbuphine group had fewer adverse reactions, better analgesia, and better satisfaction.

1. Introduction

In recent years, with the rapid development of enhanced recovery after surgery (ERAS), day surgery has emerged. Among them, enhanced recovery and adequate analgesia are an essential part of increasing the rate of day surgery [1]. Laparoscopic cholecystectomy (LC) is a typical example of laparoscopic surgery. However, about 80% of patients undergoing LC experience moderate to severe postoperative acute pain due to pneumoperitoneum and intraoperative trauma [2]. Under the influence of this pain, it may cause prolonged wound healing and infection. Postoperative cognitive impairment, prolonging the length of stay, or even developing chronic pain may also appear; these are the main reasons why LC cannot be included in the day surgery [3].

A variety of methods can be used for postoperative analgesia of LC, of which local anesthetic incision infiltration was used for somatic pain, besides warming and humidifying the carbon dioxide (CO_2) used for referred pain [4, 5]. For patients, suffering from visceral pain for day LC, weaker opioids are recommended currently [6]. As a classical μ-opioid receptor, morphine is a very effective measure of opioid pharmacodynamics, with a definite analgesic effect. However, it has a short duration of action and causes numerous adverse effects, which may not be suitable for ambulatory surgery [7]. Nalbuphine and oxycodone are two new opioid

analgesics. Both, activated κ-opioid receptor, have been a hot topic of research in recent years for the treatment of perioperative visceral pain. Opioids act by binding to receptors in the central nervous system, peripheral nervous system, and many other organ systems. Through studies, peripheral κ-opioid receptors were found to be widely distributed in the viscera, which may be the main reason for the superiority of κ-opioids in the treatment of visceral pain [8]. The κ-opioid receptor has a high concentration in the spinal cord and its agonist, nalbuphine with oxycodone, inducing only mild respiratory depression with a ceiling effect. In addition, κ receptors with analgesic and sedative effects are not cross-tolerant with μ receptors, and the analgesic effect is superimposed [9]. Oxycodone is a semisynthetic opioid analgesic and a κ_2 receptor agonist with low affinity for μ receptors, which is widely used in clinic [10]. As a κ-receptor agonist-antagonist, nalbuphine agonizes κ receptors to achieve analgesia, while antagonizing μ receptors to reduce opioid side effects, and is good postoperative analgesia and a good antagonist of opioid-induced adverse reactions [9].

However, the analgesic effects of nalbuphine and oxycodone are comparable to morphine by the results of current clinical practice. Still, the safety of both is better than morphine in terms of specific side effects [11, 12]. There are no definitive clinical studies suggesting which of these two κ-receptor agonists is more effective for prophylactic analgesia for acute postoperative pain after LC. This is a prospective randomized controlled study, which is aimed at comparing the analgesic effects and occurrence of adverse effects of nalbuphine and oxycodone for prophylactic analgesia in LC. Then, select a more suitable drug to provide a reference for future clinical practice in the day surgery mode of LC.

2. Methods

2.1. Demographic Parameters. One hundred and twenty-four patients, who underwent LC in the First Affiliated Hospital of University of Science and Technology of China, were selected from May 2019 to June 2020. Patients aged 18-65 yr, with a body mass index (BMI) of 18.5-30 kg/m^2, scheduled for daytime LC, and with American Society of Anesthesiologists (ASA) physical status of I or II, were eligible. Patients were excluded if they had severe respiratory and circulatory diseases, nervous system diseases, mental and psychological diseases, obvious abnormal liver and kidney functions, opioid allergy, or long-term abuse of drugs (including antineoplastic and analgesics) or if they had intraoperative conversion to open surgery. The study was approved by the Ethics Committee of the First Affiliated Hospital of USTC (serial number, 2019-Q (H)-001), and written informed consent was obtained from all subjects or the legal surrogate.

2.2. Experimental Grouping. Patients were randomly divided into three groups (nalbuphine group, oxycodone group, and morphine group) at an allocation ratio of 1 : 1 : 1 via block randomization generated by computer-generated randomization software. Group allocations were sealed in sequentially numbered, opaque envelopes that were opened by one trained study personnel after the induction of general anesthesia. Each envelope contained the group allocation with instructions of analgesic for the attending anesthesiologists.

The nalbuphine group (group N) was given 0.15 mg/kg nalbuphine injection before skin cutting and 0.05 mg/kg nalbuphine injection after surgery. The oxycodone group (group O) was given 0.15 mg/kg oxycodone injection before skin cutting and 0.05 mg/kg oxycodone injection after surgery. The morphine group (group M) was given 0.15 mg/kg morphine injection before skin cutting and 0.05 mg/kg morphine injection after surgery.

2.3. Anesthesia. General anesthesia was induced with by 1 μg/kg remifentanil and 0.2-0.4 mg/kg etomidate. Tracheal intubation was facilitated by 0.6 mg/kg rocuronium. Then, an I-gel laryngeal mask was placed, and a gastric tube was placed after 90 s. Mechanical ventilation was performed with a tidal volume of 6-8 ml/kg, respiratory rate of 10-14 times/min, inhalation/respiration ratio of 1/2, inhalation oxygen concentration of 50%, and End-tidal carbon dioxide partial pressure ($P_{ET}CO_2$) maintained between 35 and 45 mmHg. Experimental analgesic (diluted to 10 ml, iv.) was given before skin cutting. Anesthesia was maintained in target controlled infusion with propofol (2.0-4.0 μg/ml) and remifentanil (2.0-4.0 ng/ml), and plasma concentrations of propofol and remifentanil were adjusted to maintain a level of 27-56 (stage E0-D1) and according to 20% variations in blood pressure and/or heart rate compared with basal values. Rocuronium was given at 10 mg per injection as needed. After the operation, all anesthesia drugs were stopped and experimental analgesics were given (diluted to 10 ml, iv.). When the skin was sutured, 10 ml ropivacaine (0.5%) was given through the skin incision to infiltrate the local anesthesia layer by layer.

2.4. Surgery. All groups of patients were operated by the same group of surgeons, using the 3-hole method, and the pneumoperitoneum pressure was 14 mmHg (warming and humidifying the CO_2). An abdominal drainage tube should not be placed after surgery unless in special circumstances. After surgery, the residual CO_2 was deflated carefully.

2.5. Rescue Analgesics. In cases where patients experienced significant postoperative pain (VAS $\geq$ 4), rescue analgesics (50 mg flurbiprofen axetil injection per time) were recommended for patients. The use of rescue analgesics was recorded.

2.6. Observation Target. The patients' demographic parameters, anesthesia time, and extubation time were recorded. Before surgery, the patients were instructed to use a 100 mm VAS [0-10, 0 = no pain and 10 = worst pain imaginable] to rate the following three pain components: incisional pain was defined as a superficial pain, wound pain, or pain located in the abdominal wall. Visceral pain was defined as pain inside the abdomen. Shoulder pain was defined as a sensation of pain in the shoulder. Follow-up evaluations were conducted at 1, 2, 4, 8, 12, 16, 20, and 24 h postoperatively by anesthesiologists blinded to grouping. The degree of incision pain and visceral pain was evaluated when resting and in

motion (cough and deep breathing), respectively. And record the Ramsay sedation score (1—patient is anxious and agitated or restless or both; 2—patient is cooperative, orientated, and tranquil; 3—patient responds to commands only; asleep levels were dependent on the patient's response to a light glabellar tap or loud auditory stimulus; 4—there is a brisk response; 5—there is a sluggish response; and 6—there is no response vital signs and sleep) [13]. The pain treatment satisfaction scale (PTSS) (PTSS, 0 = no satisfaction to 10 = complete satisfaction) [14] and major adverse effects such as postoperative nausea and vomiting (PONV) (PONV four-point scale: 1 = no nausea; 2 = mild nausea; 3 = severe nausea requiring antiemetic; and 4 = retching and/or vomiting) [15] and minor adverse effects such as hypoxemia, drowsiness, dizziness, skin pruritus, and urinary retention were recorded. Rescue analgesia within 24 h after surgery and unplanned discharge (the length of stay ≥ 24 h after surgery) was also used.

2.7. Sample Size. The power calculation for the study was based on the VAS of visceral pain at rest at 1 h after surgery, which was our primary outcome. A pilot study involving 8 patients at our center found that the mean ± standard deviation (SD) of the VAS of visceral pain at rest at 1 h after surgery was 4.5 ± 1.8. In a sample size of 40 patients, a clinically significant reduction of 30% in the VAS of visceral pain at rest at 1 h after surgery at a power of 95% was observed, with a two-sided significance level of 0.05. To compensate for the possibility of dropouts, we recruited a total of 132 patients, with 44 patients per group.

2.8. Statistical Analysis. The SPSS 22.6 software was used for statistical analyses. Distribution of variables was assessed using the Kolmogorov-Smirnov test, while homogeneity of variance was evaluated using Levene's test. Quantitative data were expressed as the mean ± standard deviations ($\bar{x} \pm s$) or medians and interquartile ranges. The enumeration data are represented by the number of examples. If the measurement data conform to the normal distribution, the analysis of variance (ANOVA) for repeated measurements is adopted, while Bonferroni's method was used to compare groups. If they do not conform, the one-way ANOVA of Kruskal Wallis test is adopted and Bonferroni's method was used to compare groups. The enumeration data were performed by χ^2 test. $P < 0.05$ was considered to be statistically significant.

3. Results

3.1. Quantitative Analysis of Patients. One hundred and thirty-two patients were recruited from May 2019 to June 2020. Three patients in group M dropped out of the study, one converted to open surgery, and two did not complete date collection. Two patients in group N dropped out of the study, due to failure to complete data collection. Three patients in group O dropped out of the study, two converted to open surgery, and one did not complete date collection. One hundred and twenty-four patients completed the study: 41 in group M, 42 in group N, and 41 in group O (Figure 1). There was no statistically significant difference in the demographic parameters among the 3 groups ($P > 0.05$), and there was comparability between the three groups. (Table 1).

3.2. Hemodynamic Variables. There were no statistically significant differences in heart rate, mean arterial pressure, and oxygen saturation among the three groups at each time point (Table 2).

3.3. The VAS Score (at Rest and Movement). There was no significant difference in the VAS score of incision pain (at rest and movement) among the three groups. Compared with group M, the VAS score of visceral pain at rest in group N and group O decreased 1-8 h after surgery ($P < 0.05$). The VAS score of visceral pain at movement in group N was significantly decreased 2-20 h after surgery, and that in group O was significantly decreased 2-8 h after surgery ($P < 0.05$). There was no statistical significance in VAS scores of shoulder pain among the three groups (Figure 2, Table 3).

3.4. Anesthesia Recovery. There was no significant difference in extubation time among the three groups. Compared with group N, patients had worse sleep quality in group O and lower pain treatment satisfaction in other two groups ($P < 0.05$), while the differences between groups M and O were not statistically significant. In the case of using rescue analgesia within 24 h postoperatively, that in groups N, O, and M increased sequentially; however, the differences were not statistically significant. Unplanned discharges of patients were significantly reduced in the group N compared to group M. (Table 4). Compared with group M, Ramsay sedation score of group O was significantly increased 1-8 h after surgery, while that of group N was significantly increased 1-4 h after surgery ($P < 0.05$) (Figure 3).

3.5. Postoperative Adverse Events. The occurrence of PONV in patients was significantly reduced in group N compared to group M ($P < 0.05$), and the difference was not statistically significant in group O compared to both group M and group N. The occurrence of other side effects was reduced in both group O and group N, in which 7 patients in group M had significantly more pruritus than the other two groups, and 18 patients in group M had significantly more dizziness than 4 patients in group N. The differences were all statistically significant ($P < 0.05$) (Table 5).

4. Discussion

This study mainly found that compared with morphine, preventive use of κ-receptor agonists, nalbuphine and oxycodone, in LC can significantly reduce postoperative visceral pain. The nalbuphine group has fewer complications such as postoperative dizziness, nausea, and vomiting and has better effect in reducing early postoperative pain and better patient satisfaction.

LC has the advantages of minimally invasive and quick recovery. With the deepening of ERAS concept, daytime surgery, which completes admission, discharge and corresponding surgery, and operation within one working day, arises at the historic moment. Nowadays, more and more clinicians

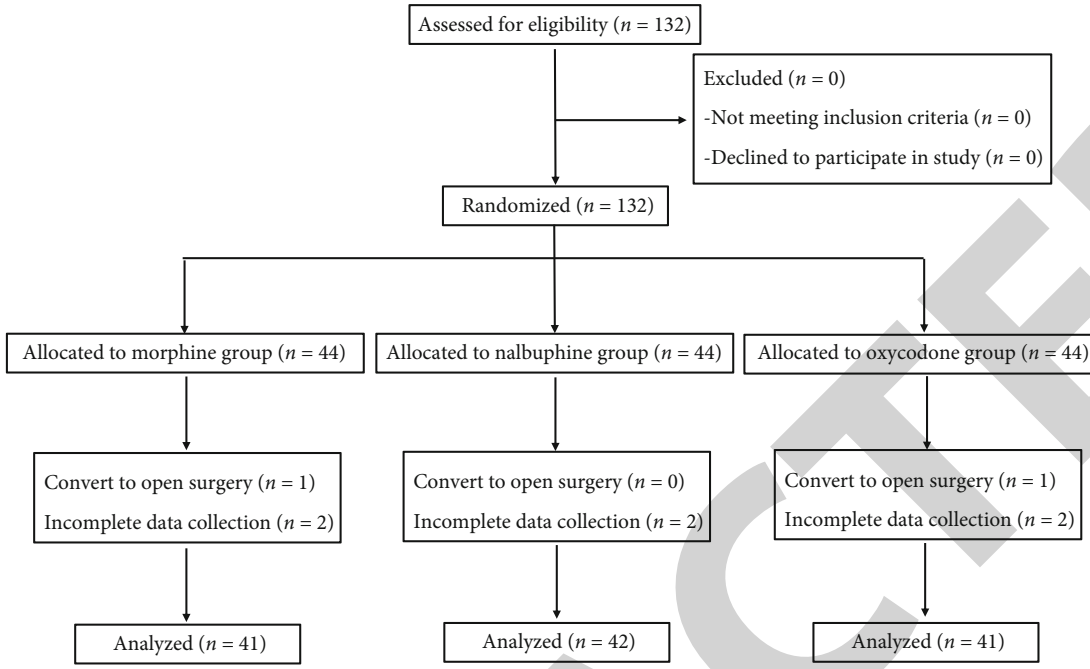

Figure 1: Flow diagram of patient recruitment.

Table 1: The demographic parameters among the three groups.

Group	Patients (n)	Men/women (*n*)	Age (years)	BMI (kg/m^2)	ASA I/II (*n*)	Time of operation (min)
M	41	13/28	45.1 ± 13.3	23.3 ± 2.4	29/12	56.3 ± 22.5
N	42	16/26	45.6 ± 10.0	23.8 ± 2.7	28/14	56.8 ± 24.3
O	41	15/26	47.3 ± 12.0	24.7 ± 2.6	28/13	56.2 ± 20.9

Values are given as the mean ± standard deviation or number of patients.

Table 2: Comparison of vital signs at different time points in three groups.

Group	Preoperative	Postoperative							
		1 h	2 h	4 h	8 h	12 h	16 h	20 h	24 h
Heart rate (times/min)									
M	77.0 ± 6.8	76.9 ± 8.1	77.8 ± 7.2	76.5 ± 5.4	75.6 ± 5.8	74.8 ± 6.2	74.2 ± 5.7	75.0 ± 6.3	75.2 ± 8.2
N	77.0 ± 8.6	76.5 ± 7.6	76.8 ± 8.5	75.0 ± 7.1	75.7 ± 7.2	74.2 ± 5.1	74.6 ± 7.9	74.6 ± 5.8	75.0 ± 6.9
O	75.5 ± 11.4	76.3 ± 9.8	76.0 ± 9.3	75.3 ± 8.2	74.9 ± 9.3	73.9 ± 8.0	74.8 ± 6.3	74.6 ± 7.0	75.5 ± 9.1
Mean arterial pressure (mmHg)									
M	92.0 ± 7.2	87.9 ± 8.6	87.7 ± 9.1	88.9 ± 6.9	88.5 ± 7.2	89.8 ± 8.8	88.3 ± 5.2	88.5 ± 7.3	90.8 ± 8.6
N	92.5 ± 8.3	85.2 ± 8.6	86.8 ± 7.7	86.2 ± 7.5	87.5 ± 6.8	88.2 ± 7.8	89.8 ± 9.2	90.5 ± 7.8	91.2 ± 6.8
O	92.3 ± 10.4	86.2 ± 8.8	86.0 ± 9.5	86.8 ± 7.2	88.9 ± 9.2	88.9 ± 8.6	89.6 ± 6.9	90.1 ± 8.0	90.5 ± 8.2
Oxygen saturation (%)									
M	97.3 ± 0.7	98.0 ± 0.8	98.9 ± 0.8	98.1 ± 1.0	97.1 ± 0.8	97.1 ± 0.8	97.1 ± 0.6	96.9 ± 0.8	97.2 ± 0.6
N	97.4 ± 0.8	98.9 ± 0.9	99.0 ± 0.9	98.8 ± 0.8	97.3 ± 0.6	97.3 ± 0.6	97.5 ± 0.8	97.3 ± 0.5	97.2 ± 0.7
O	96.9 ± 1.2	98.5 ± 1.4	98.5 ± 1.3	98.7 ± 0.9	96.7 ± 0.9	96.7 ± 0.9	97.2 ± 0.7	97.1 ± 0.7	96.8 ± 0.9

Values are given as the mean ± standard deviation.

use LC in daytime surgery. The development of daytime surgery would speed up patient turnover, reduce waiting time, reduce the risk of nosocomial infection, improve the use efficiency of medical resources, and reduce various expenses. A standardized daytime surgery system has clinical and economic win-win benefits [1]. However, postoperative pain is the main factor leading to delayed discharge of daytime surgery patients [16]. Previous studies have shown that

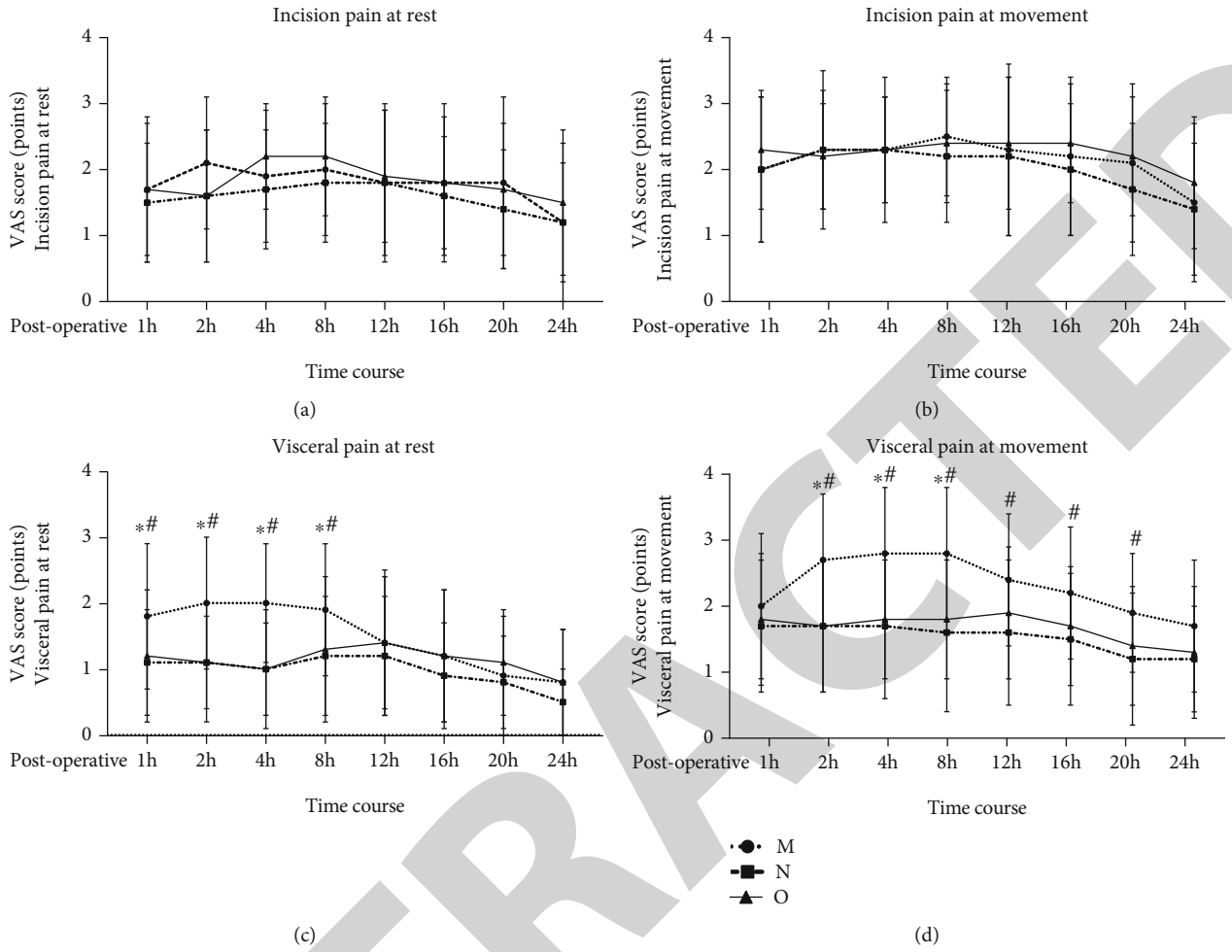

Figure 2: Postoperative VAS pain score of incision pain (a) at rest and (b) at movement; VAS pain score of visceral pain (c) at rest and (d) at movement during a 24 h postoperative period. Data are the mean with standard deviation. $^{*}P < 0.05$, group O compared with group M; $^{\#}P < 0.05$, group N compared with group M.

Table 3: VAS scores in the shoulder among the three groups at different time points.

Group	Postoperative							
	1 h	2 h	4 h	8 h	12 h	16 h	20 h	24 h
M	0.0 ± 0.0	0.0 ± 0.0	0.0 ± 0.2	0.1 ± 0.3	0.0 ± 0.2	0.0 ± 0.0	0.0 ± 0.0	0.0 ± 0.0
N	0.0 ± 0.0	0.0 ± 0.0	0.1 ± 0.3	0.1 ± 0.4	0.1 ± 0.3	0.0 ± 0.2	0.0 ± 0.0	0.0 ± 0.0
O	0.0 ± 0.0	0.0 ± 0.0	0.0 ± 0.2	0.1 ± 0.3	0.1 ± 0.2	0.0 ± 0.0	0.0 ± 0.0	0.0 ± 0.0

Values are given as the mean ± standard deviation.

Table 4: The situation of extubation.

Group	Extubation time (min)	Sleep	Rescue analgesia [*n* (%)]	PTSS	Unplanned discharge [*n* (%)]
M	15.0 (7.0, 20.0)	2 (1, 2)	5 (12.2%)	7 (6, 8)$^{\#}$	15 (36.6%)$^{\#}$
N	11.0 (5.0, 21.3)	1 (1, 2)	1 (2.3%)	8 (7, 10)*	3 (7.2%)*
O	14.5 (7.8, 20.5)	2 (1, 2)$^{\#}$	3 (7.3%)	7 (4, 10)$^{\#}$	8 (19.5%)

Values are given as medians and interquartile ranges or number of patients (%). $^{*}P < 0.05$ compared with group M; $^{\#}P < 0.05$ compared with group N. Statistical criteria: sleep (1—good, 2—average, 3—poor, and 4—insomnia).

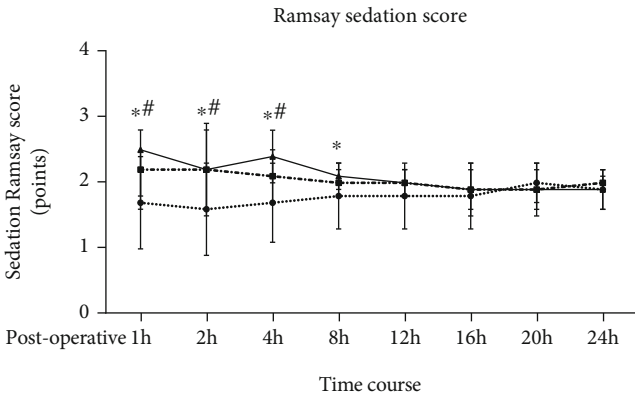

Figure 3: Postoperative Ramsay sedation score during a 24 h postoperative period. Data are the mean with standard deviation. $^{*}P < 0.05$, group O compared with group M; $^{\#}P < 0.05$, group N compared with group M.

postoperative pain mainly consists of three components: abdominal incision pain related to the incisional trauma at the port sites, visceral pain associated with tissue injury due to gallbladder dissection, and the stretching of nerve endings in the peritoneal cavity, and right shoulder pain is referred by diaphragmatic stretching. Among these pains, visceral pain is worse than incision and shoulder pain in postoperative acute pain [17]. Nalbuphine and oxycodone are the research hotspots in the treatment of postoperative visceral pain in recent years because of their agonistic effects on κ-opioid receptors.

This study found that there was no significant difference in VAS scores of incision pain (at rest and movement) among the three groups of patients, which may be related to the layer-by-layer infiltration of 0.5% ropivacaine in the three groups of patients. It also indicates that the two κ-receptor agonists may have the same analgesic effect on abdominal incision pain as morphine. The VAS scores of visceral pain (at rest and movement) in oxycodone and nalbuphine groups were significantly reduced within 2-8 hours after operation. It is suggested that the analgesic effect of oxycodone and nalbuphine on visceral pain may be better than that of morphine. This is because the two κ-receptor agonists inhibit the sensitization of peripheral pain κ-opioid receptors and the excitatory neurotransmission between the afferent nerves expressing κ-opioid receptors and the superficial neurons of the spinal cord that process pain signals. These functional κ-opioid receptors have abundant innervation not only for skin but also for visceral organs, which indicates that κ-opioid receptors are of great significance in inhibiting visceral pain [18].

On Ramsay sedation score, the mean value of morphine group was less than 2 at 1-16 hours after operation. It may be related to the imperfect analgesia in this group, which improves the arousal level and offsets the sedation induced by morphine. In an experimental pain study on sedation, it was also found that morphine had no effect on sedation variables in electroencephalograph [19]. Compared with the morphine group, the oxycodone group increased significantly 1-8 h after operation, while the nalbuphine group increased significantly 1-4 h after operation, both of which were more than 2 scores, which may be related to the sedative effect of both through central nervous system κ-opioid receptors [20].

The study also found some differences between the two κ-receptor agonists in terms of analgesic effect. Compared with that in the oxycodone group, VAS score of visceral pain at movement in the nalbuphine group was still significantly lower 12-20 h after operation. The reason may be that oxycodone is a semisynthetic opioid receptor agonist, which has double agonism of both μ-opioid receptors and κ-opioid receptors, and the half-life of oxycodone intravenous injection is 3.5 h. Nalbuphine, on the other hand, is a morphinan semisynthetic agonist-antagonist analgesic, which exerts pharmacological effects through agonist κ-opioid receptors and antagonist μ-opioid receptors with a half-life of 5 h. Although nalbuphine is an agonist antagonist, its analgesic effect is not weakened by μ-opioid receptors antagonism. This may be one of the reasons for the longer analgesic effect of nalbuphine [9, 20]. The expression and distribution of κ-opioid receptors are quite different among different internal organs, and their analgesic effect is mainly mediated by stimulating peripheral κ-opioid receptors. Under the condition of inflammation and pain sensitization, the peripheral analgesic effect of κ-opioid receptor agonists would be further enhanced. Oxycodone is a κ_2-opioid receptor agonist with relatively low affinity to μ-opioid receptors, of which the μ-opioid receptor agonism is not strong. Nalbuphine mainly exerts analgesic effect through agonist κ-opioid receptors [10, 20]. Therefore, we speculate that the longer analgesic effect of nalbuphine may also be related to the stronger selectivity of nalbuphine to κ-opioid receptors. In addition, nalbuphine can also increase the density and activity of opioid κ-opioid receptors, and then improve the analgesic effect [21]. The specific mechanisms of these two scores need a further study. We give opioids in advance before skin incision to directly prevent noxious stimulation impulses from entering the center or directly inhibit the excitability of the central nervous system, reduce, or eliminate the sensitization of the central nervous system caused by adverse stimulation. It plays a preventive analgesic role and further prolongs the time limit of the two drugs.

In the past clinical practice, the dose limitation of opioids is precisely due to its agonism of μ-opioid receptors, which leads to respiratory depression, addiction, itching, nausea, and vomiting. This study also found that the incidence of postoperative adverse reactions in the morphine group was generally higher than that in the other two groups. Previous studies have inconsistent results in comparing the side effects of morphine and oxycodone. Yanagidate and Dohi found that morphine may have a higher incidence of nausea, vomiting, and skin pruritus [22]. However, other studies show that the side effects of the two drugs may not be significantly different [23, 24]. Pedersen et al. pointed out that morphine has lower incidence of adverse reactions and higher safety than oxycodone [25]. The total number of complications and the incidence of skin pruritus in the oxycodone group were significantly lower than those in the morphine group. Although the incidence of other

Table 5: The incidence of postoperative adverse reactions in the three groups.

Group	PONV scores	Pruritus (*n*)	Uroschesis (*n*)	Respiratory depression (*n*)	Dizziness (*n*)
M	2 (1, 2)$^{\#}$	7 (17%)	2 (5%)	1 (2%)	18 (44%)$^{\#}$
N	1 (1, 1)*	0*	0	0	4 (10%)*
O	1 (1, 2)	1 (2%)*	1 (2%)	0	9 (33%)

Values are given as medians and interquartile ranges or number of patients (%). $^{*}P < 0.05$ compared with group M; $^{\#}P < 0.05$ compared with group N.

adverse reactions (such as urinary retention, nausea and vomiting, respiratory depression, and dizziness) decreased, the difference was not statistically significant. However, the adverse reactions (skin pruritus, nausea and vomiting, and dizziness) in the nalbuphine group are significantly decreased than those in the morphine group. It is also consistent with the fact that nalbuphine has lower incidence of adverse reactions and higher safety than morphine mentioned in previous studies [9, 11]. This is because nalbuphine antagonist μ-opioid receptors can prevent or alleviate side effects such as skin pruritus, dizziness, nausea, and vomiting [26], while oxycodone with double μ-opioid receptors and κ-opioid receptors agonism may increase the occurrence of postoperative adverse reactions. Therefore, the nalbuphine group may be more advantageous in the prevention of adverse reactions than the other two groups.

Pain management is an important measure in Enhanced Recovery After Surgery (ERAS). There is a significant correlation between the number and severity of postoperative adverse reactions and the decline of patient-oriented results (such as recovery quality and patient satisfaction) [27]. Previous studies had also shown that the increase of postoperative pain and nausea is significantly related to the decline of immediate postoperative recovery quality [28]. The patient's daily life, rest, wound healing, and length of stay will be affected by severe PONV. As mentioned earlier, nalbuphine has the best analgesic effect among the three groups, and the incidence of adverse reactions such as dizziness, nausea, and vomiting and skin pruritus is reduced. This is consistent with the fact that the nalbuphine group has higher sleep quality, higher pain treatment satisfaction, and shorter length of stay than the other two groups. It indicates that preventive use of nalbuphine for LC patients has higher comfort than the other analgesics, which is more in line with ERAS concept, and may be a better analgesic choice for daytime development of laparoscopic surgery.

Postoperative release of inflammatory cytokines may lead to excessive stress, immunosuppression, pain sensitization, etc., which would aggravate postoperative pain and delay postoperative rehabilitation. This study did not measure cytokines by blood sampling and compared the effects of the different κ-receptor agonists on inhibiting the release of inflammatory cytokines after operation. These will be further explored in subsequent studies.

In conclusion, compared with morphine, postoperative visceral pain will be reduced significantly in prophylactic use of κ-receptor agonists, nalbuphine, and oxycodone in daytime LC. The nalbuphine group has fewer adverse reactions such as dizziness, nausea, and vomiting and has better effect in relieving early postoperative pain, which can improve patients' satisfaction with anesthesia and shorten length of stay. Therefore, it is more recommended to apply to daytime LC surgery.

Data Availability

The data used to support the findings of this study are available from the corresponding author upon request.

Ethical Approval

The clinic study was carried out in accordance with the Declaration of Helsinki (2000) of the World Medical Association and approved by the Ethics Committee of the First Affiliated Hospital of USTC, Division of Life Sciences and Medicine, University of Science and Technology of China, and registered at Chinese Clinical Trial Registry (ChiCTR) with registration number ChiCTR1800014379.

Conflicts of Interest

The authors declare that there is no conflict of interests regarding the publication of this paper.

Authors' Contributions

Chaoliang Tang was involved in the designing and execution of experiments, data analysis, and manuscript writing; Yanhu Xie was involved in the designing of the study and proofreading of the manuscript; Chuanyao Li was involved in the designing and execution of experiments and data analysis; Wanjun Zhou, Jiawu Wang, Chengyun Hu, and Feibiao Dai were all involved in the execution of experiments and data analysis; and Zhetao Zhang was involved in the data analysis and manuscript writing. Wanjun Zhou, Jiawu Wang, and Chengyun Hu contributed equally to this work.

Acknowledgments

This study was supported by grants from the Fundamental Research Funds for the Central Universities (Grant No. WK9110000044). The authors would like to thank the enthusiastic support of the nurses of the PACU at The First Affiliated Hospital of USTC, Division of Life Sciences and Medicine, University of Science and Technology of China.

References

[1] I. Smith, T. Cooke, I. Jackson, and R. Fitzpatrick, "Rising to the challenges of achieving day surgery targets," *Anaesthesia*, vol. 61, no. 12, pp. 1191–1199, 2006.

Hindawi
BioMed Research International
Volume 2021, Article ID 3654660, 14 pages
https://doi.org/10.1155/2021/3654660

Research Article

Target Deconvolution of Fenofibrate in Nonalcoholic Fatty Liver Disease Using Bioinformatics Analysis

Ali Mahmoudi,[1] Alexandra E. Butler,[2] Tannaz Jamialahmadi,[3] and Amirhossein Sahebkar[4,5,6]

[1]*Department of Medical Biotechnology and Nanotechnology, Faculty of Medicine, Mashhad University of Medical Sciences, Iran*
[2]*Royal College of Surgeons in Ireland Bahrain, Adliya, Bahrain*
[3]*Department of Nutrition, Faculty of Medicine, Mashhad University of Medical Sciences, Mashhad, Iran*
[4]*Biotechnology Research Center, Pharmaceutical Technology Institute, Mashhad University of Medical Sciences, Mashhad, Iran*
[5]*Applied Biomedical Research Center, Mashhad University of Medical Sciences, Mashhad, Iran*
[6]*School of Pharmacy, Mashhad University of Medical Sciences, Mashhad, Iran*

Correspondence should be addressed to Amirhossein Sahebkar; amir_saheb2000@yahoo.com

Received 22 October 2021; Revised 12 November 2021; Accepted 14 December 2021; Published 26 December 2021

Academic Editor: Bing Niu

Background. Nonalcoholic fatty liver disease (NAFLD) is a prevalent form of liver damage, affecting ~25% of the global population. NAFLD comprises a spectrum of liver pathologies, from hepatic steatosis to nonalcoholic steatohepatitis (NASH), and may progress to liver fibrosis and cirrhosis. The presence of NAFLD correlates with metabolic disorders such as hyperlipidemia, obesity, blood hypertension, cardiovascular, and insulin resistance. Fenofibrate is an agonist drug for peroxisome proliferator-activated receptor alpha (PPARα), used principally for treatment of hyperlipidemia. However, fenofibrate has recently been investigated in clinical trials for treatment of other metabolic disorders such as diabetes, cardiovascular disease, and NAFLD. The evidence to date indicates that fenofibrate could improve NAFLD. While PPARα is considered to be the main target of fenofibrate, fenofibrate may exert its effect through impact on other genes and pathways thereby alleviating, and possibly reversing, NAFLD. In this study, using bioinformatics tools and gene-drug, gene-diseases databases, we sought to explore possible targets, interactions, and pathways involved in fenofibrate and NAFLD. *Methods*. We first determined significant protein interactions with fenofibrate in the STITCH database with high confidence (0.7). Next, we investigated the identified proteins on curated targets in two databases, including the DisGeNET and DISEASES databases, to determine their association with NAFLD. We finally constructed a Venn diagram for these two collections (curated genes-NAFLD and fenofibrate-STITCH) to uncover possible primary targets of fenofibrate. Then, Gene Ontology (GO) and KEGG were analyzed to detect the significantly involved targets in molecular function, biological process, cellular component, and biological pathways. A P value < 0.01 was considered the cut-off criterion. We also estimated the specificity of targets with NAFLD by investigating them in disease-gene associations (STRING) and EnrichR (DisGeNET). Finally, we verified our findings in the scientific literature. *Results*. We constructed two collections, one with 80 protein-drug interactions and the other with 95 genes associated with NAFLD. Using the Venn diagram, we identified 11 significant targets including LEP, SIRT1, ADIPOQ, PPARA, SREBF1, LDLR, GSTP1, VLDLR, SCARB1, MMP1, and APOC3 and then evaluated their biological pathways. Based on Gene Ontology, most of the targets are involved in lipid metabolism, and KEGG enrichment pathways showed the PPAR signaling pathway, AMPK signaling pathway, and NAFLD as the most significant pathways. The interrogation of those targets on authentic disease databases showed they were more specific to both steatosis and steatohepatitis liver injury than to any other diseases in these databases. Finally, we identified three significant genes, APOC3, PPARA, and SREBF1, that showed robust drug interaction with fenofibrate. *Conclusion*. Fenofibrate may exert its effect directly or indirectly, via modulation of several key targets and pathways, in the treatment of NAFLD.

1. Introduction

In recent decades, nonalcoholic fatty liver (NAFLD) has received greater attention from both healthcare professionals and the general public due to its increasing prevalence. NAFLD comprises a spectrum of liver disorders, from hepatic steatosis to nonalcoholic steatohepatitis (NASH) and, if unchecked, may progress to fibrosis and cirrhosis [1]. The hallmark of NAFLD is accumulation of fat deposits in hepatocytes, the presence of which correlates with metabolic disorders such as hyperlipidemia, obesity, hypertension, cardiovascular disease, and insulin resistance [2, 3]. The global prevalence of NAFLD is approximately ~25%, with the highest prevalence being found in the Middle East [4].

Despite the health burden it imposes, no definitive treatment for NAFLD has yet been determined, though various therapeutic approaches have been proposed. Lifestyle intervention and pharmacological interventions are the mainstays of treatment for patients with NAFLD.

As disruption of essential genes and proteins may lead to fatty liver diseases, identification of these targets enables drug discovery for treatment of NAFLD [5, 6]. Drug treatments include targeting caloric intake and disposal, inflammation, lipotoxicity, and cirrhosis [7–10]. One of the key drug targeting strategies is the modulation of hepatic fat accumulation, including targeting peroxisome proliferator-activator receptors and *de novo* lipogenesis [11]. Fenofibrate is an agonist drug for PPARα and is principally used for treatment of hyperlipidemia in spite of the presence of statins and several newer lipid-lowering agents [12–15]. PPARα is abundantly expressed in the liver and modulates various genes implicated in the catabolism of fatty acids [16]. However, it has recently been investigated in clinical trials for treatment of other metabolic disorders such as diabetes, cardiovascular disease, and NAFLD [17–19]. Additionally, reports suggest that fenofibrate could play a role in antioxidation, tumour apoptosis, anti-inflammation, and antifibrosis plus several other pliotropic effects [20–28]. Evidence from several clinical studies has shown that fenofibrate may provide benefit to patients with NASH/NAFLD [18, 29, 30].

While PPARα is recognized to be the main target of fenofibrate, this drug may exert its effect via other genes and pathways that have not been well characterized to improve and possibly reverse NAFLD/NASH. Clinical investigation is already underway using fenofibrate for the treatment of NAFLD. Using bioinformatics tools and gene-drug, gene-diseases databases, we sought to explore other targets, interactions, and pathways involving fenofibrate and NAFLD. In Figure 1, we illustrate the overall strategy employed in this study.

2. Methods

2.1. Fenofibrate and Target Search. We first searched interactions of fenofibrate in the STITCH database (http://stitch.embl.de/) to explore essential protein targets. STITCH is a platform for diagnosis interaction between chemicals and proteins. Here, we considered the high confidence cut-off (0.700) and limited species only to Homo sapiens.

2.2. Exploring Important NAFLD Genes in DISEASES and DisGeNET Databases. Next, we investigated the protein targets identified in STITCH on curated targets in two databases, the DisGeNET database (https://www.disgenet.org/ (and the DISEASES database (http://diseases.jensenlab.org/), to find their association with NAFLD. DisGeNET is a database that contains a collection of genes associated with specific diseases. That data is integrated from a variety of sources such as expert-curated repositories, the scientific literature and GWAS catalogs. DisGeNET currently covers more than 1,700 genes and 24,000 diseases and traits [31]. For association genes with NAFLD, 1,058 genes were registered in this database. Curated data contain seven primary resources: UNIPROT, ORPHANET, CTD, GENOMICS ENGLAND, CLINGEN, PSYGENET, and CGI. To achieve a curated dataset from DisGeNET, we used a plugin in the cystoscope to construct curated sources targets for NAFLD. DISEASES database is a weekly updated database that comprises diseases and gene relations from different resources, including manually curated literature, text mining, cancer mutation data, and genome-wide association research [32]. We extracted the targets from the available resources, including experiments and manually curated literature associated with NAFLD.

2.3. Venn Diagram to Obtain Important Fenofibrate Interaction Protein Targets in NAFLD. We finally created a Venn diagram (http://bioinformatics.psb.ugent.be/webtools/Venn/) for these two collections (curated genes-NAFLD and fenofibrate-STITCH) to find important targets of fenofibrate beyond the conventionally recognized targets.

2.4. Gene Ontology Pathway Enrichment Analyses for Target Proteins of Fenofibrate. Gene ontology (GO) enrichment is a popular procedure used to interpret genes and stratify them in three major categories, those that contribute to molecular function (MF), biological process, (BP) or cellular component (CC). GO was analyzed for important targets obtained from the Venn diagram using the Gene Ontology resource with the web address: http://geneontology.org. Additionally, KEGG was analyzed using the Enrichr database with the web address: https://maayanlab.cloud/Enrichr/. The KEGG pathway is a comprehensive database that maps pathways according to their metabolic interrelationships. In GO and KEGG analyses, the P value < 0.01 was considered the cut-off criterion. We also analyzed the enrichment pathways using the wikipathways plugin in Cytoscape version 3.8.2. A P value < 0.01 was considered the cut-off criterion. In addition, we estimated the specificity of obtained targets with NAFLD and investigated them in disease-gene associations (STRING) and EnrichR (DisGeNET).

3. Results

3.1. Protein Target Interaction with Fenofibrate in the STITCH Database. Screening fenofibrate in the STITCH database with high confidence (0.7) identified 80 protein

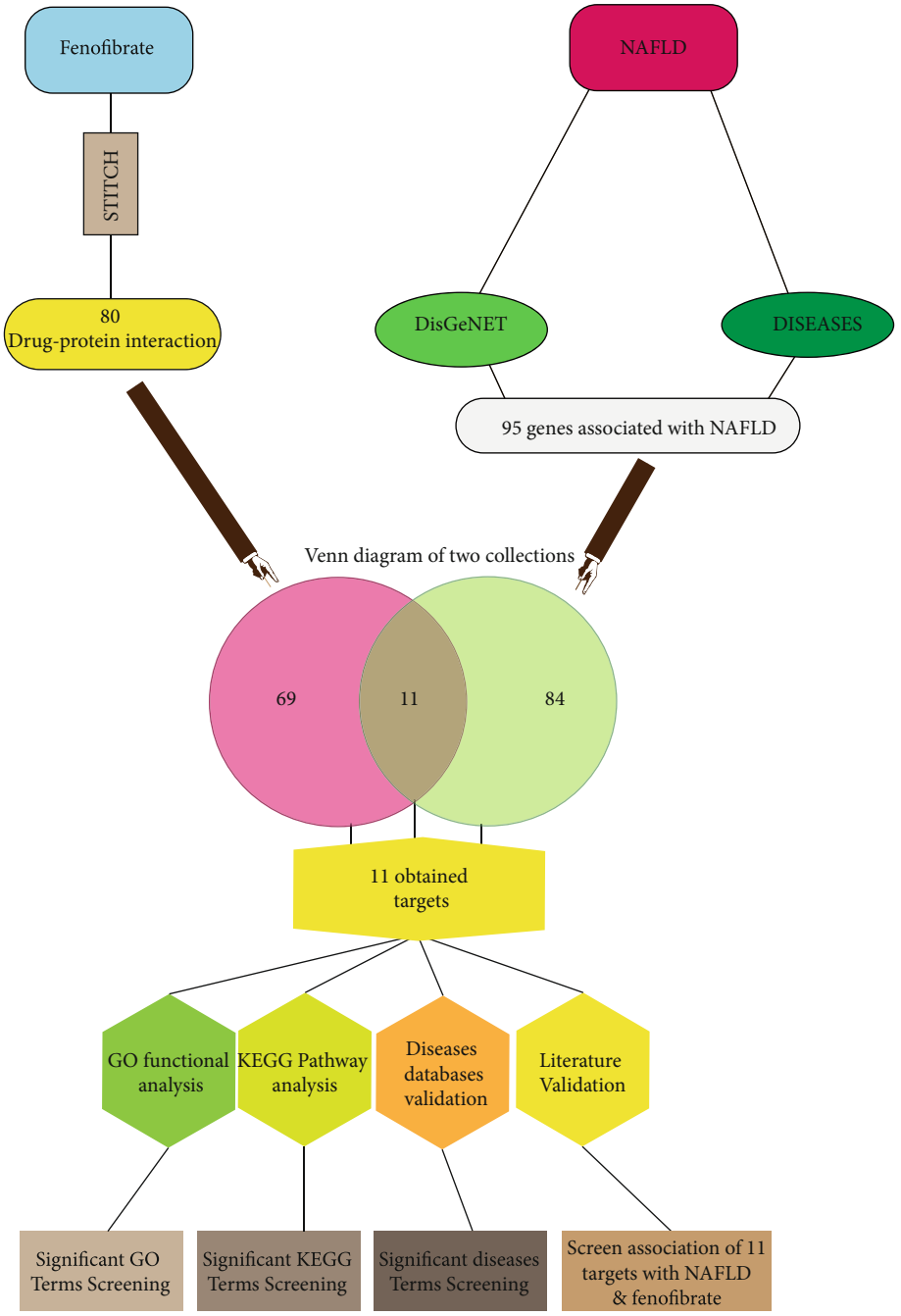

Figure 1: A comprehensive diagram illustrating the investigative strategy undertaken in the present study.

targets. The drug-protein interaction was visualized on Cytoscape (Figure 2(a)).

3.2. Discovering Curated NAFLD Genes. The curated data DisGeNet plugin on Cytoscape and DISEASES database identified 95 genes associated with NAFLD. All the data are visualized with Cytoscape software (Figure 2(a)).

3.3. Overlap of Fenofibrate Targets on the STITCH and Curated NAFLD Genes Visualized Using a Venn Diagram. A Venn diagram of the two created datasets revealed eleven candidates, including SREBF1, SCARB1, LDLR, PPARA, VLDLR, LEP, MMP1, GSTP1, SIRT1, APOC3, and ADIPOQ (Figure 2(b)) that may be directly or indirectly affected by fenofibrate. The scoring based on DisGeNET is shown in Table 1. Based on the database algorithm (genes-disease associate score), five targets (LEP, SIRT1, ADIPOQ, PPARA, and SREBF1) are the most important in NAFLD.

3.4. GO and KEGG Enrichment Analyses of Protein Targets of Fenofibrate. GO analysis of the 11 identified protein targets demonstrated major involvement in the regulation of the lipid biosynthetic process, the lipid metabolic process, and the lipid metabolic process under biological process

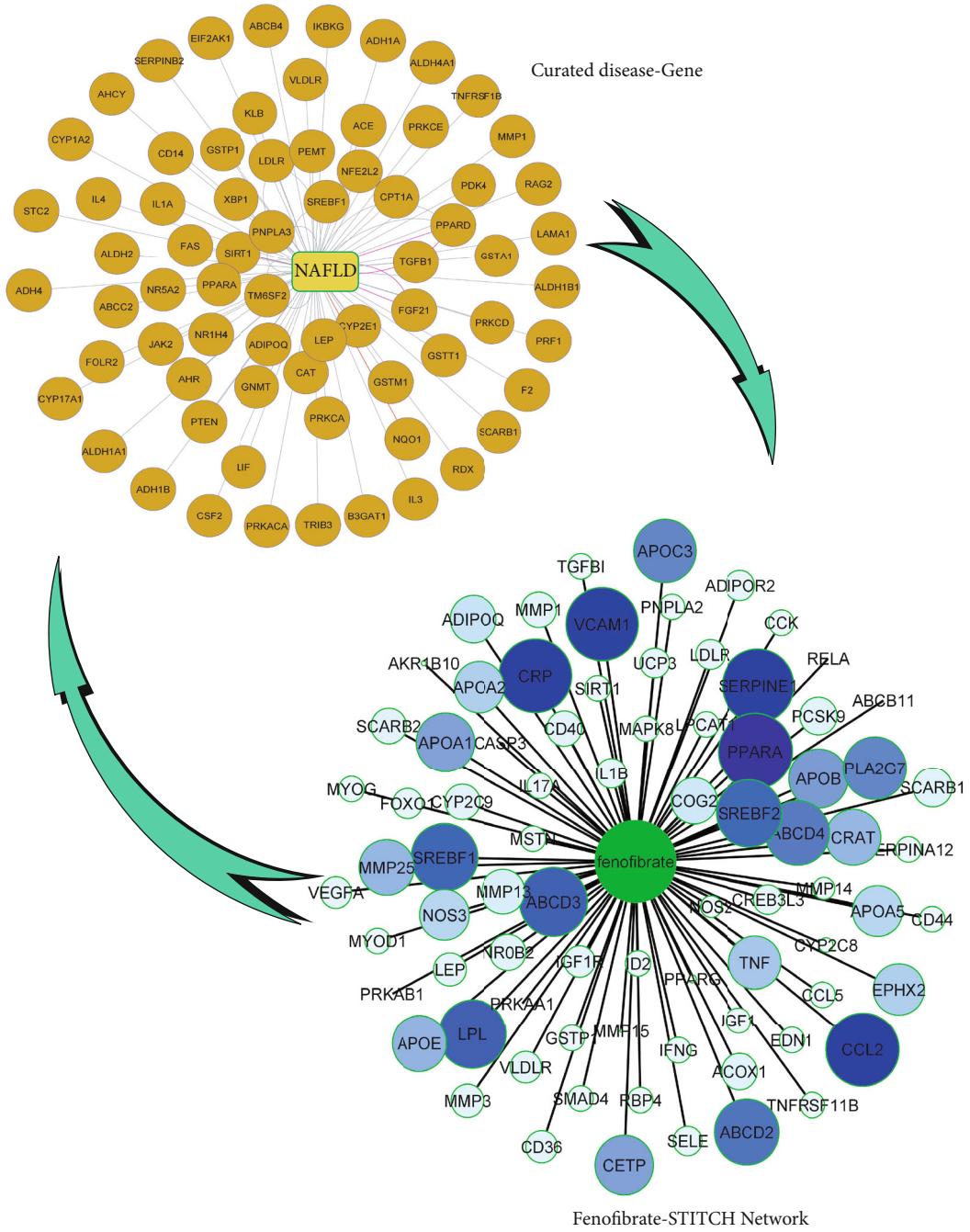

Fenofibrate-STITCH Network

(a)

Figure 2: Continued.

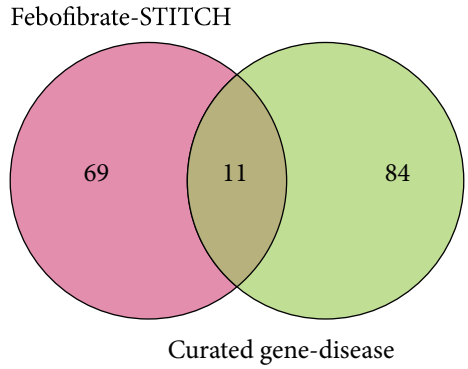

(b)

Figure 2: (a) Curated disease-gene database and fenofibrate-protein interaction visualized with Cytoscape software. (b) Venn diagram of the two datasets comprising curated disease-gene database and fenofibrate-protein interaction.

Table 1: The relationship of genes associated with NAFLD that are targets of fenofibrate (http://www.disgenet.org/).

Gene	UniProt	Gene full name	Protein class	DSI g	Score gda	STITCH score
LEP	P41159	Leptin	Plasma protein	0.349	0.4	0.829
SIRT1	Q96EB6	Sirtuin 1	Epigenetic regulator	0.378	0.4	0.8
ADIPOQ	Q15848	Adiponectin, C1Q, and collagen domain containing	Transporter	0.376	0.4	0.884
PPARA	Q07869	Peroxisome proliferator-activated receptor alpha	Nuclear receptor	0.432	0.4	0.995
SREBF1	P36956	Sterol regulatory element binding transcription factor 1	Plasma protein, transcription factor	0.518	0.38	0.962
LDLR	P01130	Low-density lipoprotein receptor	Plasma protein	0.449	0.37	0.816
GSTP1	P09211	Glutathione S-transferase pi 1	Enzyme	0.383	0.33	0.8
VLDLR	P98155	Very-low-density lipoprotein receptor	Plasma protein	0.558	0.31	0.823
SCARB1	Q8WTV0	Scavenger receptor class B member 1	Receptor	0.559	0.3	0.853
MMP1	P03956	Matrix metallopeptidase 1	Enzyme	0.385	0.3	0.872
APOC3	P02656	Apolipoprotein C3	Plasma protein	0.531	0.1	0.944

Score gda (genes-disease associate score): the gda score is based on supporting evidence that has been collated from different sources as regards the association of genes and diseases. The gda score ranges from 0 to 1, so the closer this range is to 1 indicates a stronger the association between gene and disease. DSI (disease specificity index): a gene may be associated with numerous diseases. This index indicates the specificity of diseases to a particular gene. The index ranges from 0 to 1. A gene with many disease associations has a zero DSI index and, by contrast, a gene associated with just one disease has a DSI of 1. STITCH score: the STITCH score is a confidence indicator of how likely it is that STITCH will correctly evaluate an interaction based on evidence from preceding studies and predictions. Scores range from 0 to 1, with one being the highest confidence level for interaction and 0 being the highest level of uncertainty. A score of 0.5, for example, indicates that the interaction could be 50% false (i.e., a false positive).

(Table 2). This analysis additionally showed that these protein targets were chiefly involved in lipoprotein particle receptor activity, protein-lipid complex binding, and lipoprotein particle binding under the molecular function category. Furthermore, cellular components included the lipoprotein particle, plasma lipoprotein particle, and protein-lipid complex (Table 2).

In KEGG enrichment, we observed several biological pathways. The highest *P* value pathways included the PPAR signaling pathway and the AMPK signaling pathway (Table 3).

The DISEASES database, based on the STRING algorithm, and the DisGeNETdatabase, based on the EnrichR algorithm, revealed the association of 11 of the identified proteins with NAFLD and its advanced form NASH, these diseases ranking in the top three in both databases (Table 4). Therefore, their close relationship with fatty liver disease was confirmed.

In contrast, by setting the cut-off for the STITCH database to 0.9, we identified 22 protein interactions with fenofibrate. PPARA, with a score of 0.995, was the highest ranked protein target in this PPI network. SERPINE1, CCL2, CRP, and VCAM1, with a score of 0.984, were the next most significant protein targets after PPARA in the PPI network. Moreover, protein targets were restricted to three significant genes in the Venn diagram with a preprepared curated disease database. Those three protein targets were SREBF1, APOC3, and PPARA.

We also visualized the degree of connection with high confidence (0.7) of the protein targets to fenofibrate in the NAFLD pathway. The more intense color indicates greater interaction (based on the STITCH score) (Figure 3). The

Table 2: Gene ontology enrichment analysis via Enrichr for the 11 identified genes with the best score interaction with fenofibrate.

(a) Biological process (GO)

Accession	Pathway description	Gene count	P value	FDR
GO:0046890	Regulation of lipid biosynthetic process	7	$7.07E^{-13}$	$1.11E^{-08}$
GO:0019216	Regulation of lipid metabolic process	8	$7.10E^{-13}$	$5.59E^{-09}$
GO:0034381	Llasma lipoprotein particle clearance	5	$1.76E^{-12}$	$9.25E^{-09}$
GO:0006629	Lipid metabolic process	10	$3.39E^{-12}$	$1.33E^{-08}$
GO:1905952	Regulation of lipid storage	5	$6.75E^{-11}$	$2.13E^{-07}$

(b) Molecular function (GO)

	Pathway description	Gene count	P value	FDR
GO:0030228	Lipoprotein particle receptor activity	3	$1.50E^{-07}$	$7.32E^{-04}$
GO:0044877	Protein-lipid complex binding	3	$5.57E^{-07}$	$1.36E^{-03}$
GO:0071813	Lipoprotein particle binding	3	$5.57E^{-07}$	$9.07E^{-04}$
GO:0030229	Very-low-density lipoprotein particle receptor activity	2	$3.88E^{-06}$	$4.75E^{-03}$
GO:0005041	Cargo receptor activity	3	$1.50E^{-07}$	$7.32E^{-04}$

(c) Cellular component (GO)

	Pathway description	Gene count	P value	FDR
GO:1990777	Lipoprotein particle	3	$1.11E^{-06}$	$2.20E^{-03}$
GO:0034358	Plasma lipoprotein particle	3	$1.11E^{-06}$	$1.10E^{-03}$
GO:0032994	Protein-lipid complex	3	$1.38E^{-06}$	$9.16E^{-04}$
GO:0034361	Very-low-density lipoprotein particle	2	$5.95E^{-05}$	$2.96E^{-02}$
GO:0034385	Triglyceride-rich plasma lipoprotein particle	2	$6.51E^{-05}$	$2.59E^{-02}$

FDR (false discovery rate): FDR is a stringent statistical method allowing multiple comparisons while preserving a low false-positivity rate.

Table 3: KEGG pathways for 11 critical genes interact with fenofibrate.

Num.	Pathway name	KEGG Genes	Gene count	P value
1	PPAR signaling pathway	MMP1, ADIPOQ, APOC3, PPARA	4	$5.586e-8$
2	AMPK signaling pathway	SREBF1, LEP, ADIPOQ, SIRT1	4	$3.937e-7$
3	Nonalcoholic fatty liver disease	SREBF1, LEP, ADIPOQ, PPARA	4	0.000001098
4	Cholesterol metabolism	SCARB1, APOC3, LDLR	3	0.000002392
5	Adipocytokine signaling pathway	LEP, ADIPOQ, PPARA	3	0.000006357

pathways are constructed based upon the wikipathway dataset with access number WP4396 using the Cytoscape plugin.

4. Discussion

NAFLD is a highly prevalent chronic liver disease, comprising a spectrum of liver pathologies, from hepatic steatosis to nonalcoholic steatohepatitis (NASH), and may progress to liver fibrosis and cirrhosis. [33]. NAFLD is commonly identified as a multifactorial disease with interaction amongst risk factors and susceptibility genes that play a central role in the development and phenotype of NAFLD [34]. Consequently, identifying those targets and employing suitable therapeutic agents are important steps in improving treatment modalities. Fenofibrate is a drug that is proven for treatment of hyperlipidemia. Additionally, some studies have shown positive results with fenofibrate for the treatment of NAFLD. Fenofibrate has been shown to improve NAFLD in various research studies using cell lines and animal models, as well as in clinical studies in humans. For example, it has been reported that fenofibrate reduces fat content in the liver, reverses hepatic steatosis and fibrosis, and alleviates pathological liver changes in animals with NAFLD [35, 36]. A clinical study revealed that liver

Table 4: Association of protein targets obtained in the interaction of fenofibrate with fatty liver disease in disease databases.

(a) Disease-gene associations (STRING)

Identifier	Primary name	FDR
DOID:0080208	Nonalcoholic fatty liver disease	$4.23e-07$
DOID:11716	Prediabetes syndrome	0.0037
DOID:0080547	Nonalcoholic steatohepatitis	0.0058

(b) DisGeNET (EnrichR)

	Primary name	P value
1	Nonalcoholic fatty liver disease	$1.598e-17$
2	Nonalcoholic steatohepatitis	$6.748e-17$
3	Acute coronary syndrome	$4.157e-16$

enzymes, blood pressure, and body mass index considerably improved, and that treatment with fenofibrate was advantageous due to its beneficial effects in patients with NAFLD [37]. Moreover, an *in vitro* study on steatotic HepaRG cell lines demonstrated the effect of fenofibrate on ameliorating hepatic steatosis [38]. The mechanism that has been widely purported is through fenofibrate's antagonistic effect on PPARα. However, in our study, according to the results of prediction and its interactions directly and indirectly with other targets using bioinformatics software, the mechanism of fenofibrate's mode of action may be broader than an exclusive role of PPARα antagonism. Here, we investigated and analyzed those predictions in other disease-genes, drug-protein databases and biological pathways to understand in greater depth the possible effects of fenofibrate in NAFLD.

In the work presented here, we first searched significant prediction protein interaction with high confidence for fenofibrate. Then, we probed protein interaction in association with fatty liver disease and selected the most relevant targets. In so doing, we identified 11 significant targets, including LEP, SIRT1, ADIPOQ, PPARA, SREBF1, LDLR, GSTP1, VLDLR, SCARB1, MMP1, and APOC3, and we then evaluated their biological pathways. Based on gene ontology, most of the targets were involved in lipid metabolism, and KEGG enrichment pathways showed PPAR signaling pathway, AMPK signaling pathway, and NAFLD as the most significant pathways. The targets we found among the authentic disease databases were more specific to fatty liver disease (steatosis and steatohepatitis) than other diseases in these databases. We finally identified three important significant genes, APOC3, PPARA, and SREBF1, showing robust drug interaction with fenofibrate.

The PPAR signaling pathway is comprised of three receptor subtypes, alpha, gamma, and beta/delta, which are activated by fatty acids and their derivatives. Each subtype is encoded by a separate gene. PPAR-alpha is important for lipid metabolism in the liver and functions in the clearance of circulating and cellular lipids. The function of PPAR-gamma is in the induction of adipocyte differentiation which causes increased uptake of blood glucose. PPAR-beta/delta also contributes to lipid oxidation and cell proliferation [39, 40]. By applying different agonists to this pathway, research has shown a decrease in triglycerides, modulation of circulating glucose, and an elevation in HDL [41–43]. In this way, these agonists could ameliorate NAFLD. The PPAR signaling pathway contains various genes that show enrichment in our study: based on KEGG analysis, enrichment of MMP1, ADIPOQ, APOC3, and PPARA revealed that this pathway shows a robust interaction with fenofibrate (P value: $5.586e-8$). PPAR-alpha is principally present in the liver, while PPAR-gamma is mainly expressed in adipose tissue [44]. Expression of PPAR-gamma has been reported to be significantly increased in the liver of patients and animal models with NAFLD [45–47]. This elevation might be a consequence of the expression of the adipogenic genes that induce lipid accumulation in the liver of these patients and animals with NAFLD [48].

AMPK (adenosine monophosphate-activated protein kinase) has serine/threonine kinase as its catalytic alpha subunit and beta/gamma as its regulatory subunit [49]. This pathway is involved in lipid metabolism and energy sensing, regulating glucose in numerous tissue such as the liver [50]. In our study, enrichment of SREBF1, LEP, ADIPOQ, and SIRT1 genes was found, and the AMPK pathway was significantly (P value: $3.937e-7$) shown to be influenced by fenofibrate. AMPK is regulated by phosphorylation and dephosphorylation via kinases. Activation of AMPK results in an orderly adjustment of energy balance in metabolic processes. It increases fatty acid oxidation and reduces triglyceride and cholesterol production, consequently decreasing fat accumulation [51]. Due to these actions, this pathway is considered to be a therapeutic target for a metabolic disorder such as NAFLD [52, 53]. Activation of AMPK is connected to improvement in liver inflammation and metabolism in NAFLD [54, 55]. Additionally, several studies have demonstrated that AMPK signaling pathways are involved in liver steatosis and steatohepatitis [56]. Research in 2014 indicated that fenofibrate could modulate AMPK signaling and thereby exert its therapeutic effect [57].

Research has demonstrated that lipid accumulation in the liver involves a reduction in fatty acid oxidation and VLDL secretion and upregulation of adipogenic and lipogenic pathways, through which lipoprotein particles deliver fatty acids to the liver [58]. Based on the gene ontology analysis (Table 2), important genes in these pathways operate at the three stages of biological, molecular, and cellular components and could be influenced,with high confidence, by fenofibrate.

PPARA is one of the most important genes in NAFLD and that it interacts with fenofibrate is well established. As shown in our analysis, PPARA had the highest score for interaction with fenofibrate. Moreover, its role in NAFLD was also investigated, again showing a high score. However, our aim was to investigate targets other than PPARA and, hence, here, we discuss the possible influence of other targets with fenofibrate and their role in the pathogenesis of NAFLD.

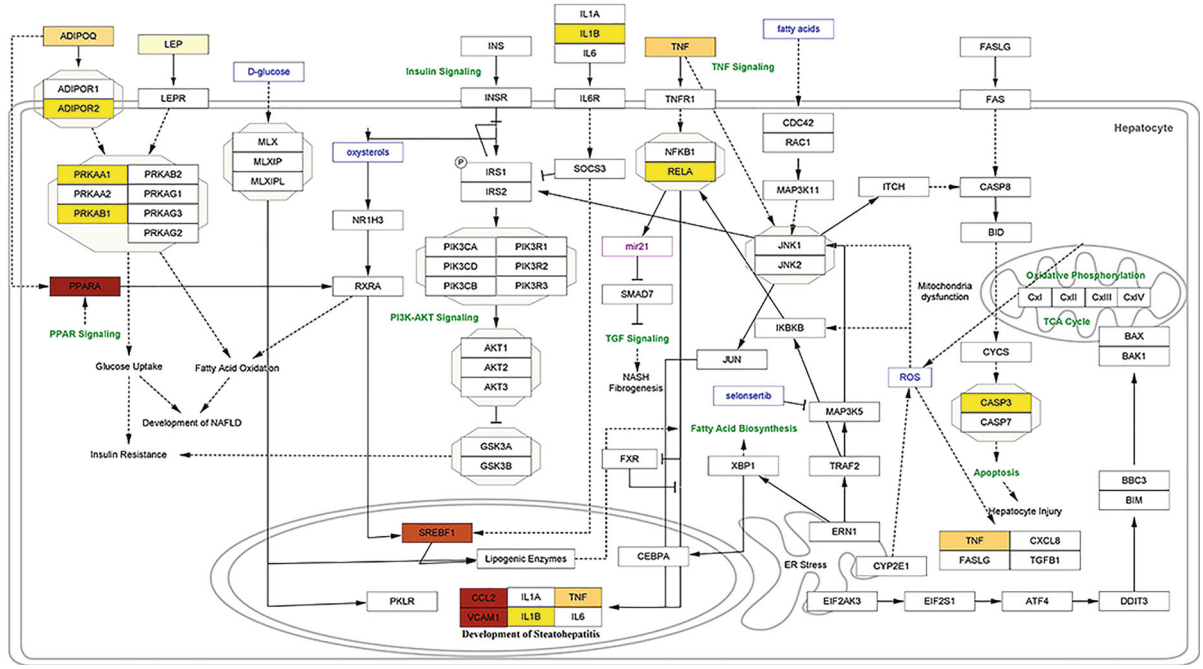

Figure 3: Visualizing protein interactions with fenofibrate in the NAFLD pathway with high confidence (0.7) based on the STITCH score. The intensity of color illustrates the degree of interaction of fenofibrate with the targets.

SREBF1 is an essential factor in modulation of lipogenesis [59]. In models of NAFLD, SREBF1 was downregulated following induction of steatosis [60]. However, in patients with NAFLD, SREBF1 was reported to be significantly higher than the control group [61]. Moreover, enhancing cleavage of SREBF2 was shown to boost lipogenesis [62]. A recent study revealed that SREBF1 is activated through zinc finger and BTB domain-containing 7A (ZBTB7A), which causes lipid accumulation and progression of NAFLD [63]. Numerous studies have reported that SREBF1 is a potential target influencing NAFLD, as evidenced by administration of various interval treatments [64–66]. A recent study in 2021 by Elsayed et al. indicated that SREBF1 elevation is a risk factor in the progression of NAFLD and that, following treatment of NAFLD, this gene was downregulated. Fenofibrate, by direct binding of PPARA to the DR1 motif of SREBF1, may induce SREBF1 expression [67]. A TRANSFAC analysis revealed that after treatment with fenofibrate, MuRF1 -/- genes commonly had a SREBF1 promoter region [68]. Other researchers showed that fenofibrate could promote CREBH products and reduce SREBF1 levels [69]. Of note, in our study (Table 1), SREBF1 had the second highest score for interaction with fenofibrate after PPARA and showed a strong relationship to NAFLD.

ADIPOQ (adiponectin) is an adipose-derived plasma protein that functions in hepatic lipoprotein-lipid metabolism [70]. Several pieces of evidence indicate that diverse polymorphisms in ADIPOQ may increase susceptibility to NAFLD [70, 71]. One study reported that the ADIPOQ methylation rate in rats with NAFLD was higher than in control animals [72]. ADIPOQ in NAFLD patients is a risk factor for progression to liver cancer, and ADIPOQ is significantly decreased in patients with liver metastases [73]. Research has shown that the methylation rate of ADIPOQ in the NAFLD rat model is higher than in controls; further, alteration of the methylation rate pattern of ADIPOQ was hepatoprotective in the NAFLD group [72]. Another study reported that the level of ADIPOQ in serum is lower in NAFLD than controls and was associated with increased liver enzymes and lipid profile changes in patients with NAFLD [74]. Several studies have suggested that fenofibrate may modulate the level of adiponectin in diabetes, cardiomyocyte hypertrophy, and hypertriglyceridemia [75–77]. Fenofibrate caused an increase in serum adiponectin [78]. Fenofibrate may enhance adiponectin expression through modulation of PPAR-alpha expression [76]. Fenofibrate may also promote adiponectin through the AMPK signaling pathway [79]. Other researchers claimed that fenofibrate significantly reduced proinflammatory biomarkers and ameliorated adipocytokines through induction of adiponectin [80]. In our study, ADIPOQ was one of the highest scoring targets in terms of drug interactions with fenofibrate and an association with NAFLD.

LEP (leptin) is a polypeptide hormone that interacts with its receptor lepRb [81]. In a number of studies, the pathogenesis of leptin in NAFLD has been investigated. The level of leptin significantly increased in the serum of patients with NAFLD and in animal models of the disease and possibly normalized with the development of hepatocyte steatosis [81–84]. Leptin may be implicated in steatosis progression via activation of the PI3-K/Akt kinase pathway via OB-R [85, 86]. Numerous studies have reported that fenofibrate affects LEP expression. Previous clinical studies have also shown that fenofibrate affects the level of leptin in patients with dyslipidemia and hypertriglyceridemia and improves insulin sensitivity [80, 87–89]. Furthermore, LEP scored

highly in both the drug interaction and diseases-relation interrogation, scoring 0.829 and 0.4, respectively.

SIRT1 is one of the important genes identified in the pathogenesis of fatty liver disease. SIRT1, a NADPH-dependent deacetylase, has a vital function in cellular processes, including stress response, transcriptional regulation, longevity, and apoptosis [90]. A number of reports implicate miRNAs that target SIRT1 in the pathogenesis of NAFLD [91–93]. SIRT1 is significantly downregulated in NAFLD [94], and interventions aimed at modulating SIRT1 have shown positive effects on NAFLD [95–99]. Fenofibrate can indirectly upregulate SIRT1 and repress hepatocyte apoptosis via SIRT1 and FoxO1 [100, 101]. The upregulation of SIRT1 may be accomplished through AMPK in TNF-α-stimulated adipocytes [102]. Another study showed that fenofibrate promotes SIRT1 expression, causing a reduction in NF-κB activity [103]. Fenofibrate has been shown to affect a reduction in fat deposition and to alleviate inflammation through SIRT1-dependent pathways [104, 105]. In our study, SIRT1 was identified as one of critical gene associations with NAFLD and exhibited a robust interaction with fenofibrate.

Apolipoprotein C3 (APOC3) is a small protein on the surface of lipoprotein particles and has a vital role in regulating triglyceride metabolism. APOC3 has a potent inhibitor effect on lipoprotein lipase [106]. A study by Pavia et al. indicated that overexpression of APOC3 results in pathological features in the liver similar to NAFLD such as inflammation, hepatocyte apoptosis, oxidative stress, and increased liver lipid content [107]. It has been reported that fenofibrate significantly reduces the level of APOC3. In this study, fenofibrate demonstrated a robust interaction with APOC3 based upon the STITCH score (high confidence: 0.944). APOC3 placed eleventh in the curated diseases database (Table 1), indicating it may have a role in the pathogenesis of NAFLD.

MMP (matrix metalloproteinase) is a proteinase that can degrade components of the extracellular matrix and diverse nonmatrix proteins. MMPs have been shown to be involved in the pathogenesis of liver diseases [108]. MMP1 may have a role in the progression of NAFLD to NASH and then to liver fibrosis [109, 110]. Two studies demonstrated that fenofibrate could decrease MMP1 and that it repressed the enzymic actions of MMP2 and MMP9 [57, 111]. MMP1, as demonstrated here, shows significant interaction with fenofibrate (high confidence score based on STITCH of 0.872).

SCARB1 (scavenger receptor class B, type I) is a high-density lipoprotein (HDL) receptor that facilitates uptake of cholesterol (Cho) from HDL to hepatocytes [112, 113]. Recently, it has been suggested that SCARB1 may be associated with NAFLD [114] and several studies suggest that fenofibrate affects SCARB1 [115–117]. Those studies have proposed that fenofibrate may enhance the degradation of SCARB1 in a postendoplasmic reticulum or postplasma membrane compartment [115]. However, it is possible that fenofibrate does not directly inhibit SCARB1 [118]. The posttranscriptional regulation of fenofibrate may be dependent upon PPARα expression [117]. According to our data shown in Table 1, SCARB1 is one of the top predicted targets for fenofibrate interaction, and investigation in the curated database revealed its relationship to NAFLD.

LDLR (low-density apolipoprotein receptor) is a mediator for cholesterol uptake in cells. It plays a crucial function in the clearance of cholesterol by the liver [119]. LDLR deficient rodents have been used to establish models of NAFLD [120, 121]. In those models, elevations in hepatic neutral and hepatic proinflammatory oxylipins were observed [122]. Some patients with NAFLD have been found to have mutations in LDLR genes [123]. Numerous studies have also demonstrated that fenofibrate affects LDLR expression; fenofibrate elevated hepatic LDLR via Akt phosphorylation and maturation of SREBP2 [124]. As shown in Table 1, LDLR was one of the eleven important genes that interacted with fenofibrate and was associated with NAFLD.

VLDLR (very-low-density lipoprotein receptor) has a critical role in modulating serum triglycerides and NAFLD progression [125]. Research on a mouse NAFLD model has demonstrated that antagonism of PPARβ/δ may regulate VLDLR and influence the serum triglyceride level and progression of NAFLD [125]. Studies have indicated that fenofibrate could influence VLDLR, but its mechanism and exact effect are still unclear [126, 127].

GSTP1 (glutathione S transferase Pi 1) is a gene that has a vital role in antioxidant defense through detoxifying foreign substances and inactivating byproducts of oxidative stress [128, 129]. Moreover, several studies published that some polymorphisms of GSTP1 are frequent in patients with NAFLD [130, 131]. The effect of fenofibrate on GSTP1 has not been studied in depth, and the available results are contradictory [132–136]. However, GSTP1 was one of eleven significant targets identified in our study and listed in Table 1.

5. Conclusion

In this study, we investigated the effect of fenofibrate on important targets in NAFLD. Our results indicate that fenofibrate may influence essential genes in NAFLD via an, as yet, undetermined mechanism. Fenofibrate could therefore benefit patients by preventing progression or even reversing severity of NAFLD. According to the results presented here, fenofibrate significantly influences essential biological pathways, including lipid metabolic processes via the PPAR signaling pathway and the AMPK signaling pathway. Notably, those targets have been validated as featuring in the pathogenesis of NAFLD. Consequently, fenofibrate may offer a significant benefit to patients with NAFLD, though further molecular and clinical investigation is required.

Data Availability

Data associated with this study are available from the authors upon a reasonable request.

Conflicts of Interest

The authors declare that they have no conflicts of interest.

References

[1] V. Manne, P. Handa, and K. V. Kowdley, "Pathophysiology of nonalcoholic fatty liver disease/nonalcoholic steatohepatitis," *Clinics in Liver Disease*, vol. 22, no. 1, pp. 23–37, 2018.

[2] F. Mansour-Ghanaei, F. Joukar, S. N. Mobaraki, S. Mavaddati, S. Hassanipour, and M. Sepehrimanesh, "Prevalence of non-alcoholic fatty liver disease in patients with diabetes mellitus, hyperlipidemia, obesity and polycystic ovary syndrome: A cross- sectional study in north of Iran," *Diabetes & Metabolic Syndrome: Clinical Research & Reviews*, vol. 13, no. 2, pp. 1591–1596, 2019.

[3] G. Targher, C. D. Byrne, and H. Tilg, "NAFLD and increased risk of cardiovascular disease: clinical associations, pathophysiological mechanisms and pharmacological implications," *Gut*, vol. 69, no. 9, pp. 1691–1705, 2020.

[4] Z. M. Younossi, A. B. Koenig, D. Abdelatif, Y. Fazel, L. Henry, and M. Wymer, "Global epidemiology of nonalcoholic fatty liver disease-meta-analytic assessment of prevalence, incidence, and outcomes," *Hepatology*, vol. 64, no. 1, pp. 73–84, 2016.

[5] S. Sookoian and C. J. Pirola, "Precision medicine in nonalcoholic fatty liver disease: new therapeutic insights from genetics and systems biology," *Clinical and Molecular Hepatology*, vol. 26, no. 4, pp. 461–475, 2020.

[6] V. Nobili, A. Alisi, L. Valenti, L. Miele, A. E. Feldstein, and N. Alkhouri, "NAFLD in children: new genes, new diagnostic modalities and new drugs," *Nature Reviews Gastroenterology & Hepatology*, vol. 16, no. 9, pp. 517–530, 2019.

[7] B. A. Neuschwander-Tetri, "Therapeutic landscape for NAFLD in 2020," *Gastroenterology*, vol. 158, no. 7, pp. 1984–1998.e3, 2020.

[8] M. Mahjoubin-Tehran, A. De Vincentis, D. P. Mikhailidis et al., "Non-alcoholic fatty liver disease and steatohepatitis: State of the art on effective therapeutics based on the gold standard method for diagnosis," *Molecular Metabolism*, vol. 50, p. 101049, 2021.

[9] M. Bagherniya, V. Nobili, C. N. Blesso, and A. Sahebkar, "Medicinal plants and bioactive natural compounds in the treatment of non-alcoholic fatty liver disease: A clinical review," *Pharmacological Research*, vol. 130, pp. 213–240, 2018.

[10] G. Ranjbar, D. P. Mikhailidis, and A. Sahebkar, "Effects of newer antidiabetic drugs on nonalcoholic fatty liver and steatohepatitis: Think out of the box!," *Metabolism*, vol. 101, p. 154001, 2019.

[11] Y. Sumida and M. Yoneda, "Current and future pharmacological therapies for NAFLD/NASH," *Journal of Gastroenterology*, vol. 53, no. 3, pp. 362–376, 2018.

[12] R. S. Rosenson, "Fenofibrate: treatment of hyperlipidemia and beyond," *Expert Review of Cardiovascular Therapy*, vol. 6, no. 10, pp. 1319–1330, 2008.

[13] M. Ruscica, N. Ferri, R. D. Santos, C. R. Sirtori, and A. Corsini, "Lipid lowering drugs: present status and future developments," *Current Atherosclerosis Reports*, vol. 23, no. 5, p. 17, 2021.

[14] A. Sahebkar and G. F. Watts, "New LDL-cholesterol lowering therapies: pharmacology, clinical trials, and relevance to acute coronary syndromes," *Clinical Therapeutics*, vol. 35, no. 8, pp. 1082–1098, 2013.

[15] A. Sahebkar and G. F. Watts, "New therapies targeting apoB metabolism for high-risk patients with inherited dyslipidaemias: what can the clinician expect?," *Cardiovascular Drugs and Therapy*, vol. 27, no. 6, pp. 559–567, 2013.

[16] S. Kersten and R. Stienstra, "The role and regulation of the peroxisome proliferator activated receptor alpha in human liver," *Biochimie*, vol. 136, pp. 75–84, 2017.

[17] M. L. Morieri, H. S. Shah, J. Sjaarda et al., "PPARAPolymorphism influences the cardiovascular benefit of Fenofibrate in type 2 Diabetes: Findings From ACCORD-Lipid," *Diabetes*, vol. 69, no. 4, pp. 771–783, 2020.

[18] J. Oscarsson, K. Önnerhag, U. Risérus et al., "Effects of free omega-3 carboxylic acids and fenofibrate on liver fat content in patients with hypertriglyceridemia and non-alcoholic fatty liver disease: a double-blind, randomized, placebo-controlled study," *Journal of Clinical Lipidology*, vol. 12, no. 6, pp. 1390–403.e4, 2018.

[19] A. Keech, R. J. Simes, P. Barter, J. Best, R. Scott, and M. R. Taskinen, "Effects of long-term fenofibrate therapy on cardiovascular events in 9795 people with type 2 diabetes mellitus (the FIELD study): randomised controlled trial," *The Lancet*, vol. 366, no. 9500, pp. 1849–1861, 2005.

[20] K. Esenboga, Ö. F. Çiçek, A. A. Oktay, P. Aribal Ayral, and A. Gürlek, "Effect of fenofibrate on serum nitric oxide levels in patients with hypertriglyceridemia," *Advances in clinical and experimental medicine: official organ Wroclaw Medical University*, vol. 28, no. 7, pp. 931–936, 2019.

[21] J. Zhang, Y. Cheng, J. Gu et al., "Fenofibrate increases cardiac autophagy via FGF21/SIRT1 and prevents fibrosis and inflammation in the hearts of Type 1 diabetic mice," *Clinical Science*, vol. 130, no. 8, pp. 625–641, 2016.

[22] J. Sun, Z. Zheng, Q. Chen, Y. Pan, M. Quan, and Y. Dai, "Fenofibrate potentiates chemosensitivity to human breast cancer cells by modulating apoptosis via AKT/NF-κB pathway," *OncoTargets and Therapy*, vol. Volume 12, pp. 773–783, 2019.

[23] M. Botta, M. Audano, A. Sahebkar, C. R. Sirtori, N. Mitro, and M. Ruscica, "PPAR agonists and metabolic syndrome: An established role?," *International Journal of Molecular Sciences*, vol. 19, no. 4, p. 1197, 2018.

[24] G. Derosa, P. Maffioli, and A. Sahebkar, "Plasma uric acid concentrations are reduced by fenofibrate: a systematic review and meta-analysis of randomized placebo-controlled trials," *Pharmacological Research*, vol. 102, pp. 63–70, 2015.

[25] G. Derosa, A. Sahebkar, and P. Maffioli, "The role of various peroxisome proliferator-activated receptors and their ligands in clinical practice," *Journal of Cellular Physiology*, vol. 233, no. 1, pp. 153–161, 2018.

[26] A. Sahebkar, M. C. Serban, D. P. Mikhailidis et al., "Head-to-head comparison of statins versus fibrates in reducing plasma fibrinogen concentrations: a systematic review and meta-analysis," *Pharmacological Research*, vol. 103, pp. 236–252, 2016.

[27] A. Sahebkar and G. F. Watts, "Role of selective peroxisome proliferator-activated receptor modulators in managing cardiometabolic disease: tale of a roller-coaster," *Diabetes, Obesity and Metabolism*, vol. 16, no. 9, pp. 780–792, 2014.

[28] H. Yaribeygi, M. T. Mohammadi, R. Rezaee, and A. Sahebkar, "Fenofibrate improves renal function by amelioration of NOX-4, IL-18, and p53 expression in an experimental model of diabetic nephropathy," *Journal of Cellular Biochemistry*, vol. 119, no. 9, pp. 7458–7469, 2018.

[29] S. M. El-Haggar and T. M. Mostafa, "Comparative clinical study between the effect of fenofibrate alone and its combination with pentoxifylline on biochemical parameters and liver stiffness in patients with non-alcoholic fatty liver disease," *Hepatology International*, vol. 9, no. 3, pp. 471–479, 2015.

[30] C. Fernández-Miranda, M. Pérez-Carreras, F. Colina, G. López-Alonso, C. Vargas, and J. A. Solís-Herruzo, "A pilot trial of fenofibrate for the treatment of non-alcoholic fatty liver disease," *Digestive and Liver Disease*, vol. 40, no. 3, pp. 200–205, 2008.

[31] J. Piñero, J. M. Ramírez-Anguita, J. Saüch-Pitarch et al., "The DisGeNET knowledge platform for disease genomics: 2019 update," *Nucleic Acids Research*, vol. 48, no. D1, pp. D845–Dd55, 2019.

[32] S. Pletscher-Frankild, A. Pallejà, K. Tsafou, J. X. Binder, and L. J. Jensen, "DISEASES: Text mining and data integration of disease-gene associations," *Methods*, vol. 74, pp. 83–89, 2015.

[33] M. C. Sinton, D. C. Hay, and A. J. Drake, "Metabolic control of gene transcription in non-alcoholic fatty liver disease: the role of the epigenome," *Clinical Epigenetics*, vol. 11, no. 1, p. 104, 2019.

[34] M. Eslam, L. Valenti, and S. Romeo, "Genetics and epigenetics of NAFLD and NASH: clinical impact," *Journal of Hepatology*, vol. 68, no. 2, pp. 268–279, 2018.

[35] M. Yan, F. L. Meng, R. J. Lu, X. Q. Jia, and X. C. Zhao, "Therapy effects of fenofibrate on alcoholic fatty liver and drug-induced fatty liver in rats," *Zhonghua Gan Zang Bing Za Zhi*, vol. 11, no. 2, pp. 86–89, 2003.

[36] J. N. van der Veen, S. Lingrell, X. Gao et al., "Fenofibrate, but not ezetimibe, prevents fatty liver disease in mice lacking phosphatidylethanolamine *N* -methyltransferase," *Journal of Lipid Research*, vol. 58, no. 4, pp. 656–667, 2017.

[37] M. Yaghoubi, S. Jafari, B. Sajedi et al., "Comparison of fenofibrate and pioglitazone effects on patients with nonalcoholic fatty liver disease," *European Journal of Gastroenterology & Hepatology*, vol. 29, no. 12, pp. 1385–1388, 2017.

[38] A. Rogue, S. Anthérieu, A. Vluggens et al., "PPAR agonists reduce steatosis in oleic acid-overloaded HepaRG cells," *Toxicology and Applied Pharmacology*, vol. 276, no. 1, pp. 73–81, 2014.

[39] V. Dubois, J. Eeckhoute, P. Lefebvre, and B. Staels, "Distinct but complementary contributions of PPAR isotypes to energy homeostasis," *The Journal of Clinical Investigation*, vol. 127, no. 4, pp. 1202–1214, 2017.

[40] A. Z. Mirza, I. I. Althagafi, and H. Shamshad, "Role of PPAR receptor in different diseases and their ligands: physiological importance and clinical implications," *European Journal of Medicinal Chemistry*, vol. 166, pp. 502–513, 2019.

[41] D. P. Kumar, R. Caffrey, J. Marioneaux et al., "The PPAR α/γ agonist saroglitazar improves insulin resistance and steatohepatitis in a diet induced animal model of nonalcoholic fatty liver disease," *Scientific Reports*, vol. 10, no. 1, p. 9330, 2020.

[42] J. Boeckmans, A. Natale, M. Rombaut et al., "Anti-NASH drug development hitches a lift on PPAR agonism," *Cells*, vol. 9, no. 1, p. 37, 2020.

[43] M. J. Westerouen van Meeteren, J. P. H. Drenth, and E. Tjwa, "Elafibranor: a potential drug for the treatment of nonalcoholic steatohepatitis (NASH)," *Expert Opinion on Investigational Drugs*, vol. 29, no. 2, pp. 117–123, 2020.

[44] K. Motojima, P. Passilly, J. M. Peters, F. J. Gonzalez, and N. Latruffe, "Expression of Putative Fatty Acid Transporter Genes Are Regulated by Peroxisome Proliferator-activated Receptor α and γ Activators in a Tissue- and Inducer-specific Manner," *The Journal of Biological Chemistry*, vol. 273, no. 27, pp. 16710–16714, 1998.

[45] P. Pettinelli and L. A. Videla, "Up-regulation of PPAR-γ mRNA expression in the liver of obese patients: an additional reinforcing lipogenic mechanism to SREBP-1c induction," *The Journal of Clinical Endocrinology and Metabolism*, vol. 96, no. 5, pp. 1424–1430, 2011.

[46] M. Nakamuta, M. Kohjima, S. Morizono et al., "Evaluation of fatty acid metabolism-related gene expression in nonalcoholic fatty liver disease," *International Journal of Molecular Medicine*, vol. 16, no. 4, pp. 631–635, 2005.

[47] J. Skat-Rørdam, D. Højland Ipsen, J. Lykkesfeldt, and P. Tveden-Nyborg, "A role of peroxisome proliferator-activated receptor γ in non-alcoholic fatty liver disease," *Basic & Clinical Pharmacology & Toxicology*, vol. 124, no. 5, pp. 528–537, 2019.

[48] K. H. Liss and B. N. Finck, "PPARs and nonalcoholic fatty liver disease," *Biochimie*, vol. 136, pp. 65–74, 2017.

[49] Z. M. Younossi, L. Henry, H. Bush, and A. Mishra, "Clinical and economic burden of nonalcoholic fatty liver disease and nonalcoholic steatohepatitis," *Clinics in Liver Disease*, vol. 22, no. 1, pp. 1–10, 2018.

[50] E. Buzzetti, M. Pinzani, and E. A. Tsochatzis, "The multiple-hit pathogenesis of non-alcoholic fatty liver disease (NAFLD)," *Metabolism*, vol. 65, no. 8, pp. 1038–1048, 2016.

[51] S. Wu and M. H. Zou, "AMPK, Mitochondrial function, and cardiovascular disease," *International journal of molecular sciences.*, vol. 21, no. 14, p. 4987, 2020.

[52] D. Garcia, K. Hellberg, A. Chaix et al., "Genetic liver-specific AMPK activation protects against diet-induced obesity and NAFLD," *Cell Reports*, vol. 26, no. 1, pp. 192–208.e6, 2019.

[53] W. Liang, A. L. Menke, A. Driessen et al., "Establishment of a general NAFLD scoring system for rodent models and comparison to human liver pathology," *PloS One*, vol. 9, no. 12, article e115922, 2014.

[54] S. Herzig and R. J. Shaw, "AMPK: guardian of metabolism and mitochondrial homeostasis," *Nature Reviews Molecular Cell Biology*, vol. 19, no. 2, pp. 121–135, 2018.

[55] B. K. Smith, K. Marcinko, E. M. Desjardins, J. S. Lally, R. J. Ford, and G. R. Steinberg, "Treatment of nonalcoholic fatty liver disease: role of AMPK," *American Journal of Physiology Endocrinology and Metabolism*, vol. 311, no. 4, pp. E730–E740, 2016.

[56] T. A. Diniz, E. A. de Lima Junior, A. A. Teixeira et al., "Aerobic training improves NAFLD markers and insulin resistance through AMPK- PPAR-α signaling in obese mice," *Life Sciences*, vol. 266, article 118868, 2021.

[57] S. C. Tsai, M. H. Tsai, C. F. Chiu et al., "AMPK-dependent signaling modulates the suppression of invasion and migration by fenofibrate in CAL 27 oral cancer cells through NF-κB pathway," *Environmental Toxicology*, vol. 31, no. 7, pp. 866–876, 2016.

[58] C. E. Foulds, L. S. Treviño, B. York, and C. L. Walker, "Endocrine-disrupting chemicals and fatty liver disease," *Nature Reviews Endocrinology*, vol. 13, no. 8, pp. 445–457, 2017.

[59] J. Han, E. Li, L. Chen et al., "The CREB coactivator CRTC2 controls hepatic lipid metabolism by regulating SREBP1," *Nature*, vol. 524, no. 7564, pp. 243–246, 2015.

[60] N. Ziamajidi, S. Khaghani, G. Hassanzadeh et al., "Amelioration by chicory seed extract of diabetes- and oleic acid-induced non- alcoholic fatty liver disease (NAFLD)/non-alcoholic steatohepatitis (NASH) via modulation of PPARα and SREBP-1," *Food and Chemical Toxicology: an international journal published for the British Industrial Biological Research Association*, vol. 58, pp. 198–209, 2013.

[61] G. Fan, T. Shi, and S. Xiao, "Clinical investigation of relationship between SIRT3 and hepatocyte steatosis in nonalcoholic fatty liver disease," *Chinese Journal of Gastroenterology*, vol. 14, no. 5, pp. 261–265, 2009.

[62] Y. R. Kim, E. J. Lee, K. O. Shin et al., "Hepatic triglyceride accumulation via endoplasmic reticulum stress-induced SREBP-1 activation is regulated by ceramide synthases," *Experimental & Molecular Medicine*, vol. 51, no. 11, pp. 1–16, 2019.

[63] J. P. Zhou, Y. D. Ren, Q. Y. Xu et al., "Obesity-induced upregulation of ZBTB7A promotes lipid accumulation through SREBP1," *BioMed Research International*, vol. 2020, Article ID 4087928, 13 pages, 2020.

[64] S. O. Lee, Y. Xu, H. Han et al., "Fermented rhus verniciflua stokes extract alleviates nonalcoholic fatty liver through the AMPK/SREBP1/PCSK9 pathway in HFD-induced nonalcoholic fatty liver animal model," *Applied Sciences*, vol. 10, no. 19, p. 6833, 2020.

[65] J. Hu, W. Hong, K. N. Yao, X. H. Zhu, Z. Y. Chen, and L. Ye, "Ursodeoxycholic acid ameliorates hepatic lipid metabolism in LO2 cells by regulating the AKT/mTOR/SREBP-1 signaling pathway," *World Journal of Gastroenterology*, vol. 25, no. 12, pp. 1492–1501, 2019.

[66] G. L. Wang, Y. C. Fu, W. C. Xu, Y. Q. Feng, S. R. Fang, and X. H. Zhou, "Resveratrol inhibits the expression of SREBP1 in cell model of steatosis via Sirt1-FOXO1 signaling pathway," *Biochemical and Biophysical Research Communications*, vol. 380, no. 3, pp. 644–649, 2009.

[67] F. Yan, Q. Wang, C. Xu et al., "Peroxisome proliferator-activated receptor α activation induces hepatic steatosis, suggesting an adverse effect," *PLoS One*, vol. 9, no. 6, 2014.

[68] T. L. Parry, G. Desai, J. C. Schisler et al., "Fenofibrate unexpectedly induces cardiac hypertrophy in mice lacking MuRF1," *Cardiovascular Pathology: the official journal of the Society for Cardiovascular Pathology*, vol. 25, no. 2, pp. 127–140, 2016.

[69] A. K. Min, J. Y. Jeong, Y. Go et al., "cAMP response element binding protein H mediates fenofibrate-induced suppression of hepatic lipogenesis," *Diabetologia*, vol. 56, no. 2, pp. 412–422, 2013.

[70] B. F. Wang, Y. Wang, R. Ao, J. Tong, and B. Y. Wang, "AdipoQT45 G and G276 T polymorphisms and susceptibility to nonalcoholic fatty liver disease among Asian populations: a meta-analysis and meta-regression," *Journal of Clinical Laboratory Analysis*, vol. 30, no. 1, pp. 47–57, 2016.

[71] M. Liu, S. Liu, M. Shang et al., "Association between ADIPOQ G276T and C11377G polymorphisms and the risk of non-alcoholic fatty liver disease: An updated meta-analysis," *Molecular Genetics & Genomic Medicine*, vol. 7, no. 5, article e624, 2019.

[72] W. J. Chen, B. Cai, H. T. Chen et al., "The role ofADIPOQ-methylation in curcumin-administrated experimental nonalcoholic fatty liver disease," *Journal of Digestive Diseases*, vol. 17, no. 12, pp. 829–836, 2016.

[73] R. Divella, A. Daniele, R. A. F. F. A. E. L. E. de Luca et al., "Synergism of adipocytokine profile andADIPOQ/TNF-αPolymorphisms in NAFLD-associated mets predict colorectal liver metastases outgrowth," *Cancer Genomics & Proteomics*, vol. 16, no. 6, pp. 519–530, 2019.

[74] A. A. Mahmoud, H. M. Moghazy, L. M. Yousef, and A. N. Mohammad, "Adiponectin rs2241766 and rs266729 gene polymorphisms in non-alcoholic fatty liver disease," *Gene Reports*, vol. 15, p. 100381, 2019.

[75] K. K. Koh, M. J. Quon, K. C. Shin et al., "Significant differential effects of omega-3 fatty acids and fenofibrate in patients with hypertriglyceridemia," *Atherosclerosis*, vol. 220, no. 2, pp. 537–544, 2012.

[76] H. L. Jen, W. H. Yin, J. W. Chen, and S. J. Lin, "Endothelin-1-induced cell hypertrophy in cardiomyocytes is improved by fenofibrate: possible roles of adiponectin," *Journal of Atherosclerosis and Thrombosis*, vol. 24, no. 5, pp. 508–517, 2017.

[77] Y. J. Hsu, L. C. Wang, W. S. Yang, C. M. Yang, and C. H. Yang, "Effects of Fenofibrate on Adiponectin Expression in Retinas of Streptozotocin- Induced Diabetic Rats," *Journal of Diabetes Research*, vol. 2014, Article ID 540326, 14 pages, 2014.

[78] K. Oki, J. Koide, S. Nakanishi, R. Nakashima, and K. Yamane, "Fenofibrate increases high molecular weight adiponectin in subjects with hypertriglyceridemia," *Endocrine Journal*, vol. 54, no. 3, pp. 431–435, 2007.

[79] P. Li, R. Shibata, S. Maruyama et al., "Fenofibrate promotes ischemia-induced revascularization through the adiponectin-dependent pathway," *American Journal of Physiology. Endocrinology and Metabolism*, vol. 299, no. 4, pp. E560–E566, 2010.

[80] K. K. Koh, M. J. Quon, S. Lim et al., "Effects of fenofibrate therapy on circulating adipocytokines in patients with primary hypertriglyceridemia," *Atherosclerosis*, vol. 214, no. 1, pp. 144–147, 2011.

[81] M. Swellam and N. Hamdy, "Association of nonalcoholic fatty liver disease with a single nucleotide polymorphism on the gene encoding leptin receptor," *IUBMB Life*, vol. 64, no. 2, pp. 180–186, 2012.

[82] Q. Zhang, J. Wang, F. Huang, Y. Yao, and L. Xu, "Leptin induces NAFLD progression through infiltrated CD8+ T lymphocytes mediating pyroptotic-like cell death of hepatocytes and macrophages," *Digestive and Liver Disease*, vol. 53, no. 5, pp. 598–605, 2021.

[83] V. Marques, M. B. Afonso, N. Bierig et al., "Adiponectin, leptin, and IGF-1 are useful diagnostic and stratification biomarkers of NAFLD," *Frontiers in Medicine*, vol. 8, 2021.

[84] L. Rotundo, A. Persaud, M. Feurdean, S. Ahlawat, and H. S. Kim, "The association of leptin with severity of non-alcoholic fatty liver disease: a population-based study," *Clinical and Molecular Hepatology*, vol. 24, no. 4, pp. 392–401, 2018.

[85] D. Xu, X. D. Huang, H. S. Luo, J. P. Yuan, H. Zhang, and J. Wu, "Impaired activation of phosphatidylinositol 3-kinase by leptin in NAFLD: a novel mechanism of hepatic leptin resistance," *World Chinese Journal of Digestology*, vol. 20, no. 32, pp. 3095–3100, 2012.

[86] D. Xu, X. D. Huang, J. P. Yuan et al., "Impaired activation of phosphatidylinositol 3-kinase by leptin is a novel mechanism

of hepatic leptin resistance in NAFLD," *Hepato-Gastroenterology*, vol. 58, no. 110-111, pp. 1703–1707, 2011.

[87] L. Buldak, A. Dulawa-Buldak, K. Labuzek, and B. Okopien, "Effects of 90-day hypolipidemic treatment on insulin resistance, adipokines and proinflammatory cytokines in patients with mixed hyperlipidemia and impaired fasting glucose," *International Journal of Clinical Pharmacology and Therapeutics*, vol. 50, no. 11, pp. 805–813, 2012.

[88] M. Florentin, E. N. Liberopoulos, C. C. Tellis, C. S. Derdemezis, M. Elisaf, and A. Tselepis, "Effects of rimonabant, as monotherapy and in combination with fenofibrate or ezetimibe, on plasma adipokine levels: a pilot study," *Angiology*, vol. 61, no. 4, pp. 365–371, 2010.

[89] T. Damci, S. Tatliagac, Z. Osar, and K. Ilkova, "Fenofibrate treatment is associated with better glycemic control and lower serum leptin and insulin levels in type 2 diabetic patients with hypertriglyceridemia," *European Journal of Internal Medicine*, vol. 14, no. 6, pp. 357–360, 2003.

[90] H. S. Ghosh, J. V. Spencer, B. Ng, M. W. McBurney, and P. D. Robbins, "Sirt1 interacts with transducin-like enhancer of split-1 to inhibit nuclear factor κB-mediated transcription," *The Biochemical Journal*, vol. 408, no. 1, pp. 105–111, 2007.

[91] L. Wang, M. Sun, Y. Cao et al., "miR-34a regulates lipid metabolism by targeting SIRT1 in non-alcoholic fatty liver disease with iron overload," *Archives of Biochemistry and Biophysics*, vol. 695, p. 108642, 2020.

[92] Y. Wang, K. Zhu, W. Yu et al., "MiR-181b regulates steatosis in nonalcoholic fatty liver disease via targeting SIRT1," *Biochemical and Biophysical Research Communications*, vol. 493, no. 1, pp. 227–232, 2017.

[93] J. K. Long, W. Dai, Y. W. Zheng, and S. P. Zhao, "MiR-122 promotes hepatic lipogenesis via inhibiting the LKB1/AMPK pathway by targeting Sirt1 in non-alcoholic fatty liver disease," *Molecular Medicine*, vol. 25, no. 1, 2019.

[94] X. Q. Deng, L. L. Chen, and N. X. Li, "The expression of SIRT1 in nonalcoholic fatty liver disease induced by high-fat diet in rats," *Liver International*, vol. 27, no. 5, pp. 708–715, 2007.

[95] Y. Zhu, R. Liu, Z. Shen, and G. Cai, "Combination of luteolin and lycopene effectively protect against the "two-hit" in NAFLD through Sirt1/AMPK signal pathway," *Life Sciences*, vol. 256, article 117990, 2020.

[96] H. Nikroo, S. R. A. Hosseini, M. Fathi, M. A. Sardar, and M. Khazaei, "The effect of aerobic, resistance, and combined training on PPAR-α, SIRT1 gene expression, and insulin resistance in high-fat diet-induced NAFLD male rats," *Physiology & Behavior*, vol. 227, p. 113149, 2020.

[97] S. Li, Q. Qian, N. Ying et al., "Activation of the AMPK-SIRT1 pathway contributes to protective effects of Salvianolic acid a against lipotoxicity in hepatocytes and NAFLD in mice," *Frontiers in Pharmacology*, vol. 11, 2020.

[98] C. C. Chyau, H. F. Wang, W. J. Zhang et al., "Antrodan alleviates high-fat and high-fructose diet-induced fatty liver disease in C57BL/6 mice model via AMPK/Sirt1/SREBP-1c/PPARγ pathway," *International Journal of Molecular Sciences*, vol. 21, no. 1, p. 360, 2020.

[99] H. Yao, X. Tao, L. Xu et al., "Dioscin alleviates non-alcoholic fatty liver disease through adjusting lipid metabolism *via* SIRT1/AMPK signaling pathway," *Pharmacological Research*, vol. 131, pp. 51–60, 2018.

[100] W. Wang, L. Bai, H. Qiao et al., "The protective effect of fenofibrate against TNF-α-induced CD40 expression through SIRT1-mediated deacetylation of NF-κB in endothelial cells," *Inflammation*, vol. 37, no. 1, pp. 177–185, 2014.

[101] W. R. Wang, E. Q. Liu, J. Y. Zhang et al., "Activation of PPAR alpha by fenofibrate inhibits apoptosis in vascular adventitial fibroblasts partly through SIRT1-mediated deacetylation of FoxO1," *Experimental Cell Research*, vol. 338, no. 1, pp. 54–63, 2015.

[102] W. Wang, Q. Lin, R. Lin et al., "PPARα agonist fenofibrate attenuates TNF-α-induced CD40 expression in 3T3-L1 adipocytes via the SIRT1-dependent signaling pathway," *Experimental Cell Research*, vol. 319, no. 10, pp. 1523–1533, 2013.

[103] N. Chen, K. Jiang, and G. G. Yan, "Effect of fenofibrate on diabetic retinopathy in rats via SIRT1/NF-κB signaling pathway," *European Review for Medical and Pharmacological Sciences*, vol. 23, no. 19, pp. 8630–8636, 2019.

[104] S. Zhao, J. Li, N. Wang et al., "Fenofibrate suppresses cellular metabolic memory of high glucose in diabetic retinopathy via a sirtuin 1-dependent signalling pathway," *Molecular Medicine Reports*, vol. 12, no. 4, pp. 6112–6118, 2015.

[105] M. Jin, T. Zhu, D. R. Tocher et al., "Dietary fenofibrate attenuated high-fat-diet-induced lipid accumulation and inflammation response partly through regulation of *ppar α* and *sirt1* in juvenile black seabream (*Acanthopagrus schlegelii*)," *Developmental and Comparative Immunology*, vol. 109, p. 103691, 2020.

[106] E. Christopoulou, V. Tsimihodimos, T. Filippatos, and M. Elisaf, "Apolipoprotein CIII and diabetes. Is there a link?," *Diabetes/Metabolism Research and Reviews*, vol. 35, no. 3, article e3118, 2019.

[107] A. A. Paiva, H. F. Raposo, A. C. Wanschel, T. R. Nardelli, and H. C. Oliveira, "Apolipoprotein CIII overexpression-induced hypertriglyceridemia increases nonalcoholic fatty liver disease in association with inflammation and cell death," *Oxidative Medicine and Cellular Longevity*, vol. 2017, Article ID 1838679, 18 pages, 2017.

[108] A. Naim, Q. Pan, and M. S. Baig, "Matrix metalloproteinases (MMPs) in liver diseases," *Journal of Clinical and Experimental Hepatology*, vol. 7, no. 4, pp. 367–372, 2017.

[109] E. H. Meng, J. M. Zhao, S. S. Wang et al., "Expression of matrix metalloproteinases in liver tissues with nonalcoholic steatohepatitis," *World Chinese Journal of Digestology*, vol. 10, no. 11, pp. 1257–1260, 2002.

[110] A. A. Mahmoud, A. S. Bakir, and S. S. Shabana, "Serum TGF-β, serum MMP-1, and HOMA-IR as non-invasive predictors of fibrosis in Egyptian patients with NAFLD," *Saudi Journal of Gastroenterology: official journal of the Saudi Gastroenterology Association*, vol. 18, no. 5, pp. 327–333, 2012.

[111] K. S. Kim, D. H. Oh, H. M. Choi et al., "Pyrrolidine dithiocarbamate, a NF-κB inhibitor, upregulates MMP-1 and MMP-13 in IL-1β-stimulated rheumatoid arthritis fibroblast-like synoviocytes," *European Journal of Pharmacology*, vol. 613, no. 1-3, pp. 167–175, 2009.

[112] X. Zhang and C. Fernández-Hernando, "The Janus-faced role of SR-BI in atherosclerosis," *Nature Metabolism*, vol. 1, no. 6, pp. 586-587, 2019.

[113] A. Helgadottir, P. Sulem, G. Thorgeirsson et al., "Rare SCARB1 mutations associate with high-density lipoprotein cholesterol but not with coronary artery disease," *European Heart Journal*, vol. 39, no. 23, pp. 2172–2178, 2018.

[114] M. Tan, J. Ye, M. Zhao, X. Ke, K. Huang, and H. Liu, "Recent developments in the regulation of cholesterol transport by natural molecules," *Phytotherapy Research*, vol. 35, no. 10, pp. 5623–5633, 2021.

[115] D. Lan and D. L. Silver, "Fenofibrate Induces a Novel Degradation Pathway for Scavenger Receptor B-I Independent of PDZK1," *The Journal of Biological Chemistry*, vol. 280, no. 24, pp. 23390–23396, 2005.

[116] U. Panzenboeck, I. Kratzer, A. Sovic et al., "Regulatory effects of synthetic liver X receptor- and peroxisome-proliferator activated receptor agonists on sterol transport pathways in polarized cerebrovascular endothelial cells," *The International Journal of Biochemistry & Cell Biology*, vol. 38, no. 8, pp. 1314–1329, 2006.

[117] P. Mardones, A. Pilon, M. Bouly et al., "Fibrates Downregulate Hepatic Scavenger Receptor Class B Type I Protein Expression in Mice," *The Journal of Biological Chemistry*, vol. 278, no. 10, pp. 7884–7890, 2003.

[118] T. J. Nieland, J. T. Shaw, F. A. Jaipuri et al., "Influence of HDL-cholesterol-elevating drugs on the in vitro activity of the HDL receptor SR-BI," *Journal of Lipid Research*, vol. 48, no. 8, pp. 1832–1845, 2007.

[119] M. Floeth, S. Elges, J. Gerss et al., "Low-density lipoprotein receptor (LDLR) is an independent adverse prognostic factor in acute myeloid leukaemia," *British Journal of Haematology*, vol. 192, no. 3, pp. 494–503, 2021.

[120] L. Álvarez-Amor, A. L. Sierra, A. Cárdenas et al., "Extra virgin olive oil improved body weight and insulin sensitivity in high fat diet-induced obese LDLr−/−.Leiden mice without attenuation of steatohepatitis," *Scientific Reports*, vol. 11, no. 1, 2021.

[121] M. H. Schoemaker, R. Kleemann, M. C. Morrison et al., "A casein hydrolysate based formulation attenuates obesity and associated nonalcoholic fatty liver disease and atherosclerosis in LDLr-/-.Leiden mice," *PLoS One*, vol. 12, no. 7, article e0180648, 2017.

[122] L. Li, G. F. Zhang, K. Lee et al., "A Western diet induced NAFLD in $LDLR^{-/-}$ mice is associated with reduced hepatic glutathione synthesis," *Free Radical Biology & Medicine*, vol. 96, pp. 13–21, 2016.

[123] E. Vilar-Gomez, S. Gawrieh, T. Liang, A. D. McIntyre, R. A. Hegele, and N. Chalasani, "Interrogation of selected genes influencing serum LDL-cholesterol levels in patients with well characterized NAFLD," *Journal of Clinical Lipidology*, vol. 15, no. 2, pp. 275–291, 2021.

[124] Z. Huang, X. Zhou, A. C. Nicholson, A. M. Gotto Jr., D. P. Hajjar, and J. Han, "Activation of peroxisome proliferator-activated receptor-α in mice induces expression of the hepatic low-density lipoprotein receptor," *British Journal of Pharmacology*, vol. 155, no. 4, pp. 596–605, 2008.

[125] M. Zarei, E. Barroso, X. Palomer et al., "Pharmacological PPARβ/δ activation upregulates VLDLR in hepatocytes," *Clínica e Investigación en Arteriosclerosis (English Edition)*, vol. 31, no. 3, pp. 111–118, 2019.

[126] S. Raza-Iqbal, T. Tanaka, M. Anai et al., "Transcriptome analysis of K-877 (a novel selective PPARα modulator (SPPARMα))-regulated genes in primary human hepatocytes and the mouse liver," *Journal of Atherosclerosis and Thrombosis*, vol. 22, no. 8, pp. 754–772, 2015.

[127] Y. Gao, W. Shen, B. Lu, Q. Zhang, Y. Hu, and Y. Chen, "Upregulation of hepatic VLDLR via PPARα is required for the triglyceride- lowering effect of fenofibrate," *Journal of Lipid Research*, vol. 55, no. 8, pp. 1622–1633, 2014.

[128] Q. Qadri, A. S. Sameer, Z. A. Shah et al., "Genetic polymorphism of the glutathione-S-transferase P1 gene (GSTP1) and susceptibility to prostate cancer in the Kashmiri population," *Genetics and Molecular Research*, vol. 10, no. 4, pp. 3038–3045, 2011.

[129] M. Hori, K. Oniki, T. Nakagawa et al., "Association between combinations of glutathione-S-transferaseM1,T1andP1genotypes and non-alcoholic fatty liver disease," *Liver International*, vol. 29, no. 2, pp. 164–168, 2009.

[130] V. P. Prysyazhnyuk, Z. I. Rossokha, and N. G. Gorovenko, "Variation in particular biochemical indicators, cytokine and adipokine profiles of the blood, and the structural and functional parameters of the liver in patients with nonalcoholic fatty liver disease and different genotypes by the polymorphic locus A313G of the GSTP1 gene," *Cytology and Genetics*, vol. 51, no. 6, pp. 455–461, 2017.

[131] M. Hashemi, E. Eskandari-Nasab, A. Fazaeli et al., "Association of genetic polymorphisms of glutathione-s-transferase genes (GSTT1,GSTM1, andGSTP1) and susceptibility to nonalcoholic fatty liver disease in Zahedan, Southeast Iran," *DNA and Cell Biology*, vol. 31, no. 5, pp. 672–677, 2012.

[132] J. Nishimura, Y. Dewa, T. Okamura et al., "Possible involvement of oxidative stress in fenofibrate-induced hepatocarcinogenesis in rats," *Archives of Toxicology*, vol. 82, no. 9, pp. 641–654, 2008.

[133] J. Nishimura, Y. Dewa, T. Okamura et al., "Role of Nrf2 and oxidative stress on fenofibrate-induced hepatocarcinogenesis in rats," *Toxicological Sciences*, vol. 106, no. 2, pp. 339–349, 2008.

[134] A. Nagyova, K. Raslova, Z. Kovacikova, V. Mongiellova, and E. Ginter, "Glutathione and glutathione-dependent enzymes in patients with hyperlipoproteinaemia treated with micronized fenofibrate," *Klinicka Biochemie a Metabolismus*, vol. 4, no. 4, pp. 242–244, 1996.

[135] M. Roques, D. Bagrel, J. Magdalou, and G. Siest, "Expression of arylhydrocarbon hydroxylase, epoxide hydrolases, glutathione S-transferase and UDP-glucuronosyltransferases in H5-6 hepatoma cells," *General Pharmacology: The Vascular System*, vol. 22, no. 4, pp. 677–684, 1991.

[136] A. Foliot, D. Touchard, and L. Mallet, "Inhibition of liver glutathione *S* -transferase activity in rats by hypolipidemic drugs related or unrelated to clofibrate," *Biochemical Pharmacology*, vol. 35, no. 10, pp. 1685–1690, 1986.

Hindawi
BioMed Research International
Volume 2021, Article ID 4989297, 11 pages
https://doi.org/10.1155/2021/4989297

Research Article

Deep Learning for Accurate Segmentation of Venous Thrombus from Black-Blood Magnetic Resonance Images: A Multicenter Study

Chuanqi Sun,[1] **Xiangyu Xiong**,[1] **Tianjing Zhang**,[2] **Xiuhong Guan**,[1] **Huan Mao**,[1] **Jing Yang**,[1] **Xiaoyong Zhang**,[2] **Yi Sun**,[3] **Hao Chen**,[1,4] **and Guoxi Xie**[1]

[1]*Department of Biomedical Engineering, The Sixth Affiliated Hospital, Guangzhou Medical University, Guangzhou, China*
[2]*Philips Healthcare, Guangzhou, China*
[3]*Siemens Healthcare, Shanghai, China*
[4]*Jiangsu JITRI Sioux Technologies Co., Ltd., Suzhou, China*

Correspondence should be addressed to Hao Chen; hao.chen.gd@gmail.com and Guoxi Xie; guoxixie@163.com

Received 9 September 2021; Revised 1 November 2021; Accepted 9 November 2021; Published 14 December 2021

Academic Editor: Jianxin Li

Objective. Deep vein thrombosis (DVT) is the third-largest cardiovascular disease, and accurate segmentation of venous thrombus from the black-blood magnetic resonance (MR) images can provide additional information for personalized DVT treatment planning. Therefore, a deep learning network is proposed to automatically segment venous thrombus with high accuracy and reliability. *Methods*. In order to train, test, and external test the developed network, total images of 110 subjects are obtained from three different centers with two different black-blood MR techniques (i.e., DANTE-SPACE and DANTE-FLASH). Two experienced radiologists manually contoured each venous thrombus, followed by reediting, to create the ground truth. 5-fold cross-validation strategy is applied for training and testing. The segmentation performance is measured on pixel and vessel segment levels. For the pixel level, the dice similarity coefficient (DSC), average Hausdorff distance (AHD), and absolute volume difference (AVD) of segmented thrombus are calculated. For the vessel segment level, the sensitivity (SE), specificity (SP), accuracy (ACC), and positive and negative predictive values (PPV and NPV) are used. *Results*. The proposed network generates segmentation results in good agreement with the ground truth. Based on the pixel level, the proposed network achieves excellent results on testing and the other two external testing sets, DSC are 0.76, 0.76, and 0.73, AHD (mm) are 4.11, 6.45, and 6.49, and AVD are 0.16, 0.18, and 0.22. On the vessel segment level, SE are 0.95, 0.93, and 0.81, SP are 0.97, 0.92, and 0.97, ACC are 0.96, 0.94, and 0.95, PPV are 0.97, 0.82, and 0.96, and NPV are 0.97, 0.96, and 0.94. *Conclusions*. The proposed deep learning network is effective and stable for fully automatic segmentation of venous thrombus on black blood MR images.

1. Introduction

Deep vein thrombosis (DVT) is now the third-largest cardiovascular disease after cerebral vascular and coronary artery disease, it occurs mainly in the lower extremities, and with the acceleration of population aging, the incidence rate of DVT is increasing year by year [1]. Failure to accurately diagnose DVT can lead to severe complications, such as postthrombotic syndrome, pulmonary embolism, lower extremity venous ulcer, and chronic pulmonary hypertension [2].

Recently, an MR black-blood thrombus imaging (BTI) technique was developed to diagnose DVT [3]. The technique uses a black-blood preparation to suppress the venous blood flow signals and thus make the thrombus be directly visualized within the black-blood venous lumen. Some studies have demonstrated that BTI is reliable and accurate for diagnosing DVT without the use of contrast agents [4, 5]. Accurate quantification of thrombus characteristics, such as thrombus distribution, signal intensities, volume, and shape, can provide additional information for personalized DVT treatment planning [6, 7].

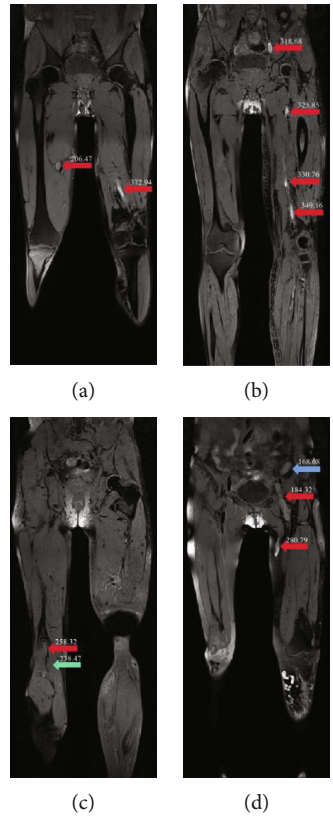

Figure 1: Representative images are obtained by BTI from four DVT patients. Images are shown with the same window and level, and the value on the arrow represents the signal intensity. (a) Different signal intensities of the thrombus (red arrows) can be observed in a patient; (b) the thrombus (red arrows) can distribute in a large area from the common iliac vein to the popliteal vein; (c) the thrombus (red arrow) may have very similar signal intensity with the adjacent muscle (green arrow); (d) iliac tissues (blue arrow) may have the similar signal intensity and shape with the thrombus (red arrow).

However, the key step to quantify these thrombus characteristics is to segment the thrombus from BTI images, which remains a challenging task at present.

The challenges of segmenting the thrombus from BTI images are due to the following reasons. Firstly, a complete BTI scan for a DVT patient can obtain hundreds of images, which makes manually contouring the thrombus from such a lot of images a tremendously difficult task. Secondly, the thrombus characteristics on BTI images hinder the performance of automatic segmentation approaches that can be directly employed on this task. These characteristics include (1) thrombus signal intensities vary in different patients and even in the same patient (Figure 1(a)), leading to difficulty in segmenting thrombus accurately; (2) thrombus locations are in a large area and random in a patient (Figure 1(b)), the unfixed thrombus locations make the segmentation work more difficult; (3) other tissues may have the very similar signal intensity and shape with the thrombus (Figures 1(c) and 1(d)), leading to the high possibility that other tissues can be misidentified as the thrombus.

In recent years, deep learning network has demonstrated enormous potential in the field of medical image segmentation [8–10]. Some automatic segmentation methods have been applied to aortic thrombus segmentation on postoperative computerized tomography angiography images [11, 12]. However, to the best of our knowledge, there are not any reports about automatic segmentation of venous thrombus on black blood MR images. Therefore, we develop a fully automatic method of venous thrombus segmentation based on deep learning network and BTI images, aiming to reduce the burden of clinicians and improve the efficiency and accuracy of DVT personalized treatment planning. The main contributions of this work are (1) three-dimensional (3D) U-shape segmentation model is incorporated into generative adversarial network (GAN) architecture for achieving accurate thrombus segmentation, especially to distinguish the tissues which may be misidentified as thrombus; (2) this work is the first attempt for the thrombus segmentation from BTI images, which can assist in making a personalized and accurate treatment plan for DVT patients; (3) the developed network has been extensively compared with state-of-the-art alternatives on the testing and other two external testing sets, which demonstrates that our proposed network achieves high accuracy and stability on the thrombus segmentation comprehensively.

2. Materials and Methods

2.1. Data Collection. Total images of 110 subjects are obtained from three different centers using two different BTI techniques. One of the BTI techniques is DANTE-SPACE which uses delay alternating with nutation for tailored excitation (DANTE) for black-blood preparation and a 3D variable flip

Table 1: Imaging parameters of DANTE-SPACE performed on 1.5 T MR scanner, DANTE-SPACE performed on 3.0 T MR scanner, and DANTE-FLASH performed on 3.0 T MR scanner.

Parameters	DANTE-SPACE (1.5 T)	DANTE-SPACE (3.0 T)	DANTE-FLASH (3.0 T)
Repetition time (ms)	650	650	5.4
Echo time (ms)	11	9.8	2.08
Turbo factor	40	40	112
Fat suppression	Yes	Yes	Yes
Flip angle	T1 variable	T1 variable	12°
FOV (mm^2)	352×352	352×352	380×380
Number of partitions	208-256	208-256	208-256
Voxel size (mm^3)	$1.4 \times 1.4 \times 1.4$	$1.1 \times 1.1 \times (1.1 - 1.3)$	$1.2 \times 1.2 \times 1.2$
Reconstructed voxel size (mm^3)	$0.7 \times 0.7 \times 0.7$	$0.5 \times 0.5 \times (0.5/0.6)$	$0.6 \times 0.6 \times 0.6$
Bandwidth (Hz/pixel)	698	710	425

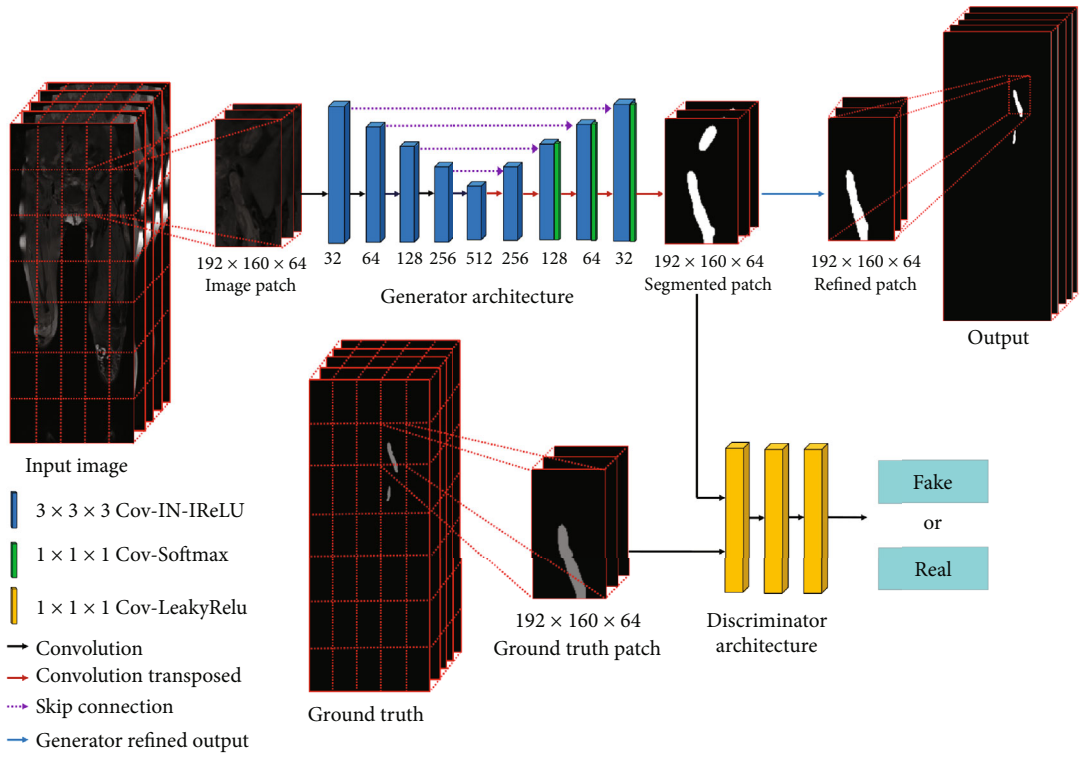

Figure 2: The workflow of the proposed network for the thrombus segmentation from BTI images. 3D segmentation model is used as the generator and its segmented patch and ground truth patch are fed into the discriminator to refine the segmentation result.

angle fast spin echo sequence (SPACE) for readout [13]. The other is DNATE-FLASH which also uses DANTE for black-blood preparation but a fast low-angle shot sequence (FLASH) for readout [14]. 85 subjects used for network training and testing are obtained from one center using DANTE-SPACE on 1.5 T MR scanners (SIEMENS Avanto, Healthcare, Erlang, Germany). 15 and 10 subjects used for external testing are obtained from other two centers using DANTE-SPACE on a 3.0 T (SIEMENS Trio, Erlang, Germany) and DANTE-FLASH on a 3.0 T (SIEMENS Skyra, Erlang, Germany) MR scanners, respectively. In order to cover the whole lower extremities, two- or three-station scans are performed using a 6-channel body coil, an 8-channel external vascular coil, and a corresponding integrated spine coil. Scan parameters are shown in Table 1. After the scans are completed, the images are then composited into a large volumetric dataset using postprocessing software (SIEMENS Syngo, Germany). The volumetric dataset covering the whole lower extremities is finally used for thrombus segmentation.

2.2. Data Preprocessing. The ground truth of thrombus lesions is manually contoured with the consensus between two experienced radiologists on the BTI images. To enable

our proposed network to learn venous thrombus features properly, all patients are resampled to the median voxel spacing of their respective dataset, where third-order spline interpolation is used for image data and nearest-neighbor interpolation for the corresponding ground truth. Then, the z-score normalization is applied to guarantee that the grey values of the same tissue among different MR images are close to each other [15]. Input images are cropped with a sliding window approach, in which the window size equals the patch size (height × width × channel, $192 \times 160 \times 64$) used during network training, and adjacent images overlap by half of the size of a patch. Random rotations, random scaling, and elastic deformations are applied to increase the dataset size to avoid overfitting.

2.3. Deep Learning Network Architecture. The deep learning network based on generative adversarial network (GAN) is proposed for automatic venous thrombus segmentation (as shown in Figure 2). The three-dimensional (3D) U-shape segmentation model is trained as the generator, and the 3D discriminator jointly supervises the segmentation performance in the proposed network. This strategy forces the network to train a more powerful generator to avoid segmentation errors. The proposed segmentation network is implemented by a 3D end-to-end patch-based GAN model (image patch size, $192 \times 160 \times 64$), which takes the lower extremity black blood MR images as input and outputs equal-sized venous thrombus segmentation. Firstly, in the generator stage, the architecture of 3D U-shape generator contains encoding and decoding phases. The encoding phase with downconvolution blocks is used to extract the feature information of venous thrombus, and the decoding phase with upconvolution blocks is adopted to reconstruct the feature maps to probability maps. All the down- and upconvolution blocks contain $3 \times 3 \times 3$ convolution, instance normalization, and Leaky ReLu layer. Furthermore, the last three upconvolution blocks contain $1 \times 1 \times 1$ convolution and softmax layer additionally. Between each downconvolution block and corresponding upconvolution block, skip connection layers are applied for feature fusion of high- and low-resolution feature maps. Also, the combination of cross-entropy loss and soft dice loss is adopted as the loss function in the generator. Secondly, in the discriminator stage, the 3D discriminator is used to judge the authenticity of generated segmentation results against the reference manual ground truth, which contains three $1 \times 1 \times 1$ convolution layers and uses Leaky ReLu as the activation function. The generator and discriminator networks are optimized one after the other in a zero-sum game framework. The generator's training objective is to increase the judgment error of the discriminator by producing novel segmented venous thrombus that is indistinguishable from the ground truth. The discriminator's training objective is to decrease the judgment error of the discriminator network and enhance the ability of differentiating the real from the fake. Adversarial loss is applied in both networks so that the generator produces more realistic segmentation, while the discriminator becomes more skilled at flagging segmented venous thrombus against ground truth. Finally, the refined patch of the generator will be restored to the original size according to the patch location and voxel spacing.

Table 2: Results of the different loss function based on the proposed network.

Method	DSC	AHD (mm)	AVD
L_{CE}	0.70 ± 0.09	8.36 ± 5.21	0.26 ± 0.11
L_{SD}	0.72 ± 0.03	6.52 ± 4.01	0.23 ± 0.10
L_{CE} and L_{SD}	0.73 ± 0.02	5.68 ± 3.24	0.20 ± 0.09
L_{CE} and L_{GAN}	0.73 ± 0.04	6.56 ± 3.23	0.20 ± 0.10
L_{SD} and L_{GAN}	0.72 ± 0.02	5.93 ± 2.38	0.21 ± 0.08
L_{CE} and L_{SD} and L_{GAN}	**0.75 ± 0.03**	**5.12 ± 2.13**	**0.18 ± 0.07**

Table 3: Representative results of parameter sensitivity analysis of the loss function for the proposed network.

λ_1	λ_2	λ_3	DSC	AHD (mm)	AVD
1.0	1.0	0.5	0.74 ± 0.02	5.52 ± 3.21	0.20 ± 0.08
1.0	1.0	1.0	0.75 ± 0.03	5.12 ± 2.13	0.18 ± 0.07
1.0	1.0	2.0	0.71 ± 0.06	7.42 ± 4.68	0.25 ± 0.12
1.0	0.5	1.0	0.74 ± 0.04	5.43 ± 3.23	0.20 ± 0.10
1.0	0.6	1.0	0.75 ± 0.03	4.86 ± 2.14	0.18 ± 0.06
0.4	**0.6**	**1.0**	**0.76 ± 0.01**	**4.11 ± 1.01**	**0.16 ± 0.02**
0.5	0.6	1.0	0.75 ± 0.01	4.63 ± 2.04	0.17 ± 0.05

Table 4: The segmentation comparison between different networks based on the pixel level.

Method	DSC	AHD (mm)	AVD
3D U-Net	0.65 ± 0.05	12.07 ± 8.89	0.26 ± 0.09
V-Net	0.63 ± 0.04	16.62 ± 11.05	0.28 ± 0.06
3D nnU-Net	0.76 ± 0.02	5.49 ± 3.10	0.20 ± 0.08
Cascade nnU-Net	0.75 ± 0.03	6.36 ± 3.83	0.22 ± 0.04
Ours	**0.76 ± 0.01**	**4.11 ± 1.01**	**0.16 ± 0.02**

2.4. Loss Function. The total objective function (L_{total}) in the developed network is the summation of the losses from generator and discriminator as

$$L_{total} = \lambda_1 L_{CE} + \lambda_2 L_{SD} + \lambda_3 L_{GAN}, \tag{1}$$

where λ_1, λ_2, and λ_3 are weights, L_{CE}, L_{SD}, and L_{GAN} are cross-entropy loss, soft dice loss, and GAN loss, respectively. They are defined as

$$L_{CE} = \sum_{i=1}^{N} (y_i \cdot \log x_i + (1 - y_i) \cdot \log (1 - x_i)), \tag{2}$$

$$L_{SD} = 1 - \frac{2\sum_{i=1}^{N} x_i y_i}{\sum_{i=1}^{N} x_i^2 + \sum_{i=1}^{N} y_i^2}, \tag{3}$$

$$L_{GAN} = L_{MSE}\left\{E_y\left[\log D_{\theta_D}(y)\right] + E_{x_i}\left[\log\left(1 - D_{\theta_D}\left(G_{\theta_G}(x_i)\right)\right)\right]\right\}, \tag{4}$$

Table 5: The segmentation comparison between different networks based on the vessel segment level.

Method	SE	SP	ACC	PPV	NPV
3D U-Net	0.51 ± 0.14	0.76 ± 0.05	0.69 ± 0.05	0.47 ± 0.10	0.78 ± 0.05
V-Net	0.77 ± 0.18	0.83 ± 0.03	0.81 ± 0.07	0.63 ± 0.09	0.90 ± 0.08
3D nnU-Net	0.94 ± 0.07	0.89 ± 0.06	0.91 ± 0.06	0.79 ± 0.12	0.96 ± 0.04
Cascade nnU-Net	0.86 ± 0.14	0.90 ± 0.03	0.89 ± 0.05	0.77 ± 0.09	0.94 ± 0.06
Ours	**0.95 ± 0.07**	**0.97 ± 0.02**	**0.96 ± 0.03**	**0.97 ± 0.04**	**0.97 ± 0.04**

where x_i denotes the predicted probability of the ith pixel, y_i is the corresponding ground truth, and N is the number of pixels. L_{MSE} is the mean square error (MSE); θ_G and θ_D, respectively, represent the parameters for the generator and discriminator in GAN. The L_{CE} is used to describe the distance of probability distributions between segmented venous thrombus and ground truth. Employing L_{CE} can segment high intensity and large area thrombus clearly [16]. L_{SD} is used here to solve the data imbalanced exists in the whole lower extremity MR images because the size of some venous thrombus is much smaller than background [17]. Due to the similar intensity and shape between thrombus and other tissue, L_{GAN} is used to identify thrombus areas strictly, and it learns the mapping from the input black blood MR images to ground truth [18].

2.5. Network Training and Testing. This work is performed using Pytorch on a workstation equipped with an NVIDIA TITAN V 12G GPU. During the network training and testing, 85 subjects obtained by DANTE-SPACE from the 1.5 T MR scanner are randomly divided into five groups for 5-fold cross-validation strategy. For each cross-validation, four groups of patients are used as training sets, and the remaining group is a testing set. 15 and 10 subjects obtained from the other two centers are used for external testing. During training, the parameters are set as follows: basic learning rate, 3×10^{-4}; batch size, 2; and Adam is performed as optimization. After adequate training on the network, testing sets are used to test the network's performance.

2.6. Evaluation Metrics. Metrics based on pixel and vessel segment level are adopted to evaluate the difference between segmentation results and ground truth. The pixel level evaluation metrics, including dice similarity coefficient (DSC), absolute volume difference (AVD), and average Hausdorff distance (AHD), are given by

$$\mathrm{DSC} = \frac{2\mathrm{TP}}{2\mathrm{TP} + \mathrm{FP} + \mathrm{FN}}, \tag{5}$$

$$\mathrm{AVD} = \frac{|\mathrm{GT}\text{-}P|}{\mathrm{GT}}, \tag{6}$$

$$\mathrm{AHD} = \frac{1}{|\mathrm{GT}|}\left(\sum_{gt \in \mathrm{GT}} d(gt, P)\right), \tag{7}$$

where TP denotes the true positive, FP denotes false positive, FN denotes false negative, P denotes prediction, GT denotes ground truth, p and gt are two points in P and GT, and d denotes Hausdorff distance.

The deep veins of one leg can be divided into 13 vessel segments, including inferior vena cava, common iliac vein, internal iliac vein, external iliac vein, common femoral vein, deep femoral vein, superficial femoral vein, popliteal vein, anterior tibial vein, posterior tibial vein, fibular vein, great saphenous vein, and small saphenous vein [19]. As correctly identifying which vessel segment occurs thrombosis is important for treatment-decision making [20]. The evaluation metrics based on vessel segment level include sensitivity (SE), specificity (SP), accuracy (ACC), positive predictive value (PPV), and negative predictive value (NPV). These metrics can be calculated according to Equations (8)–(12), respectively.

$$\mathrm{SE} = \frac{\mathrm{TP}}{\mathrm{TP} + \mathrm{FN}}, \tag{8}$$

$$\mathrm{SP} = \frac{\mathrm{TN}}{\mathrm{TN} + \mathrm{FP}}, \tag{9}$$

$$\mathrm{ACC} = \frac{\mathrm{TP} + \mathrm{TN}}{\mathrm{TP} + \mathrm{FP} + \mathrm{TN} + \mathrm{FN}}, \tag{10}$$

$$\mathrm{PPV} = \frac{\mathrm{TP}}{\mathrm{TP} + \mathrm{FP}}, \tag{11}$$

$$\mathrm{NPV} = \frac{\mathrm{TN}}{\mathrm{TN} + \mathrm{FN}}, \tag{12}$$

where TP, FP, TN, and FN are true positive, false positive, true negative, and false negative based on the vessel segment level.

2.7. Ablation Experiment and Parameter Sensitivity Analysis. In this work, we select and combine L_{CE}, L_{SD}, and L_{GAN} in our proposed network, and then, we did an ablation experiment to employ different loss function in the network (seen as below Table 2). Results in the table demonstrate that the loss functions combination is capable of improving the performance of segmentation.

After the loss function ablation experiment, we did a more detailed parameter sensitivity analysis. We defined $L_{\mathrm{total}} = \lambda_1 L_{\mathrm{CE}} + \lambda_2 L_{\mathrm{SD}} + \lambda_3 L_{\mathrm{GAN}}$, λ_1, λ_2, and λ_3 are weights; these are empirically set to 0.4, 0.6, and 1.0 based on the observation on the validation set. We have done multiple experiments on the adjustment of these weights and show some representative parameter results here (see Table 3). As the discriminative strategy is essential in the proposed network, we first select the correct λ_3 value for the GAN loss; secondly, we keep λ_3 and λ_1 values unchanged, and adjust

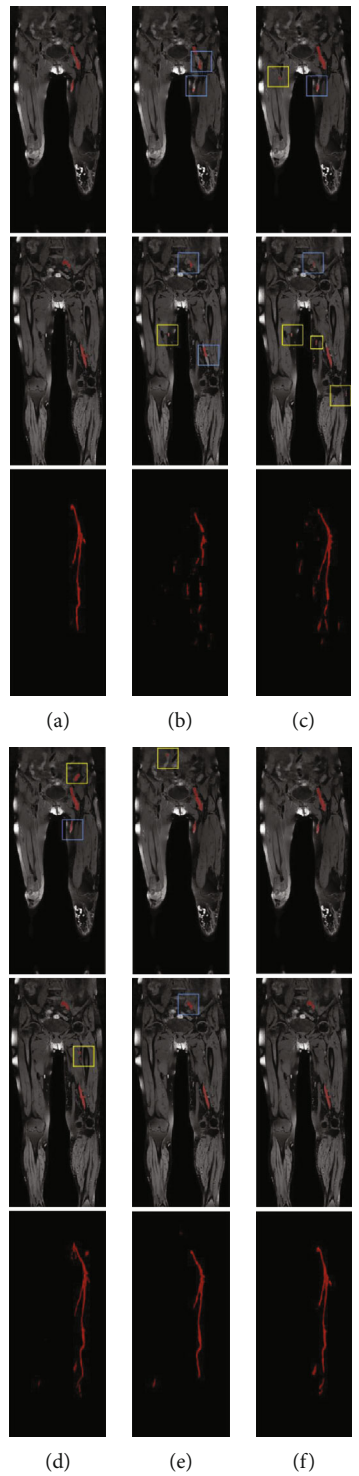

Figure 3: Representative thrombus segmentation results of different networks for a patient. (a) Ground truth, (b) 3D U-Net, (c) V-Net, (d) 3D nnU-Net, (e) Cascade nnU-Net, (f) our proposed network. The first two rows show the segmentation result from the coronal plane, and the last row is to observe the full result directly from the maximum intensity projection (MIP). Red areas in the different models indicate the ground truth and the segmentation result. Yellow boxes highlight some oversegmentation errors. Blue boxes indicate the loss area of DVT segmentation results.

Table 6: The segmentation comparison between different networks based on the pixel level from 3.0 T DANTE-SPACE.

Method	DSC	AHD (mm)	AVD
3D U-Net	0.57 ± 0.10	25.60 ± 10.69	0.37 ± 0.12
V-Net	0.53 ± 0.13	27.50 ± 11.41	0.45 ± 0.20
3D nnU-Net	0.75 ± 0.09	7.42 ± 4.31	0.20 ± 0.09
Cascade nnU-Net	0.71 ± 0.15	11.20 ± 5.16	0.27 ± 0.11
Ours	**0.76 ± 0.06**	**6.45 ± 3.41**	**0.18 ± 0.09**

Table 7: The segmentation comparison between different networks based on the vessel segment level from 3.0 T DANTE-SPACE.

Method	SE	SP	ACC	PPV	NPV
3D U-Net	0.56 ± 0.07	0.54 ± 0.20	0.54 ± 0.19	0.32 ± 0.09	0.82 ± 0.10
V-Net	0.53 ± 0.06	0.40 ± 0.20	0.38 ± 0.20	0.23 ± 0.05	0.77 ± 0.15
3D nnU-Net	0.91 ± 0.08	0.80 ± 0.13	0.85 ± 0.06	0.58 ± 0.10	0.93 ± 0.02
Cascade nnU-Net	0.70 ± 0.28	0.90 ± 0.08	0.84 ± 0.10	0.70 ± 0.24	0.89 ± 0.10
Ours	**0.93 ± 0.06**	**0.92 ± 0.09**	**0.94 ± 0.05**	**0.82 ± 0.18**	**0.96 ± 0.02**

the appropriate λ_2 value; finally, we choose the most suitable λ_1 value to get the best segmentation performance.

3. Results

The proposed deep learning network is compared with several existing medical image segmentation models, i.e., 3D U-Net [21], V-Net [22], 3D nnU-Net, and Cascade nnU-Net [23]. Since 3D deep learning networks have demonstrated their superiority on volumetric medical image segmentation task [24, 25], the developed network is only compared with these state-of-the-art 3D deep learning-based models.

3.1. Internal Test. The quantitative performances based on pixel level of automatic venous thrombus segmentation are summarized in Table 4. All numbers in the table referred to the mean ± standard deviation values of 5-fold cross-validation experiments. Compared with other models, our network provides the best values of DSC (0.76 ± 0.01), AHD (4.11 ± 1.01), and AVD (0.16 ± 0.02).

Table 5 demonstrates the results of quantitative results based on the vessel segment level. Our network outperforms other models in terms of SE (0.95 ± 0.07), SP (0.97 ± 0.02), ACC (0.96 ± 0.03), PPV (0.97 ± 0.04), and NPV (0.97 ± 0.04).

Representative segmentation results are shown in Figure 3. The segmentation results of 3D U-Net can only segment the rough outline of the thrombus and has some segmentation errors on misidentifying other tissue as thrombus and discontinuity segmentation of the thrombus (Figure 3(b)). V-Net performs better than 3D U-Net in eliminating discontinuity (Figure 3(c), blue box) of the result but still misidentifies some tissues as thrombus (Figure 3(c), yellow box). 3D nnU-Net gets much better results than 3D U-Net and V-Net (Figure 3(d)); it achieves excellent scores in DSC, AHD, and AVD. However, 3D nnU-Net also misidentifies iliac and muscle tissues as thrombus (Figure 3(d)). Cascade nnU-Net cascades a low-resolution network and a high-resolution network, but the misidentification problem remains unsolved (Figure 3(e)). Compared to 3D U-Net, V-Net, 3D nnU-Net, and Cascade nnU-Net, our developed network can reduce the segmentation errors and match with the ground truth well (Figure 3(f)).

3.2. External Test. For the external test set obtained by DANTE-SPACE on the 3.0 T MR scanner, the segmentation results are shown in Tables 6 and 7. Our proposed network achieves the best results on the venous thrombus segmentation in terms of DSC, AHD, and AVD based on the pixel level, as well as SE, SP, ACC, PPV, and NPV based on the vessel segment level. Representative segmentation results from a patient are shown in Figure 4. Other models may have incomplete segmentation of the thrombus area (Figure 4, blue box) and misidentify the muscle area as thrombus (Figure 4, yellow box); the proposed network has avoided the above errors. The last row of whole lower extremity venous thrombus MIP images shows that the segmentation result of the proposed network can also avoid misidentification errors on 3.0 T DANTE-SPACE images.

For the other external test set obtained by DANT-FLASH on the 3.0 T MR scanner, the segmentation results are shown in Tables 8 and 9. Results suggest that our network remains to achieve the best thrombus segmentation performance compared with other models. Representative segmentation results from a patient are shown in Figure 5. The proposed network has avoided some segmentation problems, such as incomplete segmentation of low-intensity thrombus area (Figure 5, blue box) and segment the popliteal bone area into thrombus (Figure 5, yellow box) in other models. The venous thrombus coronal and MIP segmentation results demonstrate that the proposed network can also match with the ground truth well on the DANTE-FLASH images.

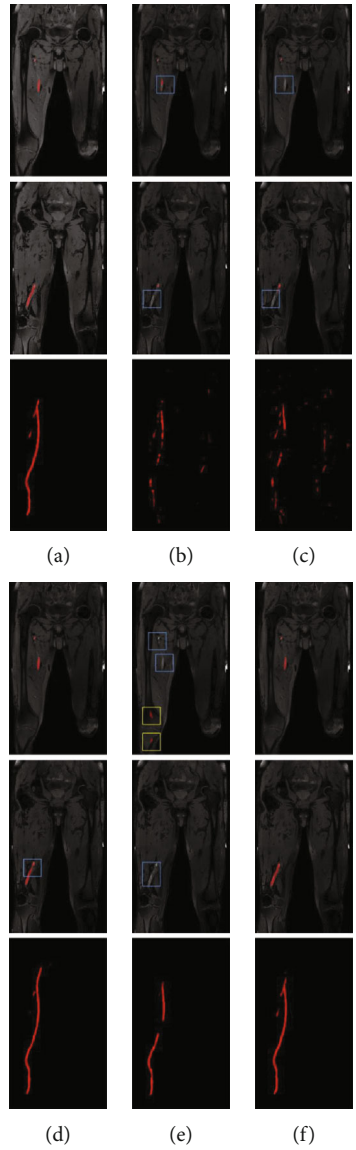

Figure 4: Representative segmentation results of a patient obtained from an external center by DANTE-SPACE techniques. (a) Ground truth, (b) 3D U-Net, (c) V-Net, (d) 3D nnU-Net, (e) Cascade nnU-Net, (f) our proposed network.

Table 8: The segmentation comparison between different networks based on the pixel level from 3.0 T DANTE-FLASH.

Method	DSC	AHD (mm)	AVD
3D U-Net	0.42 ± 0.11	57.46 ± 13.58	0.44 ± 0.17
V-Net	0.38 ± 0.14	75.33 ± 12.91	0.65 ± 0.21
3D nnU-Net	0.73 ± 0.13	7.27 ± 5.42	0.24 ± 0.13
Cascade nnU-Net	0.68 ± 0.16	13.56 ± 7.63	0.38 ± 0.15
Ours	**0.73 ± 0.11**	**6.49 ± 3.57**	**0.22 ± 0.12**

4. Discussion

A deep learning network is proposed for automatic venous thrombus segmentation from BTI images with high accuracy and reliability. This network is tested and externally tested by subjects from three different centers and compared with 3D U-Net, V-Net, 3D nnU-Net, and Cascade nnU-Net models. Extensive experimental results based on the pixel level, vessel segment level, and venous thrombus segmentation figures demonstrate that the proposed network achieves superior segmentation performance to state-of-the-art models, indicating the great potential of assisting the DVT diagnosis in clinics.

Deep learning-based medical image segmentation models have achieved unprecedented segmentation performance [26]. However, due to the difficulties described in Figure 1, current deep learning models cannot be directly used for segmenting thrombus from BTI images. These difficulties lead to the most common segmentation error: the tissue with similar thrombus signal intensities and shapes is easily misidentified as thrombus (Figure 3). To address this issue, the proposed network uses 3D segmentation model as the generator and jointly adopts 3D discriminator to supervise generator's performance

Table 9: The segmentation comparison between different networks based on the vessel segment level from 3.0 T DANTE-FLASH.

Method	SE	SP	ACC	PPV	NPV
3D U-Net	0.53 ± 0.29	0.68 ± 0.18	0.65 ± 0.15	0.41 ± 0.15	0.81 ± 0.12
V-Net	0.57 ± 0.25	0.59 ± 0.17	0.57 ± 0.15	0.33 ± 0.17	0.78 ± 0.14
3D nnU-Net	0.81 ± 0.14	0.88 ± 0.09	0.89 ± 0.05	0.72 ± 0.21	0.93 ± 0.06
Cascade nnU-Net	0.64 ± 0.17	0.83 ± 0.04	0.79 ± 0.04	0.52 ± 0.17	0.88 ± 0.06
Ours	**0.81 ± 0.12**	**0.97 ± 0.02**	**0.95 ± 0.04**	**0.96 ± 0.10**	**0.94 ± 0.05**

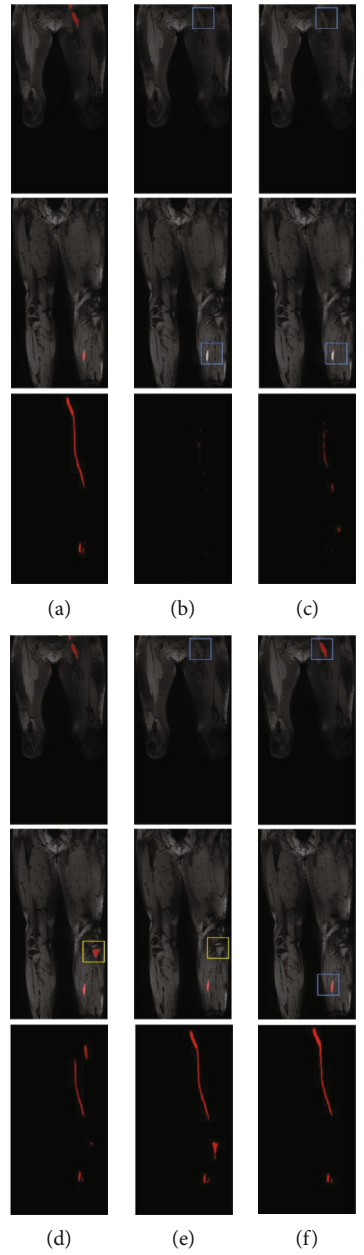

Figure 5: Representative segmentation results of a patient obtained from an external center by DANTE-FLASH techniques. (a) Ground truth, (b) 3D U-Net, (c) V-Net, (d) 3D nnU-Net, (e) Cascade nnU-Net, (f) our proposed network.

and enhance the capability of accurate thrombus segmentation, especially to distinguish the thrombus from other similar tissues. Experiment results demonstrated this strategy could reduce the segmentation errors from the abdomen and bone, making the segmentation results closer to the ground truth. Moreover, this proposed network also outperforms other models on the external testing sets in terms of reducing misidentification errors (Figures 4 and 5).

To evaluate the robustness of a neural network, an external test set is necessary [27]. In this work, two kinds of external subjects are tested between different models. One kind of external subject is acquired by DANTE-SPACE on 3.0 T MR scanner, and the other one is acquired by DANTE-FLASH on another 3.0 T MR scanner (Table 1). As the sequences and scanners used for acquiring these external subjects are quite different from those for acquiring training and testing, the image properties (i.e., signal-to-noise ratio and contrast-to-noise ratio) could also be different and may lead to poor segmentation performance on external subjects. Nevertheless, external testing results demonstrate that our proposed network still has the best segmentation performance compared with other models (Table 6–9). The excellent generalization ability of the proposed network due to the following two reasons. Firstly, this network uses the similar segmentation structure of nnU-Net as the generator, and nnU-Net has already proved the generalization ability on dozens of public medical datasets. Moreover, this proposed network uses a discriminator strategy forces model to train a more powerful generator than normal nnU-Net on generalization performance. Secondly, although the image properties of the training and the external testing sets are different, they all belonged to BTI images on which the venous blood is black, and the thrombus is located within the black-blood veins. This is an important prerequisite for excellent generalization performance.

The success of the thrombus segmentation from BTI images can be beneficial to clinical practices. Personalized treatment of DVT patients depends on an accurate diagnosis of the thrombus locations, especially the thrombus signal characteristics. Previous studies demonstrated that the thrombus shape and signal intensity can be used to identify the recurrent DVT, the DVT stage, and the prognosis of DVT treatments [28]. As the thrombus could be automatically segmented from BTI images, quantitative analysis of the thrombus characteristics becomes an easy task.

There are also two limitations in this work. Firstly, the training DVT subjects are still insufficient, and more data should be collected to construct a more robust model. Secondly, because of constraints by long training time, we were not able to perform model embedding experiments to improve the venous segmentation performance [29]. However, as a pilot experiment, the developed network has shown promising results despite all the limitations and will provide insights into future studies.

5. Conclusions

A novel deep learning network based on GAN is developed for accurate and automatic thrombus segmentation from BTI images. Experiment results demonstrated that the developed network is more accurate and stable compared with other state-of-the-art models. It has the potential to be an automatic method to assist the diagnosis of DVT in clinics.

Data Availability

The black blood MR data used to support the findings of this study are currently under embargo while the research findings are commercialized. Requests for data, 6 months after publication of this article, will be considered by the corresponding author.

Disclosure

Chuanqi Sun and Xiangyu Xiong are co-first authors.

Conflicts of Interest

The authors declare that they have no conflicts of interest.

Authors' Contributions

Chuanqi Sun and Xiangyu Xiong share equal contribution.

Acknowledgments

The study was funded by the National Natural Science Foundation of China (nos. 81971607 and 81729003) and the Science and Technology Program of Guangzhou (no. 202102080566).

References

[1] F. A. Spencer, C. Emery, D. Lessard et al., "The Worcester venous thromboembolism study: a population-based study of the clinical epidemiology of venous thromboembolism," *Journal of General Internal Medicine*, vol. 21, no. 7, pp. 722–727, 2006.

[2] M. Di Nisio, N. van Es, and H. R. Büller, "Deep vein thrombosis and pulmonary embolism," *The Lancet*, vol. 388, no. 10063, pp. 3060–3073, 2016.

[3] G. Xie, H. Chen, X. He et al., "Black-blood thrombus imaging (BTI): a contrast-free cardiovascular magnetic resonance approach for the diagnosis of non-acute deep vein thrombosis," *Journal of Cardiovascular Magnetic Resonance*, vol. 19, no. 1, p. 4, 2017.

[4] H. Chen, X. He, G. Xie et al., "Cardiovascular magnetic resonance black-blood thrombus imaging for the diagnosis of acute deep vein thrombosis at 1.5 tesla," *Journal of Cardiovascular Magnetic Resonance*, vol. 20, no. 1, p. 42, 2018.

[5] Y. Ye, X. He, C. Huang et al., "Comparison between the diagnostic performance of 1.5 T and 3.0 T field strengths for detecting deep vein thrombosis using magnetic resonance black-blood thrombus imaging," *Clinical and Applied Thrombosis/Hemostasis*, vol. 26, pp. 107602962092123–107602962092128, 2020.

[6] K. Ouriel, R. K. Greenberg, R. M. Green, J. M. Massullo, and D. R. Goines, "A volumetric index for the quantification of deep venous thrombosis," *Journal of Vascular Surgery*, vol. 30, no. 6, pp. 1060–1066, 1999.

[7] M. Tan, G. C. Mol, C. J. van Rooden et al., "Magnetic resonance direct thrombus imaging differentiates acute recurrent ipsilateral deep vein thrombosis from residual thrombosis," *Blood*, vol. 124, no. 4, pp. 623–627, 2014.

[8] D. Shen, G. Wu, and H. I. Suk, "Deep learning in medical image analysis," *Annual Review of Biomedical Engineering*, vol. 19, pp. 221–248, 2017.

[9] G. Litjens, T. Kooi, B. E. Bejnordi et al., "A survey on deep learning in medical image analysis," *Medical Image Analysis*, vol. 42, pp. 60–88, 2017.

[10] J. Chen, M. Zhong, J. Li, D. Wang, T. Qian, and H. Tu, "Effective deep attributed network representation learning with topology adapted smoothing," *IEEE Trans Cybern*, vol. 99, pp. 1–12, 2021.

[11] K. López-Linares, L. Kabongo, N. Lete et al., "DCNN-based automatic segmentation and quantification of aortic thrombus Volume: Influence of the Training Approach," in *Intravascular Imaging and Computer Assisted Stenting, and Large-Scale Annotation of Biomedical Data and Expert Label Synthesis*, vol. 10552, Springer, Chambridge, 2017.

[12] K. López-Linares, N. Aranjuelo, L. Kabongo et al., "Fully automatic detection and segmentation of abdominal aortic thrombus in post-operative CTA images using deep convolutional neural networks," *Medical image analysis*, vol. 46, pp. 202–214, 2018.

[13] G. Zhuang, C. Tang, X. He et al., "DANTE-SPACE: a new technical tool for DVT on 1.5T MRI," *The International Journal of Cardiovascular Imaging*, vol. 35, no. 12, pp. 2231–2237, 2019.

[14] G. Xie, N. Zhang, Y. Xie et al., "DANTE-prepared three-dimensional FLASH: a fast isotropic-resolution MR approach to morphological evaluation of the peripheral arterial wall at 3 tesla," *Journal of Magnetic Resonance Imaging*, vol. 43, no. 2, pp. 343–351, 2016.

[15] J. C. Reinhold, B. E. Dewey, A. Carass, and J. L. Prince, "Evaluating the impact of intensity normalization on MR image synthesis," 2018, https://arxiv.org/abs/1812.04652.

[16] Y. Zhou, X. Wang, M. Zhang, J. Zhu, and Q. J. I. A. Wu, "MPCE: A maximum probability based cross entropy loss function for neural network Classification," *IEEE Access*, vol. 7, no. 99, pp. 146331–146341, 2019.

[17] J. Bertels, D. Robben, D. Vandermeulen, and P. Suetens, "Theoretical analysis and experimental validation of volume bias of soft Dice optimized segmentation maps in the context of inherent uncertainty," *Medical Image Analysis*, vol. 67, article 101833, 2021.

[18] P. Isola, J.-Y. Zhu, T. Zhou, and A. A. Efros, "Image-to-image translation with conditional adversarial networks," in *Proceedings of the IEEE conference on computer vision and pattern recognition*, pp. 1125–1134, Honolulu, HI, USA, 2017.

[19] S. Hochauf, R. Sternitzky, and S. M. Schellong, "Structure and function of the peripheral venous system," *Herz*, vol. 32, no. 1, pp. 3–9, 2007.

[20] J. M. Kang, K. H. Park, S. Ahn et al., "Rivaroxaban after thrombolysis in acute iliofemoral venous thrombosis: a randomized, open-labeled, multicenter trial," *Scientific Reports*, vol. 9, no. 1, p. 20356, 2019.

[21] O. Ronneberger, P. Fischer, and T. Brox, "U-Net: Convolutional Networks for Biomedical Image Segmentation," in *International Conference on Medical Image Computing and Computer-Assisted Intervention*, Springer, Springer International Publishing, 2015.

[22] F. Milletari, N. Navab, and S. Ahmadi, "V-net: fully convolutional neural networks for volumetric medical image segmentation," in *IEEE Transactions on Medical Imaging*, pp. 565–571, Stanford, CA, USA, 2016.

[23] F. Isensee, P. F. Jaeger, S. A. A. Kohl, J. Petersen, and K. H. Maier-Hein, "nnU-Net: a self-configuring method for deep learning-based biomedical image segmentation," *Nature Methods*, vol. 18, no. 2, pp. 203–211, 2021.

[24] H. Zheng, L. Qian, Y. Qin, Y. Gu, and J. Yang, "Improving the slice interaction of 2.5D CNN for automatic pancreas segmentation," *Medical Physics*, vol. 47, no. 11, pp. 5543–5554, 2020.

[25] J. Duan, G. Bello, J. Schlemper et al., "Automatic 3D bi-ventricular segmentation of cardiac images by a shape-refined Multi- Task deep learning approach," *IEEE Transactions on Medical Imaging*, vol. 38, no. 9, pp. 2151–2164, 2019.

[26] B. Sahiner, A. Pezeshk, L. M. Hadjiiski et al., "Deep learning in medical imaging and radiation therapy," *Medical Physics*, vol. 46, no. 1, pp. e1–e36, 2019.

[27] D. A. Bluemke, L. Moy, M. A. Bredella et al., "Assessing radiology research on artificial intelligence: a brief guide for authors, reviewers, and readers-from theRadiologyEditorial board," *Radiology*, vol. 294, no. 3, pp. 487–489, 2020.

[28] X. Yang, F. Wu, Y. Liu et al., "Predictors of successful endovascular treatment in severe cerebral venous sinus thrombosis," *Annals of Clinical Translational Neurology*, vol. 6, no. 4, pp. 755–761, 2019.

[29] G. Xue, M. Zhong, J. Li, J. Chen, C. Zhai, and R. Kong, "Dynamic network embedding survey," 2021, http://arxiv.org/abs/2103.15447.

Hindawi
BioMed Research International
Volume 2024, Article ID 9845801, 1 page
https://doi.org/10.1155/2024/9845801

Retraction

Retracted: Comparison of Curative Complications between Mammotome-Assisted Minimally Invasive Resection and Conventional Open Resection for Breast Neoplasm: A Retrospective Clinical Study

BioMed Research International

Received 12 March 2024; Accepted 12 March 2024; Published 20 March 2024

This article has been retracted by Hindawi following an investigation undertaken by the publisher [1]. This investigation has uncovered evidence of one or more of the following indicators of systematic manipulation of the publication process:

(1) Discrepancies in scope

(2) Discrepancies in the description of the research reported

(3) Discrepancies between the availability of data and the research described

(4) Inappropriate citations

(5) Incoherent, meaningless and/or irrelevant content included in the article

(6) Manipulated or compromised peer review

The presence of these indicators undermines our confidence in the integrity of the article's content and we cannot, therefore, vouch for its reliability. Please note that this notice is intended solely to alert readers that the content of this article is unreliable. We have not investigated whether authors were aware of or involved in the systematic manipulation of the publication process.

Wiley and Hindawi regrets that the usual quality checks did not identify these issues before publication and have since put additional measures in place to safeguard research integrity.

We wish to credit our own Research Integrity and Research Publishing teams and anonymous and named external researchers and research integrity experts for contributing to this investigation.

The corresponding author, as the representative of all authors, has been given the opportunity to register their agreement or disagreement to this retraction. We have kept a record of any response received.

References

[1] R. Li, J. Li, S. Chen, B. Xiao, L. Liu, and N. Zhu, "Comparison of Curative Complications between Mammotome-Assisted Minimally Invasive Resection and Conventional Open Resection for Breast Neoplasm: A Retrospective Clinical Study," *BioMed Research International*, vol. 2021, Article ID 7739628, 4 pages, 2021.

Hindawi
BioMed Research International
Volume 2021, Article ID 7739628, 4 pages
https://doi.org/10.1155/2021/7739628

Research Article

Comparison of Curative Complications between Mammotome-Assisted Minimally Invasive Resection and Conventional Open Resection for Breast Neoplasm: A Retrospective Clinical Study

Rui Li,[1] Jingyan Li,[1] Shanzheng Chen,[1] Binglan Xiao,[1] Lihua Liu,[1] and Ning Zhu[2]

[1]*Loudi City Central Hospital, Loudi, 417000 Hunan, China*
[2]*Hunan University of Medicine, Huaihua, 418000 Hunan, China*

Correspondence should be addressed to Ning Zhu; 82478637@qq.com

Received 19 August 2021; Revised 20 September 2021; Accepted 29 October 2021; Published 17 November 2021

Academic Editor: Suren R. Sooranna

Background. To know the clinical value of mammotome-assisted minimally invasive resection (MAMIR) in the treatment of patients with breast neoplasm, we performed a retrospective clinical study for the patients treated with the MAMIR and conventional open resection (COR). *Methods*. Postoperative complications were compared between 40 patients treated with the MAMIR and 40 patients treated with the COR. The postoperative complications mainly included intraoperative blood loss, hospitalization days, operative time, surgical scar, and incidence of postoperative complications. *Results*. We found that the amount of intraoperative blood loss, hospitalization days, operative time, surgical scar, and incidence of postoperative complications in the MAMIR group were significantly lower than those of patients in the COR group. *Conclusion*. Our results indicated that patients with breast neoplasm treated with the MAMIR had better outcomes, which reinforced the advantage of this approach.

1. Introduction

Breast neoplasms are a wide spectrum of pathologies from benign proliferations, high-risk lesions, precursor lesions, to invasive malignancies. Breast cancer is the most commonly diagnosed cancer and the leading cause of cancer death [1]. In 2020, there were almost 2.3 million new breast cancer cases and 0.68 million breast cancer deaths [1]. Surgery is a common treatment for cancers, including breast cancers [2–4]. Most patients with breast cancer who undergo surgery also need additional treatments, such as chemotherapy, hormone therapy, or radiation [5–7]. Breast cancer is the most common type of cancer with high incidence [1]. However, most breast neoplasm patients are determined to be noncancerous [8]. Breast neoplasm is a relatively common disease in women, which is more common in women of reproductive age, including benign tumors and malignant tumors. Although those benign tumors do not invade the surrounding tissue, they will interfere with the function of the breast if they are not surgically removed. Therefore, no matter if the patient's breast tumor is benign or malignant, surgical resection is necessary [9, 10]. Mammotome minimally invasive mastectomy is a minimally invasive mastectomy for breast masses under the guidance of ultrasound and according to the relevant principle of vacuum negative pressure suction [11–13]. It has the advantages of high accuracy of positioning, less bleeding, and better aesthetic appearance [13–15]. To know the clinical value of the mammotome-assisted minimally invasive resection (MAMIR) in the treatment of patients with breast neoplasm, we performed a retrospective comparative analysis of MAMIR and conventional open resection (COR) in the present study.

2. Materials and Methods

2.1. Object. This study was approved by the Ethics and Research Committees of Loudi City Central Hospital (Loudi, China) and was conducted in accordance with the principles

outlined in the Declaration of Helsinki. We collected 80 patients who underwent breast resection treatment in our department from May 2019 to May 2021 for this retrospective study, of which there were 40 patients treated with MAMIR and 40 patients treated with COR.

Measurement of breast tumor size: Siemens Acuson S3000 Ultrasound Machine was used to diagnose the tumor size before the surgery, and the transverse and longitudinal diameters of tumors were measured in millimeters. *Measurement of surgical incision size*: at the first dressing change after surgery, a millimeter ruler was used to measure surgical incision size (accurate to millimeter).

2.2. Inclusion/Exclusion Criteria. Inclusion criteria: (1) patients should be diagnosed as benign or potentially benign by physical examination, color ultrasound, mammography, and histopathology according to bi-RADS classification criteria; (2) the maximum diameter of the patient's tumor should be less than 30 mm; and (3) both the patient and the patient's family members need to have read and signed the informed consent, which was reviewed and confirmed by the medical ethics committee.

Exclusion criteria: (1) patients whose preoperative pathological properties are not clear or suspected to be breast cancer or whose postoperative pathological diagnosis is malignant tumor; (2) patients with breast implants; (3) patients with contraindications to surgery; (4) the patient's maximum tumor diameter was greater than 30 mm; and (5) patients with hemangioma, coagulopathy, mental disorders, and other diseases need to be excluded.

2.3. Operative Method. Conventional open resection: after anesthesia is administered, the nipple is treated as the center to form a radial or arcuate surgical incision around the areola. The incision length is 2-4 cm. The skin, fat, and glands were incised and separated around the neoplasm to expose the neoplasm. The mass and surrounding normal tissue were excised, sutured, and bandaged.

Mammotome-assisted minimally invasive resection: according to the location of the patient's neoplasm, the appropriate posture was selected, the patient's back was properly padded, local anesthesia was carried out, and the surgical site was exposed. The needle insertion direction was determined according to the ultrasonic examination results. The incision length was 4 mm, hidden in the areola, midaxillary line, and lower margin of the mammary gland. Guided by B-ultrasound, a rotating breast cutter was placed below the lesion. The grooves of the rotary knife are aligned with the lesion, and the lesion is rotated and the specimen is extracted. After the tumor was completely resected with B-ultrasound, pressure hemostasis was performed. After 10-20 minutes of pressure, we cover with a bandage. The elastic bandage was applied with pressure for 48-72 hours.

2.4. Statistical Analysis. IBM SPSS 22 software is used for statistical analysis. A chi-square test is used for counting data, and t-test is used for measurement data. Data were presented in the form of mean ± SEM.

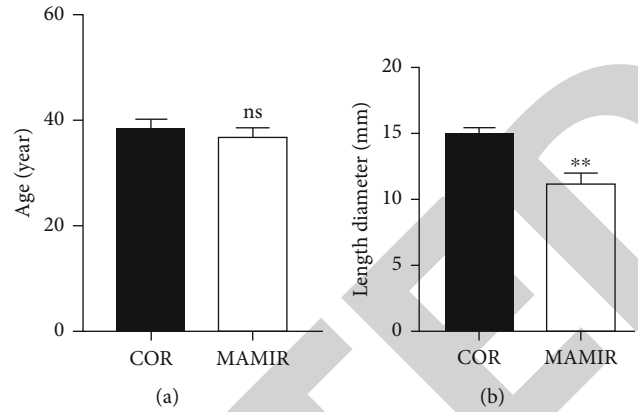

Figure 1: Comparison of clinical features. (a) Comparison of age in patients treated with the MAMIR and COR. (b) Comparison of tumor size in patients treated with the MAMIR and COR. MAMIR, $n = 40$; COR, $n = 40$. $^{*}p < 0.05$, $^{**}p < 0.01$, $^{***}p < 0.001$.

3. Results

3.1. Comparison of Clinical Features. We collected 40 patients who underwent MAMIR and 40 patients who underwent COR in our department from May 2019 to May 2021. There was no significant difference in age between the MAMIR group and the COR group (Figure 1(a)). However, the tumor size of patients treated with MAMIR was significantly smaller than that of patients treated with COR (Figure 1(b)).

3.2. Comparison of Clinical Complications. We performed the comparison analyses for the clinical complications, including the amount of intraoperative blood loss, hospitalization days, operative time, and surgical scar in the MAMIR group and the COR group. The results indicated that the amount of intraoperative blood loss in the MAMIR group was significantly reduced by about 50% (Figure 2(a)). Both the hospitalization days and the operative time of patients treated with MAMIR were significantly lower than those of patients treated with COR (Figures 2(b) and 2(c)). Spontaneously, we also found that the size of the surgical scar was also significantly smaller in the MAMIR group (Figure 2(d)).

We previously found that the tumor size in the MAMIR group was significantly smaller than that in the COR group. Then, we performed the correlation analyses for the amount of intraoperative blood loss, hospitalization days, operative time, and surgical scar with the treatment manner. The results indicated that the treatment manner was correlated with the intraoperative blood loss, hospitalization days, operative time, and surgical scar (Figure 2(e)).

3.3. Comparison of Postoperative Complications. Additionally, we also performed the comparison analyses for the postoperative complications, including local hematoma, fat liquefaction, and infection. In the COR group, we found 2 cases of local hematoma, 3 cases of fat liquefaction, and 1 case of infection. In the MAMIR group, we found 1 case of

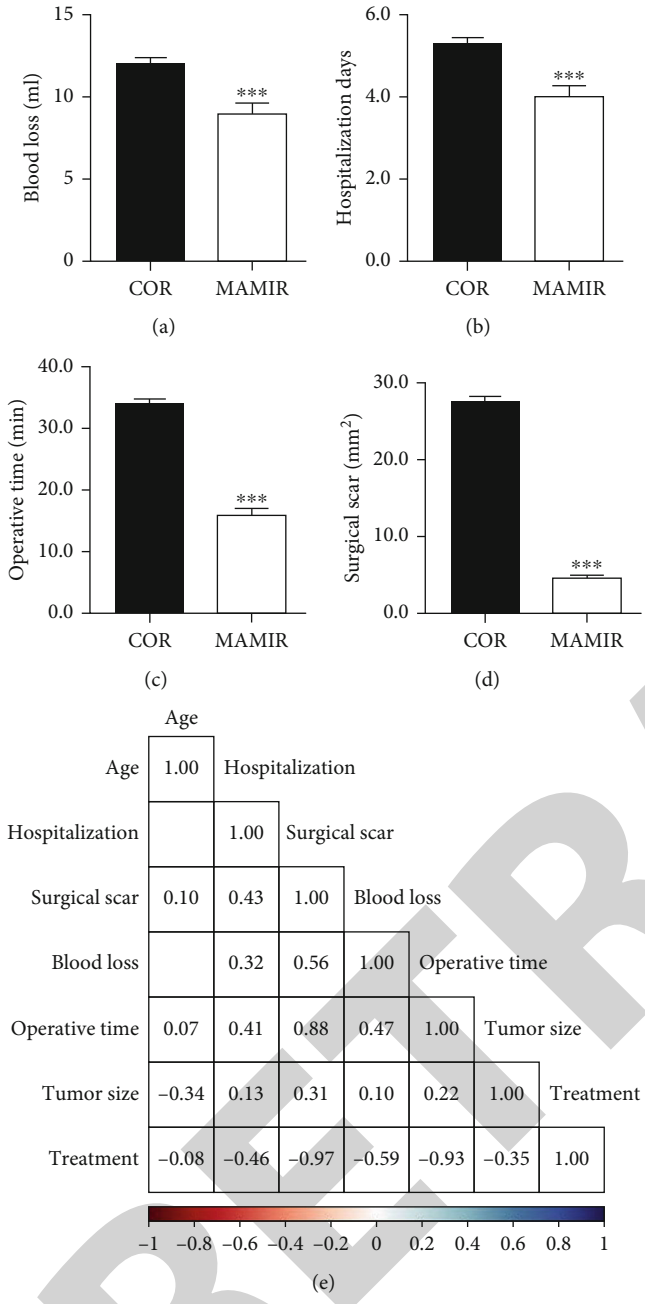

Figure 2: Comparison of clinical complications. (a–d) Comparison of intraoperative blood loss (a), hospitalization days (b), operative time (c), and surgical scar (d) in patients treated with the MAMIR and COR. (e) Correlation analyses of treatment manner with the clinical complications. MAMIR, $n = 40$; COR, $n = 40$. $^{*}p < 0.05$, $^{**}p < 0.01$, $^{***}p < 0.001$.

local hematoma. The chi-square test showed no significant difference between them (Table 1).

Subsequently, we performed the chi-square for all postoperative complications, and found that the total rate of postoperative complications in the MAMIR group was 2.5%, which was significantly lower that of the COR group (15%) (Table 2).

Table 1: Local hematoma/fat liquefaction/infection comparison.

Group	Local hematoma		Fat liquefaction		Infection comparison	
	No	Yes	No	Yes	No	Yes
COR	38	2	37	3	39	1
MAMIR	39	1	40	0	40	0
X^2	0.346		3.117		1.013	
p	0.556		0.077		0.314	

Table 2: Postoperative complication comparison.

Group	Local hematoma & fat liquefaction & infection comparison	
	No	Yes
COR	34	6
MAMIR	39	1
X^2	3.914	
p	0.048	

4. Discussions

Breast neoplasm is a relatively common disease in women. Surgical resection of breast masses is often performed clinically. However, it is difficult to remove a small breast mass with traditional open surgery. In addition, the incision is relatively large, leaving a large scar on the breast, which is not easy to be accepted by patients with breast tumors [16, 17]. Mammotome minimally invasive mastectomy is a minimally invasive mastectomy for breast masses under the guidance of ultrasound and according to the relevant principle of vacuum negative pressure suction [11–13]. It has the advantages of high accuracy of positioning, less bleeding, and better aesthetic appearance [13–15].

To know the clinical value of MAMIR and COR for the treatment of patients with breast neoplasm, we performed comparison analyses for 40 patients who underwent mammotome minimally invasive surgery and 40 patients who underwent conventional open surgery. We found that the amount of intraoperative blood loss, hospitalization days, operation time, and surgical scar in the test group were significantly lower than those in the control group. The total rate of postoperative complications in the mammotome minimally invasive surgery group was significantly better than that of the conventional open surgery group. Our results suggest that minimally invasive mastectomy is better in treating breast tumors than traditional open surgery, which reinforced the advantage of the surgery treatment [18–20].

Data Availability

The datasets generated and analyzed for the current study are available.

Hindawi
BioMed Research International
Volume 2024, Article ID 9784929, 1 page
https://doi.org/10.1155/2024/9784929

Retraction

Retracted: A Bioinformatics Approach for the Prediction of Immunogenic Properties and Structure of the SARS-COV-2 B.1.617.1 Variant Spike Protein

BioMed Research International

Received 12 March 2024; Accepted 12 March 2024; Published 20 March 2024

This article has been retracted by Hindawi following an investigation undertaken by the publisher [1]. This investigation has uncovered evidence of one or more of the following indicators of systematic manipulation of the publication process:

(1) Discrepancies in scope

(2) Discrepancies in the description of the research reported

(3) Discrepancies between the availability of data and the research described

(4) Inappropriate citations

(5) Incoherent, meaningless and/or irrelevant content included in the article

(6) Manipulated or compromised peer review

The presence of these indicators undermines our confidence in the integrity of the article's content and we cannot, therefore, vouch for its reliability. Please note that this notice is intended solely to alert readers that the content of this article is unreliable. We have not investigated whether authors were aware of or involved in the systematic manipulation of the publication process.

Wiley and Hindawi regrets that the usual quality checks did not identify these issues before publication and have since put additional measures in place to safeguard research integrity.

We wish to credit our own Research Integrity and Research Publishing teams and anonymous and named external researchers and research integrity experts for contributing to this investigation.

The corresponding author, as the representative of all authors, has been given the opportunity to register their agreement or disagreement to this retraction. We have kept a record of any response received.

References

[1] V. K. Srivastava, S. Kaushik, G. Bhargava, A. Jain, J. Saxena, and A. Jyoti, "A Bioinformatics Approach for the Prediction of Immunogenic Properties and Structure of the SARS-COV-2 B.1.617.1 Variant Spike Protein," *BioMed Research International*, vol. 2021, Article ID 7251119, 8 pages, 2021.

Hindawi
BioMed Research International
Volume 2021, Article ID 7251119, 8 pages
https://doi.org/10.1155/2021/7251119

Research Article

A Bioinformatics Approach for the Prediction of Immunogenic Properties and Structure of the SARS-COV-2 B.1.617.1 Variant Spike Protein

Vijay Kumar Srivastava,[1] **Sanket Kaushik**,[1] **Gazal Bhargava**,[1] **Ajay Jain**,[1] **Juhi Saxena**,[2] **and Anupam Jyoti**[2]

[1]*Amity Institute of Biotechnology, Amity University Rajasthan, Amity Education Valley, Kant Kalwar, NH-11C, Jaipur-Delhi Highway, Jaipur, India*
[2]*Faculty of Applied Sciences and Biotechnology, Shoolini University of Biotechnology and Management Sciences, Bajhol, Solan, Himachal Pradesh, India*

Correspondence should be addressed to Anupam Jyoti; anupamjyoti@rediffmail.com

Vijay Kumar Srivastava, Sanket Kaushik, and Gazal Bhargava contributed equally to this work.

Received 15 July 2021; Revised 16 September 2021; Accepted 17 September 2021; Published 5 October 2021

Academic Editor: Andrey Cherstvy

Background. B.1.617.1, a variant of severe acute respiratory syndrome coronavirus-2 (SARS-CoV-2) causing respiratory illness is responsible for the second wave of COVID-19 and associated with a high incidence of infectivity and mortality. To mitigate the B.1.617.1 variant of SARS-CoV-2, deciphering the protein structure and immunological responses by employing bioinformatics tools for data mining and analysis is pivotal. *Objectives*. Here, an in silico approach was employed for deciphering the structure and immune function of the subunit of spike (S) protein of SARS-CoV-2 B.1.617.1 variant. *Methods*. The partial amino acid sequence of SARS-CoV-2 B.1.617.1 variant S protein was analyzed, and its putative secondary and tertiary structure was predicted. Immunogenic analyses including B- and T-cell epitopes, interferon-gamma (IFN-γ) response, chemokine, and protective antigens for SARS-CoV 2 S proteins were predicted using appropriate tools. *Results*. B.1.617.1 variant S protein sequence was found to be highly stable and amphipathic. ABCpred and CTLpred analyses led to the identification of two potential antigenic B cell and T cell epitopes with starting amino acid positions at 60 and 82 (for B cell epitopes) and 54 and 98 (for T cell epitopes) having prediction scores > 0.8. Further, RAMPAGE tool was used for determining the allowed and disallowed regions of the three-dimensional predicted structure of SARS-CoV-2 B.1.617.1 variant S protein. *Conclusion*. Together, the in silico analysis revealed the predicted structure of partial S protein, immunogenic properties, and possible regions for S protein of SARS-CoV-2 and provides a valuable prelude for engineering the targeted vaccine or drug against B.1.617.1 variant of SARS-CoV-2.

1. Introduction

Coronaviruses (CoVs), belonging to the family Coronaviridae, are enveloped nonsegmented, single-stranded positive-sense RNA viruses and infect humans and various animals (bats, birds, camels, cats, dogs, and mice) [1]. Based on the genome sequence, CoVs have been further categorized into four genera, i.e., the alpha, beta, gamma, and delta [2]. Six different species of CoVs infecting humans, all belonging to betacoronavirus, have been identified, i.e., human coronavirus (HCoV) 229E, HCoV-OC43, SARS-CoV, HCoV-NL63, HCoV-HKU1, and Middle East respiratory syndrome coronavirus (MERS-CoV). Except for SARS-CoV and MERS-CoV, the other four viruses cause the common cold in immunocompromised subjects [3].

In 2003, the SARS-CoV emerged in Guangdong province in South China, which causes severe acute respiratory syndrome [4]. In 2012, the Middle East respiratory syndrome (MERS) was first identified in Saudi Arabia infecting ~2500 of which more than 800 resulted in death and rapidly spread in 27 countries across the globe [5]. Both SARS-CoV and MERS-CoV are zoonotic, and in human, they infect the upper respiratory tract causing common cold as well as lower respiratory tract resulting in bronchitis, whooping cough, and pneumonia [4, 5], and till to date, there is no approved therapeutic molecule for the treatment.

In December 2019, a large number of cases with pneumonia were reported and epidemiologically linked with the seafood market in Wuhan in Hubei province in China [6]. The causative agent was identified as novel CoV using state-of-art next-generation sequencing technology of the specimen isolated from the patient. Further, it has been coined the name SARS-CoV-2 due to 87% sequence similarity with the two bat-derived SARS-like CoV strains (bat-SL-CoVZC45 and bat-SL-CoVZXC21) having single-stranded RNA genome with size from 29 to 30 Kb [7, 8]. On 11 February 2020, the World Health Organization (WHO) named COVID-19 for the new disease caused by SARS-CoV-2 (https://www.who.int/emergencies/diseases/novel-coronavirus-2019/technical-guidance/naming-the-coronavirus-disease-(covid-2019)-and-the-virus-that-causes-it). COVID-19 rapidly spread across Asia (India, Iran, Japan, Pakistan, Saudi Arabia, South Korea, and Turkey), Europe (France, Germany, Italy, Netherlands, Switzerland, and the UK), North America (Mexico and the USA), South America (Brazil, Chile, and Peru), Africa (Algeria, Egypt, Ghana, Nigeria, and South Africa), and Oceania (Australia, New Zealand, and French Polynesia) (https://covid19.who.int/). The menace remains unabated and is continuously ravaging in other parts of the world. As of September 16, 2021, globally, there have been 225,680,357 confirmed cases of COVID-19, including 4,644,740 deaths (https://covid19.who.int/). Human to human transmission of SARS-CoV-2 has been reported, and infected patients are diagnosed with fever, cough, fatigue, and difficulty breathing [9, 10].

SARS-CoV-2 genome encodes several nonstructural, structural, and accessory proteins [11]. There has been a global endeavour by the researchers to decipher the structural-functional relations of the important proteins of SARS-CoV-2, to get an insight into the mechanistic details of their binding targets on human cells [11–15]. The S protein on the virus interacts with the angiotensin-converting enzyme 2 (ACE2) receptor present over human cells led to the internalization of SARS-CoV-2 within the cells [16]. Mutations in the S protein have been reported to enhance the binding with ACE2 [17]. The therapeutic strategies to inhibit the host recognition, and attachment of host with the virus by targeting S protein could be an attractive paradigm for developing anti-SARS-CoV-2 drugs.

The ongoing global spread of SARS-CoV-2 has led to the emergence of new strains with profound and stable mutations. Among these strains, B.1.617.1 lineage first identified in India and subsequently spread to the other parts of the world are characterized by mutations in S as well as other proteins. This lineage has been categorized as variants of interest by CDC, hence underscoring the importance of study in terms of physiochemical properties, immunogenic potential, and protein structure prediction.

Table 1: Physiochemical properties of the QUX03874.1 S protein from SARS-CoV-2 computed using ExPASy ProtParam tool.

No.	Properties	QUX03874.1
1.	Number of amino acids	167
2.	Molecular weight (kDa)	18.608
3.	Formula	$C_{837}H_{1268}N_{226}O_{247}S_5$
4.	Total number of atoms	2583
5.	Theoretical pI	9.09
6.	EC	20650
7.	AI	65.33
8.	GRAVY	-0.458 (hydrophilic)
9.	II	14.45 (protein is stable)

Both patient/host response and virus-specific information are pivotal in the clinical management of the disease including diagnosis and therapeutics. Recognition of the pathogen key protein by host cells to induce the immune system is of paramount importance as this is helpful in the designing of the vaccine. Identifying key pathogenic protein using homology modeling, a state-of-the-art bioinformatics tool is a viable strategy for designing of vaccine and therapeutic molecule. Further, identification of the permissible and nonpermissible regions is critical for identifying the potential drug targets with therapeutic efficacy.

Here, the in silico approach was employed to decipher the structure and function of the partial S protein of SARS-CoV-2 B.1.617.1 variant S protein. The SWISS-MODEL and PyMOL were used for the analysis of the amino acid sequence of SARS-CoV-2 B.1.617.1 variant S protein, and the prediction of the putative secondary and tertiary structure. Further, the ABCpred, TCLpred, CHEMOpred, and Vaxijen servers were used for identifying the immunoepitopes in the B.1.617.1 variant S protein. The RAMPAGE tool was then used for deducing and analyzing the Ramachandran plot for predicting the permissible and nonpermissible regions of the three-dimensional (3 D) structure of the SARS-CoV-2 B.1.617.1 variant S protein.

2. Materials and Methods

2.1. Physiochemical Characterization. ProtParam tool (http://web.expasy.org/protparam/) on ExPASy server was used for determining the physicochemical properties, i.e., molecular weight (Mw), isoelectric point (pI), amino acid composition, extinction coefficient (EC), instability index (II), aliphatic index (AI), and grand average of hydropathicity (GRAVY) of QUX03874.1 S protein [18].

2.2. In Silico Prediction of Immunogenic Properties. Online tools including ABCpred [19], CTLpred [20], CHEMOpred [21], and Vaxijen server [22] were used to predict B-cell

Table 2: Prediction of epitopes (B and CTL), IFN-γ response, and probable antigen of SARS-CoV-2 B.1.617.1 variant S protein (QUX03874.1).

B-cell epitope				CTL epitope				Antigen potential	Chemokine
Rank	Position	Sequences/IFN-γ response	Score	Rank	Position	Sequences/IFN-γ response	Score	Prediction score	Prediction
1	60	TEIYQAGSTPCNGVQG/negative	0.93	1	54	FERDISTEI/negative	1.00	0.5656	Nonchemokine
2	82	LQSYGFQPTNGVGYQP/negative	0.90	2	98	YRVVVLSFE/negative	0.99		Nonchemokine

epitopes, CTL epitopes, chemokines, and protective antigen, respectively. B-cell epitopes in B.1.617.1 variant S protein QUX03874.1 were predicted using ABCpred tool (http://www.imtech.res.in/raghava/abcpred/). The QUX03874.1 S protein was also screened for the presence of potential CTL epitopes using CTLPred online server (http://www.imtech.res.in/raghava/ctlpred/). Both ABCpred and CTLpred are based on machine learning techniques such as artificial neural network and support vector machine, and epitope prediction was performed by employing a fixed-length pattern for the identification of continuous B-cell and T-cell epitopes with the threshold for scoring was set at 0.8. A higher score was commensurate with a higher probability of the existing epitope. Further, the antigenicity of the peptides was predicted using VaxiJen v2.0 tool (http://www.ddg-pharmfac.net/vaxijen/VaxiJen/VaxiJen.html). Further, interferon-gamma (IFN-γ) response for predicted epitopes was evaluated using the IFNepitope (http://crdd.osdd.net/raghava/ifnepitope/index.php) [23]. For the prediction of chemokines, ChemoPred, a support vector machine-based approach (https://webs.iiitd.edu.in/raghava/chemopred/index.html) was used with default parameters.

2.3. Alignment of the Sequence. The primary S protein sequence from SARS-CoV-2 B.1.617.1 variant, QUX03874.1, was identified from the ExPASy database [24]. The BLASTP against the Protein Data Bank (PDB) was carried out to determine the protein template for the QUX03874.1 and subsequent prediction of the model. The search revealed an identical sequence from Homo sapiens viral protein (Human SARS coronavirus) with PDB entry 7KQE [25]. This sequence was then used for in silico modeling. ClustalW tool [26] was used for the equivalent sequence alignment with 7KQE as a template.

2.4. Structure Prediction and Validation. SWISS-MODEL, a fully automated server that creates protein structure homology modeling [27], was used to predict the 3D structure of QUX03874.1 (partial S protein) from SARS-CoV-2 B.1.617.1 variant. The program comprises three steps, i.e., (i) the PDB file of the structures (7KQE), (ii) the alignment of the target sequence and recognized structures, and (iii) the visualization of the predicted structure using PyMol (http://www.pymol.org/). The Qualitative Model Energy ANalysis (QMEAN) and Global Model Quality Estimation (GMQE) values of the SWISS-MODEL server were used for assessing the fidelity of the structure. PROCHECK determines the stereochemical quality of the protein structure (http://www.ebi.ac.uk/thornton-srv/software/PROCHECK) [28] and was thus used for determining the attributes of the predicted 3D structure of SARS-CoV-2 B.1.617.1 variant S protein (QUX03874.1). Further, RAMPAGE was used to decipher the Ramachandran plot analysis of the model, which revealed the phi versus psi dihedral angles for each residue in the input PDB file, and also exhibited the allowed and disallowed regions for the in silico structured model based on the density-dependent smoothing.

Table 3: Sequence identity between the template and the modeled structure.

Modeled structure	Most favored regions	Additional allowed regions	Generously allowed regions	Disallowed regions
QUX03874.1	84.2%	15.8%	0.0%	0.0%

3. Results

3.1. Physicochemical Properties of the Proteins. The physicochemical properties of the protein QUX03874.1 of SARS-CoV-2 B.1.617.1 variant S protein were determined, which comprise 167 amino acids, and its molecular weight, total number of atoms, pI, and net charge are presented in Table 1. For QUX03874.1, the GRAVY index was -0.458, which indicated their hydrophilic nature. The II value of 14.45 for QUX03874.1, suggested the stability of this protein. Moreover, AI value of 65.33 for QUX03874.1 corroborated its stability over a wide range of temperature regime and consistent with earlier studies [29, 30].

3.2. Immunogenic Properties of SARS-CoV-2 B.1.617.1 Variant S Protein. The ABCpred and CTLpred were used for the determination of B-cell and T-cell epitopes for S protein of SARS-CoV-2 B.1.617.1 variant. Scores > 0.51 account for the potential epitope, and its higher probability. Therefore, the threshold value was set at 0.51 for a putative antigen. For the SARS-CoV-2 B.1.617.1 variant S protein, two potential B-cell and two T-cell linear epitopes revealed scores ≥ the threshold value of 0.8, which suggested their high propensity of being recognized (Table 2). B-cell epitope predictions showed 12 sequences having probability to be as

```
7KQE        APGQTGKIADYNYKLPDDFTGCVIAWNSNNLDSKVGGNYNYLYRLFRKSNLKPFERDIST   60
QUX03874.1  APGQTGKIADYNYKLPDDFTGCVIAWNSNNLDSKVGGNYNYRYRLFRKSNLKPFERDIST   60

7KQE        EIYQAGSTPCNGVEGFNCYFPLQSYGFQPTNGVGYQPYRVVVLSFELLHAPATVCGPKKS   120
QUX03874.1  EIYQAGSTPCNGVQGFNCYFPLQSYGFQPTNGVGYQPYRVVVLSFELLHAPATVCGPKKS   120

7KQE        TNLVKNKCVNFNFNGLTGTGVLTESNKKFLPFQQFGRDIADTTDAVR 167
QUX03874.1  TNLVKNKCVNFNFNGLTGTGVLTESNKKFLPFQQFGRDIADTTDAVR 167
```

Figure 1: Sequence alignment of QUX03874.1 protein with the 7KQE from *Homo sapiens* viral protein: the amino acids that differ in the alignment were highlighted with blue color.

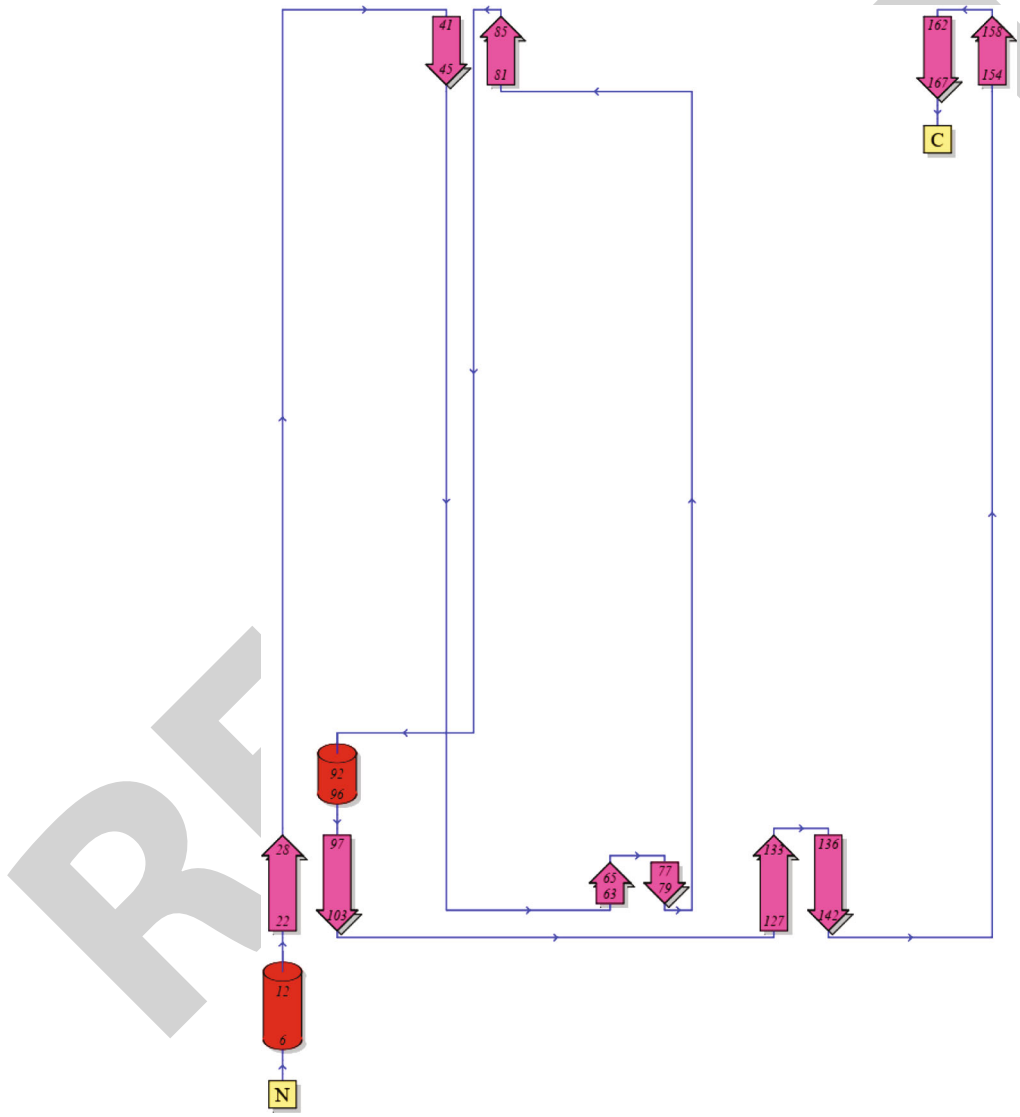

Figure 2: Topology diagram of S protein showing the overall fold: α-helices are indicated by red cylinders and β-sheets by pink arrow.

epitope with score > 0.51. Among these, two peptide sequences TEIYQAGSTPCNGVQG and LQSYGFQPTNGVGYQP peptides at 60 and 82 positions were highly antigenic with scores 0.93 and 0.9, respectively. T-cell epitope predictions displayed 46 sequences as probable CTL epitope with score > 0.51. Among these, two peptides' sequences FERDISTEI and YRVVVLSFE at 54 and 98 positions with a highly antigenic score of 1 and 0.99, respectively. Further, QUX03874.1 of SARS-CoV-2 S protein displayed antigenic response with a score 0.56 and no

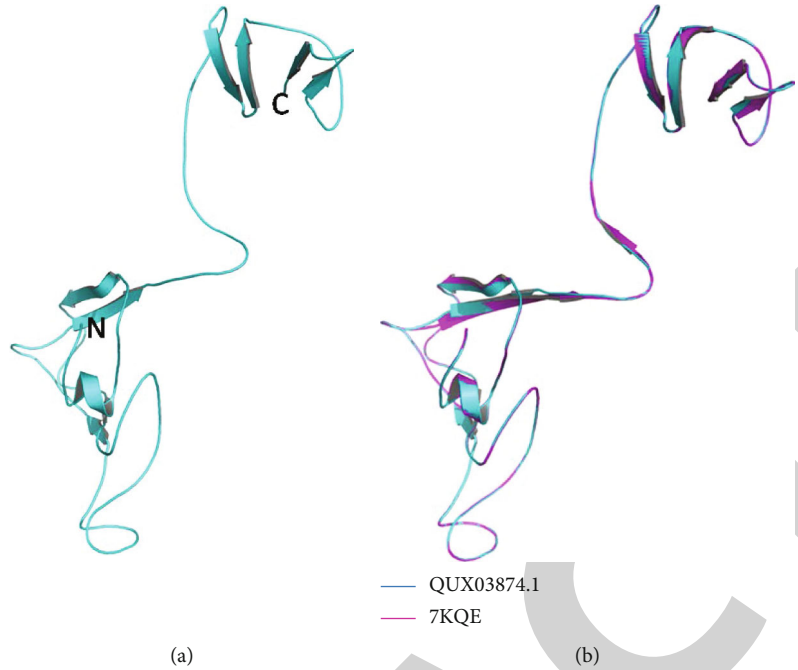

Figure 3: Homology modeling and superposition of the structures from QUX03874.1 protein. (a) Modeled structure of QUX03874.1 represented as cyan color and N and C terminal marked. (b) Superposition of QUX03874.1 with the template 7KQE represented as cyan and purple in color, respectively.

Table 4: Ramachandran plot statistics of modeled structure of the QUX03874.1 S protein from SARS-CoV-2 B.1.617.1 variant.

Accession number	Template	Sequence identity (%)	RMSD deviation (Å)
QUX03874.1	7KQE	98.8	0.23

IFN-γ response as predicted using the VaxiJen v2.0 and IFNepitope tool, respectively.

3.3. In Silico Molecular Modeling of QUX03874.1 Coding Sequences of SARS-CoV-2 B.1.617.1 Variant S Protein. The sequence alignment of QUX03874.1 with the known structure 7KQE indicated that apart from the high % sequence identity (Table 3), some of the residues marked as stars are different from the known structure (Figure 1). The predicted topology showed that QUX03874.1 protein comprises two helices and five beta sheets (Figure 2). For the subsequent analysis, 7KQE was used as a reference for modeling the QUX03874.1 protein based on the already recognized electron microscopic structure of Homo sapiens viral protein (Human SARS coronavirus). The model generated was accurate for the angle and length of the bonds. SWISS-MODEL was then employed for generating a single model from the ClustalX files generated through sequence alignment and visualized qualitatively and quantitatively, which revealed the lowest root mean square deviation (RMSD) value with the template (Table 3; Figures 3(a) and 3(b)). Subsequently, the PROCHECK was employed for deciphering the stereochemistry (psi and phi angles) of the models, which produced several files comprising detailed data of the amino acids and the stringency of the generated structure (Table 4; Figure 4) in concurrence with the structures of the similar resolution [31]. The Ramachandran plot analysis of the recognized structures of QUX03874.1 revealed 84.2% of amino acids are in the most favored regions and 15.8% in additionally allowed regions, and no amino acid detected in the generously allowed and disallowed regions. Overall, the analysis revealed the fidelity of the predicted model and concurred with the 7KQE.

4. Discussion

The COVID-19 pandemic has resulted in a loss of more than 4 million human life with maximum casualties in the USA, Brazil, India, Mexico, Peru, Russian Federation, the UK, and Italy (as of September 16, 2021; https://www.worldometers.info/coronavirus/#countries). Further on, mutations and emergence of new variants of SARS-CoV-2 led to the surge of the second and third waves of COVID-19, and it has cost many lives. Among the different variants, B.1.617.1 has rapidly spread in India and to several countries throughout the world. Recent report has suggested that this variant is 6.8-fold less susceptible to neutralization by sera from COVID-19 convalescent and Moderna- and Pfizer-vaccinated individuals [32].

The number of deaths continues to increase across the globe, and there seems to be no respite from this menace. Therefore, there has been an unprecedented global endeavor almost at the war footing by the researchers to design and develop a potent vaccine against SARS-COV-2 B.1.617.1 variant to mitigate highly contagious and life-threatening COVID-19. In this context, an in silico approach for

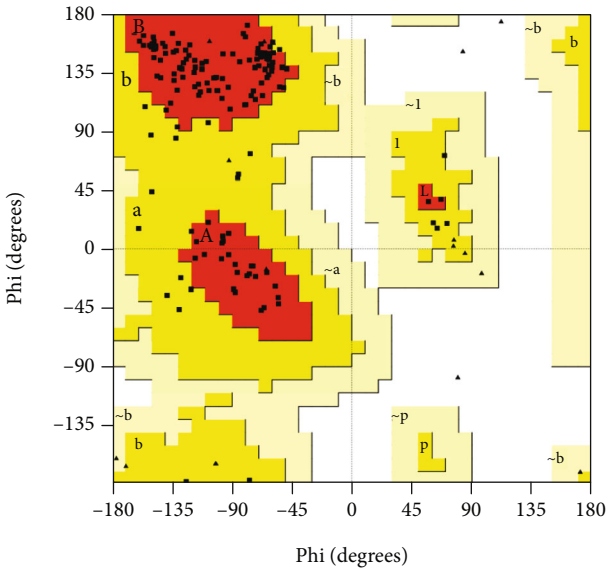

Figure 4: Ramachandran plot generated by PROCHECK software show Psi and Phi bond angles, white regions coincide to sterically disallowed region, red areas coincide to allowed regions, and yellow regions correspond to the atoms in the generously allowed regions for QUX03874.1.

deciphering the structure and function of the S protein of SARS-CoV-2 B.1.617.1 variant is a pivotal prelude to the development of a potent vaccine.

In the current paper, we have predicted the structure and functions of SARS-CoV-2 B.1.617.1 variant partial S protein using state of art bioinformatics approach. The validity of the predicted structure was also studied. Further, immunogenic properties of B.1.617.1 variant S protein using B-cell epitopes, T-cell epitopes, chemokines, antigen, and IFN-γ response prediction tools were also employed.

The 3D structures of some of the important proteins of SARS-CoV-2 have now been predicted [33–36; https://www.rcsb.org/]. Here, various physicochemical properties of the protein QUX03874.1 of B.1.617.1 variant S protein were deciphered. The high II values of protein (Table 1) and its hydrophilic nature suggested its high stability and thus deemed to be a potential candidate for engineering vaccine against COVID-19. The specific residues present in the protein act as antigenic epitopes [19].

In silico tool ABCpred, CTLpred, CHEMOpred, and Vaxijen servers were used for predicting the immunogenic properties of B.1.617.1 variant S protein (Table 2). Two potential B-cell linear epitopes were predicted with scores equal or more than 0.8 in QUX03874.1. This is in agreement with the recent study where B-cell epitopes have been predicted using Bepipred 2.0 [13, 37]. We also predicted and analyzed T cell epitopes in B.1.617.1 variant S protein. We found two potential T-cell epitopes with scores equal or above 0.99 in QUX03874.1. Hence, upon SARS-CoV-2 infection, both the arms of adaptive immunity (B and T cells) are likely to elicit immunological responses. The predicted immunoepitopes may play an important role in the initiation of the immune response.

The topology of the B.1.617.1 variant S protein revealed the fold comprising α-helices and β-sheets (Figure 2). It is the most prominent protein structure spanning the plasma membrane and can form hydrogen bonds, which confers stability [38]. Superimposition of QUX03874.1 with 7KQE revealed a high degree of structural overlap and sequence similarity, which was corroborated with the lowest RMSD (Table 3; Figures 3(a) and 3(b)). An earlier study has also reported an inverse correlation between the high incidence of the structural and sequence identity and RMSD value [39]. The QMEAN, *Z*-score, and analysis of the Ramachandran plot validated the high-quality of the 3D structure of QUX03874.1 (Table 4; Figure 4) and concurred with an earlier study on the hypothetical protein MG_377 in *Mycoplasma genitalium* [41]. The predicted model of QUX03874.1 could be used as a template for identifying the interaction of the protein and docking with the ligand and putative drugs, which may aid in the discovery of novel drug molecules for fighting the viral disease. However, at present, the function of QUX03874.1 remains enigmatic and merits in-depth studies involving their three-dimensional X-ray structural analysis and posttranslational modifications.

5. Conclusion

An in silico approach was employed for deciphering the structure and key immunogenic properties, for partial S protein of SARS-CoV-2 B.1.617.1 variant. The study provides valuable insights that could be useful for the development of monoclonal antibodies, inhibitors, or vaccines targeting S protein of SARS-CoV-2 B.1.617.1 variant, as well as diagnostic tools shortly, which warrants empirical validation by rigorous and stringent wet-lab experiments.

Data Availability

All the data in this manuscript is available with the corresponding author upon formal request.

Conflicts of Interest

The authors declare no conflict of interest.

Authors' Contributions

Vijay Kumar Srivastava, Sanket Kaushik, and Gazal Bhargava contributed equally to this work.

References

[1] S. R. Weiss and J. L. Leibowitz, "Coronavirus pathogenesis," *Advances in Virus Research*, vol. 81, pp. 85–164, 2011.

[2] S. Su, G. Wong, W. Shi et al., "Epidemiology, genetic recombination, and pathogenesis of coronaviruses," *Trends in Microbiology*, vol. 24, no. 6, pp. 490–502, 2016.

[3] J. Cui, F. Li, and Z.-L. Shi, "Origin and evolution of pathogenic coronaviruses," *Nature Reviews Microbiology*, vol. 17, no. 3, pp. 181–192, 2019.

[4] N. S. Zhong, B. J. Zheng, Y. M. Li et al., "Epidemiology and cause of severe acute respiratory syndrome (SARS) in Guangdong, People's Republic of China, in February, 2003," *The Lancet*, vol. 362, no. 9393, pp. 1353–1358, 2003.

[5] A. M. Zaki, S. van Boheemen, T. M. Bestebroer, A. D. M. E. Osterhaus, and R. A. M. Fouchier, "Isolation of a novel coronavirus from a man with pneumonia in Saudi Arabia," *New England Journal of Medicine*, vol. 367, no. 19, pp. 1814–1820, 2012.

[6] H. Lu, C. W. Stratton, and Y.-W. Tang, "Outbreak of pneumonia of unknown etiology in Wuhan, China: the mystery and the miracle," *Journal of Medical Virology*, vol. 92, no. 4, pp. 401-402, 2020.

[7] J. Chen, "Pathogenicity and transmissibility of 2019-nCoV–A quick overview and comparison with other emerging viruses," *Microbes and Infection*, vol. 22, no. 2, pp. 69–71, 2020.

[8] N. Zhu, D. Zhang, W. Wang et al., "A novel coronavirus from patients with pneumonia in China, 2019," *The New England Journal of Medicine*, vol. 382, no. 8, pp. 727–733, 2020.

[9] J. F. W. Chan, S. Yuan, K. H. Kok et al., "A familial cluster of pneumonia associated with the 2019 novel coronavirus indicating person-to-person transmission: a study of a family cluster," *The Lancet*, vol. 395, no. 10223, pp. 514–523, 2020.

[10] C. Huang, Y. Wang, X. Li et al., "Clinical features of patients infected with 2019 novel coronavirus in Wuhan, China," *The lancet*, vol. 395, no. 10223, pp. 497–506, 2020.

[11] S. Srinivasan, H. Cui, Z. Gao et al., "Structural genomics of SARS-CoV-2 indicates evolutionary conserved functional regions of viral proteins," *Viruses*, vol. 12, no. 4, p. 360, 2020.

[12] D. Wrapp, N. Wang, K. S. Corbett et al., "Cryo-EM structure of the 2019-nCoV spike in the prefusion conformation," *Science*, vol. 367, no. 6483, pp. 1260–1263, 2020.

[13] A. Grifoni, J. Sidney, Y. Zhang, R. H. Scheuermann, B. Peters, and A. Sette, "A sequence homology and bioinformatic approach can predict candidate targets for immune responses to SARS-CoV-2," *Cell Host & Microbe*, vol. 27, no. 4, pp. 671–680.e2, 2020.

[14] R. S. Joshi, S. S. Jagdale, S. B. Bansode et al., "Discovery of potential multi-target-directed ligands by targeting host-specific SARS-CoV-2 structurally conserved main protease," *Journal of Biomolecular Structure and Dynamics*, vol. 39, no. 9, pp. 3099–3114, 2021.

[15] J. Shang, G. Ye, K. Shi et al., "Structural basis of receptor recognition by SARS-CoV-2," *Nature*, vol. 581, no. 7807, pp. 221–224, 2020.

[16] F. Li, W. Li, M. Farzan, and S. C. Harrison, "Structure of SARS coronavirus spike receptor-binding domain complexed with receptor," *Science*, vol. 309, no. 5742, pp. 1864–1868, 2005.

[17] Y. Wan, J. Shang, R. Graham, R. S. Baric, and F. Li, "Receptor recognition by the novel coronavirus from Wuhan: an analysis based on decade-long structural studies of SARS coronavirus," *Journal of Virology*, vol. 94, no. 7, pp. e00127–e00320, 2020.

[18] E. Gasteiger, C. Hoogland, A. Gattiker et al., "Protein identification and analysis tools on the ExPASy server," *The proteomics protocols handbook*, pp. 571–607, 2005.

[19] S. Saha and G. P. S. Raghava, "Prediction of continuous B-cell epitopes in an antigen using recurrent neural network," *Proteins: Structure, Function, and Bioinformatics*, vol. 65, no. 1, pp. 40–48, 2006.

[20] S. Lata and G. P. S. Raghava, "Prediction and classification of chemokines and their receptors," *Protein Engineering, Design & Selection*, vol. 22, no. 7, pp. 441–444, 2009.

[21] I. A. Doytchinova and D. R. Flower, "VaxiJen: a server for prediction of protective antigens, tumour antigens and subunit vaccines," *BMC Bioinformatics*, vol. 8, no. 1, pp. 1–7, 2007.

[22] S. K. Dhanda, P. Vir, and G. P. S. Raghava, "Designing of interferon-gamma inducing MHC class-II binders," *Biology direct*, vol. 8, no. 1, pp. 1–15, 2013.

[23] P. Artimo, M. Jonnalagedda, K. Arnold et al., "ExPASy: SIB bioinformatics resource portal," *Nucleic Acids Research*, vol. 40, no. W1, pp. W597–W603, 2012.

[24] QCRG Structural Biology Consortium, C. J. Bracken, S. A. Lim et al., "Bi-paratopic and multivalent VH domains block ACE2 binding and neutralize SARS-CoV-2," *Nature Chemical Biology*, vol. 17, no. 1, pp. 113–121, 2021.

[25] M. A. Larkin, G. Blackshields, N. P. Brown et al., "Clustal W and Clustal X version 2.0.," *bioinformatics*, vol. 23, no. 21, pp. 2947-2948, 2007.

[26] B. Webb and A. Sali, "Comparative protein structure modeling using MODELLER," *Current Protocols in Bioinformatics*, vol. 54, no. 1, pp. 5-6, 2016.

[27] R. A. Laskowski, M. W. MacArthur, D. S. Moss, and J. M. Thornton, "*PROCHECK*: a program to check the stereochemical quality of protein structures," *Journal of Applied Crystallography*, vol. 26, no. 2, pp. 283–291, 1993.

[28] K. Guruprasad, B. V. B. Reddy, and M. W. Pandit, "Correlation between stability of a protein and its dipeptide composition: a novel approach for predictingin vivostability of a protein from its primary sequence," *Protein Engineering, Design and Selection*, vol. 4, no. 2, pp. 155–161, 1991.

[29] A. Ikai, "Thermostability and aliphatic index of globular proteins," *The Journal of Biochemistry*, vol. 88, no. 6, pp. 1895–1898, 1980.

[30] E. W. Lamirande, M. L. DeDiego, A. Roberts et al., "A live attenuated severe acute respiratory syndrome coronavirus is immunogenic and efficacious in golden Syrian hamsters," *Journal of virology*, vol. 82, no. 15, pp. 7721–7724, 2008.

[31] V. V. Edara, L. Lai, M. Sahoo et al., "Infection and vaccine-induced neutralizing antibody responses to the SARS-CoV-2 B. 1.617. 1 variant," 2021, https://www.biorxiv.org/content/10.1101/2021.05.09.443299v1.abstract.

[32] L. Zhang, D. Lin, X. Sun et al., "Crystal structure of SARS-CoV-2 main protease provides a basis for design of improved α-ketoamide inhibitors," *Science*, vol. 368, no. 6489, pp. 409–412, 2020.

[33] A. C. Walls, Y.-J. Park, M. A. Tortorici, A. Wall, A. T. McGuire, and D. Veesler, "Structure, function, and antigenicity of the SARS-CoV-2 spike glycoprotein," *Cell*, vol. 181, no. 2, pp. 281–292.e6, 2020.

[34] R. Yan, Y. Zhang, Y. Li, L. Xia, Y. Guo, and Q. Zhou, "Structural basis for the recognition of SARS-CoV-2 by full-length human ACE2," *Science*, vol. 367, no. 6485, pp. 1444–1448, 2020.

[35] H. Zhang, J. M. Penninger, Y. Li, N. Zhong, and A. S. Slutsky, "Angiotensin-converting enzyme 2 (ACE2) as a SARS-CoV-2 receptor: molecular mechanisms and potential therapeutic target," *Intensive Care Medicine*, vol. 46, no. 4, pp. 586–590, 2020.

[36] D. O'Neil, C. Swanton, A. Jones, P. G. Medd, N. Rayment, and B. Chain, "IFN-gamma down-regulates MHC expression and antigen processing in a human B cell line," *The Journal of Immunology*, vol. 162, no. 2, pp. 791–798, 1999.

[37] S.-C. Chen, S.-Y. Lo, H.-C. Ma, and H.-C. Li, "Expression and membrane integration of SARS-CoV E protein and its

Hindawi
BioMed Research International
Volume 2024, Article ID 9836392, 1 page
https://doi.org/10.1155/2024/9836392

Retraction

Retracted: Lineage Contribution of PDGFRα-Expressing Cells in the Developing Mouse Eye

BioMed Research International

Received 12 March 2024; Accepted 12 March 2024; Published 20 March 2024

This article has been retracted by Hindawi following an investigation undertaken by the publisher [1]. This investigation has uncovered evidence of one or more of the following indicators of systematic manipulation of the publication process:

(1) Discrepancies in scope

(2) Discrepancies in the description of the research reported

(3) Discrepancies between the availability of data and the research described

(4) Inappropriate citations

(5) Incoherent, meaningless and/or irrelevant content included in the article

(6) Manipulated or compromised peer review

The presence of these indicators undermines our confidence in the integrity of the article's content and we cannot, therefore, vouch for its reliability. Please note that this notice is intended solely to alert readers that the content of this article is unreliable. We have not investigated whether authors were aware of or involved in the systematic manipulation of the publication process.

Wiley and Hindawi regrets that the usual quality checks did not identify these issues before publication and have since put additional measures in place to safeguard research integrity.

We wish to credit our own Research Integrity and Research Publishing teams and anonymous and named external researchers and research integrity experts for contributing to this investigation.

The corresponding author, as the representative of all authors, has been given the opportunity to register their agreement or disagreement to this retraction. We have kept a record of any response received.

References

[1] D. Zhuo, Y. Diao, X. Li, Y. Huang, and L. Wang, "Lineage Contribution of PDGFRα-Expressing Cells in the Developing Mouse Eye," *BioMed Research International*, vol. 2021, Article ID 4982227, 10 pages, 2021.

Hindawi
BioMed Research International
Volume 2021, Article ID 4982227, 10 pages
https://doi.org/10.1155/2021/4982227

Research Article

Lineage Contribution of PDGFRα-Expressing Cells in the Developing Mouse Eye

Deyi Zhuo, Yumei Diao, Xiaoqi Li, Yifei Huang, and Liqiang Wang

Department of Ophthalmology, The Third Medical Center of Chinese PLA General Hospital, Beijing 100853, China

Correspondence should be addressed to Liqiang Wang; liqiangw301@163.com

Received 5 June 2021; Revised 16 June 2021; Accepted 21 June 2021; Published 5 July 2021

Academic Editor: Bing Niu

PDGFRα signaling is critically important in ocular development. Previous data on PDGFRα lacks an expression map with high spatial and temporal resolution and lineage information. In this study, we aim to present a detailed PDGFRα expression and lineage map from early embryogenesis to adulthood. PDGFRα-CreER; mT/mG reporter mice were analyzed. mEGFP-positive cells contributed to multiple ocular lineages in a spatiotemporally regulated manner. A dynamic PDGFRα expression was identified in corneal stromal cells, lens epithelial cells, lens fiber cells, and retinal astrocytes during the entire period of eye development, while PDGFRα expression in retinal astrocytes from E17.5 onwards and in Müller glial cells was identified within two weeks after birth. By revealing detailed characterization of gene expression and function, we present a comprehensive map of PDGFRα-expressing cells in the eye for a better understanding of PDGFRα signaling's role during eye development.

1. Introduction

The vertebrate eye is a very complex organ, and its development has been widely characterized [1, 2]. Ocular development commences during gastrulation with the single central eye field (late gastrula stage). The singular eye field subsequently splits into two lateral parts to form the optic vesicle and the lens placode (placode stage, E9.5 in the mouse) [3]. Shortly afterwards, the lens placode invaginates to a lens pit, which occurs coordinately with optic cup invagination (lens pit stage, E10.5 in the mouse) [4]. At E11.5 in the mouse (optic cup stage), the future cornea, lens, and retina become visible. The anterior eye tissues evolve to form the surface ectoderm, lens, and corneal epithelium, while the surrounding neural crest cells give rise to the corneal stroma and corneal endothelium [5]. The retina comes from the underlying neural ectoderm. Development of the eye depends on the proper function of various transcription factors and signaling pathways [6, 7].

The PDGF family consists of two receptor genes, PDGFRα and PDGFRβ, and four ligand genes, PDGF-A, PDGF-B, PDGF-C, and PDGF-D [8–10]. PDGF-A and PDGF-C exclusively bind and activate PDGFRα in vivo [11, 12]. PDGFRα signaling has a broader role in embryogenesis and function during organogenesis, such as lung alveogenesis, intestinal villus morphogenesis, hair morphogenesis, testis spermatogenesis, and oligodendrogenesis [13]. PDGFRα signaling is also essential in ocular development, particularly involving the cornea, lens, and retina. PDGFRα null embryos display developmental abnormalities in multiple organs and systems, and this could even result in embryonic lethality [14–16]. Homozygous Patch mutation in mice, which is a deletion of the gene encoding PDGFRα, presents a thinned cornea and a decreased number of fiber cells within the mutant lens [17]. A detailed analysis of the PDGFRα null lens shows retarded elongation of primary lens fiber cells, anteriorly shifted transitional zone, and smaller lens size [18]. Overexpression of PDGF-A under the αA-crystallin promoter results in lenticular defects and hyperplasia of retinal astrocytes [19, 20].

PDGFRα expression has been detected in the embryonic eye using immunohistochemistry (IHC) and/or RNA in situ hybridization (ISH) in early studies [19]. However, ISH is technically difficult to perform on adult tissues [21]. Moreover, IHC-based expression studies often cannot explain the potential fate and lineage of the cells that express the gene

of interest [22]. In addition, only very few studies have focused on PDGFRα's role in the embryonic and postnatal eye simultaneously. Due to limited spatial and temporal resolution, the existing data is not able to provide sufficient information as to which ocular lineage(s) expresses PDGFRα or its expression duration in that lineage. Therefore, the spatiotemporal requirement for PDGFRα in ocular development remains to be elucidated.

In this study, we map the detailed expression and lineage analyses of PDGFRα from embryonic to adult ages in the eye, aiming at comprehensively understanding PDGFRα signaling during eye development.

2. Materials and Methods

2.1. Animals. PDGFRα-CreER^{T2} transgenic mice are crossmated with ACTB-tdTomato, -EGFP reporter mice in order to generate PDGFRα-CreERT2; mT/mG mice [23]. Genotyping is performed as previously described. To genotype the CreER^{T2} allele, PCR Genotyping is performed with genomic DNA extracted from tail tip with sense primer (5′-ATCCCATCAGCTCACAGACTTCGGA-3′) and antisense primer (5′-GCTCTTCGCCCTTAGACACCATAGG-3′) specific for the CreER^{T2}. To detect the wild-type PDGFRα allele, sense primer (5′-ATCCCATCAGCTCACAGACTTCGGA-3′) and antisense primer (5′-CAAGAGGCAACACGGATAAAGTTCA-3′) are used for PCR. The PCR products for CreER^{T2} wild-type and knock-in alleles are 353 bp and 243 bp, respectively. To genotype mice expressing the mT/mG transgene, three primers are used: mT/mG wild type 5′-CTCTGCTGCCTCCTGGCTTCT-3′, mT/mG wild type 5′-CGAGGCGGATCACAAGCAATA-3′, and mT/mG 5′-TCAATGGGCGGGGGTCGTT-3′. The PCR products for mT/mG wild-type and knock-in alleles are 330 bp and 250 bp, respectively. All procedures regarding the use and the handling of animals were approved by the Institutional Animal Care and Use Committee of the General Hospital of Chinese PLA. The approval number from Animal Experiment Committee is SQ2020112.

2.2. Tamoxifen Administration. The day of vaginal plug formation is designated as E0.5. Pregnant females receive a single intraperitoneal injection with tamoxifen (Sigma) at 50 μg/g body weight (20 mg/mL in 90% corn oil/10% 4-OHT). Pregnant female mice are treated with tamoxifen at E9.5, E11.5, E13.5, E15.5, and E17.5 of gestation according to the needs. Tamoxifen's postnatal intraperitoneal dosage is 180 μg/g/day for 3 days. For lineage tracing experiments, 6~8 embryos are used at each time point.

2.3. Immunofluorescence. Cryosections of the eyeball (8-10 μm) are incubated at room temperature in blocking solution (10% normal goat serum+0.3% Triton X-100 in PBS) for 45 minutes. Antibodies used for immunofluorescence are as follows: rabbit anti-ALDH3A1 (1 : 100; Proteintech), mouse anti-α B crystallin (1 : 200; Abcam), rabbit anti-GFAP (1 : 500; Abcam), rabbit anti-BRN3A (1 : 100; Abcam), rabbit anti-Sox9 (1 : 100; Abcam), rabbit anti-glutamine synthetase (1 : 400; Abcam), and rabbit anti- PDGFRα (1 : 500; Abcam). Secondary antibodies used are donkey-anti-rabbit Alexa Fluor-647 (1 : 400, Abcam) and goat-anti-mouse Alexa Fluor-647 (1 : 400, Abcam). All-section immunofluorescence data shown are imaged and photographed on a Zeiss spinning-disk confocal microscope (SDCM).

2.4. RNA Isolation and Quantitative PCR (qPCR). Total RNA is isolated with a RNeasy Micro kit (Qiagen) and reverse transcribed using a First-Strand cDNA Synthesis kit (Servicebio) according to the manufacturer's protocol. qPCR is performed using 400 ng of cDNA, 2× SYBR Green qPCR Master Mix (Servicebio), and the following primers: PDGFRα, forward primer CCTCATCTCCTGCCAGCTCTT, and reverse primer CTCCTCACTTCTGATTTCCACG.

2.5. Statistical Analysis. Data is presented as mean ± SEM. Differences between calculated averages are considered significant when $P < 0.05$ by Student's t-test. qPCR results between the different time points are studied by using a two-way ANOVA with Tukey's multiple comparisons test.

3. Results

3.1. PDGFRα-Expressing Cells in the Adult Mouse. When we perform tamoxifen administration on adult mice and collect eyeballs 7 days later, we observe the expression of PDGFRα in their adipose cells (Figures 1(a) and 1(e)), bone marrow stromal cells (Figures 1(b) and 1(f)), kidney mesangial cells (Figures 1(c) and 1(g)), and hepatic stellate cells (Figures 1(d) and 1(h)). In the eye of an adult mouse, mEGFP-positive cells are observed in the cornea, lens, iris, ciliary body, drainage structures, retina, optic nerve, and sclera (Figure 1(i)). mEGFP-positive cells in the iris, ciliary body, drainage structures, and sclera are most likely to be stromal cells. The expression map of PDGFRα cells and their descendants in the cornea (Figure 1(j)), lens (Figure 1(k)), and retina (Figure 1(l)) are investigated in more detail. mEGFP-positive cells are located mainly in the corneal stroma, lens epithelial and differentiating fibers, and the retina's ganglion cell layer (GCL). Several antibodies, including ALDH3A1 (a corneal crystallin), αB crystallin (a lens crystallin), and GFAP (a known glial marker), are used to identify mEGFP-positive cells in the eye. Staining of eye sections demonstrates that corneal stromal cells, lens epithelial, fiber cells, and retinal astrocytes contained mEGFP.

3.2. PDGFRα-Expressing Cells Contribute to Corneal Lineages in the Embryonic and Postnatal Stages. After a single dose of tamoxifen administration at E11.5, embryos that are harvested at E12.5 show the mEGFP-labeled cells are weakly dispersed in the prospective cornea, originating from the periocular mesenchyme (POM) (Figure 2(a)). When the eyes are harvested at P0 (Figure 2(i)) after a single dose of tamoxifen at E11.5, mEGFP-positive cells are shown to be confined to the corneal stroma. Other POM-contributing structures including the sclera, iris, and ciliary body, meanwhile, are found to contain mEGFP-positive cells. When these E11.5 tamoxifen-induced embryos are harvested at P14 (Figure 3(a)), it is confirmed that mEGFP-positive cells in

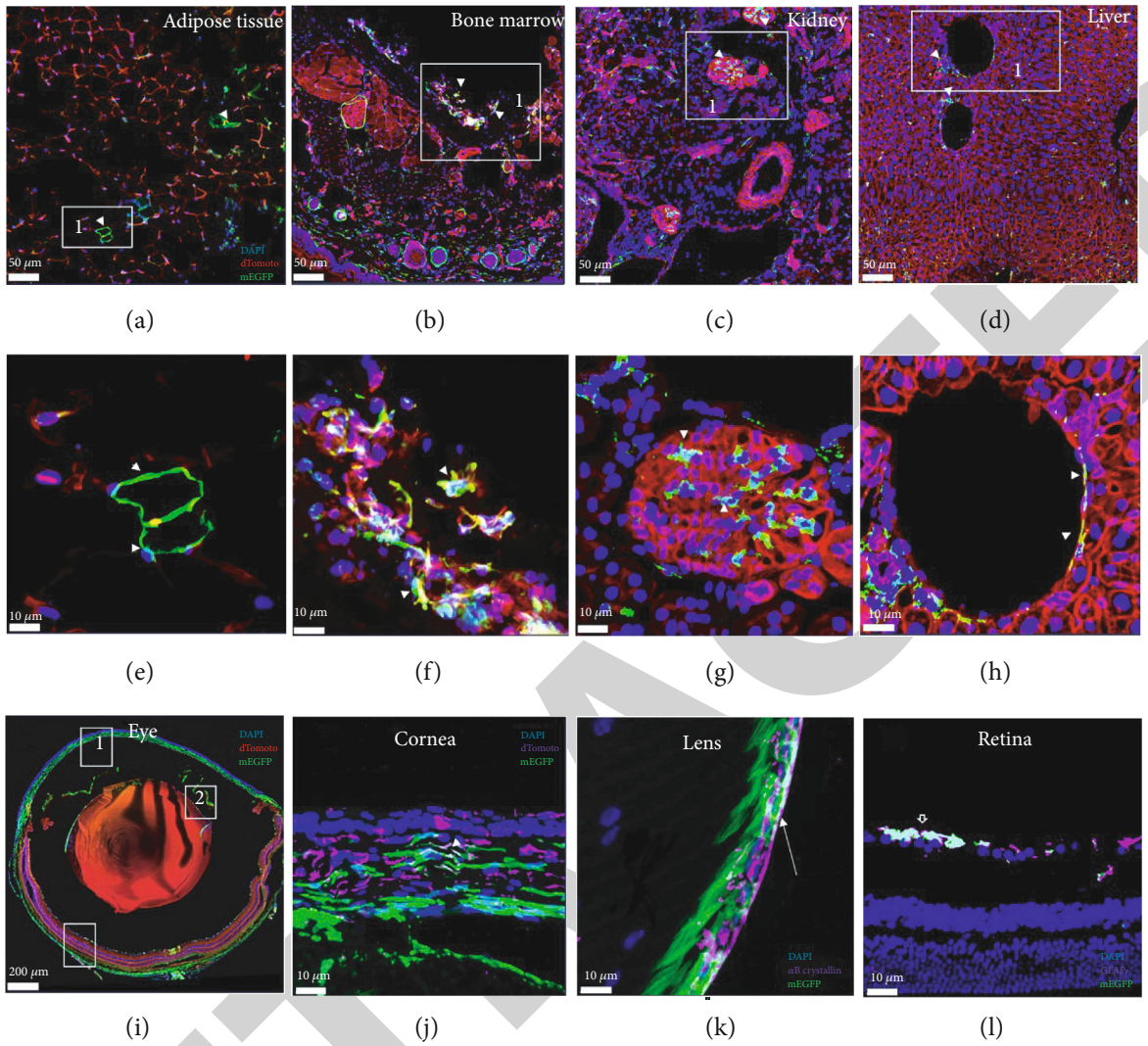

Figure 1: Cells expressing PDGFRα lineage in the adipose tissue, tail, kidney, liver, and adult eye (P60). Tamoxifen is administrated to an adult for 3 consecutive days and harvested at the seventh day. (a, e) Arrowheads point mEGFP staining in the adipose cells. (b, f) Arrowheads point mEGFP staining in the bone marrow stromal cells. (c, g) Arrowheads point mEGFP staining in the kidney mesangial cells. (d, h) Arrowheads point mEGFP staining in the hepatic stellate cells. (j–l) mEGFP-positive cells in the cornea, lens, and retina. (j) Arrowheads mark mEGFP-positive cells coexpressing ALDH3A1. (k) Arrows mark mEGFP-positive cells coexpressing αB-crystallin. (l) Hollow arrowheads mark mEGFP-positive cells coexpressing GFAP.

the cornea are keratocytes (Figure 3(b)). A similar expression pattern is seen with embryos induced with a single dose of tamoxifen at E13.5~E14.5 (Figures 2(b), 2(j), and 3(f)), when the POM cells between the anterior epithelium of the lens vesicle and the surface epithelium condense to form several flat layers that are separated from each other by a loose fibrillar extracellular matrix. In the stage when the posterior POM cells closest to the lens are flattened to form an endothelial monolayer (E15.5~E16.5), PDGFRα expression in the corneal stroma is induced to higher levels compared to previous time points by a single dose of tamoxifen. (Figures 2(c), 2(k), and 3(j)). When the eyes are administrated with tamoxifen at E17.5 (Figures 2(d), 2(l), and 3(n)), mEGFP-positive cells in the cornea are further increased and restricted to the corneal stroma.

For the analysis of the postnatal stages of eye development, four time points (P1, P3, P7, and P14) are selected to inject tamoxifen, and mouse eyes are harvested at P30. After birth, the PDGFRα expression is similar to E18.5 (Figures 4(b), 4(f), and 4(j)). As the eyelids start opening between P12 and P14 (Figure 4(n)), the corneal stroma significantly thickens, and the keratinocytes' nuclei continues to flatten with chromatin condensation. The flattened and matured keratinocytes stay mEGFP positive. At the latest analyzed time point (P60), cornea development is completed. At this stage, PDGFRα is still expressing in corneal stromal cells (Figure 1(j)).

Our results, therefore, indicate that although there are some differences in expression levels, PDGFRα expression is persistent not only in early corneal mesenchymal

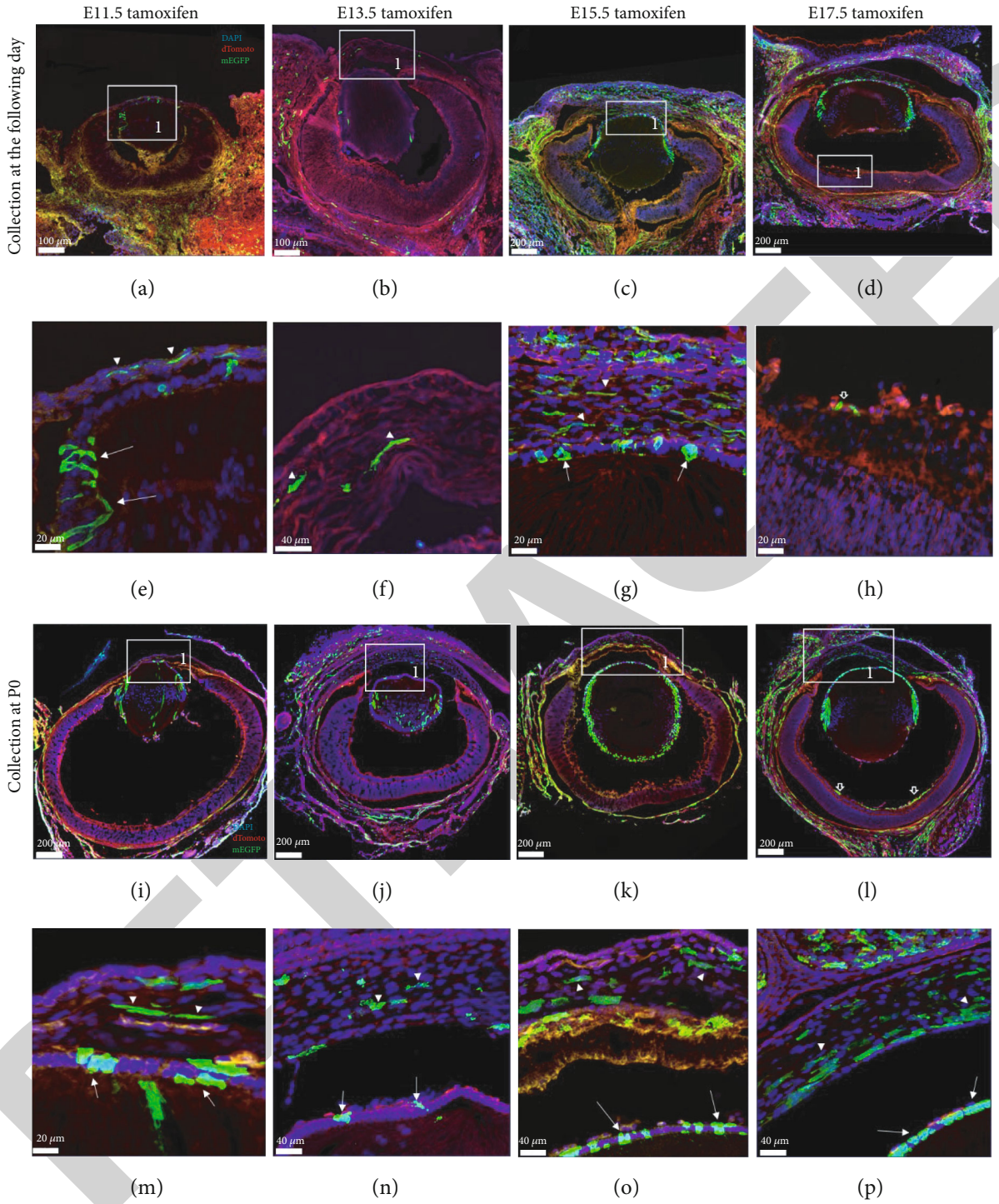

Figure 2: Cells expressing PDGFR*α* lineage in the embryonic eye. (a, e, i, and m) Tamoxifen is administrated at E11.5. (b, f, j, and n) Tamoxifen is administrated at E13.5. (c, g, k, and o) Tamoxifen is administrated at E15.5. (d, h, l, and p) Tamoxifen is administrated at E17.5. (a–h) Eyes are collected one day after tamoxifen administration. (i–p) Eyes are collected at P0. Arrowheads, arrows, and hollow arrowheads point mEGFP-positive cells in the cornea, lens, and retina, respectively.

progenitors at embryonic stages but also in the differentiated keratocytes in adulthood.

3.3. PDGFRα-Expressing Cells Contribute to Lens Lineages in the Embryonic and Postnatal Stages. At E12.5 (Figure 2(a)), when the lens vesicle is filled by the primary lens fibers, the epithelial cells divide and move to the lens equator (LE), mEGFP-positive cells are induced in the germinative zone, and lens bow (equator) after a single dose of tamoxifen at E11.5. Eyes harvested at P0 (Figure 2(i)) or P14

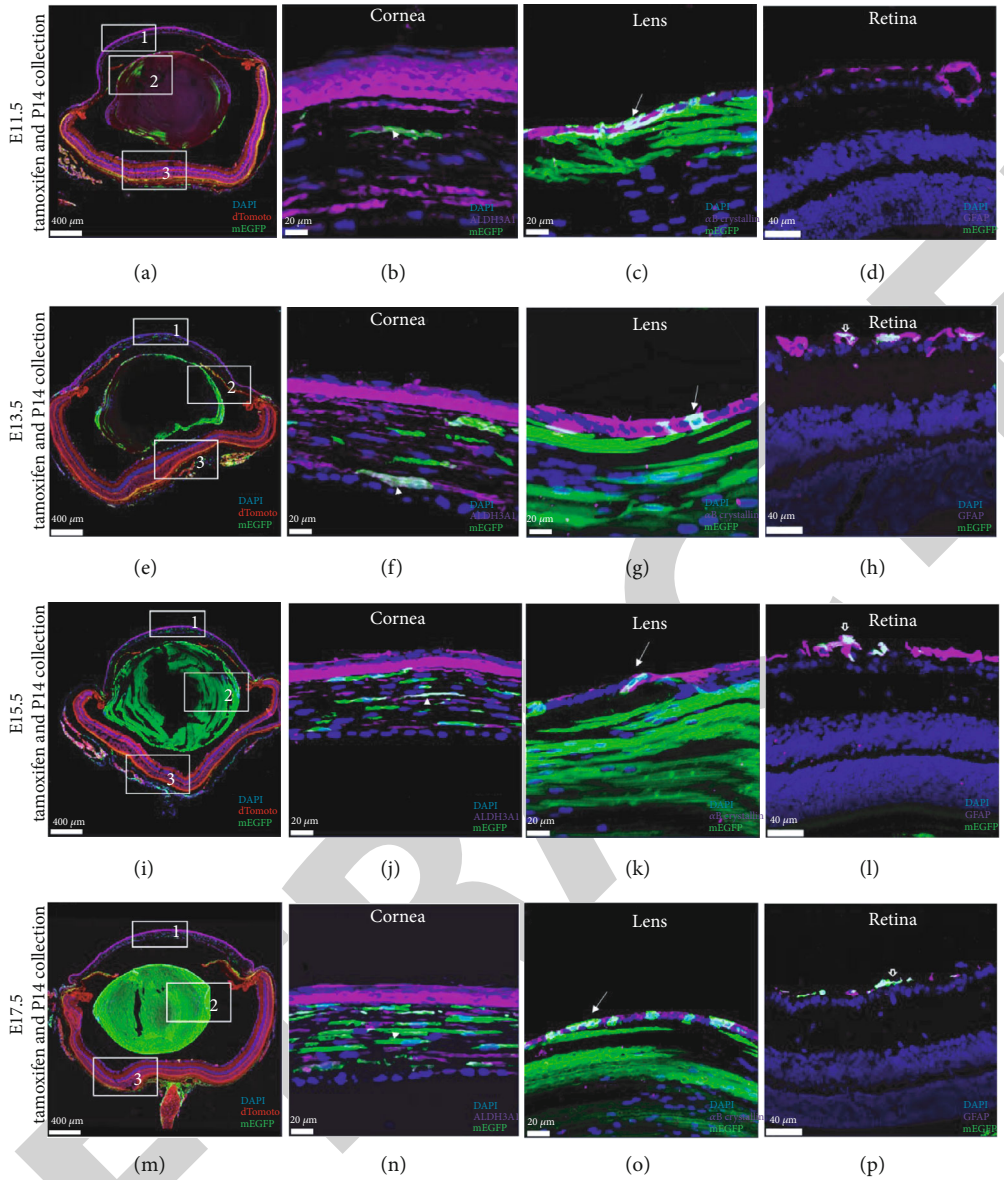

Figure 3: Cells expressing PDGFRα lineage from the embryonic to the postnatal eye. (b–d) Eyes are administrated with tamoxifen at E11.5 and collected at P14. (f–h) Eyes are administrated with tamoxifen at E13.5 and collected at P14. (j–l) Eyes are administrated with tamoxifen at E15.5 and collected at P14. (n–p) Eyes are administrated with tamoxifen at E17.5 and collected at P14. Arrowheads, arrows, and hollow arrowheads mark mEGFP-positive cells coexpressing ALDH3A1, αB-crystallin, and GFAP, respectively.

(Figure 3(c)) after a single dose of tamoxifen at E11.5 show PDGFRα expression in the lens epithelial cells and lens primary and secondary fiber cells. At E14.5, when the primary lens fibers elongate to close the lumen of lens vesicle, the PDGFRα expression is induced to be found in the lens epithelial cells after a single dose of tamoxifen at E13.5 (Figure 2(b)). We also detect PDGFRα expression in the majority of lens epithelial cells and their newly differentiated secondary lens fiber cells after a single dose of tamoxifen at E13.5, followed by consecutive days without treatment until P0 (Figure 2(j)) or P14 (Figure 3(g)). After a single dose of tamoxifen administration at E15.5, when the epithelial cells differentiate into secondary lens fiber cells, PDGFRα expression is induced in the lens epithelial and secondary fiber cells both in the short-term tracing experiments and long-term tracing experiments (Figures 2(c), 2(k), and 3(k)). The PDGFRα expression pattern of embryos induced at E17.5 and harvested E18.5 or later (Figures 2(d), 2(l), and 3(n)) is similar to those of embryos induced at E15.5.

As a result, mice induced at the postnatal stage (P1, P3, P7, and P14) and harvested at P30 exhibit mEGFP labeling of the entire lens epithelial cells and their differentiated lens secondary fiber cells (Figure 3), similar to E17.5-tamoxifen-induced embryos (Figures 4(c), 4(g), and 4(k)). Interestingly, at P14 (Figure 4(o)), when the centre of the lens is free of cellular organelles, such as nuclei and mitochondria, fewer

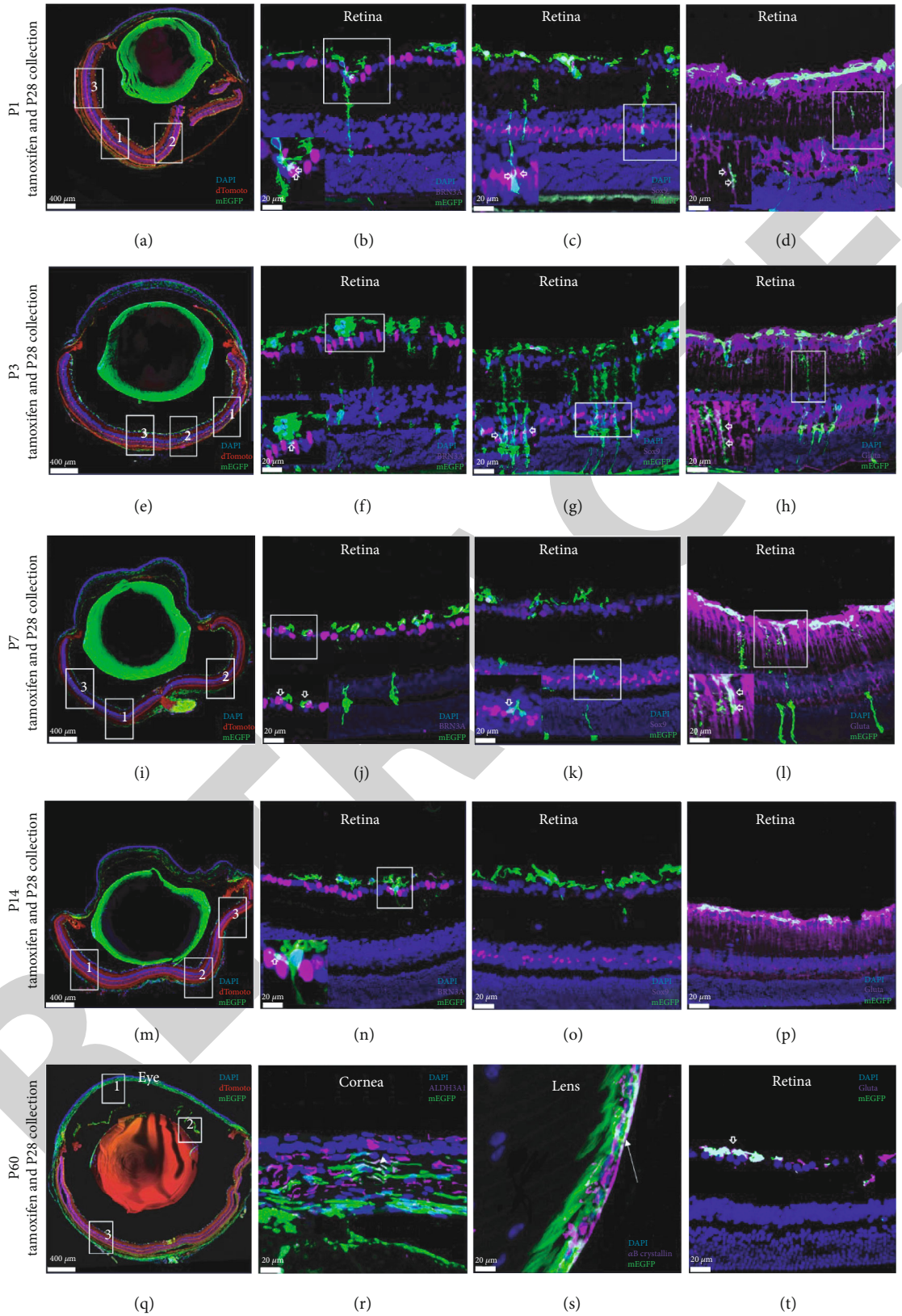

Figure 4: Cells expressing PDGFRα lineage in the postnatal eye. (b–d) Eyes are administrated with tamoxifen at P1 and collected at P28. (f–h) Eyes are administrated with tamoxifen at P3 and collected at P28. (j–l) Eyes are administrated with tamoxifen at P7 and collected at P28. (n–p) Eyes are administrated with tamoxifen at P14 and collected at P28. (b, f, j, and n) mEGFP-positive cells are not coexpressing BRA3A (a ganglion cell marker). (c, g, k, and o) Hollow arrowheads mark mEGFP-positive cells coexpressing Sox9. (d, h, l, and p) Hollow arrowheads mark mEGFP-positive cells coexpressing glutamine synthetase.

mEGFP-positive cells are in the secondary lens fibers and anterior lens epithelium than P1~P7. In adult eyes (P60) after tamoxifen administration for 3 consecutive days, the expression of PDGFRα is confined to the lens epithelial cells, most of which is located in the lens bow (Figure 1(k)).

Collectively, PDGFRα expression in the lens lineages is constant and presents all throughout the ages examined, whereas its expression levels in the lens epithelial cells and fiber cells decrease markedly in adults.

3.4. PDGFRα-Expressing Cells Contribute to Retinal Lineages in the Embryonic and Postnatal Stages. At E11.5, when the retina's two layers (outer and inner layers) are closely attached, we administer a single dose of tamoxifen. One day later, embryos are harvested, and the results show that mEGFP-positive cells are not detected in the retina (Figure 2(a)), even after birth (P0 and P14 collecting eyes). Embryos induced at E13.5 and harvested at E14.5 show that PDGFRα is not expressed in the retina (Figure 2(b)), and we fail to detect any mEGFP-positive cells in the neuroblastic layer (NBL), ganglionic cell layer (GCL), or inner plexiform layer (IPL) in E13.5 tamoxifen-induced embryos harvested at P0 (Figure 2(j)). However, the retinas harvested at P14 (Figure 3(h)) show dispersed PDGFRα expression in the nerve fiber layer (NFL), and these mEGFP-positive cells are colabeled with GFAP (astrocytes). The PDGFRα expression pattern of E15.5 tamoxifen-induced embryos (Figures 2(c), 2(k), and 3(l)) is similar to E13.5 tamoxifen-induced embryos. The mEGFP-positive cells in the retina are first detected at E18.5 harvested embryos after a single dose of tamoxifen at E17.5 (Figure 2(d)). When the eyes are harvested at P0 (Figure 2(l)) after a single dose of tamoxifen at E17.5, it shows that PDGFRα expression is confined to the centre of the retinal nerve's fiber layer. However, mEGFP-positive cells migrate to the retina's periphery at P14 harvested eyes (Figure 3(p)). Moreover, mEGFP-positive cells will not reach the periphery of the retina until P7 (data not shown).

In the postnatal retina, a completely different PDGFRα expression pattern is observed. In neonatal mice tamoxifen induced at P1, P3, and P7 and harvested at P30 (Figures 4(d), 4(h), and 4(l)), retinal astrocytes stay mEGFP positive in the nerve fiber layer, and some cells with radial fiber morphology also express mEGFP. Müller glial cells labeled by Sox9 and glutamine synthetase coexpress mEGFP. However, their expression decreases, and when embryos induced at P14 and harvested at P30 (Figure 4(p)), such expression is only visible in the nerve fiber layer, whereas they have vanished in the Müller glial cells. After tamoxifen administration for 3 consecutive days in adults (Figure 1(l)), PDGFRα expression is only present in retinal astrocytes.

Overall, our analyses suggest that PDGFRα is expressed in the astrocyte precursor cells that give rise to retinal astrocytes from E17.5 to adult stages, and a small portion of immature Müller glial cells within two weeks after birth.

3.5. mRNA Levels Support mEGFP Expression Data. qPCR is used to verify the changes in expression pattern observed in the reporter mice at RNA level. The cornea, lens, and retina cannot be separated well at E11.5, so mRNA from wild-type eyes at other corresponding time points is analyzed, and E13.5 is used as the control. In general, PCR results are basically consistent with the obtained expression pattern data. PDGFRα mRNA levels in the cornea start low at E13.5 and E15.5, followed by a significant increase at E17.5 (Figure 5(a)). From birth to maturity, PDGFRα mRNA remains at a high level, confirming mEGFP expression patterns in the cornea. PDGFRα mRNA levels in the lens start high at embryonic time points and decrease significantly at P7, to fall gradually to a vestigial level at P60 (Figure 5(b)). However, mEGFP-positive cells decrease significantly at P14 in the lens. Nevertheless, qPCR remains high in agreement with mEGFP expression patterns. The qPCR data for the retina is also consistent with the mEGFP expression data. PDGFRα mRNA abundance starts at a very low level in early embryonic time points and increases gradually, reaching the peak at P1~P7 (Figure 5(c)). Once the eyelids start opening, PDGFRα mRNA levels decrease significantly and maintain such levels.

4. Discussion

Although several reports [19] have clarified the importance of PDGFR-A during the development of cornea, lens, and retina, the PDGFRα's potential role has remained less clear in eye development. Our study provides PDGFRα expression maps with high spatial and temporal resolution and fate maps of PDGFRα-expressing cells. Moreover, we attempt to further explore the PDGFRα's role in the progressive formation of the eye by blocking PDGFRα signals at postnatal stages.

While PDGFRα expression in the developing cornea has not been analyzed in detail before, and albeit, there are very few reports [19] on the PDGFRα expression during corneal development, the results herein provide new information about PDGFRα signaling in the cornea. In early studies [19] of in situ hybridizations, PDGFRα mRNA is found to be highly expressed in the corneal stroma and periocular mesenchyme (POM) in the E15 mouse eyes. The identity and fate of these cells, however, remain unknown. In our short-term tracing experiments, we observed that PDGFRα could be expressed in the cornea as early as E12.5, when the POM began to migrate into the space between the anterior epithelium of the lens vesicle (LV) and the surface ectoderm (SE). In our long-term tracing experiments, we, however, do not detect the PDGFRα expression in the corneal endothelial cells, although both the corneal endothelial and corneal stromal cells were derived from POM [18, 24].

From E11.5~E17.5, PDGFRα-expressing cells gradually increase to very high level and are highly expressed throughout the postnatal corneal development. Early reports, using PDGFRα-GFP mouse, found PDGFRα expression in the corneal stroma in adults [25]. However, in the current study, PDGFRα cells and their descendants are confined to the corneal stroma at all examined ages, and marker analyses uncover that these cells are keratocytes, the most abundant group of cells in the corneal stroma. In contrast to the mouse cornea, PDGFRα is found on the corneal stromal keratocytes, corneal endothelial cells, and, to a much lesser extent, on the

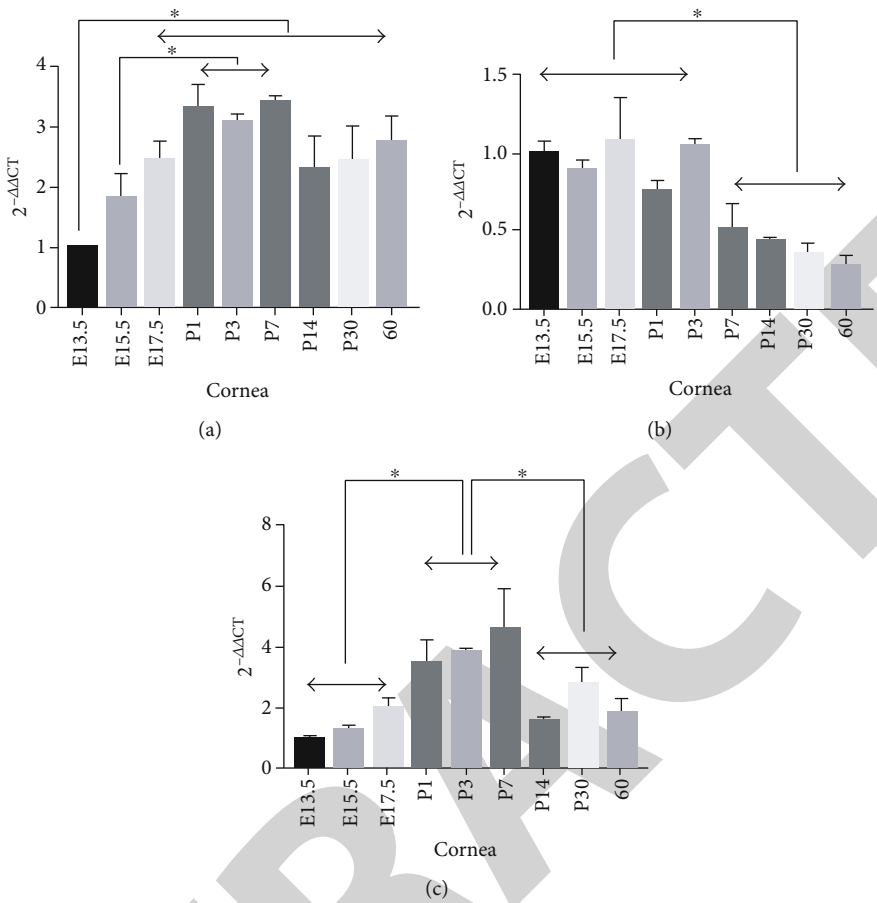

Figure 5: PDGFRα gene expression. Cornea (a), lens (b), and retina (c) quantitative PCR results (mean + SEM) at different developmental time points. E13.5 is selected as a reference sample, and base values set at 1. Fold change is represented on the y-axis ($2^{-\Delta\Delta Ct}$). $^*P < 0.05$, two-way ANOVA, and Tukey's multiple comparisons test.

epithelial cells in sections of human corneas [26]. Hence, attention should be payed to the different PDGFRα expression patterns among different species.

At embryonic and postnatal stages, we observed PDGFRα-expressing cells were localized to the lens epithelium and their differentiating lens fibers, partly in accordance with recent studies [19, 27]. However, a few differences might be pointed out. (1) Our short-term tracing experiments and immunostaining experiments indicated that PDGFRα-expressing cells were expressed at very early embryonic stages (E10.5), when the lens vesicle had just detached from the surface ectoderm and had a large central cavity. (2) PDGFRα expression had been restricted to the lens epithelium in our immunostaining experiments and previous studies using ISH or IHC [18, 27]. However, our long-term tracing experiments reveal that PDGFRα-expressing cells contribute to the lens epithelial and fiber cells. Therefore, in the differentiation process of the lens epithelial cells into fiber ones, the PDGFRα expression gradually decreases, or even stops. (3) As the lens continues to develop, the PDGFRα-expressing cells become more localized to the proliferating epithelial and fiber cells at the lens equator. Lens fiber cells in the posterior lens are not able to express PDGFRα in adults, even after long-term lineage tracing. The decline of PDGFRα expression in the fiber cells corresponds to the fiber cells' final differentiation process; the fiber cells lose their mitochondria and cell nuclei [3].

Our short-term tracing results concerning PDGFRα expression in the developing retina are in agreement with previous reports [20, 27], confirming the dynamic expression variation between different developmental stages. At early embryogenesis, PDGFRα is not expressed in the retina until E17.5. At E17.5~E18.5, PDGFRα expression is distributed in the centre of the retina. The mEGFP-positive cells in the centre of the retina's inner surface are astrocytes, instead of retinal ganglion cells (RGCs). These results conform to a previous report by Mudhar et al. [27], in which PDGFRα mRNA was observed at the optic nerve head (ONH) from E14 and spread across the retina's inner surface starting at E18. However, PDGFRα is not expressed in the retina until P1 in our immunostaining experiments. The difference between immunostaining experiments and short-term tracing experiments may be due to the fact that only a small number of cells in the nerve fiber layer expressed PDGFRα between E17.5 and E18.5, which are not detected by immunostaining. Interestingly, in our long-term tracing experiments, when eyes are

Table 1: Summary of the spatiotemporally specific contribution of the PDGFRα-expressing cells to the developing eye.

	Corneal stromal cells	Lens epithelial cells/fiber cells	Retinal astrocytes	Retinal Müller glial cells
E11.5	+	+++	-	
E13.5	+	+++	-	-
E15.5	++	+++	-	-
E17.5	+++	+++	+	-
P1	+++	+++	++	++
P3	+++	+++	+++	+++
P7	+++	+++	+++	+++
P14	+++	++	+++	-
P60	+++	+	+++	-

The (+) and (-) indicate the presence and absence of mEGFP-positive cells in the cornea, lens, and retina, respectively, with (+++) indicating highest levels of mEGFP-positive cells present.

harvested at P14 after a single dose of tamoxifen at E13.5 or E15.5, PDGFRα expression is detected in the retina's inner surface. Our results confirm the data by Mudhar et al. that the optic nerve head expresses PDGFRα from E14 and does not migrate to the retina at this time, whereas it will start to migrate around E18.

Postnatally, our findings on PDGFRα expression in the retina correspond with recent studies [27, 28]. PDGFRα expression in astrocytes in the nerve fiber layer persists throughout postnatal life into adulthood. Expression of PDGFRα significantly increases at P1~P7 and is associated with Sox9 and glutamine synthetase expression. A band of PDGFRα-expressing cells emerging in the INL is previously reported at P2. PDGFRα-expressing cells in the INL are most likely either bipolar neurons or Müller glia [27]. Our present data identifies a subpopulation of Müller glia cells in the INL, as cells expressing PDGFRα in the postnatal neural retina. No PDGFRα staining is visible in the INL of mice older than P14, which contradicts a previous study using PDGFRα-EGFP mice. Takahama et al. [25] reported that a subpopulation of amacrine cells in the inner nuclear layer expressed PDGFRα in the adult mouse retina. However, the number of these amacrine cells was very small, which may be the reason why we did not observe them.

Expectedly, PDGFRα mRNA levels do not fully match the expression of mEGFP. This is likely because mEGFP-positive cells represent PDGFRα-positive cells and their progeny cells, whereas these progeny cells may not express PDGFRα. Thus, mEGFP could be considered relevant as a contemporary or historic marker for PDGFRα expression. More studies are needed to comprehensively understand the PDGFRα's expression pattern in the eye.

5. Conclusions

Our expression and lineage tracing studies with PDGFRα CreERT2; mT/mG mice provide a comprehensive map of the PDGFRα expression in various ocular lineages and identify the major cell types involved in PDGFRα signaling during eye development (Table 1). Our findings not only confirm the previously reported expression patterns but also add new information of cell fate.

Data Availability

The datasets analyzed during the current study are available from the corresponding author on reasonable request.

Conflicts of Interest

No authors have conflict of interest to declare.

Acknowledgments

This study is supported by grant 2017YFA0103204 from the National Key R&D Program of China.

References

[1] S. Van Cruchten, V. Vrolyk, M. F. Perron Lepage et al., "Pre- and postnatal development of the eye: a species comparison," *Birth Defects Res*, vol. 109, no. 19, pp. 1540–1567, 2017.

[2] J. Graw, "The genetic and molecular basis of congenital eye defects," *Nature Reviews. Genetics*, vol. 4, no. 11, pp. 876–888, 2003.

[3] J. Graw, "Eye development," *Current Topics in Developmental Biology*, vol. 90, pp. 343–386, 2010.

[4] J. B. Miesfeld and N. L. Brown, "Eye organogenesis: a hierarchical view of ocular development," *Current Topics in Developmental Biology*, vol. 132, pp. 351–393, 2019.

[5] A. Cvekl and E. R. Tamm, "Anterior eye development and ocular mesenchyme: new insights from mouse models and human diseases," *BioEssays*, vol. 26, no. 4, pp. 374–386, 2004.

[6] R. Ohsawa and R. Kageyama, "Regulation of retinal cell fate specification by multiple transcription factors," *Brain Research*, vol. 1192, pp. 90–98, 2008.

[7] E. Collomb, Y. Yang, S. Foriel, S. Cadau, D. J. Pearton, and D. Dhouailly, "The corneal epithelium and lens develop independently from a common pool of precursors," *Developmental Dynamics*, vol. 242, no. 5, pp. 401–413, 2013.

[8] N. Noskovicova, M. Petrek, O. Eickelberg, and K. Heinzelmann, "Platelet-derived growth factor signaling in the lung. From lung development and disease to clinical studies," *American Journal of Respiratory Cell and Molecular Biology*, vol. 52, no. 3, pp. 263–284, 2015.

[9] S. Basciani, S. Mariani, G. Spera, and L. Gnessi, "Role of platelet-derived growth factors in the testis," *Endocrine Reviews*, vol. 31, no. 6, pp. 916–939, 2010.

[10] E. Folestad, A. Kunath, and D. Wagsater, "PDGF-C and PDGF-D signaling in vascular diseases and animal models," *Molecular Aspects of Medicine*, vol. 62, pp. 1–11, 2018.

[11] A. Kumar and X. Li, "PDGF-C and PDGF-D in ocular diseases," *Molecular Aspects of Medicine*, vol. 62, pp. 33–43, 2018.

[12] B. M. Klinkhammer, J. Floege, and P. Boor, "PDGF in organ fibrosis," *Molecular Aspects of Medicine*, vol. 62, pp. 44–62, 2018.

[13] J. Andrae, R. Gallini, and C. Betsholtz, "Role of platelet-derived growth factors in physiology and medicine," *Genes & Development*, vol. 22, no. 10, pp. 1276–1312, 2008.